SOOT FORMATION AND EVOLUTION CHARACTERISTICS OF PREMIXED HYDROCARBON FLAMES

JIANG XIAO

PhD

The Hong Kong Polytechnic University

2022

The Hong Kong Polytechnic University

Department of Mechanical Engineering

Soot Formation and Evolution Characteristics of Premixed Hydrocarbon Flames

Jiang Xiao

A thesis submitted in partial fulfillment of the requirements
for the Degree of Doctor of Philosophy

January 2022

Certificate of Originality

I hereby declare that this thesis is my own work and that, to the best of my knowledge and belief, it reproduces no material previously published or written, nor material that has been accepted for the award of any other degree or diploma, except where due acknowledgement has been made in the text.

_____ (Signed)

JIANG Xiao (Name of student)

Abstract

Soot particles formed during the incomplete combustion of hydrocarbons not only reduce the efficiency of many combustion devices but also adversely affect the global climate, air quality and human health. The study of soot formation and evolution processes is of great importance to predict and control soot emissions. In the present study, the newly proposed and developed weighted fraction Monte Carlo (WFMC) method with reactive force fields (ReaxFF) molecular dynamics (MD) simulations are used to gain better insight into the soot formation and evolution processes.

The new WFMC method is firstly proposed by introducing the additional fraction function based on the concept of weighted numerical particles to reduce the stochastic error. The WFMC method is validated by comparing its numerical simulation results with the corresponding analytical solutions, sectional method and other Monte Carlo (MC) method schemes (i.e., direct simulation Monte Carlo (DSMC) and multi-Monte Carlo (MMC) methods) in excellent agreement. The stochastic errors obtained by different MC method schemes are further studied, and the results show that the WFMC method can significantly reduce the stochastic error for higher-order moments and particle size distribution (PSD) over the larger particle size regime with a slightly higher computational cost.

The further development of this new WFMC method is then combined with the Lagrangian particle tracking (LPT) and coupled with the detailed soot model to

study soot formation and evolution in ethylene laminar premixed flames. The LPT-WFMC method is validated by both the experimental results and the numerical results of the DSMC and MMC methods. The evolution of soot number density, volume fraction and particle size distribution are investigated for different flame conditions which shows that LPT-WFMC method can extend the soot PSDs and reduce the statistical error for larger particle size regime. The effects of different parameters in the soot model on the soot PSDs are investigated by the parametric sensitivity analysis.

In order to study the atomic aspect of soot nucleation, the physical dimerization of different polycyclic aromatic hydrocarbon (PAH) structures is studied by the MD simulations. The collisional association and dissociation processes of each PAH species are investigated for different temperatures, impact parameters and orientations. The dissociation of the PAH dimers is also statistically analyzed by using the Rice-Ramsperger-Kassel (RRK) theory of unimolecular dissociation to gain a deeper insight of the energy transformation, and the contributions of intermolecular and intramolecular degrees of freedom.

Finally, the soot formation and evolution processes are studied by using ReaxFF MD simulations for different carbon dioxide additions. The transformation from PAH precursors to the final soot nanoparticle under three stages of soot formation and evolution processes including nucleation, surface growth and coagulation, and graphitization is observed. The chemical effects of different carbon dioxide additions on the soot properties and reaction pathways are also analyzed.

In summary, the newly proposed and developed LPT-WFMC method in the present study has demonstrated high capability in predicting soot PSDs. Meanwhile, the ReaxFF MD simulations in the present study also provide a better understanding of the soot nucleation process.

Acknowledgements

I would like to extend my sincerest thanks and gratitude to my Supervisor, Prof. Tat Leung Chan for his comprehensive support, inspiring guidance, valuable feedback, understanding, patience and encouragement throughout my study at the Department of Mechanical Engineering, The Hong Kong Polytechnic University (PolyU). His enthusiasm and flexibility allowed the research to develop into interesting new directions. I appreciate his extensive knowledge and respectable attitude towards academic research as well as his kind and generous support to me. I would also like to extend my thanks to Dr. Hongmei Liu and Dr. Shuyuan Liu of Prof. Chan's research group for their kind guidance and selfless help.

I would like to express my appreciation to the Scientific Officer, Mr. Raymond Chan and Technical Officer, Mr. Chris Tsang for their invaluable technical support. My appreciation also goes to the administrative supporting staff, Ms. Lily Tam and Ms. Michelle Lai who provided kind administrative support. I would also like to express my thanks to the financial support from the research studentship granted by PolyU for accomplishing this research work. I am also grateful to Mr. Chunhui Ai, Mr. Xingyi Shi and Mr. Wang Fei in the research offices, and other friends in Hong Kong for their friendship and help during my study at PolyU.

Finally, I wish to express my heartfelt gratitude to my family members for their love, support, understanding and encouragement during my study at PolyU.

Table of Contents

List of Figures

List of Tables

Nomenclature

A_s	surface density of soot particles (cm^2/cm^3)
A_v	Avogadro's number (1/mol)
BO_{ij}	bond order between atoms i and j
C	fraction constant
C_0	waiting-time parameter
C_D	drag coefficient
C_{ij}	coagulation rate between particle, i and j (1/s)
C_{mass}	mass of a carbon atom (kg)
d_A	diameter of a single aromatic ring (m)
d_c	collision diameter (m)
d_f	diameter of a fluid molecule (m)
d_g	gyration diameter (m)
d_{PAH}	diameter of the incipient PAH species (m)
d_{pp}	diameter of a primary particle (m)
d_{soot}	diameter of a soot particle (m)
D	diffusion coefficient (m^2/s)
D_f	fractal dimension
E_0	unimolecular threshold energy (kJ/kmol)
E_a	activation energy (kJ/kmol)
E_f	activation energy of of soot formation (kJ/kmol)
E_{kin}	kinetic energy energy of a system (kJ/kmol)

E_O	activation energy of soot oxidation (kJ/kmol)
E_{pot}	potential energy of a system (kJ/kmol)
E_{rel}	relative translational energy (kJ/kmol)
E_{total}	total energy of a system (kJ/kmol)
f_{drag}	drag force (N)
G	condensation kernel (m^3/s)
H	enthalpy (kJ)
J_0	nucleation kernel (/s)
k	rate constant for association and dissociation
k_B	Boltzmann constant (J/K)
k_f	pre-fractal factor
Kn	Knudsen number
L_0	impact parameters (m)
L_x	representative length scale of particles (m)
m_i	mass of atom, i (kg)
$m_{v,u}$	reduced mass of particles v and u (kg)
M_C	molecular weight of a C atom (kg/kmol)
M_k	kth order moment
M_{fuel}	mass concentration of vaporized fuel (kg/m^3)
M_{growth}	contributions of soot mass concentration from surface growth (kg/m^3)
M_{nucl}	contributions of soot mass concentration from nucleation (kg/m^3)

M_{ox}	contributions of soot mass concentration from oxidation (kg/m^3)
M_{soot}	soot mass concentration (kg/m^3)
n	number density of aerosol particles (#/m^3)
n_p	number of primary particles
N_{coag}	contributions of soot number density from coagulation (#/m^3)
$N_{C,PAH}$	number of carbon atoms in the incipient PAH species
N_i	particle number within the ith section
N_{nucl}	contributions of soot number density from nucleation (#/m^3)
N_{soot}	soot number density (kg/m^3)
$p_{critical}$	critical ratio
p_i	momentum of particle i (kg·m/s)
p_u	partial pressure of unburned fuel (Pa)
P	pressure (Pa)
P^{birth}	probability of survived numerical particles
q_i	heat flux (W/m^2)
r_i	coordinate of particle i (m)
r_0	equilibrium bond length (m)
Re_p	relative particle Reynolds number
R_u	universal gas constant (kJ/(K·kmol))
s	number of degrees of freedom
S_D	parametric sensitivity on particle size
S_n	parametric sensitivity on particle number density

St	Stokes number
Δt	time-step (s)
δt	time-step (s)
T_u	local temperature (K)
u_f	fluid velocity (m/s)
u_i	ith-component velocity (m/s)
$\overline{u}_i$	average soot particle velocity in each cell i
$u_{p,j}$	velocity of jth particle in each cell i
u_T	thermophoretic velocity (m/s)
v	volume of a particle (m^3)
v''	new size after the coagulation event (m^3)
v'''	new size after the probabilistic removal (m^3)
V	volume of simulation box (m^3)
$V_{k,i}$	kth species diffusive velocity (m/s)
$V_{c,i}$	velocity of correction diffusion (m/s)
$V_{ok,i}$	velocities of ordinary diffusion of kth species (m/s)
$V_{Tk,i}$	velocities of thermal diffusion of kth species (m/s)
w_i	weight of the numerical particle
$\overline{w}$	average particle weight in each size interval
w''	new weight after the coagulation event
w'''	new weight after the probabilistic removal
W_k	kth species of molecular weight (kg/kmol)
x_i	coordinate of ith-component

$x\mathrm{C}_{\mathrm{soot}}\mathrm{–H}$	number of sites per soot surface area (#/m^2)
$x\mathrm{C}_{\mathrm{soot}}\cdot$	number of dehydrogenated sites per surface area (#/m^2)
X_k	mole fraction of kth species
Y_k	mass fraction of kth species

Greek Symbols

α	aging factor
α_{ij}	fraction function
α_m	accommodation factor
β	collision kernel function (m^3/s)
Γ	arbitrary particle properties
ε	depth of attractive well (m)
Θ_k	thermal diffusion ratio of kth species
κ	volume viscosity (Pa·s)
λ	heat conduction coefficient (W/(m · K))
λ_f	mean free path of a fluid molecule (m)
μ	dynamic viscosity (Pa·s)
ρ	density (kg/m^3)
ρ_f	density of fluid (kg/m^3)
ρ_s	density of soot particle (kg/m^3)
ρ_{soot}	density of soot particle (kg/m^3)

σ	collision diameter for the pair of atoms (m)
σ^2	variance of algorithm
τ	waiting time (s)
τ_f	flow characteristic time (s)
τ_{ij}	viscous stress tensor (Pa)
τ_p	particle relaxation time (s)
γ	sticking probability
ϕ	local unburned equivalence ratio
Φ_{ij}	coagulation rate from the group of physical particles, i and j (#/s)
χ	expected conserved scalar
$\dot{\omega}_k$	kth species molar production rate (mol/s)
ω_{NSC}	NSC soot mass oxidation rate per unit surface area (kg/(m^2·s))
$\dot{\omega}_T$	chemical source term of energy (kJ/(m^3·s))

Abbreviations

amu	atomic mass unit
AALH	aromatic aliphatically linked hydrocarbon
ADLH	aromatic directly linked hydrocarbon
APLH	aromatic pericondensed polycyclic hydrocarbon
CAHM	carbon-addition-hydrogen-migration
CFD	computational fluid dynamics
CG	conjugate gradient
cPAHs	curved polycyclic aromatic hydrocarbons
C.O.M.	center-of-mass
DFT	density functional theory
DFT-D3	dispersion corrected density function theory
DQMOM	direct quadrature method of moments
DWOSMC	differentially weighted operator splitting Monte Carlo
EEM	electronegativity equalization method
EFF	exponential fraction function
EGR	exhaust gas recirculation
FF	force field
FGR	flue gas recirculation
FVM	finite volume method
GC/MS	gas chromatography/mass spectrometry
GDE	general dynamic equation

HAB	height above burner
HACA	H-abstraction-carbon-addition
HFF	hyperbolic fraction function
HMMC	higher-order moment conserving
HR-AFM	high resolution atomic force microscopy
HRTEM	high-resolution transmission electron microscopy
IVR	intramolecular vibrational energy redistribution
LII	laser induced incandescence
LMMS	laser microprobe mass spectrometry
LPT	Lagrangian particle tracking
MC	Monte Carlo
MD	molecular dynamics
MFA	mass flow algorithm
MMC	multi-Monte Carlo
MOMIC	method of moments with interpolative closure
MOMs	methods of moments
ODEs	ordinary differential equations
OSMC	operator splitting Monte Carlo
PAHs	polycyclic aromatic hydrocarbons
PBEs	population balance equations
PE	potential energy
PISO	pressure-implicit with splitting of operators
PM3	parametric method 3

PSD	particle size distribution
QEQ	electronegativity equilibration
QM	quantum mechanics
QMOM	quadrature method of moments
ReaxFF	reactive force field
RSD	relative standard deviation
RSRs	resonance-stabilized radicals
SMPS	scanning mobility particle sizer
SMs	sectional methods
SWOSMC	stochastically weighted operator splitting Monte Carlo
SWPM	stochastic weighted particle method
TEMOM	Taylor expansion method of moments
WFA	weighted flow algorithms
WFMC	weighted fraction Monte Carlo

Chapter 1 Introduction

1.1 Research Background and Scope

Combustion occurs in many different engineering applications such as internal combustion engines, power plants, waste incinerators and burning fossil fuels etc. Currently, fossil fuel combustion is the primary source of energy production (more than 80%) (Orhan et al., 2015; Dale, 2021). However, the generation of energy from fossil fuels is also a major source of air pollutants such as carbon dioxide (CO_2), sulfur oxides (SOx), nitrogen oxides (NO_X), polycyclic aromatic hydrocarbons (PAHs) and soot/black carbon particles (Wang et al., 2021b). These by-products of hydrocarbon fuel combustion not only reduce the efficiency of combustion systems but may also have adverse effect on the global climate, air quality and human health (Saggese, 2015; Seinfeld and Pandis, 2016; Shen et al., 2021). Especially, the nano and ultrafine particles (i.e., less than 0.1 μm or 100 nm in diameter) are the most harmful ones because they can penetrate the human respiratory system and deposit on the lungs (Jacobson, 2010; Saggese, 2015; Saini et al., 2021). In addition, the soot particle surfaces consist of organic compounds such as PAHs in combustion and other toxic substances can cause a risk to the respiratory system (Ong, 2017; Saini et al., 2021). Short term effects include pulmonary and cardiac diseases which can result in early death as well as pregnancy losses. Long term effects include cancer, disease of the respiratory system, fetal side of human placenta, etc. (Waldheim, 2014; Bové et al., 2019; Holder et al., 2021).

From environmental aspects, soot emissions can pose adverse effects on air quality such as reducing visibility (Brown et al., 2003; Kelesidis and Pratsinis, 2021). Before settling on the ground, the airborne spread of soot/black carbon particles can act as nuclei for cloud formation, which can lead to secondary environmental problems such as changing precipitation and snowfall patterns (Pueschel et al., 1997; Ong, 2017). Since soot particles can strongly absorb solar energy, soot emission is regarded as one of the most important sources for global warming (Jacobson, 2001; Martin et al., 2022). Moreover, soot emissions also show some effects on global and regional climate change (Bond et al., 2013).

Despite the adverse effects of the soot particles on health and environment, there are also many applications in industrial fields of the soot particle formation. The soot particles play an important role of radiative heat transfer in the combustion system (Wang, 2011; Martin et al., 2022). Besides, carbon black had been a widely used material in prehistoric cave paintings (Martin, 2020). Nowadays, carbon black is also widely used as pigment for printing, paints, coatings and reinforcement of rubber products (e.g., tires) (Findik et al., 2004; Keller, 2019; Pascazio et al., 2021).

Due to the above-mentioned aspects of the soot or black carbon particles, it is necessary to gain deeper understanding of the soot particle formation and evolution processes for improving the combustion efficiency and controlling the soot particle evolution and formation (Bockhorn, 2013). It is generally agreed that soot particles consist of solid carbon and a few other elements including hydrogen and oxygen produced by the hydrocarbon pyrolysis in the high temperature zone of combustion. The soot emission from combustion process is

usually determined by many different processes (e.g., soot inception and oxidation). The details of these combustion processes have been an important topic of considerable debate for many years. In general, the aromatic substances grow by adding other small hydrocarbon molecules to generate larger PAHs (Singh, 2006; Reizer et al., 2021). Growing of the polyaromatic hydrocarbons finally lumps into the smallest detectable particles with size around 1 nm (i.e., 1×10^{-9} m) in diameter and mass of approximately 1000 atomic mass unit (amu) (Kennedy, 1997). Figure 1.1 shows a conceptual schematic of this overall soot formation process (Wang and Chung, 2019).

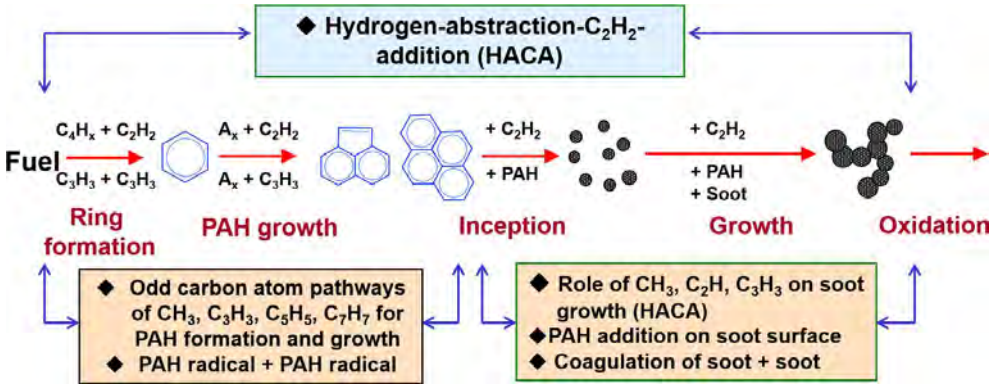

Figure 1.1 Schematic of overall pathways for soot formation (Wang and Chung, 2019).

Many experimental techniques for soot diagnostics have been developed. Optical investigative techniques (e.g., laser induced incandescence (LII)) are non-intrusive methods which do not perturb the flames under the experimental investigation. High temporal resolution and information of three-dimensional flame structures can be provided (Cenker, 2014; Xiong et al., 2021). Probe sampling of the emitted soot particles is an ex-situ method. This ex-situ method can be applied to study the structure and morphology of soot particles (Battin-Leclerc et al., 2013). But such detail information cannot be obtained by using optical imaging techniques

(Ong, 2017; Kim et al., 2021). However, the experimental methods are difficult to set up and costly, and the information obtained is not temporally and spatially complete. Hence, development of advanced computational methods for studying and understanding the soot formation and evolution processes in flame is essential due to the feasibility and cost-efficiency of numerical approach.

Soot formation and evolution involve various complex and concurrent chemical and physical processes: the fluid mechanics to predict the flow field, combustion model to predict the change in thermodynamic and chemical properties, and aerosol dynamics model to predict the particle size distribution (Chong, 2018). Many soot models have been proposed, which could be classified into three categories (Kennedy, 1997; Valencia et al., 2021): empirical model, semi–empirical model and detailed model. The empirical model is attempted to capture the trends of soot particle emission via construction of the correlation of the specific experimental conditions (Micklow and Gong, 2002; Valencia et al., 2021). Semi–empirical models are developed for combining the empirical model with mathematical equations to describe the soot particle concentration/number density, volume and mass fractions (Kazakov and Foster, 1998; Valencia et al., 2021). The most famous classical semi–empirical model is the two–step model (Nishida and Hiroyasu, 1989). These models consist of two competitive reactions including formation and oxidation of the soot in Arrhenius type. By contrast, the detailed soot models could provide details of the soot formation and evolution processes. The model contains the description of chemical kinetics and reaction mechanisms in all phases, and includes the gaseous chemistry and aerosol dynamics. In these soot models, the soot particles are usually considered to be generated by the collision of the large

polycyclic aromatic hydrocarbons. Then the population of these soot particles may evolve through collisions among themselves and surface reactions with gas-phase species. These particle behaviors could be governed by the population balance equations (PBEs) (Marchisio and Fox, 2013; Raman and Fox, 2016), which is also called the general dynamic equation (GDE) (Friedlander, 2000; Zhou and Chan, 2016). PBEs are convection-diffusion equations with the source terms including nucleation, surface growth, coagulation and oxidization. Since PBEs are the partial integral-differential equations, analytical solutions of the PBEs exist for only several simple cases (Smoluchowski, 1916; Aldous, 1999; Ramkrishna, 2000). As a result, some numerical methods are developed for obtaining the precise numerical solutions. These numerical methods can be classified into three categories: sectional methods (SMs) (Gelbard et al., 1980; Jeong and Choi, 2001; Prakash et al., 2003; Mitrakos et al., 2007; Woo et al., 2021); methods of moments (MOMs) (Frenklach, 2002a; Yu et al., 2008; Lin and Chen, 2013; Yu and Chan, 2015; Chan et al., 2018; Liu et al., 2019b; Jiang et al., 2021) and Monte Carlo (MC) methods (Haibo et al., 2005; Zhao et al., 2009; Zhou and He, 2014; Zhou et al., 2014; Liu and Chan, 2017b; Liu and Chan, 2018b; Jiang and Chan, 2021a; Boje and Kraft, 2022).

SMs have the moderate costs of computational resources, however, the algorithm for the sectional method could be complex (Wei and Kruis, 2013; Woo et al., 2021). MOMs are highly computational efficient, but it has some requirements on particle size distribution as the initial condition, which is a variable parameter during the numerical simulation (Wei and Kruis, 2013; Jiang et al., 2021). The MOMs have the high performance only for the lognormal particle size distribution. To overcome the shortcoming of the MOMs, the new Taylor expansion

method of moments (TEMOM) was proposed which exhibits a significant advantage in computational efficiency by comparison with other methods of moments and the sectional methods (Yu et al., 2008; Yu and Chan, 2015). MC methods are by far the most accurate method. A typical flow chart of MC algorithm is shown in Figure 1.2 (Efendiev, 2004). MC methods can be easily incorporated with several particle internal coordinates (Yapp et al., 2016; Boje and Kraft, 2022). However, the statistical variance and high computational cost are the main limitations of MC methods (Xu et al., 2015; Zhou et al., 2020; Jiang and Chan, 2021a). Since only a finite number of numerical particles could be simulated, the uncertainty of particle size distribution (PSD) function is inevitable.

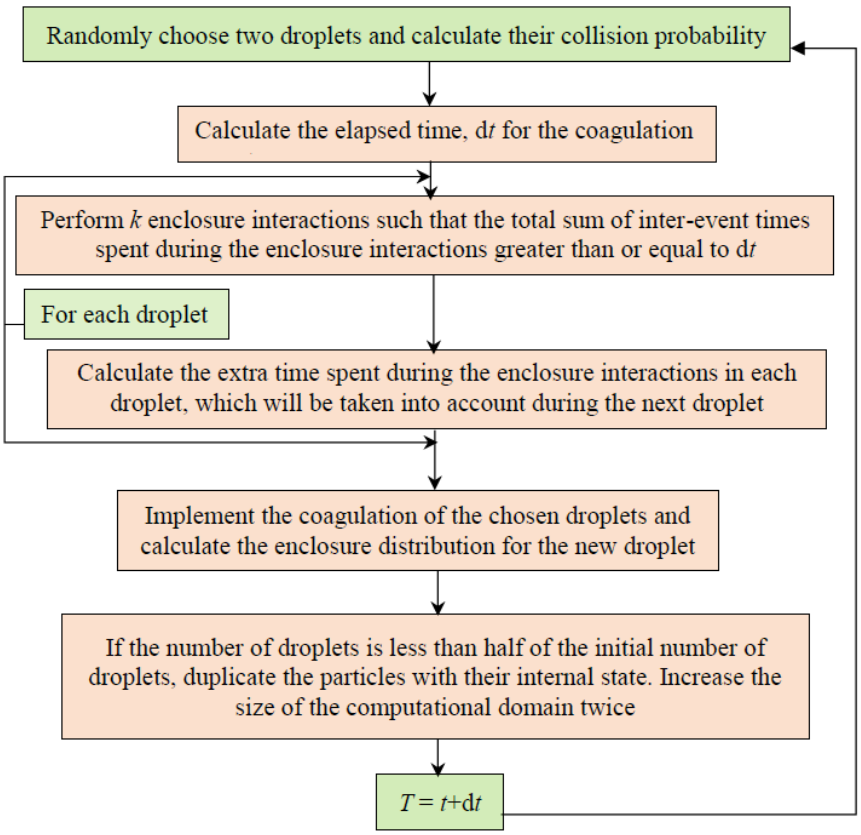

Figure 1.2 A typical flow chart of Monte Carlo algorithm (Efendiev, 2004).

In order to reduce the statistical noise of MC methods, the weighted Monte Carlo method is developed. Different weighted MC method schemes including multi-Monte Carlo (MMC) method (Zhao et al., 2005b), mass flow algorithm (MFA) (Eibeck and Wagner, 2001a), weighted flow algorithms (WFA) (DeVille et al., 2011) and stochastic weighted particle method (SWPM) (Patterson et al., 2011; Menz et al., 2013) were proposed and shown to possess higher computational efficiency and lower stochastic error. However, the weight function in MMC method is not adjustable, which may limit the application of MMC methods. To overcome this limitation, WFMC method (Jiang and Chan, 2021a) has recently been developed based on MMC method in the present study. The proposed WFMC method aims to solve PBEs for aerosol dynamics with minimized stochastic errors by introducing the adjustable weighted function.

Apart from the aerosol dynamics, soot formation and evolution should also consider the reacting flow fields. In order to gain a deeper understanding of the soot formation and evolution in the flame, it is necessary to solve the coupling transport equations between PBEs and the governing equations of reacting flow. The numerical modelling for describing the coupled aerosol dynamics and fluid flow can be classified into Eulerian and Lagrangian methods (He and Zhao, 2016; Murer et al., 2021). In the Eulerian description of the particle, the particle is treated as a continuum phase and its governing equations are developed on a control volume, which is in a similar form as that for the fluid phase (Tsantilis et al., 2002; Olin et al., 2015; Rodrigues et al., 2018; Murer et al., 2021). In the Lagrangian description of particles, each particle is treated as a discrete phase and is tracked individually. The trajectory of particle can be obtained under Lagrangian description

(Hu et al., 2001; di Veroli and Rigopoulos, 2010; Sweet et al., 2018; Kong et al., 2021). Both of these Eulerian and Lagrangian methods have been developed and reported (Patankar and Joseph, 2001; Kruis et al., 2012; Olin et al., 2015; Liu and Chan, 2017a; Patel et al., 2017; Murer et al., 2021; Panchal and Menon, 2021). In the present study, the coupling PBEs of aerosol dynamics and detailed soot model with computational fluid dynamics (CFD) approach is achieved by Lagrangian particle tracking (LPT) method. Soot particles are treated as a dispersed Lagrangian particle, and the information about the individual soot particle trajectory can then be obtained.

Although numerous soot models have been proposed and developed, an accurate soot modelling study still requires a thorough knowledge of the soot inception and growth mechanism (Shabnam et al., 2019). However, the soot inception from small hydrocarbon molecules to the incipient soot particles still needs further study. Three conceptual routes could be assumed for soot inception. In Figure 1.3, mechanism A is described by the precursor which grows from “two-dimensional” polyaromatic hydrocarbons to curved fullerene-like structures (Wang, 2011; Martin et al., 2022); mechanisms B and C show the physical coagulation of medium-sized polyaromatic hydrocarbons into stacked clusters (Frenklach and Wang, 1994; Herdman and Miller, 2008; Martin et al., 2022) and the reaction or chemical collision of PAHs to crosslinked three-dimensional structures (Richter et al., 2000; Violi et al., 2002; Keller, 2019; Martin et al., 2022), respectively. Though all these pathways which have contributed to soot inception process in flame, their relative significance or possibility at various flame conditions is still not well known. In addition, apart from the above possible nucleation mechanisms, many new soot

nucleation mechanisms have also been proposed including resonance-stabilized radicals (RSRs) chain reaction mechanism (Johansson et al., 2018), the mechanism of combining physical aromatic ring stacking and covalent bonding for rim-based pentagonal rings species (Martin et al., 2019), physical/chemical nucleation mechanism of curved PAHs (cPAHs) (Martin et al., 2017) and the aromatic penta-linked hydrocarbons mechanism (Pascazio et al., 2020).

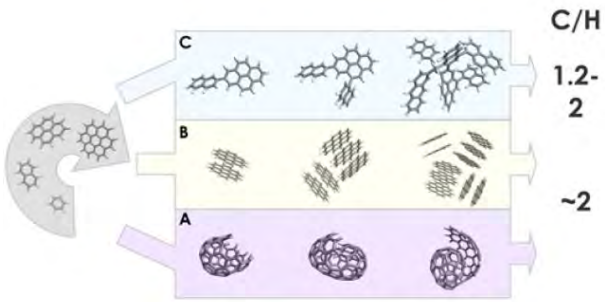

Figure 1.3 Conceptual mechanisms of soot particle nucleation (Wang, 2011).

To gain a comprehensive understanding of soot nucleation mechanism at atomistic level, a computationally feasible method is required. Quantum mechanics (QM) based density functional theory (DFT) can provide information on chemical reactions. However, the QM based methods are always limited to a small system size because of the high computational costs which are unsuitable for observing meaningful chemistry in combustion (Morawietz and Artrith, 2021). Empirical methods such as tight binding or force field (FF) based methods can provide reasonably chosen time scale without having much computational cost. These molecular potentials are non-reactive cases due to rigid connectivity requirements which also defeats the purpose of simulation of hydrocarbon combustion. Therefore, the reactive force field (ReaxFF) has thus been developed to incorporate bond breaking and bond formation into the force field potentials (van Duin et al., 2001).

ReaxFF is based on bond-order/bond-distance formulation to dynamically simulate chemical reactions in various systems of solid/liquid/gas interfaces. As opposed to empirical force field methods, ReaxFF can provide reasonable description of chemical reactivity and products formation of sufficiently larger systems (> 1000 atoms) while maintaining sufficient accuracy as QM based DFT methods. In the present study, the ReaxFF with molecular dynamics (MD) are adopted for gaining better insight of soot nucleation mechanism.

1.2 Research Motivation and Objectives

The stochastic error in Monte Carlo (MC) method is inevitable while the weight distribution in traditional weighted MC method schemes (e.g., direct simulation Monte Carlo (DSMC) method, multi-Monte Carlo (MMC) method) is not adjustable. In the present study, a weighted fraction Monte Carlo (WFMC) method is firstly proposed and developed on the basis of MMC method with the adjustable weight function and operator splitting technique for reducing the statistical noise of MC method (Jiang and Chan, 2021a). The new WFMC method is then coupled into computational fluid dynamics (CFD) by Lagrangian particle tracking (LPT) method. The developed LPT-WFMC is further applied to study soot formation and evolution in ethylene laminar premixed flame (Jiang and Chan, 2021b)**.** Soot nucleation can significantly affect the particle size distribution (PSD) in the numerical simulation by the detailed soot models but soot nucleation mechanism is still not fully understood. One of the most widely used soot nucleation mechanisms (i.e., physical dimerization of PAH) is investigated by using the reactive force field (ReaxFF) with molecular dynamics (MD) simulation for gaining better understanding of soot nucleation mechanism. Finally, both physical and chemical

processes in the transformation from polycyclic aromatic hydrocarbons (PAHs) to the soot particle in the ethylene flame are investigated for different carbon dioxide additions by using ReaxFF MD simulations. The relevant physical and chemical processes in soot formation and evolution, and the effects of the carbon dioxide addition on the soot formation and evolution pathways are also investigated.

The objectives of the present study are as follows:

1. To gain deeper knowledge of the soot dynamic processes including nucleation, surface growth, coagulation, condensation etc., and the development of the detailed soot models;

2. To validate a proposed weighted fraction Monte Carlo (WFMC) method with the results of theoretical/sectional method;

3. To develop a coupled computational fluid dynamics (CFD) and with Monte Carlo (MC) method in reacting flow and soot aerosol dynamics in combustion, with Lagrangian particle tracking (LPT) method for describing the soot particles, and the validation in laminar premixed flame with the consideration of the soot particle size distribution (PSD) and sensitivity of soot model parameters; and

4. To investigate possible physical and chemical pathways of soot nucleation including the dimerization of PAHs and transformation from PAHs to soot nanoparticles by using the reactive force field (ReaxFF) with molecular dynamics (MD) simulations.

1.3 Outline of the Thesis

Chapter 1 introduces an overview of the background and scope related to the present study, indicating knowledge gap of the numerical simulations of soot formation and evolution in flames. The aims and objectives of the present study are intended to fill the knowledge gap.

Chapter 2 provides a more detailed literature review of soot aerosol dynamics and soot nucleation mechanism including the knowledge and understanding obtained from recent research studies, and introducing the recent development and up-to-date studies of aerosol dynamics and soot models.

Chapter 3 provides theoretical fundamentals of the present study, which includes the basic mathematical equations and the descriptions of relevant numerical models that will be used in Chapters 4 to 7.

Chapter 4 provides a proposed and developed weighted fraction Monte Carlo (WFMC) method with its validation and applications to complex aerosol dynamics.

Chapter 5 provides further development of Lagrangian particle tracking coupled with weighted fraction Monte Carlo (LPT-WFMC) method which enables numerical simulation of aerosol dynamics in complex flow fields, with applications to the study of soot formation and evolution in laminar premixed flames.

Chapter 6 provides the atomistic insight of the dynamics of association and dissociation in the physical dimerization process of polycyclic aromatic hydrocarbons (PAHs) by using the reactive force field (ReaxFF) with molecular dynamics (MD) simulations.

Chapter 7 provides the physical and chemical properties evolution of soot nanoparticles under the conditions of ethylene premixed flames with carbon dioxide additions by using ReaxFF MD simulations.

Chapter 8 provides the conclusions and major scientific findings revealed by the present study and some recommendations for future work.

Chapter 2 Literature Review

2.1 Soot Characteristics

Soot particles are typically the product of fuel rich combustion and mostly formed in high temperature zone. The soot structure and composition have already been thoroughly discussed in many research studies (Donnet, 1994; Kim et al., 2006; Xi and Zhong, 2006; Kelesidis and Pratsinis, 2021). Mature soot particles are shown in the form of fractal-like structures which are resulted from the clustering of spheric primary particles (Dobbins and Subramaniasivam, 1994; Kholghy and Kelesidis, 2021). Figure 2.1 shows the structure of the soot particle.

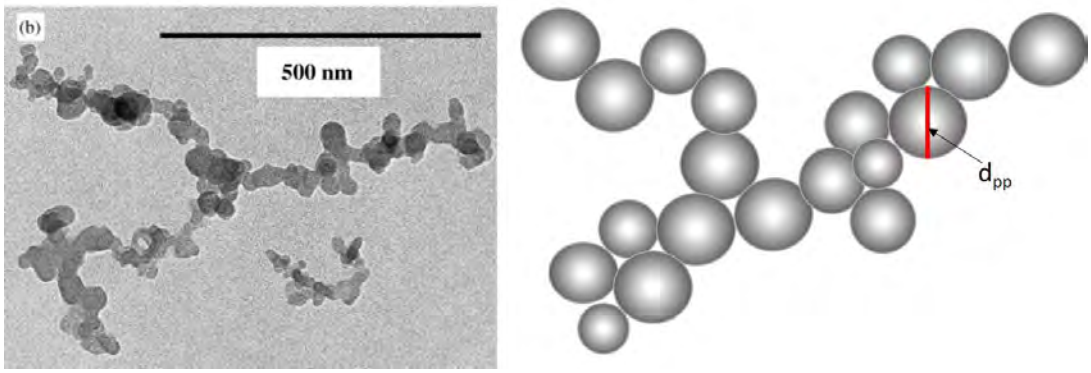

(a) (b)

Figure 2.1 The structure of the typical soot particles: (a) transmission electron microscopy images of soot aggregate and (b) Schematic representation of aggregate with the diameter of a primary particle, d_{pp} (Wentzel et al., 2003).

During the combustion process, the nascent soot particles are first formed and assumed to be spherical particles ranging from 1 to 5 nm in diameter (Dederichs, 2004). Their spherical appearance and absence of aggregation are the indication of liquid-like behavior and assumption of coalescence of particle upon collision (Dobbins and Subramaniasivam, 1994; Pascazio et al., 2021). Laser microprobe

mass spectrometry (LMMS) (Dobbins et al., 1995; Dobbins et al., 1998), gas chromatography/mass spectrometry (GC/MS) (Blevins et al., 2002; Shariatmadar et al., 2022) and high-resolution transmission electron microscopy (HRTEM) (Alfè et al., 2009; Hu et al., 2022) measurements have indicated that the nascent soot particles could be considered as polymer-like structures with molecular masses for polycyclic aromatic hydrocarbons (PAHs) ranged from 152 to 302 amu. Elemental analysis of nascent soot particles shows that these particles have a low atomic C/H ratio of ranging from 1.6 to 4 which can also be associated with their high chemical reactivity (Alfè et al., 2009; Fan et al., 2022).

Simultaneous collision of soot particles ranged from 1 to 5 nm in diameter. Addition of soot mass by surface reaction with gaseous species and graphitization of soot particles by loss of H atoms result in the transformation from nascent soot particles to aggregate carbonaceous and hardened primary particles (Dobbins and Subramaniasivam, 1994; D'Anna, 2009; Zhou et al., 2022). The nascent particles may also be absorbed onto the surface of the aggregates upon collision (Dobbins and Subramaniasivam, 1994; Martin et al., 2022).

Primary soot particles consist of small spherical units and the standard deviations of the distributions of primary particle sizes are ranged from 15% to 25% of the mean primary particle diameter (Köylü et al., 1995; Morán et al., 2021). In addition, the primary particle diameters are usually less than 60 nm (Köylü et al., 1995; Martin et al., 2022). The primary soot particles within the aggregate have nearly identical diameter. Soot aggregates have a widely varying number of primary particles ranging from a few to several thousands (Köylü et al., 1995; Agarwal et al., 2019; Martin et al., 2022). The long chain soot

aggregates and a wide range of soot particle size distributions create the complexity in soot characterization and modelling. This complication is addressed by experimental evidence that soot aggregates show a fractal-like structure (Yazicioglu et al., 2001; Kelesidis and Pratsinis, 2021). These soot aggregates have a universal fractal dimension, D_f around 1.8, even when an aggregate is composed of two or three primary particles (Sorensen and Feke, 1996; Karlsson et al., 2022). Fractal dimension is used to calculate the surface area and rate of change in aggregate size. The theory of fractal aerosols can be applied to describe the fractal-like soot aggregates for both laser measurements and numerical simulations (Dobbins and Subramaniasivam, 1994; Amin and Roberts, 2021). Gas chromatography/mass spectrometry (GC/MS) (Blevins et al., 2002; Wang et al., 2021a) and liquid chromatography measurements of soot particles (Feitelberg et al., 1993; Apicella et al., 2022) have shown the presence of 2 to 10 ring PAHs which are regarded as the components of the mature soot particles. The transformation from nascent soot particles to mature soot aggregates is accompanied by increasing hydrocarbon ratio (C/H) which results in higher density for aggregates (i.e., ρ_s = 1.77 to 2.00 g/cm^3) (Haynes and Wagner, 1981; Pascazio et al., 2021) compared to the nascent soot particles (i.e., ρ_s = 1.20 to 1.50 g/cm^3) (Zhao et al., 2007; Pascazio et al., 2021).

2.2 Soot Formation in Flames

Soot formation is the transition from gas-phase species to a condensed carbonaceous nanoparticle. Currently, no detailed mechanism can fully explain this rapid and important process despite some extensive literature studies (Haynes and Wagner, 1981; Glassman, 1989; Martin et al., 2022). Soot formation and evolution

processes can basically be divided into five main stages (Richter et al., 2000; Martin et al., 2022):

1. Formation of soot precursors (molecular zone);
2. Carbonaceous nanoparticle formation (particle zone);
3. Surface growth of soot particles by reaction/condensation with small molecule species or PAHs;
4. Coagulation by the interaction between the collisional particle pairs; and
5. Oxidation of soot particles via the reacting with oxidants.

The above-mentioned five stages are not strictly distinct but overlap and influence each other (Martin et al., 2022). The oxidation process competes with the soot formation throughout these processes. These processes in soot formation will be briefly introduced in the following Sections 2.2.1 to 2.2.5.

2.2.1 Formation of soot precursors

While many molecular species are suggested to contribute to soot formation, PAHs are considered as the most important soot precursors (Haynes and Wagner, 1981; Appel et al., 2000; Richter et al., 2000; Cai et al., 2022). Therefore, the formation of the first aromatic ring from smaller hydrocarbon species is the key process in the formation of PAHs which is also essential for soot nucleation. The pyrolysis of hydrocarbon fuel produces the C1-C5 compounds including acetylene C_2H_2 through radical-induced fragmentation. The different chemical pathways for forming the first aromatic ring from the C1-C5 compounds are shown in Figure 2.2 (Hansen et al., 2009).

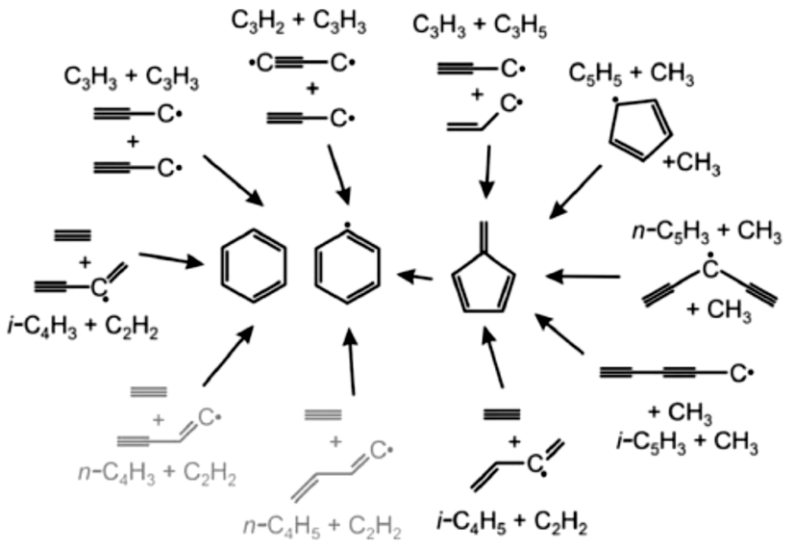

Figure 2.2 First aromatic ring formation (Hansen et al., 2009).

Further growth of the aromatic ring to forming the PAHs by the H-abstraction-carbon-addition (HACA) mechanism was firstly proposed by Frenklach and Wang (1994). Figure 2.3 shows a reaction pathway of the HACA mechanism, including the changes in the Gibbs free energy and the evolution of some reactive species (Wang, 2011).

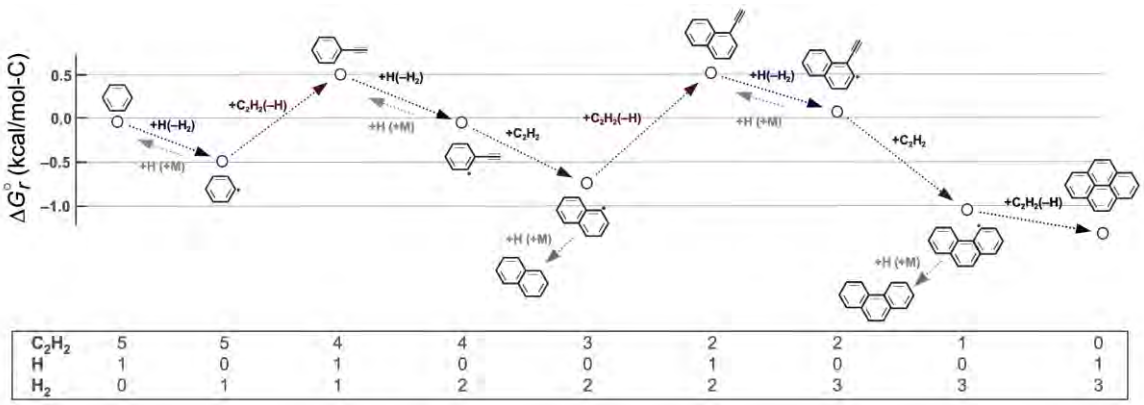

Figure 2.3 The reaction pathway of HACA mechanism (Wang, 2011).

In fact, the PAH growth via the above-mentioned HACA mechanism is the most thermodynamically stable pathway (Ong, 2017). Stein and Fahr (1985) pointed out that the formation of larger molecule species via HACA mechanism

under flame condition favors the structures called “island of stability” or the “stabilomers” by considering the thermodynamic stability of PAH.

2.2.2 Soot nucleation

Soot nucleation is the process of transformation from gas-phase species to soot particles. Many mechanisms have been proposed for the soot nucleation in hydrocarbon flames which can be classified into three concepts by Wang (2011) as shown in Figure 2.4: Pathway A, the chemical growth via HACA mechanism to the formation of fullerene-like structures; Pathway B, the physical dimerization of PAHs to the formation of PAH clusters; and Pathway C, the chemical collision of PAHs to the formation of crosslinked three-dimensional structures.

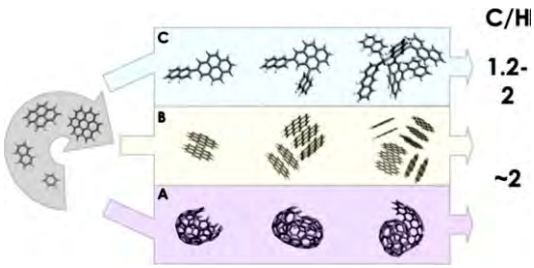

Figure 2.4 Mechanisms of soot particle nucleation (Wang, 2011).

.

Pathway A is the mass growth of soot particles via the chemical growth pathway (i.e., HACA mechanism) forming fullerene-like structures. Experimental evidence of fullerene-like structures was found in the benzene flame in the fuel rich combustion condition (Homann, 1998). Similar structures were also found in kinetic Monte Carlo and molecular dynamic studies (Violi, 2004). However, it has been argued that the chemical growth via the HACA mechanism is too slow when compared with the measured soot nucleation rates (Frenklach and Wang, 1994; Wang, 2011; Keller, 2019; Frenklach and Mebel, 2020; Martin et al., 2022).

Pathway B is the physical agglomeration of PAHs forming dimers and pathway C is the chemical collision of PAHs and aryl radicals forming crosslinked three-dimensional structures. These two mechanisms can explain the bimodality of soot particle size distribution (PSD) which is observed in many premixed flame studies (Zhao et al., 2003; Singh et al., 2006; Huo et al., 2021). However, both the experimental and theoretical results of Sabbah et al (2010) showed that the physical dimerization of pyrene cannot play an important role in soot nucleation. Herdman and Miller (2008) investigated the binding energy of PAH dimers by the molecular force fields, and found that the binding energies of homomolecular dimers rise rapidly with molecular size. The binding energies for the self-interactions of a series of PAHs were presented by Wang (2011) as shown in Figure 2.5. Based on the results of binding energies obtained, the theoretical calculations show that small to medium sized PAH dimers are thermodynamically unstable and are unlikely to play an important role in soot nucleation under flame conditions (Wang, 2011; Zhang et al., 2019). For the pathway C, high concentrations of the hydrogen (H) atom and aryl radical are required. However, this mechanism cannot account for the nucleation at post-flame region where the H atom concentration is too low to initiate such reactions (Wang, 2011).

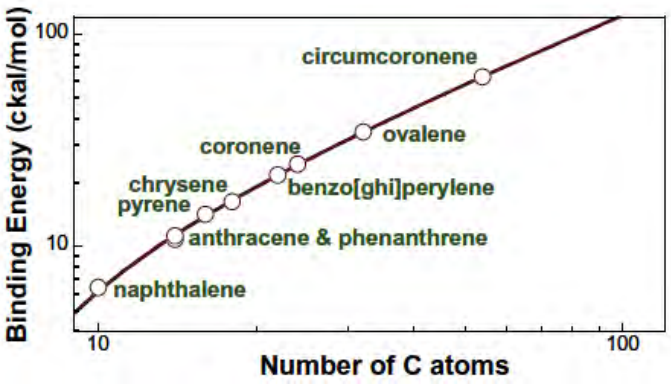

Figure 2.5 Binding energies of PAH dimers (Wang, 2011).

2.2.3 Soot surface growth

Soot surface growth is the mass growth of soot particles by reacting and absorbing the gas-phase hydrocarbons molecules on soot surfaces. The previous studies demonstrated that acetylene is the dominant mass growth species (Harris and Weiner, 1983; Appel et al., 2000; Frenklach, 2002b; Xie et al., 2021). The research group of Professor Frenklach (Frenklach and Wang, 1994; Appel et al., 2000; Frenklach, 2002b) suggested that surface growth can be described via HACA mechanism which is analogous to the reaction sequence of soot precursor growth. In the HACA mechanism for the soot surface growth, H-abstraction is required for generating an aryl radical site with further acetylene addition (Frenklach, 2002b). Therefore, HACA mechanism for the reaction rate of soot surface growth is dependent on the concentration of hydrogen atom (H•). However, the experimental studies showed that soot mass continues to increase even in the post flame region where the concentration of H• is very low (Haynes and Wagner, 1981; Pejpichestakul, 2019).

Another soot surface growth process is the PAH condensation (Macadam et al., 1996; Appel et al., 2000; Yuan et al., 2021). Similar to the pathway B of soot nucleation by colliding of PAH molecules to form soot particles, the collision event also can occur between PAH molecules and soot particles, and results in the PAH condensation on the soot surface. Macadam et al. (1996) showed that the soot surface growth via PAH condensation is more significant under acetylene-lean conditions while the soot surface growth via HACA mechanism will be dominant in acetylene-rich conditions. The surface growth reaction on soot formation is described by the process that the reaction occurred between the reactive soot surface and gas-phase molecules. The reactivity of soot particle surface is

the so called aging factor or active surface site fraction, α (Keller, 2019). The aging factor is calculated based on the number of active surface sites on the soot particle surface (Frenklach, 2002b; Khosousi and Dworkin, 2015; Gu et al., 2021). The previous experimental studies showed several factors that influence the reactivity of surface sites including particle size (Frenklach, 2002b), particle age (Haynes and Wagner, 1981; Harris and Weiner, 1985; Frenklach, 2002b) and temperature (Woods and Haynes, 1991). A decrease of surface reactivity for aging soot can be found in the experimental study (Veshkini et al., 2014), such phenomenon is the so called "surface ageing" and it is necessary to include the surface ageing effect in the soot modelling**.** Furthermore, Kraft et al. (2005) modelled the correlation between the particle age and the active surface sites which shows the higher reactivity for "younger" soot particles. The conception of thermal age is introduced for quantifying the effect of temperature and time involved in the flame. The other "surface ageing" model can be found in literature (Veshkini et al., 2014; Khosousi and Dworkin, 2015; Liu et al., 2021d).

2.2.4 Soot particle coagulation

Soot particle coagulation can be described as the physical processes in the collision of two particles to form the larger soot particles. Coagulation processes include coalescence and aggregation as described by Kazakov and Frenklach (1998). Coalescence is commonly happened between the nascent soot particles. The liquid like behavior of the nascent soot particles leads to collision and merging of the soot particles (Dobbins et al., 1995). Aggregation is a process that two soot particles are collided and sticked, then a complex fractal-like aggregate structure is formed. Aggregation usually occurs in the collision of mature soot particles. There are some

intermediate results between coalescence and aggregation after particle collisions, where particles are partially merged (Megaridis and Dobbins, 1989). Coagulation process could be described by Smoluchowski's equations in aerosol dynamics as follows:

$$\frac{\partial n(v,t)}{\partial t} = \frac{1}{2}\int_0^v \beta(u, v-u)n(u,t)n(v-u,t)du - \int_0^\infty \beta(v,u)n(v,t)n(u,t)du \qquad (2\text{-}1)$$

where $\beta(u, v)$ is the collision kernel function which represents the collision rate for two particles with volumes, u and v. The symmetric coagulation kernel describes the rate of collision events occurred for the given particle size. The form of coagulation kernel is determined by considering the physics involved in the particle-particle interaction. In general, the particle transport are mainly controlled by Brownian motion, gravity settling and turbulent flow (Meyer and Deglon, 2011), the latter two terms being not important in the context of soot particles (Shaohua, 2018). A classification based on the Knudsen number (Kn) is used to define collision kernels for different regimes. The Knudsen number is defined as:

$$Kn = \frac{2\lambda_f}{L_x} \qquad (2\text{-}2)$$

$$\lambda_f = \frac{k_B T}{\sqrt{2}\pi d_f^2 P} \qquad (2\text{-}3)$$

where λ_f is the mean free path of a fluid molecule, L_x is a representative length scale of particles (i.e., a typical particle's collision diameter, d_c) and d_f is the diameter of a fluid molecule. For Kn > 10, coagulation kernel in the free molecular regime is used while Kn < 0.1, coagulation kernel in the continuum regime is used. For $0.1 \leq Kn \leq 10$, coagulation kernel in the intermediate regime is calculated by the harmonic mean of coagulation kernel in the free molecular and continuum regimes.

However, D'Alessio et al. (2005) showed that not all particles will stick together during the collision events because thermal rebound effects by van der Waals forces play an important role over the interaction of particles under flame temperature conditions. As a result, the coagulation efficiency is introduced to describe the sticking probability of two particles upon collision. In addition, the coagulation frequency enhancement factor is also introduced to account for the effect of van der Waals attraction between soot particles during the collision process (Ouyang et al., 2012; Hou et al., 2020b; Kholghy and Kelesidis, 2021).

2.2.5 Soot oxidation

Soot oxidation process always competes with the soot formation and the mass growth because of the soot mass removal by reacting with the oxidizers (i.e., OH•, O• and O_2) (Jander and Wagner, 1990; Stanmore et al., 2001; Mueller et al., 2011; Bockhorn, 2013; Wang et al., 2021c). Soot oxidation occurs during the entire process of the soot formation and evolution (Lahaye, 2013; Siegla, 2013). Oxidation-induced fragmentation of soot aggregates is a case of soot oxidation where oxygen penetrates into particle structures before oxidation takes place. Once the soot aggregate structures are sufficiently weakened, the soot aggregates break apart into small fragments (Neoh et al., 1985; Xu et al., 2003; Martin et al., 2022).

Among different oxidizers like oxygen (O_2), oxygen atom (O), hydroxide (OH), nitric oxide (NO), nitrogen dioxide (NO_2), water (H_2O) and carbon monoxide (CO), OH and O_2 are regarded as the most important oxidation reactants due to their high contribution to the soot oxidation process (Lee et al., 1962; Nagle and

Strickland-Constable, 1962; Stanmore et al., 2001; Liu et al., 2003; Hagen et al., 2021). Liu et al (2003) showed that the OH is the dominant species under fuel-rich condition while the O_2 is more important under fuel-lean condition. Oxidation by other species has also been investigated in the literature (Stanmore et al., 2001; Liu et al., 2003; Hagen et al., 2021).

2.3 Modelling of Soot Formation

Soot modelling has multiscale problems because it includes a variety of time and length scales such as angstroms for atomic level scales (i.e., 10^{-10} m), nanometers for dimers and soot particles (i.e., 10^{-9} m), millimeters for flow scales (i.e., 10^{-3} m), and centimeters for burner geometry (i.e., 10^{-2} m). To address the multiscale problems, the smallest/shortest length/time scales should be taken into account to model the processes based on the physical understanding. One of the difficulties is strike a balance between the accuracy and simplicity of the soot model.

Kennedy (1997) reported the achievement of development on early soot models. According to the time/length scales and the model complication, soot models can be classified into three categories: empirical soot models, semi-empirical soot models and detailed soot models.

2.3.1 Empirical models

Empirical soot models are developed based on the experimental correlations between soot formation rates and combustion conditions. The correlations usually reflect the influence of different flame parameters (e.g., pressure, temperature, and equivalence ratio) on the soot behavior. These correlations are coupled with flame

models to relate the amount of soot produced with the operating conditions. The empirical models are easy to implement and have a high computational efficiency. As a result, the empirical models have been widely used in combustion engineering fields. However, the empirical model cannot reflect the detailed insights of soot formation processes.

Tesner et al. (1971) proposed the empirical soot model including a branched-chain process and soot nucleation. The soot formation is considered as the adsorption and reaction of radical species on the soot precursor surface in their model. Khan and Greeves (1974) developed another empirical model which assumed that the soot particle size is kept constant and the formation rate of soot is only dependent on nucleation. The formation rate of soot is given as:

$$\frac{dM_{\text{soot}}}{dt} = cp_u\phi^n \exp(-\frac{E}{RT_u}) \tag{2-4}$$

where M_{soot} is the soot mass concentration, c and n are model constants, E is the activation energy of soot formation, p_u is the partial pressure of unburned fuel, ϕ is the local unburned equivalence ratio and T_u is the local temperature (Ong, 2017). Despite the simplicity and limited physical basis of Khan and Greeves model (Khan and Greeves, 1974), the correct orders of magnitude of soot concentration can be obtained (Coelho and Carvalho, 1995).

Another empirical soot model was developed by Hiroyasu et al. (1983) which assumed that soot formation rate is only dependent on pressure, temperature, and concentration of hydrocarbon fuel and oxygen. The details of soot formation/oxidation processes are ignored. The formation rate of soot is expressed in Arrhenius type equation as:

$$\frac{dM_{\text{soot}}}{dt} = (\frac{dM_{\text{soot}}}{dt})_{\text{formation}} - (\frac{dM_{\text{soot}}}{dt})_{\text{oxidation}} \quad (2\text{-}5)$$

$$(\frac{dM_{\text{soot}}}{dt})_{\text{formation}} = A_f M_{\text{fuel}} p^{0.5} \exp(-\frac{E_f}{RT}) \quad (2\text{-}6)$$

$$(\frac{dM_{\text{soot}}}{dt})_{\text{oxidation}} = A_O M_{\text{soot}} X_{O_2} p^{1.8} \exp(-\frac{E_O}{RT}) \quad (2\text{-}7)$$

where M_{fuel} and M_{soot} are the mass of vaporized fuel and soot particle, respectively, X_{O_2} is the mole fraction of oxygen, p is the pressure, E_f and E_O are activation energies of soot formation and oxidation, respectively, A_f and A_O are model constants which can be obtained by the available fitting experimental data (Chong, 2018).

For a more accurate modelling of soot oxidation, Nagle and Strickland-Constable (NSC) soot oxidation model (Nagle and Strickland-Constable, 1962) is applied to Equation (2-8) for improving the details of soot oxidation process. Considering the experimental study of carbon graphite oxidation (Strickland-Constable, 1944), the reactive sites of C atoms on the soot particles can be classified into more reactive sites “A” and less reactive sites “B”. The conversion of “A” sites to “B” sites is also considered as the temperature increased (Ong, 2017). The oxidation reaction rate of soot particles in the empirical model is given as:

$$(\frac{dM_{\text{soot}}}{dt})_{\text{oxidation}} = \frac{6M_{\text{C}}}{\rho_{\text{soot}} d_{\text{soot}}} M_{\text{soot}} \omega_{\text{NSC}} \quad (2\text{-}8)$$

where M_{C}, ρ_{soot} and d_{soot} are the molecular weight of a C atom (12.01 g/mol), the density of a soot particle and the diameter of a soot particle, respectively. ω_{NSC} is the NSC soot mass oxidation rate per unit surface area (Ong, 2017).

The Hiroyasu's model has been widely applied in simulation of soot transport in the engines combustion environments (Patterson et al., 1994; Pachano et al., 2021).

In addition, this model has been applied to multi-dimensional combustion simulations (Komninos and Rakopoulos, 2012; Pachano et al., 2021). However, the Hiroyasu's model (Hiroyasu et al., 1983) has oversimplified the soot formation processes. The effect of hydrocarbon fuel type on soot formation is ignored, and only the soot oxidation by O_2 is considered in the model (Vander Wal and Tomasek, 2003). These simplifications result in the underestimation of soot concentration (Patterson et al., 1994). Thus, the improvement of Hiroyasu's model is required for accurate predictions of the soot formation and evolution in internal combustion engines (Golovitchev et al., 1999; Rakopoulos et al., 2004; Tao et al., 2005; Pachano et al., 2021; Singh and Agarwal, 2022).

2.3.2 Semi-empirical soot models

Semi-empirical soot models are proposed by the combination of the empirical model and mathematical description to model the soot population properties (i.e., number density, volume and mass fractions). The most widely used semi-empirical soot model belongs to the two-equation model (Fairweather et al., 1992; Moss et al., 1995; Guo et al., 2021). Semi-empirical method makes general assumptions about soot particle shape, precursor species and surface area in modeling soot formation (Chong, 2018). Firstly, semi-empirical soot model assumes that soot particles are spherical (Chong, 2018). Secondly, acetylene (C_2H_2) species is the soot precursor that directly forms the incipient soot (Chong, 2018). Thirdly, the rates of surface growth and oxidation are assumed to be linear to the soot surface area. Lastly, O_2 is the only species responsible for oxidizing soot particles. The soot oxidation does not affect the soot number density directly (Chong, 2018).

Fairweather et al. (1992) developed a semi-empirical soot model where the soot inception is only dependent on the C_2H_2 concentration. Thus, reduced chemical mechanism can be applied to the model without the complex PAH mechanism. Soot volume fraction (SVF) and soot number density of their model are expressed as follows:

$$\frac{dM_{\text{soot}}}{dt} = A_1 \frac{dM_{\text{nucl}}}{dt} + A_2 \frac{dM_{\text{growth}}}{dt} - A_3 \frac{dM_{\text{ox}}}{dt} \tag{2-9}$$

$$\frac{dN_{\text{soot}}}{dt} = A_4 \frac{dN_{\text{nucl}}}{dt} - A_5 \frac{dN_{\text{coag}}}{dt} \tag{2-10}$$

where M_{nucl}, M_{growth} and M_{ox} are the contributions of soot mass concentration from the nucleation, surface growth, and oxidation, respectively. N_{soot} is the soot number density, N_{nucl} and N_{coag} are the contributions of soot number density from nucleation and coagulation, respectively. A_i =1, 2…5 are the model parameters (Ong, 2017).

The Fairweather semi-empirical soot model was further modified by Woolley et al. (2009) for including soot nucleation by benzene molecules and adding the mechanism of soot oxidation by hydroxyl. Moss et al. (1995) improved the two-equation model by using different rate expressions to describe nucleation, surface growth, oxidation, and coagulation. Lindstedt et al. (1994) proposed a new soot model where the reaction steps for soot nucleation, growth and agglomeration are incorporated. More details on these models can be found in Omidvarborna et al. (2015) and Valencia et al. (2021). Although these models are easy to be implemented and are computationally efficient, they suffer from a narrow applicability range because the detailed mechanisms for soot formation and oxidation are neglected. The calibration for model parameters is usually necessary for different combustion conditions.

2.3.3 Detailed soot models

The final classification is made up of the detailed soot models. These are complicated and computationally intensive models which require detailed chemical kinetic mechanisms and aerosol dynamics theories. Detailed models can describe the pyrolysis and oxidation processes as well as the formation and growth of PAH species. PAH formation and growth involve a broad range of species and pathways and thus the chemical mechanisms include hundreds of species and thousands of reactions, even for simple hydrocarbon fuels (Appel et al., 2000; Ranzi et al., 2012; Slavinskaya et al., 2012; Wang et al., 2013; Martin et al., 2022). The detailed soot models can provide insight into the underlying mechanisms of soot formation, however, the problem of using these detailed soot models is the high computational costs. Therefore, most detailed soot models are restricted to modelling the simple geometry (i.e., one-dimensional/two-dimensional) and laminar flow (Ong, 2017; Li et al., 2021a; Liu et al., 2022; Nobili et al., 2022; Shao et al., 2022).

The detailed combustion chemistry with aerosol dynamics theories is required for the detailed soot models. They tend to be more general than the simplified models (i.e., empirical models and semi- empirical models). Detailed soot model can also provide further insights into the soot formation phenomenon. In contrast to simplified soot models which usually use the monodispersed to describe particles in the free-molecular regime, some detailed soot models apply advanced aerosol dynamics which could solve the structures of soot aggregates, provide particle size distributions and model particle collision in the transition and continuum regimes for the practical fluid-particle systems. One of a widely used detailed soot model is proposed by Frenklach and Wang (1994) and

Frenklach (2002b). In their detailed soot model, the reactions are described to start from hydrocarbon fuel pyrolysis to the PAH formation by the detailed chemistry. The nucleation by PAH molecules, surface growth chemistry via HACA reaction and coagulation are also included in their model.

2.4 Soot Aerosol Dynamics Modelling

Since soot modelling involved different aerosol dynamics processes, these particle processes are usually described by the population balance equations (PBEs) (Marchisio and Fox, 2013; Raman and Fox, 2016) which involve partial differential equations. Due to the complexity of PBEs, analytical solutions rarely exist. Proper numerical methods are needed to handle these PBEs. These numerical methods can be classified into three categories: sectional methods (SMs) (Gelbard et al., 1980; Jeong and Choi, 2001; Prakash et al., 2003; Mitrakos et al., 2007; Woo et al., 2021); methods of moments (MOMs) (Frenklach, 2002a; Yu et al., 2008; Lin and Chen, 2013; Yu and Chan, 2015; Chan et al., 2018; Liu et al., 2019b; Jiang et al., 2021) and Monte Carlo (MC) methods (Haibo et al., 2005; Zhao et al., 2009; Zhou and He, 2014; Zhou et al., 2014; Liu and Chan, 2017b; Liu and Chan, 2018b; Jiang and Chan, 2021a; Boje and Kraft, 2022).

2.4.1 Sectional method

Sectional method refers to a class of methods that discretize the PSD into many sections or bins by considering the internal coordinates of the particles and transforming the PBEs into a series of ordinary differential equations (ODEs) (Bowal, 2020). As a result, the evolution of the sectional quantities such as the total

particle number and particle size within each section can be well described. The PSD in the sectional method is described in a discretized form as:

$$N_x = \sum_{i=1}^{M} N_i \delta(x - x_i) \tag{2-11}$$

where x_i is the discretized particle size and N_i is the particle number within the ith section. M is the number of sections used to divide the particle size range. The choice of the discretization scheme is significant for determining the accuracy and computational efficiency of sectional method (Cheung et al., 2009; Shiea et al., 2020). If the particle size domain is divided to sections with identical section size, large numbers of sections are necessary to achieve higher computational accuracy, but this also leads to higher computational cost. Batterham et al. (1981) proposed a discretization scheme where the section sizes are in a geometric series (i.e., $x_{i+1}/x_i = 2$), thus enabling a wider range of particle sizes covered in a useful approach. The resulting PSD is then discretized at specific section sizes, (i.e., x_1, $2x_1$, $4x_1$, etc.). For the particles with odd sizes, for example $3x_1$, they are evenly split and relocated at $2x_1$ and $4x_1$. This leads to the conservation of the particle sizes while the particle number cannot be conserved. Hounslow et al. (1988) modified this sectional method by introducing a correction factor to the overall change rate of the particle numbers. As a result, both the particle number and size can be conserved. Prakash et al. (2003) proposed the simplified sectional method by discretizing the PSD with a nodal form. The algorithm of this model is shown in Figure 2.6. The particle size space is discretized into multiple nodal points and particles are distributed at these nodal points. Nucleation happens at the nodal with a critical size v^* and coagulation occurs between the considered nodal points.

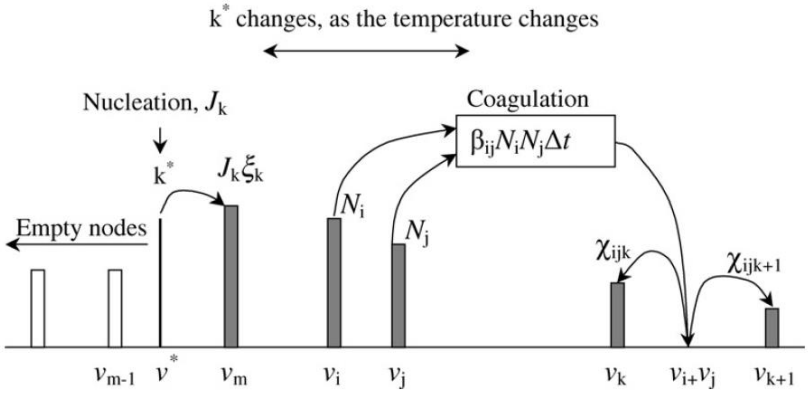

Figure 2.6 The algorithm of sectional method (Prakash et al., 2003).

One shortcoming of these fixed sectional methods is that they tend to overestimate the number for the largest particles. To overcome this problem, moving sectional method is developed by changing pivotal size adapting to the non-uniformity of PSD (Kumar and Ramkrishna, 1996b). Comparison between the fixed sectional method and the moving sectional method indicates that results obtained with the moving sectional method are much accurate and closer to the analytical solutions.

However, the sectional methods (Kumar and Ramkrishna, 1996a; Kumar and Ramkrishna, 1996b) can only conserve two moments in the discretized solution, hence are considered as low order section method. For this kind of sectional methods, the computational accuracy can only be increased slowly by adopting more sections at the expense of high computational cost. Alopaeus et al. (2006) proposed the new sectional method based on the method from the research group of Kumar and Ramkrishna (Kumar and Ramkrishna, 1996a; Kumar and Ramkrishna, 1996b) to conserve more than two moments, resulting in a higher-order moment conserving (HMMC) sectional method. Unlike the sectional methods of Kumar and Ramkrishna (Kumar and Ramkrishna, 1996a; Kumar and Ramkrishna, 1996b) where

the population of particles within each section is approximated by two nodes of that section. In HMMC sectional method, a linear operator transformation scheme is introduced to distribute the sectional particle population to a larger number of section nodes. As a result, an arbitrary number of moments can be conserved. It is found that the computational accuracy can be increased significantly with more moments conserved while the computational cost is increased slowly (Alopaeus et al., 2006). In theory, this HHMC sectional method can conserve as many moments as needed. However, the conservation of too many moments leads to an ill-conditioned matrix and the positivity of the moment-distribution transformation elements cannot be guaranteed.

2.4.2 Method of moments

The method of moments (MOM) is one of the earliest and simplest methods for solving population balance equations (PBEs) (Hulburt and Katz, 1964; Barrett and Webb, 1998; Aamir, 2010; Shiea et al., 2020). In the moment method, the non-linear integral-differential PBEs is transformed into a set of coupled ODEs for moments of the distribution. Such a method is easy to implement and has high computationally efficiency, but it may lose details of PSD. However, information on the representation of some integral quantities by using only a few lower-order moments will suffice for many practical cases. In MOM, the *k*th order moment is defined as:

$$M_k = \int_0^\infty v^k n(v) dv \tag{2-12}$$

The low-order moments usually have some practical meaning, such as M_0 is the total particle number density and M_1 is the total particle mass/volume faction.

By applying the moments transformation to Smoluchowski equation (Smoluchowski, 1916), the evolution of *k*th order moment for coagulation process is expressed as:

$$\frac{dM_k}{dt} = \int_0^\infty \int_0^\infty [(v+u)^k - v^k - u^k]\beta(v,u)n(v,t)n(u,t)dvdu \quad (2\text{-}13)$$

However, the moment source terms are often unclosed for soot particles. Since the realistic coagulation kernel function is used, the fractional-order or even negative-order moments are present in the source terms which cannot be directly derived but should be modelled to close the moment equations (Barrett and Webb, 1998; Massot et al., 2010; Mueller et al., 2011; Valencia et al., 2021). In order to handle these closure problems, numerous methods of moments have been proposed. In the method of moments with interpolative closure (MOMIC) (Frenklach, 2002a), the closure of moment equations is solved by the polynomial interpolation of the logarithm of the integer-order moments which can be directly obtained during the numerical simulations. MOMIC shows high accuracy in the particle nucleation, surface growth and coagulation problems. The quadrature-method of moments (QMOM) developed by McGraw (1997) solved the unclosed terms by applying the n-point Gauss-Christoffel quadrature. Based on the QMOM, the research group of Marchisio and Fox (Marchisio et al., 2003a; Marchisio et al., 2003b; Marchisio and Fox, 2005) proposed the direct quadrature method of moments (DQMOM) where the quadrature abscissas and weights are directly tracked from the transported moments without using the product-difference (PD) algorithm (Gordon, 1968). Yu et al. (2008) first developed Taylor-series expansion method of moments (TEMOM) for solving the PBEs in Brownian collision kernel where the closure of the moment equations is solved by applying the Taylor-series expansion (Chan et al., 2018; Liu et al., 2019b).

2.4.3 Monte Carlo method

Monte Carlo (MC) method is capable to solve the complex aerosol system. Compared with MOM and SM, MC method can easily describe the evolution of particle internal coordinates without losing much computational efficiency (Kraft, 2005; Zhao et al., 2011; Zhao and Zheng, 2011; Menz and Kraft, 2013; Boje and Kraft, 2022). In addition, MC method can directly track the particle population evolution. Thus, the detailed PSD can be provided. Figure 2.7 shows a typical flow chart of Monte Carlo algorithm (Efendiev, 2004).

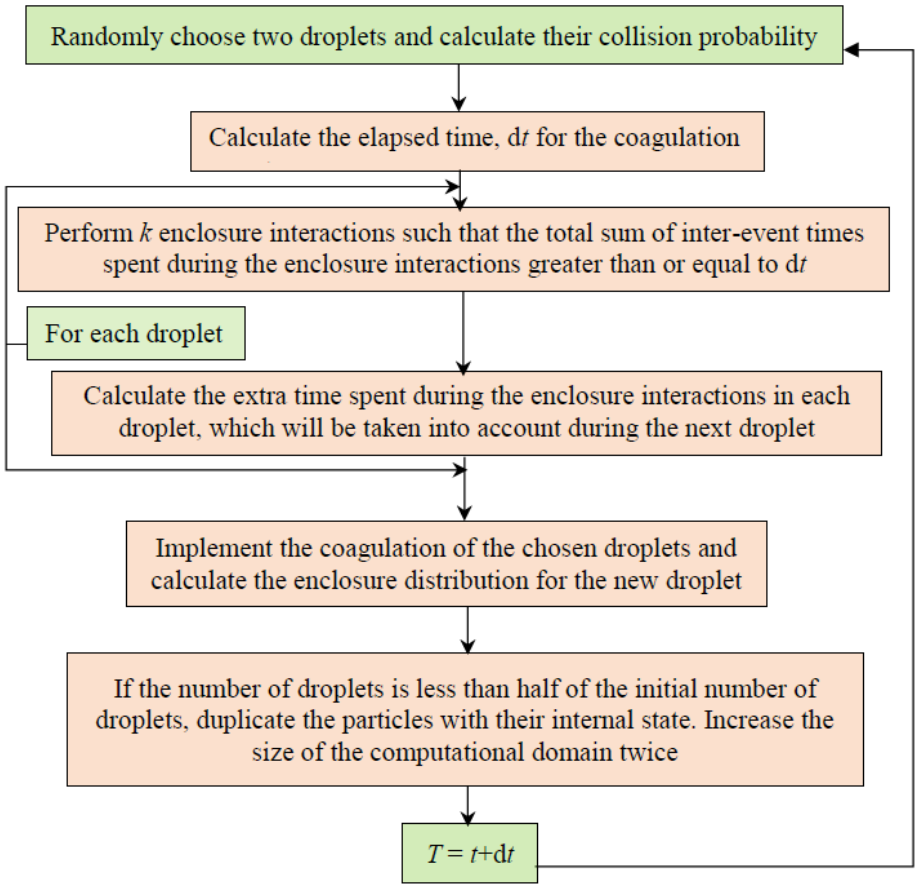

Figure 2.7 A typical flow chart of Monte Carlo algorithm (Efendiev, 2004).

Gillespie (1975) firstly developed the direct simulation Monte Carlo (DSMC) method to solve Smoluchowski equation, which is the fundamental basis of many

further developments. In the processes of the DSMC method, the individual coagulation events are separated by waiting time with an exponential distribution. The waiting time, τ is given as:

$$P(\tau \geq \tau_0)=\exp(C_0\tau_0) \tag{2-14}$$

where C_0 is the waiting-time parameter and is expressed as:

$$C_0=\sum_{i=1}^{N-1}\sum_{j=i+1}^{N} C_{ij}=\frac{1}{V}\sum_{1\leq i\neq j\leq n}\beta(x_i,x_j) \tag{2-15}$$

where V is the simulation volume which all particles are assumed to be dispersed homogenously. For each event, particle indices, i and j can be selected according to the probabilities as:

$$P(i,j)=\frac{C_{ij}}{C_0}=\frac{\beta(x_i,x_j)}{\sum_{1\leq i\neq j\leq n}\beta(x_i,x_j)} \tag{2-16}$$

Then particles i and j are removed and a particle of size, $x_i + x_j$ is formed.

DSMC method is the simplest and the most widely used MC method. It can be easily used to the aerosol dynamic systems without involving the discretization of the particle size domain (Ramkrishna, 2000; Meimaroglou and Kiparissides, 2014; Boje and Kraft, 2022). With DSMC method, the physical particles are represented by a set of numerical particles whose size is essential to ensure the accuracy of the method. Since only a finite number of numerical particles can be simulated, uncertainty of PSD function is inevitable. Such uncertainty could be reduced by enough number of repetitions of numerical simulations to limit the statistical noise (e.g., variance, standard deviation). However, there are always a few numerical particles at the edges of the PSD which result in poorly representation of edges of the particle size spectrum in the numerical simulation. The problem of the numerical

uncertainty in stochastic method becomes more severe when the PSD is in logarithmic form (Zhao et al., 2009).

In recent years, some modifications on the DSMC have been developed for improving computational efficiency and accuracy (Goodson and Kraft, 2002; Balthasar and Kraft, 2003; Singh et al., 2005; Zhao et al., 2005b; Zhao and Zheng, 2009; Patterson and Wagner, 2012; Jiang and Chan, 2021a; Boje and Kraft, 2022). The number of the numerical particles is maintained within a certain range during the numerical simulation in order to ensure the computational efficiency and accuracy. Hence the adjustment actions are introduced and performed on the number of the numerical particles such as constant number MC (Smith and Matsoukas, 1998; Lee and Matsoukas, 2000; Omar and Rohani, 2017; Boje and Kraft, 2022) and constant volume MC (Kruis et al., 2000; Maisels et al., 2004; Boje and Kraft, 2022). Depending on the determination of the time step, DSMC method can be classified into time-driven (Liffman, 1992; Debry et al., 2003; Jiang and Chan, 2021a) and event-driven (Shah et al., 1977; Efendiev and Zachariah, 2002; Du et al., 2022). In time-driven MC, the time step is determined explicitly at each simulation step. Then all the particle events occur simultaneously at a time interval. By contrast, the particle events take place consecutively during the simulation in event-driven MC. The occurrence of individual particle event is determined according to the event probabilities.

To speed up the MC algorithm, Eibeck and Wagner (2000) introduced the majorant kernel method which uses an acceptance-rejection technique and fictitious jumps in order to reduce the numerical efforts and choose the collision pairs. Zhou et al. (2014) proposed the operator splitting Monte Carlo (OSMC)

method. In the OSMC method, the operator splitting method is applied to separate the aerosol dynamic processes into deterministic (i.e., nucleation, surface growth) and stochastic parts (i.e., coagulation). The OSMC method is flexible and has high computational efficiency for simulating the aerosol dynamic systems. The flowchart of OSMC method is shown in Figure 2.8.

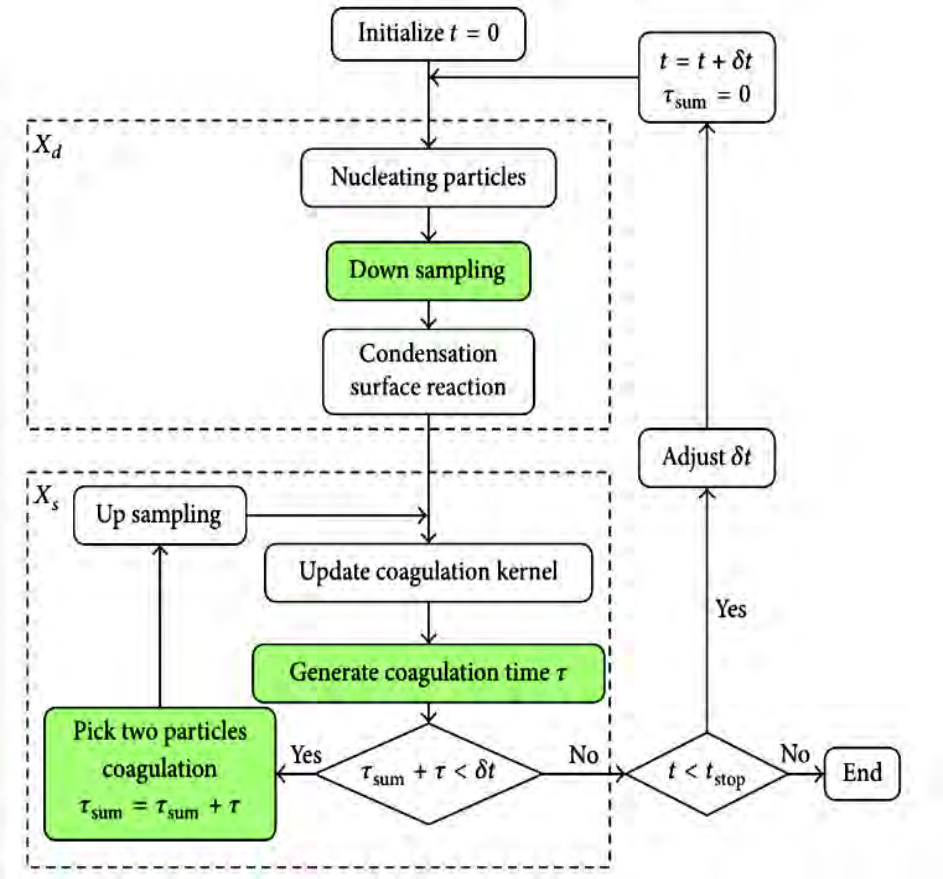

Figure 2.8 Flowchart of the OSMC (Zhou et al., 2014).

In order to reduce the statistical noise, the differentially weighted schemes were adopted for coagulation dynamics and the mass flow algorithm (MFA) was developed (Babovsky, 1999; Eibeck and Wagner, 2001b). The computational efficiency and stochastic noise reduction can be greatly improved. In addition, DeVille et al. (2011) proposed the weighted flow algorithms (WFA) to simulate

particle coagulation with arbitrary forms of weighting function, especially for power-law form in the particle size. For the reduction of statistical noise, the multi-Monte Carlo (MMC) method was developed by the research group of Professor Zhao (Zhao et al., 2005b; Zhao et al., 2009), which proposed the conception called 'fictitious particles'. The number of fictitious particles and the volume of simulation box can both keep constant by using this conception. MMC method shows high computational efficiency and accuracy, and enables wide application in many population balance problems. Kotalczyk and Kruis (2017) introduced 'stochastic resolution' for constructing constant-number coagulation scheme using the asymmetric coagulation kernel function. Recently, another modification of weighted particle schemes on the stochastically and differentially weighted operator splitting Monte Carlo methods (i.e., SWOSMC and DWOSMC) methods has been developed by Professor Chan's research group at the Department of Mechanical Engineering, PolyU (Liu and Chan, 2017b; Liu and Chan, 2018b) for improving the computational efficiency and accuracy by combination of the operator splitting and weighted particle schemes.

For numerical simulation of soot formation, MC methods have several advantages. It can be applied to simulate all the aerosol dynamic processes with no closure problems. It is very efficient and its solution is convergent to the exact solution of the PBEs. MC methods have successfully been used to study the soot formation and oxidation processes in premixed laminar flames (Balthasar and Kraft, 2003; Singh et al., 2005; Hou et al., 2020a), stagnation flames (Yapp et al., 2016; Boje and Kraft, 2022) as well as internal combustion engines (Mosbach et al., 2009; Wang et al., 2016; Liu et al., 2021a).

2.5 Molecular Dynamics Study

Molecular dynamics (MD) is the technique of modeling molecular systems as classical many-body system. MD is particularly useful for examining detailed molecular interactions, which are difficult to study experimentally. The advantage of MD is that it can obtain the deterministic trajectories for each atom in a simulation system. The researchers can also study the energy transfer on the nanoscale, equilibrium and transport properties of complex system based on the MD simulations. One of the earliest applications of MD was the study of phase transitions (Alder and Wainwright, 1959). MD was also found applications in physics, chemistry, biochemistry, material science and other engineering branches (Mann et al., 2002; Salmaso and Moro, 2018; Liguori et al., 2020; Krishna et al., 2021; Li et al., 2021b).

In general, the MD simulations are conducted by repeating three steps: computing interatomic forces, determining atomic accelerations and integrating atomic positions in time. Using the results from classical mechanics, the interatomic forces are determined from the gradient of the potential energy (PE) function (Frenkel and Smit, 2001) as:

$$\vec{F}_{ij} = -\nabla U_{ij}(\vec{R}) \tag{2-17}$$

where $\vec{F}_{ij}$ is the force between atoms, *i* and *j*, $U_{ij}(\vec{R})$ is the potential energy function which depends on the set of atomic coordinates, $\vec{R}=\{\vec{r}_1,\vec{r}_2,\cdots\vec{r}_N\}$. For an isolated system containing a fixed number of atoms, *N* in a fixed volume, Newton's second law may be applied to determine the atomic accelerations (Frenkel and Smit, 2001) as:

$$m_i \frac{d^2 \vec{r}_i}{dt^2} = \sum_{j=1}^{N-1} \vec{F}_{ij} \tag{2-18}$$

where m_i is the mass and $\vec{r}_i$ is the position of atom, *i*. The atomic accelerations can then be numerically integrated to yield the time evolution of the atomic positions of the system by using the velocity Verlet-algorithm.

The potential energy (PE) function ultimately determines the realism of MD and is therefore the single most important aspect of the MD simulations. At each time step of MD simulations, the PE function predicts the interatomic forces and the total potential energy of the simulation system. Thus, the PE function is able to predict the equilibrium geometries and vibrational frequencies of the molecules being studied with reasonable accuracy. Additionally, the PE function must reliably represent the "physics" that one wishes to study such as long-range interactions, transition state geometries or bond energies. With that in mind, the calculation of interatomic forces is the most computationally demanding part of the MD simulations, and the PE function is typically calculated tens of thousands of times during a single simulation. Hence, the computational expense of solving the PE function must be relatively low. In the end, PE function is typically a balance between sufficient physical accuracy and reasonable computational efficiency. The most famous empirical PE function is the Lennard-Jones potential (Lennard-Jones, 1931), which is given as:

$$U(r_{ij}) = 4\varepsilon \left[\left(\frac{\sigma}{r_{ij}} \right)^{12} - \left(\frac{\sigma}{r_{ij}} \right)^{6} \right] \tag{2-19}$$

where ε is the depth of attractive well and σ is the collision diameter for the pair of atoms. The collision diameter for two dissimilar atoms is found through

the arithmetic mean of the respective collision diameters (Steinfeld et al., 1999).

In its long history, the Lennard-Jones potential has been remarkably successful in MD simulations for reproducing phenomena such as phase transitions (Carey, 2002; Kanda et al., 2021), two body scattering (Alakoskela and Kinnunen, 2001; Leverant et al., 2021), and the properties of liquids (Hsu and Mou, 1992; Stephan et al., 2021). However, the Lennard-Jones potential is of limited use in modeling polyatomic systems with complex geometries due to its potential depends only on distances between two atoms. Some modified PE functions have been developed to overcome these problems. One widely used example of such a multibody force field is the Stillinger-Weber potential (Stillinger and Weber, 1985). In order to reproduce condensed phase silicon, the Stillinger-Weber potential includes three body interaction terms that favor tetrahedral bond angles (Stillinger and Weber, 1985). By utilizing the parametric method 3 (PM3) (Stewart, 1989), the semi-empirical quantum mechanical method as the interatomic multi-body PE function and on-the-fly quantum potential were developed. Semi-empirical quantum mechanical methods represent an attractive balance between computational efficiency and accuracy when compared with the empirical PE functions and ab initio methods. Semi-empirical method is essentially quantum mechanics method, yet it is different from ab initio techniques in that it uses a simplified Hamiltonian which is tuned to reproduce the experimental data (Krossing and Slattery, 2006).

By applying MD method on the study of physical nucleation of soot, Chung and Violi (2011) performed MD calculation to study the growth of PAH dimers to soot aggregates and showed that the aliphatic chains added to aromatic

sites can accelerate the growth of soot particles at high temperatures regime (Mao et al., 2017b). Schuetz and Frenklach (2002) used the molecular dynamics with the on-the-fly quantum potential to investigate the physical formation mechanism of PAH dimers, and deduced that the transformation from translational energy to internal rotational and vibrational energies supports PAH dimers to have a longer lifetime.

All these molecular dynamics simulations and Monte Carlo calculations are based on semi-empirical or empirical potential which can only depict the physical inception (Shabnam et al., 2019). However, Sirignano et al. (2012) reported in the counter-flow ethylene flame that at temperature above 1500K, the nascent soot particles composed of PAHs through the chemical bonds are also ubiquitous. Hence, another numerical simulation method was used to overcome the problems of the computational efficiency and the numerical number of atoms. Reactive force fields molecular dynamics (ReaxFF MD) simulation was proposed to solve the dynamic system problem with both physical and chemical processes with large numerical atom numbers, but has the affordable numerical simulation time (van Duin et al., 2001). ReaxFF MD simulation has the ability to capture the chemical reactions. ReaxFF also has a potential that it can depict the breaking and forming of chemical bonds based on bond order which overcomes the limitation of the classical MD methods for describing the chemical reactions. The parameters are widely optimized by the experimental data and the quantum mechanics methods for improving computational accuracy (Han et al. 2017). It can quickly calculate the large physical/chemical models (> 1000 atoms) with precise numerical results (approximation to the density-functional theory (DFT) method) (Russo Jr and

van Duin, 2011). Besides the bonded interaction energy terms, the ReaxFF can also describe conjugated, hydrogen bonding etc., which are significant for simulating chemical/physical interaction between the aromatic species in the soot nucleation events (Russo Jr and van Duin, 2011; Yuan et al., 2019; Wang et al., 2021a; Hou et al., 2022).

In several previous molecular dynamic studies on soot formation, ReaxFF is applied to model chemical growth of soot particles. Qian et al. (2011) studied the benzene combustion by utilizing the ReaxFF and found the formation of fullerene-like structures by gradually removing hydrogen atom from the simulation boxes. Han et al. (2017) found the formation of PAH-like molecules and graphitization from PAH-like to fullerenic nanoparticles in their ReaxFF MD simulations of jet fuel combustion. Xue et al. (2017) studied the pyrolysis of methane with ReaxFF at various temperatures and densities, and found the formation of fullerene-like nanocavities. The research group of Professor You (Mao et al., 2017a; Mao et al., 2017b; Mao et al., 2018) conducted the binary collision to investigate the dimerization processes of different PAH molecules/radicals under different temperatures and impact parameters by using ReaxFF MD simulations. In addition, the clustering behavior of different PAH molecules at different temperatures have also been studied. They found that the clustering of PAHs can be divided into physical nucleation, no nucleation and chemical nucleation. Mao and Luo (2019) further studied the effect of trace metal (Fe) atoms on the PAH fragmentation, growth and soot nucleation by ReaxFF MD simulations. Yuan et al. (2019) also studied the soot nucleation at flame temperature by ReaxFF MD simulation. Apart from the PAH molecules, several reactive molecules/radicals (i.e., C_2H_2, OH) also

were taken into consideration. Keller et al (2019) studied bond formation reactions between soot precursors and their role in the soot nucleation. The formation of different structures during ReaxFF MD simulation is observed, which are the structures of aromatic directly linked hydrocarbon (ADLH), aromatic pericondensed polycyclic hydrocarbon (APLH) and aromatic aliphatically linked hydrocarbon (AALH). Zhao et al. (2020) have investigated the chemical effect of the hydrogen addition on the soot formation and evolution in ethylene flames at high temperature using ReaxFF MD simulations. Recently, Kwon and Xuan (2021) have investigated the pyrolysis of bio-derived dioxolane fuels with their sooting tendency at high temperature using ReaxFF MD simulations. Hou et al. (2022) have studied the reactive coagulation of incipient soot nanoparticles by simulating the coagulation process of two PAH clusters with diameter around 2 nm. The high densities (i.e., 0.2 g/cc) and high temperatures (i.e., 2000–3000 K) have often been applied in the ReaxFF MD simulation of soot formation and evolution to accelerate the MD simulation because the time scales of MD simulations (~nanoseconds) are orders of magnitude lower than the time scale of soot formation (~milliseconds) obtained from the experimental results (Shabnam et al., 2019; Martin et al., 2022).

2.6 Summary of Literature Review

In the scientific and environmental fields, the study of soot formation and evolution is significantly required. Hence, the development of advanced and efficient numerical methods for formation and evolution is also essentially needed.

Since soot formation and evolution are involved in many different physical and chemical phenomena (e.g., fluid flow, thermodynamic processes, chemical

reactions and aerosol dynamics processes etc.), efficient numerical methods for modelling soot are essentially required. Monte Carlo (MC) methods are widely applied in the soot modelling due to their high computational accuracy and efficiency. However, the high computational cost and stochastic noise always limit their applications. Thus, the MC methods with the higher computational accuracy and efficiency are essentially required to be developed and applied to the fields of soot modelling. Another problem in the soot modelling that is related to the knowledge of soot nucleation mechanism of which related knowledge still remains the least understood due to the complex nature of both physical and chemical processes in the soot nucleation. Therefore, it is important to have a better understanding of the soot nucleation mechanisms.

The fundamental concepts, knowledge and methods of soot formation and evolution are introduced in this chapter to reveal the development and state-of-the-art in these research areas. Many researchers have attempted to fill the knowledge gap for this important research area. The literature review is summarized as follows:

1. Understanding soot formation and evolution processes is of great importance for many different research areas (e.g., nanoparticle synthesis, industrial soot emission control, energy efficiency improvement and fuel loss reduction etc.). There are four stages related to the soot formation and evolution processes including nucleation, surface growth, coagulation and oxidation. Soot nucleation mechanism still remains the least understood due to its complex nature.

2. Soot modelling can be divided into three categories, namely empirical soot models, semi-empirical soot models and detailed soot models. Empirical soot

models are formulated by the reaction rate constants of soot kinetics that are correlations of experimental data. The semi-empirical models solve the rate equations of soot formation with the input of some experimental data. Detailed soot models require detailed chemical kinetic mechanisms and aerosol dynamics theories.

3. There are generally three advanced numerical methods for solving soot aerosol dynamics (i.e., sectional methods (SMs); methods of moments (MOMs) and Monte Carlo (MC) methods). In contrast, MC method is capable to solve the complex aerosol systems and incorporate several internal coordinates without causing much additional computational cost. In addition, it is able to directly track the particle population evolution so that a detailed particle size distribution (PSD) can be provided.

4. Many improvements on MC methods have been proposed and developed to enhance the computational efficiency and reduce the stochastic error for example, weighted particle scheme and operator splitting technique.

5. Eulerian-Lagrangian method is an appropriate numerical method for directly tracking the particle population evolution. Soot PSDs are also affected by many factors in the soot modelling: stick coefficient, thermophores, soot morphology assumption, etc.

6. Three conceptual pathways have been proposed and developed for soot nucleation mechanism; however, these pathways still cannot fully explain the soot nucleation phenomenon. Since soot nucleation involves the complex physical and chemical phenomena, a better understanding of soot nucleation is essential for modelling soot formation and evolution.

7. ReaxFF molecular dynamics (MD) simulations provide a suitable numerical tool to investigate the soot formation and evolution at atomic level due to its nature. Compared with classical MD simulation, the ReaxFF MD simulation is able to simulate both physical and chemical processes due to their ability to modelling the chemical bond formation and destruction processes. Compared with quantum mechanics (QM) methods, ReaxFF MD simulation is more computational cost-efficient without losing much computational accuracy.

Chapter 3 Theoretical Fundamentals of the Present Study

3.1 Introduction

This chapter briefly introduces the fundamental theories of the population balance equations (PBEs), Monte Carlo (MC) methods, combustion and reactive flows, soot models and molecular dynamics (MD) simulations.

3.2 Population Balance Equation

3.2.1 Overview

Population balance modelling is a widely used mathematical tool in chemical and mechanical engineering, with applications to crystallisation, granulation, pharmaceutical science, cell populations, polymerisation and aerosols. The population balance equations (PBEs) are used to quantify the dynamics of particulate processes in each application. In the fields of aerosol science studies, the evolution of particle systems can be described by the PBEs (Marchisio and Fox, 2013), which is also called the general dynamic equation (GDE) (Friedlander, 2000). The PBEs describe the temporal property distribution changes of a particle. It can be thought as a balance law of the number of an individual property of the population. The PBEs can be written (Friedlander, 2000) as:

$$\frac{\partial n}{\partial t}+\nabla \cdot n\dot{u}=\nabla \cdot D\nabla n+\left[\frac{\partial n}{\partial t}\right]_{\text{nucl}}+\left[\frac{\partial n}{\partial t}\right]_{\text{growth}}+\left[\frac{\partial n}{\partial t}\right]_{\text{coag}} \tag{3-1}$$

where n is the number density of aerosol particles, u is the velocity of flow field, and D is the diffusion coefficient. The second term on the left-hand side of Equation (3-1) represents the convection term of aerosol particles in the gas phase,

and first term on the right-hand side of Equation (3-1) represents the diffusion term. Another three terms on the right-hand side of Equation (3-1) describe nucleation, surface growth and coagulation processes, respectively.

The dynamic PBEs describes the continuous evolution of particle size distribution (PSD) or other distributions of more than one property, and any changes of population properties are described via different particle mechanisms. In the spatially homogeneous systems, the spatial variation is neglected, thus the PBEs can be written (Rigopoulos and Jones, 2003) as:

$$\frac{\partial n(v,t)}{\partial t} = \frac{1}{2}\int_0^v \beta(u,v-u)n(u,t)n(v-u,t)du - \int_0^\infty \beta(v,u)n(v,t)n(u,t)du + \frac{\partial(G(v)\cdot n(v,t))}{\partial t} + J_0\delta(v-v_0) \tag{3-2}$$

where $\beta(v, u)$, $G(v)$ and J_0 are the coagulation, condensation and nucleation kernel functions, respectively. The left-hand side of Equation (3-2) is the unsteady or accumulation term. On the right-hand side of Equation (3-2), the first two terms are the coagulation birth term and the coagulation loss term, respectively. The 1/2 in the coagulation birth term is placed in front of the integral to prevent double counting of all possible particle collisions. The third term is the surface growth combined with the oxidation mechanism. The last term is nucleation.

3.2.2 The solution of PBEs

Since PBEs is a set of the complex partial integral-differential equations, analytical solutions are available only for very simplified cases (Smoluchowski, 1916; Zhou et al., 2014). Computational methods are needed to approximate the integral and differential terms of PBEs especially in spatially distributed systems.

These developed numerical methods for solving PBEs can be divided into three different numerical methods: sectional methods (SMs) (Gelbard et al., 1980; Jeong and Choi, 2001; Prakash et al., 2003; Mitrakos et al., 2007; Woo et al., 2021); methods of moments (MOM) (Frenklach, 2002a; Yu et al., 2008; Lin and Chen, 2013; Yu and Chan, 2015; Chan et al., 2018; Liu et al., 2019b; Jiang et al., 2021) and Monte Carlo (MC) methods (Haibo et al., 2005; Zhao et al., 2009; Zhou and He, 2014; Zhou et al., 2014; Liu and Chan, 2017b; Liu and Chan, 2018b; Jiang and Chan, 2021a; Boje and Kraft, 2022).

MC methods are developed based on performing numerous fictitious experiments with random numbers to represent the behavior of real particles (Ramkrishna, 2000), and the population of real particles can be described by a set of computational particles. MC methods are attractive methods for solving the PBEs due to the discrete nature of the MC methods. As a result, the aerosol dynamic processes (e.g., particle breakage and coalescence processes) can be easily modelled by MC methods (Ramkrishna, 2000). Gillespie (1975) derived direct simulation Monte Carlo (DSMC) method to describe the Markov chain for coagulation process as the stochastic process. The fundamental algorithm is briefly introduced below:

The probability for any coagulation event occurred at a random time, τ can satisfy the Poisson distribution in Equation (3-3) (Gillespie, 1975):

$$P(\tau \geq \tau_0) = \exp(-C_0\tau_0) \tag{3-3}$$

where

$$C_0 = \sum_{i=1}^{N-1} \sum_{j=i+1}^{N} C_{ij} \tag{3-4}$$

$$C_{ij} = \frac{\beta(v_i, v_j)}{V} \tag{3-5}$$

where i and j are the indexes of numerical particles, N, and v_i and v_j are the sizes of the related collisional pair. C_{ij} is the coagulation rate in simulation box volume, V between particles, i and j. C_0 is the total coagulation rate between any two particles which determines the time intervals between two coagulation events. The coagulation pairs are then chosen by the probability (Gillespie, 1975):

$$P(i, j) = \frac{C_{ij}}{C_0} \tag{3-6}$$

After a coagulation event, the particles i and j are then removed and a new particle with the size of $v_i + v_j$ is formed.

3.3 Governing Equations for Combustion

3.3.1 Overview

Combustion is one of the most important phenomena involved in many different physical and chemical problems (e.g., fluid flow fields, thermodynamic properties and chemical reactions). These problems are always concurrent and coupled in combustion phenomena. In order to describe combustion phenomena mathematically, the basic concepts and equations for combustion is required including the conservation equations, thermodynamics and chemical kinetics. Conservation equations are formulated to describe the conservation of physical properties in the system by laws of nature. Considering the combustion phenomena, some basic variables are considered for describing the system which include the mass, momentum, energy, and species mass fractions. According to the conservation equations, the changes of these variables in an infinitesimal control

volume can be described by the transportation of the variable through the boundaries of the control volume and the source terms in the control volume. The conservation equations for describing the combustion phenomena are a set of partial differential equations (PDEs) which are also coupled due to the complex and concurrent nature of these different physical/chemical processes.

3.3.2 Conservation equations

The conservation equations for gas phase combustion include the conservation of mass, momentum and energy, and species mass fractions. These conservation equations are given (Kuo, 1986; Hairuddin, 2014) below:

3.3.2.1 Conservation of mass

For the conservation of mass:

$$\frac{\partial \rho}{\partial t} + \frac{\partial \rho u_i}{\partial x_i} = 0 \tag{3-7}$$

where x_i is the coordinate of ith-component, ρ is the density of mixture (gas and soot) and u_i is the ith-component velocity.

3.3.2.2 Conservation of momentum

For the conservation of momentum:

$$\frac{\partial \rho u_j}{\partial t} + \frac{\partial \rho u_i u_j}{\partial x_i} = -\frac{\partial P}{\partial x_j} + \frac{\partial \tau_{ij}}{\partial x_i} \tag{3-8}$$

where P is the pressure and τ_{ij} is viscous stress tensor which is explicitly given by:

$$\tau_{ij} = \mu\left(\frac{\partial u_i}{\partial x_j} + \frac{\partial u_j}{\partial x_j}\right) + \left(\kappa - \frac{2}{3}\mu\right)\left(\frac{\partial u_k}{\partial x_k}\delta_{ij}\right) \tag{3-9}$$

where μ and κ are the shear and volume viscosity, respectively.

3.3.2.3 Conservation of species mass fractions

For conservation of species mass fractions:

$$\frac{\partial \rho Y_k}{\partial t}+\frac{\partial \rho u_i Y_k}{\partial x_i}=-\frac{\partial \rho Y_k V_{k,i}}{\partial x_i}+W_k \dot{\omega}_k+S_k \tag{3-10}$$

where Y_k is the kth species mass fraction, $V_{k,i}$ is the kth species diffusive velocity, W_k is the kth species molecular weight and $\dot{\omega}_k$ is the kth species molar production rate. The chemical reaction source term, $\dot{\omega}_k$ includes the contributions from soot nucleation, surface condensation and oxidation processes (i.e., the interactions between soot formation/oxidation and gas-phase chemistry).

3.3.2.4 Conservation of energy

For the conservation of energy:

$$\frac{\partial \rho E}{\partial t}+\frac{\partial \rho u_i E}{\partial x_i}=-\frac{\partial q_i}{\partial x_i}-\frac{\partial u_i P}{\partial x_i}+\frac{\partial u_j \tau_{ij}}{\partial x_i}+\dot{\omega}_T \tag{3-11}$$

where E is the internal energy of gaseous mixtures, $\dot{\omega}_T$ is the chemical source term of energy and q_i is the heat flux which is explicitly given by Kee et al. (1986) as:

$$q_i=-\lambda \frac{\partial T}{\partial x_i}+\sum_{k=1}^{N} \rho Y_k V_{k,i} h_k \tag{3-12}$$

where λ is the heat conduction coefficient of gaseous mixture. The diffusion velocity of the kth gaseous species is calculated (Kee et al., 1986) as:

$$V_{k,i}=V_{ok,i}+V_{Tk,i}+V_{c,i} \tag{3-13}$$

where $V_{ok,i}$ and $V_{Tk,i}$ are the velocities of ordinary and thermal diffusions of kth species, respectively, and $V_{c,i}$ is the velocity of correction diffusion.

The velocities of ordinary and thermal diffusions of *k*th species are calculated based on the approximate mixture-averaged formulation (Kee et al., 1986) as:

$$V_{ok,i} = -\frac{D_k}{X_k}\frac{\partial X_k}{\partial x_i} \tag{3-14}$$

$$V_{Tk,i} = \frac{D_k \Theta_k}{X_k}\frac{1}{T}\frac{\partial T}{\partial x_i} \tag{3-15}$$

where X_k is the mole fraction of *k*th species; Θ_k is the thermal diffusion ratio of *k*th species. D_k is the diffusion coefficient of gaseous mixture for the *k*th species and is calculated (Kee et al., 1986) as:

$$D_k = -\frac{1\text{-}Y_k}{\sum_{j=1, j\neq k}^{N}\frac{X_j}{D_{k,j}}} \tag{3-16}$$

where $D_{k,j}$ is the binary diffusion coefficient.

The velocity of correction diffusion, $V_{c,j}$ is used to ensure that the summation of the mass fractions of gas phase species and soot is equal to unity (Kee et al., 1986).

3.3.3 Thermodynamics and chemical kinetics

Thermodynamics studies the different forms of energy transformation. For the needs of numerical simulations, the thermodynamics are often stored as polynomials in *T*. Some of these thermodynamic values are given by experimental data, and most of the thermodynamic properties data are developed by theoretical calculations based on the semi-empirical schemes relating thermodynamics to molecular structures (Kee et al., 1986; Noroozi and Smith, 2021).

Heat capacities are expressed as NASA polynomials form (Stull, 1965; Burcat, 1984; Warnatz et al., 1990; Yan et al., 2022), which can be used to calculate

the enthalpy, the entropy and the equilibrium constant. Usually the molar heat capacity ($C_p^0=C_V^0+R_u$) is expressed as the polynomials interpolation of T (e.g., the fourth order polynomial equation) (Kee et al., 1986):

$$\frac{C_p^0}{R_u} = a_1 + a_2 \cdot T + a_3 \cdot T^2 + a_4 \cdot T^3 + a_5 \cdot T^4 \tag{3-17}$$

where a_1, ..., a_5 are constants, and R_u is the universal gas constant. In addition, the enthalpy can be expressed as an integration (Kee et al., 1986):

$$H_T^0 = a_6^* \cdot R_u + \int_{T'=298K}^{T} C_P^0 \, \mathrm{d}T' \tag{3-18}$$

where $a_6^* \cdot R_u = H_{298\mathrm{K}}^0$. The enthalpy at temperature T can be calculated by integrating the heat capacity in Equation (3-17) (Kee et al., 1986) as:

$$\frac{H_T^0}{R_u} = a_6 + a_1 \cdot T + \frac{a_2}{2} \cdot T^2 + \frac{a_3}{3} \cdot T^3 + \frac{a_4}{4} \cdot T^4 + \frac{a_5}{5} \cdot T^5 \tag{3-19}$$

The coefficient a_6 which is different from a_6^* can be given by setting T = 298K as the reference temperature. H^0 (298K) is equal to the enthalpy of formation at 298 K.

Chemical kinetics are used to express the rate of chemical reactions: how rapidly reactants are consumed and products are generated, and how the rates are affected by the changes of the combustion conditions. The detailed reaction mechanisms are based on the elementary reactions. For a given reaction, the elementary reaction, r is written (Turns, 1996) as :

$$\sum_{s=1}^{S} \nu_{rs}^{(e)} A_s \xrightarrow{k_r} \sum_{s=1}^{S} \nu_{rs}^{(P)} A_s \tag{3-20}$$

then the rate law illustrates the rate of transformation process and specifies

the dependence of the chemical reaction rate on the temperature, pressure and concentration of the reactants. For a specific *i* species in chemical reaction, *r* (Turns, 1996) as:

$$\left(\frac{\partial c_i}{\partial t}\right)_{\text{chem},r} = k_r(v_{ri}^{(P)} - v_{ri}^{(e)})\prod_{s=1}^{S} c_s^{v_{rs}^{(e)}} \tag{3-21}$$

where $v_{rs}^{(e)}$ and $v_{rs}^{(P)}$ denote the stoichiometric coefficients of reactants and products, respectively, and c_s is the concentration of the *s*th species (Vishwanathan and Reitz, 2010).

The coefficient of reaction rate, *k* is strongly nonlinear with temperature, and it can be written (Peter Atkins and De Paula, 2014) as:

$$k = AT^b \cdot \exp(-\frac{E_a}{R_u T}) \tag{3-22}$$

where *T* is the temperature, R_u is the universal gas constant, *A* is the pre-exponential factor or frequency factor, *n* is the temperature exponent and E_a is the activation energy.

3.4 Soot Formation

3.4.1 Overview

The study of soot formation and evolution is a challenging task because the soot formation and evolution processes involve the problems of both gas and solid phases. Consequently, modelling the soot formation and evolution not only requires an accurate description of the gas-phase species, but also the physical and chemical properties of soot particles should be precisely modelled. In general,

the formation and evolution of soot particles can be divided into four stages: particle nucleation, coagulation, condensation and surface reaction.

Unfortunately, the knowledge of soot formation is still not fully understood. There are still many uncertainties in understanding the full kinetics of soot formation especially nucleation. Numerous soot models have been developed till now to provide the insights of soot formation and evolution processes under different flame conditions. These soot models are basically divided into empirical, semi-empirical and detailed models, respectively.

3.4.2 Soot models

Empirical soot models are formulated by the reaction rate constants of the soot kinetics that are correlations of experimental data (Kennedy, 1997; Valencia et al., 2021). The advantage of these soot models is that the agreement can be excellent with relatively simple chemistry and reduced computational effort. The drawback is that these soot models have limited applicability to incorporate other types of combustion modes, hydrocarbon fuels, and pressure conditions. The semi-empirical models solve the rate equations of soot formation with some experimental inputs (Kennedy, 1997; Ali, 2014; Valencia et al., 2021). Finally, the detailed soot models solve the rate equations of soot formation from the elementary state with minimal experimental input. This is considered the best soot model that generates a global soot model to work under different conditions. The majority of the soot models is a semi-empirical acetylene-based soot model. Detailed soot models are represented primarily by PAH-based soot models.

Detailed chemical gas-phase mechanisms and detailed soot modelling was developed by the research group of Professor Frencklach (Appel et al., 2000). The gas-phase chemistry includes PAH formation up to pyrene ($C_{16}H_{10}$) which is the heaviest hydrocarbon species in this mechanism and acts as a soot precursor. In the detailed soot model, nucleation is usually described as dimerization of one (Appel et al., 2000; Sirignano and Russo, 2021) or more (Blanquart and Pitsch, 2009a; Gleason et al., 2021) PAH species with most notably pyrene molecules. The nucleation terms can be obtained by applying the kinetic theory (Blanquart and Pitsch, 2009b) as:

$$J_0 = \frac{2.2}{\rho}\sqrt{\frac{4\pi k_B T}{C_{\text{mass}} N_{C,\text{PAH}}}} d_{\text{PAH}}^2 A_v^2 [\text{PAH}]^2 \tag{3-23}$$

where k_B is the Boltzmann constant, C_{mass} is the mass of a carbon atom, $N_{C,\text{PAH}}$ is the number of carbon atoms in the incipient PAH species, d_{PAH} is the diameter of the incipient PAH species (Wang et al., 2018) and can be approximately given (Zhang, 2009) as:

$$d_{\text{PAH}} = d_A \sqrt{\frac{2N_{C,\text{PAH}}}{3}} \tag{3-24}$$

where d_A is the size of a single aromatic ring and is equal to $1.395\sqrt{3}$ (Frenklach and Wang, 1994), A_v is Avogadro's number and [PAH] is the molar concentration of the PAH species (Wang et al., 2018).

Surface growth is always described by the hydrogen abstraction acetylene addition (HACA) mechanism in the detailed soot model (Frenklach and Wang, 1994; Wang et al., 2018). The whole soot surface reaction scheme is listed in Table 3.1 (Appel et al., 2000).

Table 3.1 HACA-based soot surface growth and oxidation reactions (Appel et al., 2000).

No.	Reaction	A (cm^3 /mol·s)	b	E_a (kcal/mol)
S1	C_{soot}–H+H⇆C_{soot}•+H_2	4.2×10^{13}	0.0	13.0
S2	C_{soot}–H+OH⇆C_{soot}•+H_2O	1.0×10^{10}	0.73	1.43
S3	C_{soot}•+H⟶C_{soot}–H	2.0×10^{13}	0.0	0.0
S4	C_{soot}•+C_2H_2⟶C_{soot}–H+H	8.0×10^{7}	1.56	3.8
S5	C_{soot}•+O_2⟶2CO + product	2.2×10^{12}	0.0	7.5
S6	C_{soot}–H+OH⟶CO + product	-	$\gamma = 0.13$	-

Apart from the reaction of soot particles with OH radicals (S6) which is described by applying kinetic theory with a reaction probability OH of 0.13 (Neoh et al., 1985), the other surface reactions are modelled based on the conception of surface reactive sites (i.e., an armchair site on the particle surface) which are carbon atoms either saturated (C_{soot}–H) or dehydrogenated (C_{soot}•) (Keller, 2019). The concentration of saturated sites, [C_{soot}–H] (mole/cc) is given by Appel et al. (2000):

$$[C_{soot} - H] = \frac{xC_{soot} - H \times A_s}{A_v} \tag{3-25}$$

where $x$$C_{soot}$–H is the number of sites per unit soot surface area which is regarded as a constant value of 2.3×10^{15} sites/cm^2 (Appel et al., 2000), A_s (cm^2/cm^3) is the surface density of soot particles and A_v is the Avogadro's number (1/mol). The HACA surface reaction scheme also assumes an empirical parameter, α to describe the fraction of reactive surface sites available for the HACA reaction

(Bowal, 2020). It is derived by considering the probability of collision between gaseous species molecules and the reactive edge planes instead of unreactive basal planes of soot particles. In addition, the experimental evidence shows that not all of the edge carbons are available for HACA reaction (Frenklach and Wang, 1991; Martin et al., 2022). Hence, the supposed availability of fraction of reactive surface sites should also be taken into consideration when modelling HACA reaction. The temperature-dependent values of parameter were experimentally confirmed by the research group of Professor Faeth (Xu et al., 1998).

The rate of individual reactions (R4 for example) for a soot particle *i* can be calculated by Appel et al. (2000):

$$R_{i,4} = 2C_{\text{mass}} k_4 [\text{C}_2\text{H}_2] \frac{\alpha \times x\text{C}_{\text{soot}}\text{•} \times A_{s,i} \times N_i}{A_v} \tag{3-26}$$

where k_4 is the pre-site rate coefficient calculated based on Table 3.1, $[C_2H_2]$ is the molar concentration of C_2H_2, $x\text{C}_{\text{soot}}$• is the number of dehydrogenated sites (C_{soot}•) per unit surface area, $A_{s,i}$ is the surface area of particle *I*, A_v is the Avogadro's number and N_i is the number density of particle *i* (Bockhorn, 2013). Assuming a steady state for C_{soot}•, $x\text{C}_{\text{soot}}$• can be calculated (Appel et al., 2000) as:

$$x\text{C}_{\text{soot}}\text{•} = \frac{(k_1[\text{H}] + k_2[\text{OH}]) \times x\text{C}_{\text{soot}} - \text{H}}{k_{-1}[\text{H}_2] + k_{-2}[\text{H}_2\text{O}] + k_3[\text{H}] + k_4[\text{C}_2\text{H}_2] + k_5[\text{O}_2]} \tag{3.27}$$

Finally, the surface growth rate of particle *i*, $R_{i,4}$ (g/(cm^3·s)) can be calculated by Appel et al. (2000):

$$R_{i,4} = \frac{2C_{\text{mass}} k_4 [\text{C}_2\text{H}_2] \alpha A_{s,i} N_i}{A_v} \times \frac{(k_1[\text{H}] + k_2[\text{OH}]) \times x\text{C}_{\text{soot}} - \text{H}}{k_{-1}[\text{H}_2] + k_{-2}[\text{H}_2\text{O}] + k_3[\text{H}] + k_4[\text{C}_2\text{H}_2] + k_5[\text{O}_2]} \tag{3-28}$$

The collision of PAH species with soot particles results in condensation of PAH species on soot surfaces with the increase of the soot mass. The condensation rate can be obtained via the collision theory between PAH molecules and soot particles (Park et al., 2005). Considering the fact that not all collisions can result in condensation (Kronholm and Howard, 2000), a PAH-soot surface condensation efficiency is introduced for describing the probability of sticking in the collision between PAH molecules and soot particles.

The soot coagulation process can be well described by the collision kernel in the different ranges of Knudsen number, Kn. For Kn > 10, the collision kernel of free molecular regime should be used and its form is given (Friedlander, 2000) as:

$$\beta^{fm}(v,u) = 2.2\sqrt{\frac{\pi k_B T}{2m_{v,u}}}(d_c(v)+d_c(u))^2 \tag{3-29}$$

where $m_{v,u}$ is the reduced mass of particles v and u (Blanquart and Pitsch, 2009b) and the multiplier of 2.2 is the van der Waals enhancement factor (Frenklach and Wang, 1994). For Kn < 0.1, the collision kernel of continuum regime is used (Friedlander, 2000) as:

$$\beta^{c}(v,u) = \frac{2k_B T}{3\mu}(d_c(v)+d_c(u))(\frac{1}{d_c(v)}+\frac{1}{d_c(u)}) \tag{3-30}$$

where μ is the dynamic viscosity of fluids. For $0.1 \le Kn \le 10$, the collision kernel of intermediate regime can be obtained by the harmonic mean of $\beta^{fm}(v,u)$ and $\beta^{c}(v,u)$ (Friedlander, 2000) as:

$$\beta^{int}(v,u) = \frac{\beta^{fm}(v,u)\beta^{c}(v,u)}{\beta^{fm}(v,u)+\beta^{c}(v,u)} \tag{3-31}$$

3.5 Molecular Dynamics (MD) Simulation

3.5.1 Overview

Molecular dynamics (MD) simulation is an approach which has been widely used to simulate the dynamic behaviors of the atomic systems. With the development of the MD approach, many different force fields have been proposed for different research fields and applications in order to increase the accuracy and efficiency of MD simulations. The dynamic behaviors and thermodynamic properties of many systems can be investigated via MD approach such as those involving novel material applications and biological systems (Razavi et al., 2014; Cygan and Kubicki, 2018; Sun et al., 2021). In MD simulations, the motion of a system is treated with Newton's equations of motion and the interactions between atoms are determined by the force field potential without describing the electronic interactions explicitly in quantum mechanics. The brief description of MD approach is given below.

In statistical mechanics, the total energy (E_{total}) of a system corresponds to the Hamiltonian of a system including both kinetic and potential energy functions can be given (Frenkel and Smit, 2001) as:

$$E_{\text{total}} = \sum_{i=1}^{N} E_{\text{kin}}(p_i) + \sum_{i=1}^{N} E_{\text{pot}}(r_i) \tag{3-32}$$

where r_i and p_i are the coordinate and momentum of each particle i, respectively. In the classical Newtonian mechanics, the kinetic energy can be defined (Frenkel and Smit, 2001) as:

$$E_{\text{kin}} = \sum_{i=1}^{N} \frac{p_i^2}{2m_i} = \sum_{i=1}^{N} \frac{1}{2} m_i v_i^2 \tag{3-33}$$

where m_i and v_i are the mass and velocity of the particle i, respectively. If it is assumed that no external force acting on the system, the system can be described by the attractive and repulsive interactions between particles. The motion of these particles is governed by the classical Newtonian laws. The forces on each particle can be expressed (Frenkel and Smit, 2001) as:

$$f_i = -\nabla_{ri} E_{\text{pot}} \tag{3-34}$$

where ∇_{ri} is the gradient of potential energy for the particle i at coordinate r_i. From the above descriptions and equations (Equations 3.32 to 3.34), it is now possible to obtain the complete information of the position and momentum of atoms at all times for the system. Consequently, the dynamic behaviors and thermodynamic properties of the system can be determined. The time evolution of system is governed by the classical Newtonian mechanics which can be performed by using an integration algorithm. One common approach is the velocity Verlet-algorithm, which advances a time step Δt with the evolution of the particle coordinates is expressed (Frenkel and Smit, 2001) as:

$$r(t+\Delta t) = r(t) + \frac{\Delta t}{m} p(t) + \frac{\Delta t^2}{2m} f(t) \tag{3-35}$$

$$p(t+\Delta t) = p(t) + \frac{1}{2}\Delta t(f(t) + f(t+\Delta t)) \tag{3-36}$$

Following Equations 3-35 and 3-36, the position and momentum of each particle are known. Hence, the microstates of a system with a number of particles can be determined. The thermodynamic properties (e.g., enthalpy, entropy and heat capacity) of a system can be determined by ensemble averaging.

3.5.2 Reactive force fields

Section 3.5.1 introduces the theoretical fundamentals of the MD simulation approach. However, the classical MD simulations with traditional force fields cannot simulate the chemical reaction since the classical MD simulation is incapable to model bond formation and breakage. To overcome the limitation of classical MD simulation, the reactive force field (ReaxFF) was firstly proposed by van Duin et al. (2001). The basic concept of ReaxFF is to describe the interaction between particles by introducing the potential energy functions with the dependence of bond order. As a result, the ReaxFF is capable to model bond breakage and formation for chemical reactions (Senftle et al., 2016; Vashisth et al., 2018; Li et al., 2021b).

An important concept in ReaxFF is the bond order, BO_{ij} which is defined as the function of the interatomic distance r_{ij} between atoms i and j. The bond order term includes three exponential functions for the σ bond, the first π bond and the double π bond between two atoms (Senftle et al., 2016) as:

$$\begin{aligned} \mathrm{BO}_{ij} &= \mathrm{BO}_{ij}^{\sigma} + \mathrm{BO}_{ij}^{\pi} + \mathrm{BO}_{ij}^{\pi\pi} \\ &= \exp\left[p_{\mathrm{bo1}} \left(\frac{r_{ij}}{r_0^{\sigma}} \right)^{p_{\mathrm{bo2}}} \right] + \exp\left[p_{\mathrm{bo3}} \left(\frac{r_{ij}}{r_0^{\pi}} \right)^{p_{\mathrm{bo4}}} \right] \exp\left[p_{\mathrm{bo5}} \left(\frac{r_{ij}}{r_0^{\pi\pi}} \right)^{p_{\mathrm{bo6}}} \right] \end{aligned} \tag{3-37}$$

where r_0 is the equilibrium bond length and p_{bo} is the empirical parameters. These are parameterized by quantum mechanics (QM) calculations and experimental data. Equation (3-37) is continuous containing no discontinuities for transitions between σ, π and $\pi\pi$ bonds. It provides the differentiability of potential energy surface to calculate the interatomic forces. The total potential energy of the system in ReaxFF is described by Senftle et al. (2016):

$$E_{\text{system}} = E_{\text{bond}} + E_{\text{over}} + E_{\text{angle}} + E_{\text{tors}} + E_{\text{vdWaals}} + E_{\text{Coulomb}} + E_{\text{Specific}} \quad (3\text{-}38)$$

where E_{system} is a total potential energy of the system, E_{bond} is a bond energy described by the bond order which is the continuous function of interatomic distance, E_{over} is a penalty term for over coordination to avoid the over coordination of atoms, which is based on atomic valence rules, E_{angle} and E_{tors} are the three-body valence angle energy and four-body torsion angle energy, E_{Coulomb} and E_{vdWaals} are the energy terms for describing the Coulomb and Van der Waals interactions, respectively, E_{Specific} is energy term which is only applied to the specific system in order to obtain the properties of interest, such as lone-pair, conjugation, hydrogen binding, and C_2 corrections (Senftle et al., 2016).

To model the polarization and charges in the particles, ReaxFF applied the approach based on the electronegativity equalization method (EEM) (Mortier et al., 1986) and the electronegativity equilibration (QEQ) (Rappe and Goddard III, 1991; Keller, 2019). The computational costs are much lower than quantum-chemical or semi-empirical methods by applying the ReaxFF to the molecular dynamics simulation, while the ReaxFF MD remains comparable computational accuracy with QM methods. Therefore, ReaxFF is appropriate for simulating the complex reactive systems as well as non-reactive systems containing large hydrocarbon molecules with a long-time scale simulation such as soot formation in the combustion flame environments.

3.6 Summary

The basis of fundamental theories in the present study are described and formulated including the Monte Carlo (MC) method, soot modelling and molecular dynamics (MD) method. The fundamental concepts and assumptions as well as mathematical theories and governing equations (i.e., population balance equations (PBEs), MC methods, conservation equations in combustion), and descriptions of molecular dynamics (MD) and reactive force field (ReaxFF) are presented so that the research methodologies developed and used in the present study can be more easily reassembled.

Chapter 4 Development of Weighted Fraction Monte Carlo Method

4.1 Introduction

The purpose of this chapter is to propose and develop a new weighted fraction Monte Carlo method (WFMC) method which demonstrates the ability of statistical noise reduction in the Monte Carlo (MC) simulation. In the MC simulation, the stochastic error in the particle size distribution (PSD) function is inevitable because a finite number of numerical particles can be used for the numerical simulation. Some modified numerical algorithms have been developed to improve the computational efficiency and accuracy of stochastic methods, including the weighted flow algorithm (WFA) (DeVille et al., 2011; DeVille et al., 2019) and multi-Monte Carlo (MMC) (Zhao et al., 2009; Kotalczyk and Kruis, 2017) methods. However, the weight of the numerical particles in MMC method is not adjustable, which may limit the applications of MMC method. By introducing the additional fraction function (α) and the probabilistic removal process, WFMC is newly proposed and developed.

Three typical cases with constant kernel, free-molecular coagulation kernel and different initial distributions for particle coagulation are simulated and validated for the newly proposed and developed WFMC method. The critical stochastic error of different order moments is further studied with three different MC (i.e., WFMC, DSMC and MMC) method schemes. Meanwhile, the computational efficiency of these MC methods is also investigated and compared. In addition, the main novelty of the proposed and developed WFMC method is fraction function and random

removal process, the effects of different fraction functions on weight function, computational efficiency and accuracy of this numerical algorithm are also fully analyzed.

4.2 Numerical Methodology

4.2.1 Smoluchowski equation and Monte Carlo method

Smoluchowski equation describes the time evolution of particle size distribution (PSD) by coagulation process (Smoluchowski, 1916) as:

$$\frac{\partial n(v,t)}{\partial t} = \frac{1}{2}\int_0^v \beta(u, v-u)n(u,t)n(v-u,t)du - \int_0^\infty \beta(v,u)n(v,t)n(u,t)du \qquad (4\text{-}1)$$

where $n(v, t)$ is the particle number density of volume, v at time, t and $\beta(u, v)$ is the coagulation kernel function which describes the coagulation rate for two particles with volumes, u and v, respectively.

Gillespie (1975) applied the direct simulation Monte Carlo (DSMC) method in the fields of aerosol dynamics for solving Smoluchowski equation, which is the cornerstone of further developments. The basic of numerical algorithm is described as below. The probability for any coagulation event occurred at a random time, τ, will satisfy the Poisson distribution (Gillespie, 1975) as:

$$P(\tau \geq \tau_0) = \exp(-C_0\tau_0) \qquad (4\text{-}2)$$

where

$$C_0 = \sum_{i=1}^{N-1}\sum_{j=i+1}^{N} C_{ij} \qquad (4\text{-}3)$$

$$C_{ij} = \frac{\beta(v_i, v_j)}{V} \qquad (4\text{-}4)$$

where i and j are the indexes of numerical particles, N, and v_i and v_j are the sizes of the related collisional pair. C_{ij} represents the coagulation rate in simulation box volume, V, between particles, i and j. C_0 represents the total coagulation rate between any two particles which determines the time intervals between two coagulation events. The coagulation pairs are then chosen by the probability:

$$P(i,j)=\frac{C_{ij}}{C_0} \tag{4-4}$$

After a coagulation event, the particle i and particle j are then removed and a new particle with the size of $v_i + v_j$ is formed.

4.2.2 Derivation of coagulation rate

In classical DSMC method, numerical particles are assigned with the same weight. The number of numerical particles at different intervals of particle size is proportional to their particle number density. Such equally weighted scheme always results in a poor representation at the tails of particle size spectrum where the particle number density is very low and thus leads to the large stochastic error and limited PSD, and restricts the application of classical DSMC method (Zhao et al., 2009). To overcome the inherent limitation in the DSMC method, the differentially weighted particle scheme is then introduced by considering that each numerical particle corresponds to some numbers of physical particles, and the actions are implemented on the numerical particles with some probabilities instead of directly implementing on the real physical particles (DeVille et al., 2011).

A new coagulation rule for the weighted numerical particles is required to be constructed, which determines the coagulation rates between weighted numerical

particles. In more detail, the coagulation rule depends on how to perform the coagulation event between a coagulation pair, and then the jump Markov process is constructed based on this new coagulation rule (Zhao and Zheng, 2009).

In the differentially weighted particle scheme, a numerical particle, *i* represents the number of physical particles, w_i with the size of v_i, thus *i* represents a group of physical particles with number concentration, w_i/V. This analysis is the same for the numerical particle, *j*. From the definition of collision kernel function (Friedlander, 2000), the number of real coagulation events occurring between *i*th-group and *j*th-group per unit time and volume is given as:

$$\Phi_{ij} = \beta_{ij} \times \frac{w_i}{V} \times \frac{w_j}{V} \tag{4-6}$$

where β_{ij} is the collision kernel function of particles, *i* and *j*. Φ_{ij} is the coagulation rate from the group of physical particles, *i* and *j*, respectively.

From the point of view of Zhao et al. (2009), the new probabilistic coagulation rule is constructed by considering that a coagulation event is related to two numerical particles but not every real particle. In fact, only a subset of real particles is considered to participate in a coagulation event. For example, the number of real coagulation events between numerical particles *i* and *j* in the MMC method are:

$$\Omega = \min(w_i, w_j) \tag{4-7}$$

Compared with MMC method, by considering that there are less real coagulation events occurred between numerical particles *i* and *j*, the number of real coagulation events is then given as:

$$\Omega'=\alpha_{ij}\min(w_i,w_j);\qquad \alpha_{ij}\le 1 \tag{4-8}$$

where α_{ij} is the fraction function. It should be noted that the fraction function, α_{ij} cannot be larger than 1 because the upper bound of the number of coagulation pairs between numerical particles *i* and *j* is min(w_i, w_j). In addition, the fraction function is not restricted to be a constant, it can be the function of any specific properties (e.g., particle weight or particle volume or simulation time) of the numerical particles, *i* and *j* considered for coagulation.

No matter which coagulation rule is adopted, the coagulation rate of a physical particle from the same numerical particle in the simulation volume *V* should always be the same and is expressed as:

$$\Omega C_{ij}=\Omega' C'_{ij}=V\Phi_{ij} \tag{4-9}$$

$$\begin{aligned} C'_{ij}&=\frac{1}{\Omega'}\Phi_{ij}=\frac{1}{\alpha_{ij}}\frac{\max(w_i,w_j)\beta_{ij}}{V}\\ &=\frac{\beta'_{ij}}{V}\end{aligned} \tag{4-10}$$

where C'_{ij} is new coagulation rate of numerical particle pairs, *i* and *j,* with numerical simulation volume, *V*, $\beta'_{ij}=\max(w_i,w_j)\beta_{ij}/\alpha_{ij}$ is normalized coagulation kernel where β'_{ij} is related not only to the size of the particles but also related to their other specific properties. Then the new jump Markov model of the WFMC method is constructed based on β'_{ij}.

The waiting time between two successive coagulation events of numerical particle obeys the exponential distribution as:

$$P(\tau)=C_0'\exp(-C_0'\tau) \tag{4-11}$$

where

$$C_0' = \sum_{i=1}^{N} \sum_{j<i} C_{ij}' \tag{4-12}$$

For time-driven Monte Carlo scheme, the occurrence probability of a coagulation event of numerical particle within Δt and V, $P_{\text{coag}}^{'}(\Delta t)$ is an exponentially distributed random variable (Garcia et al., 1987):

$$P_{\text{coag}}'(\Delta t) = 1 - \exp(-\Delta t C_0') \tag{4-13}$$

The coagulation particle pairs can be randomly selected by the cumulative probability method (Liffman, 1992) or the acceptance-rejection method (Lin et al., 2002). However, acceptance-rejection method adopts simpler and more straightforward criterion to choose the particle pairs when compared with cumulative probability method (Wei and Kruis, 2013). Hence, the acceptance-rejection method is used in the present study, and a possible particle pair, i, j, is first selected randomly. Then, if the following condition is satisfied, the numerical particles, i and j, are accepted as a coagulation particle pair:

$$r \le \beta_{ij}' / \max_{\forall k, \forall m}(\beta_{km}') \tag{4-14}$$

where r is random number $r \sim U[0,1]$.

4.2.3 Treating a coagulation event

Once the particles, i and j, of coagulation pair are selected, then a numerical particle, i, will coagulate with its coagulation particle partner, j. As a result, some number of physical particles from the numerical particle, i, will also coagulate with those from the numerical particle, j. However, if the numerical particles, i and j, have

different weights (e.g., $w_i > w_j$), that means there are not enough physical particles in the numerical particle, *j* to make particle pairs with those from the numerical particle, *i*. Therefore, after coagulation events between particle pairs with different weights, these physical particles could be separated into two parts of "coagulated" physical particles and "non-coagulated" physical particles, respectively.

After a coagulation event, the new weight of $w''_{\text{coag}} = \alpha_{ij}\min(w_i, w_j)$ is assigned to the coagulated numerical particle with a new volume (i.e., is equal to the volume summation of two coagulation particle partners) while the new weights for other two numerical particles are equal to the number of non-coagulated real particles. The weights for these two numerical particles are calculated as $w_i'' = w_i - \alpha_{ij}\min(w_i, w_j)$ and $w_j'' = w_j - \alpha_{ij}\min(w_i, w_j)$, respectively. If a coagulation particle pair has equal weight and all physical particles will be coagulated, then these physical particles will be separated into two groups. With an equal weight to two numerical particles, these operations of treating a coagulation event are similar to the work of Kotalczyk and Kruis (2017). The consequences of a coagulation event could be denoted as:

$$\text{if } w_i \neq w_j, \begin{cases} w_i'' = w_i - \alpha_{ij}\min(w_i, w_j); \quad v_i'' = v_i \\ w_j'' = w_j - \alpha_{ij}\min(w_i, w_j); \quad v_j'' = v_j \\ w_{\text{coag}}'' = \alpha_{ij}\min(w_i, w_j); \quad v_{\text{coag}}'' = v_i + v_j \end{cases} \tag{4-15}$$

$$\text{if } w_i = w_j, \begin{cases} w_i'' = w_i / 2; \quad v_i'' = v_i + v_j \\ w_j'' = w_j / 2; \quad v_j'' = v_i + v_j \end{cases} \tag{4-16}$$

where w'' and v'' represent the new weight or size after the coagulation event, respectively. From Equations (4-15) and (4-16), mass is conserved during coagulation. It should be noted that the number of numerical particles maintains

constant when $\alpha_{ij} \equiv 1$, where WFMC method coincides with the MMC method under this condition (Zhao and Zheng, 2009). Although WFMC method can assimilate to some traditional differential weighted MC method schemes under some specific conditions, it also proves that WFMC method is actually a new MC method scheme in more general cases. Compared with traditional MMC method, the weight distribution in WFMC is adjustable. For other weighted particle schemes e.g., mass-flow algorithm (MFA) (Babovsky, 1999; Eibeck and Wagner, 2001a) and weighted flow algorithm (WFA) (DeVille et al., 2011) , the weight of numerical particle is not explicitly given in WFMC method which coincides with MMC method.

4.2.4 Probabilistic removal

For two coagulated numerical particles with different weights for $\alpha_{ij} < 1$, the additional new numerical particle has to be created as the results from the coagulation event (in Equation (4-15)). The number of numerical particles will continuously increase which leads to non-constant-number schemes (Kotalczyk and Kruis, 2017). The statistical accuracy and computational efficiency vary as the total number of numerical particles changes.

In order to maintain the number of numerical particles, the new coagulation rule for treating the coagulation event must be constructed. To achieve the constant number scheme, the common method is by the removal of one selected numerical particle partner after the coagulation event, and then the weight of other particle partner is adjusted to ensure that the particle properties are statistically unchanged (e.g., the expectation of particle number/mass). Such method is always adopted in Monte-Carlo simulation. For the constant-number method (Lee and Matsoukas,

2000), the additional numerical particles are randomly removed after fragmentation events to force the number of numerical particles in the simulation remained constant. For the algorithms of stochastic weighted particle method schemes (Eibeck and Wagner, 2001a; DeVille et al., 2011; Patterson et al., 2011), to solve the Smoluchowski coagulation equation for weighted particle, the particle creation and destruction processes is also introduced, with the probability of p_{birth} and p_{death}, respectively. In the present study, a new probabilistic removal scheme is constructed based on previous study. The probabilistic removal scheme can keep not only constant number of numerical particles, but also guarantees that the statistics of the particle properties remain on the average intact before and after this probabilistic removal. The probability of random removal and weight of particles should be determined. The schematic implementation of this probabilistic removal is shown in Figure 4.1.

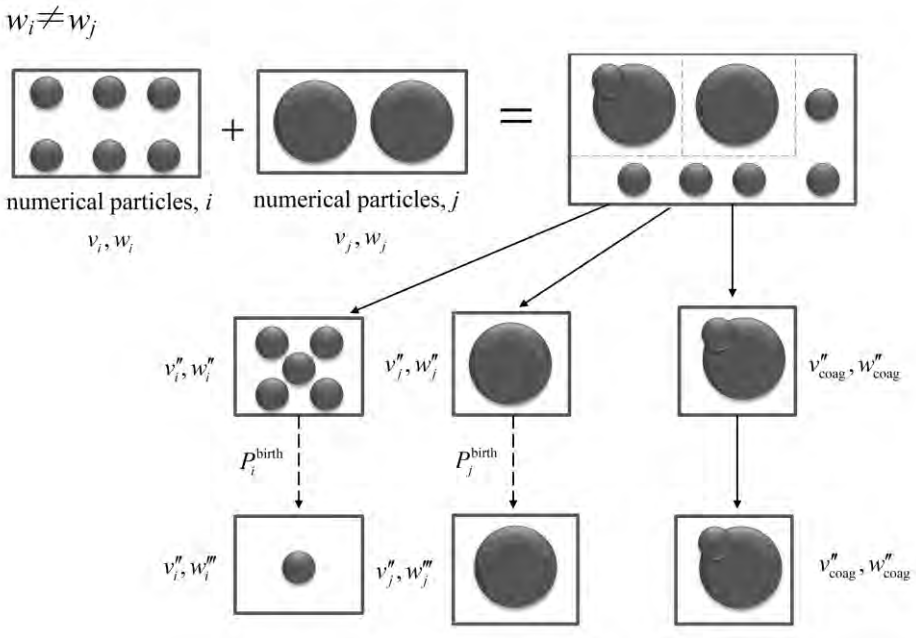

Figure 4.1 Treating a coagulation event with the probabilistic removal (Jiang and Chan, 2021a).

When a numerical particle *i* coagulates with a coagulation pair *j*, it means that some real particles from numerical particle *i* coagulate with those from numerical particle *j*. After a coagulation event, these particle particles can be divided into three groups: "coagulated" real particles and "non-coagulated" real particles from *i*th and *j*th numerical particles. They then follow the probabilistic removal in order to ensure that number of numerical particles is kept constant. The "coagulated" particles are always added and keep their weights to the next stage. One of the "non-coagulated" particle is removed, and the other one numerical particle can then be survived following the probability of P_i^{birth} and P_j^{birth} , respectively. For example, with probabilityof P_i^{birth}, the *i*th particle is remained and *j*th particle is removed, otherwise *j*th particle is remained and *i*th particle is removed. w''' means numerical weight after probabilistic removal which should be adjusted simultaneously to ensure conservation of particle properties.

To make sure that only one numerical particle is removed, the probability of survived numerical particles, *i* and *j*, P_i^{birth} and P_j^{birth} should satisfy as:

$$P_i^{\text{birth}} + P_j^{\text{birth}} = 1 \tag{4-17}$$

To satisfy conservation of some particle properties (e.g., particle number/mass) during this random removal, the new weight after the random removal particles, w_i''' and w_j''', should satisfy as follows:

$$\begin{cases} w_i'''\chi_i = w_i''\chi_i + w_j''\chi_j \\ w_j'''\chi_j = w_i''\chi_i + w_j''\chi_j \end{cases} \tag{4-18}$$

where χ_i and χ_j represent the expected conserved scalar of particles, *i* and *j*. For $\chi_i \equiv 1$, the number of representing real particle does not change during this

random removal, which is called the conserve number removal scheme in the present numerical model development. For $\chi_i \equiv v_i$, where v_i is the volume of numerical particle, *i*, the total mass/volume of representing real particles does not change during this random removal, which is called the conserve volume removal scheme in the present numerical model development.

By combining the Equations (4-15) and (4-18), it can be expressed as:

$$\begin{cases} w_i''' = w_i - \alpha_{ij}\min(w_i, w_j) + [w_j - \alpha_{ij}\min(w_i, w_j)]\dfrac{\chi_j}{\chi_i} \\ w_j''' = w_j - \alpha_{ij}\min(w_i, w_j) + [w_i - \alpha_{ij}\min(w_i, w_j)]\dfrac{\chi_i}{\chi_j} \end{cases} \tag{4-19}$$

In order to maintain the arbitrary particle properties, Γ_i, they are statistically unchanged before/after the random removal. The expectation of these particle properties after the random removal must equal to those before random removal, therefore P_i^{birth} and P_j^{birth} should also satisfy as:

$$\Gamma_i w_i''' P_i^{\text{birth}} + \Gamma_j w_j''' P_j^{\text{birth}} = \Gamma_i w_i'' + \Gamma_j w_j'' \tag{4-20}$$

By combining Equations (4-15), (4-17), (4-19) and (4-20), the probability of the remaining coagulation particles, *i* and *j*, P_i^{birth} and P_j^{birth} can then be obtained as:

$$\begin{cases} P_i^{\text{birth}} = \dfrac{w_i - \alpha_{ij}\min(w_i, w_j)}{w_i - \alpha_{ij}\min(w_i, w_j) + [w_j - \alpha_{ij}\min(w_i, w_j)]\dfrac{\chi_j}{\chi_i}} \\ P_j^{\text{birth}} = \dfrac{w_j - \alpha_{ij}\min(w_i, w_j)}{w_j - \alpha_{ij}\min(w_i, w_j) + [w_i - \alpha_{ij}\min(w_i, w_j)]\dfrac{\chi_i}{\chi_j}} \end{cases} \tag{4-21}$$

The above method is called the probabilistic removal. After implementing the probabilistic removal, the constant number scheme still remains without loss of its inherent computational accuracy.

Numerical Algorithm I: Weighted fraction Monte-Carlo (WFMC) method for particle coagulation (Jiang and Chan, 2021a).

Step 1.	Initialize time $t = 0$. Set the initial particle size matrix, $X_1, X_2, \ldots, X_N$ of N particles.
Step 2.	Calculate the fraction function, α_{ij}, and coalescence kernels, $C_{ij}^{'}$, for $N(N-1)/2$ as unique particle pairs.
Step 3.	Specify the stopping time, t_{stop}, and the time step, Δt.
Step 4.	Randomly choose r from a uniformly particle distribution in [0, 1]. If $r \le P'_{coag}(\Delta t) = 1 - \exp(-\Delta t C'_0)$, then go to Step 5, else go to Step 9.
Step 5.	Generate a coagulation pair of random numerical particles, i, j, and random number, r_1, from a uniform distribution in [0, 1] by using Monte Carlo method.
Step 6.	If $r_1 \le \beta'_{ij} / \max_{\forall k,\forall m}(\beta'_{km})$, then go to Step 7, else go back to Step 5.
Step 7.	Generate the random number, r_2, from a uniformly distribution in [0, 1]. If $r_2 \le P_i^{birth}$, the particle, X_j, is removed and the weight of w_i''' is assigned to the particle, X_i, else the particle, X_i, is removed and the weight of w_j''' is assigned to particle, X_j.
Step 8.	Add a new particle with the size, $X_i + X_j$, and the weight of $\alpha_{ij}\min(w_i, w_j)$.
Step 9.	Advance time, t by using time step, Δt.
Step 10.	If $t > t_{stop}$, the calculation is terminated, else go to Step 11.
Step 11.	Update the coagulation rate, $C_{ij}^{'}$, for new particle pairs.
Step 12.	Return to Step 4.

The values of total coagulation rate, $C_0^{'}$, for all numerical particles must be re-evaluated after a coagulation event since the size and weight of the coagulation particle pair are changed during coagulation event. In the present study, the smart bookkeeping method (Kruis et al., 2000) are used to evaluate value of $C_0^{'}$ in order

to avoid a large time of recalculations of the coagulation rates for particles not participating in coagulation events. The details of the proposed and developed WFMC method are summarized and listed in Numerical Algorithm I.

4.2.5 Choice of fraction functions

The general algorithms for WFMC method with arbitrary fraction functions, α are derived in the description of Sections 4.2.1 to 4.2.4. However, from the expression of probabilistic removal, if there is a large size discrepancy between particle pairs of *i* and *j*, the fluctuation of number (for conserve volume removal scheme) or mass (for conserve number removal scheme) will be introduced, and results in additional stochastic error. To minimize this kind of stochastic error, an appropriate fraction function must be derived. For the probabilistic removal of numerical particle pairs with large size discrepancy, the fraction functions should be closed to 1 or equal to 1, thus the stochasticity of this probabilistic removal can be ignored. This could be formulated as:

$$\lim_{\max(v_i,v_j)/\min(v_i,v_j)\to\infty} \alpha_{ij} = 1 \tag{4-22}$$

where v_i is the volume of numerical particle, *i*. For the present numerical studies, the fraction functions are focused on three forms in Equations (4-23) to (4-25) as:

$$\alpha_{ij} = \begin{cases} C, & \text{if} \quad \max(v_i,v_j)/\min(v_i,v_j) \le p_{\text{critical}} \\ 1, & \text{if} \quad \max(v_i,v_j)/\min(v_i,v_j) > p_{\text{critical}} \end{cases} \tag{4-23}$$

where $C < 1$ is the fraction constant and $P_{\text{critical}} > 1$ is the critical ratio. This form of function is called stepwise constant fraction function in Equation (4-23). The other two forms are also introduced as:

$$\alpha_{ij} = \frac{1}{1+\min(v_i, v_j)/\max(v_i, v_j)} \tag{4-24}$$

$$\alpha_{ij} = 1 - 2^{-\max(v_i, v_j)/\min(v_i, v_j)} \tag{4-25}$$

which are called hyperbolic fraction function (HFF) in Equation (4-24) and exponential fraction function (EFF) in Equation (4-25), respectively.

4.2.6 Connection to the mass flow algorithm

The mass-flow algorithm (MFA) was proposed by Babovsky (1999) and Eibeck and Wagner (2001a). In MFA, a numerical particle of size v_i represents a number $1/v_i$ of a real particle of the same size where the weight function is $w(v_i)$ is $1/v_i$. The algorithm of MFA is given as:

The coagulation pair, i and j, is chosen with rate as

$$\beta_{ij}^{\mathrm{MFA}} = \beta_{ij}\left(\frac{1}{v_i} + \frac{1}{v_j}\right) \tag{4-26}$$

The algorithm always adds the particle $v_i + v_j$ to the population and then one of the v_i or v_j is removed. With probability $v_i/(v_i + v_j)$, the particle v_i is removed, otherwise the particle v_j is removed.

To compare the MFA and WFMC methods, HFF type of fraction function is chosen with the conserved volume removal scheme and an initial weight of $w(v_i) = 1/v_i$ for the numerical particles in WFMC method. Equations (4-19) and (4-21), and coagulation kernel is then expressed as:

$$\beta_{ij}^{\mathrm{WFMC}} = \beta_{ij}\left(\frac{1}{v_i} + \frac{1}{v_j}\right) \tag{4-27}$$

$$\begin{cases} w_i^{\mathrm{WFMC}} = \dfrac{1}{v_i}; \quad v_i^{\mathrm{WFMC}} = v_i \\ w_j^{\mathrm{WFMC}} = \dfrac{1}{v_j}; \quad v_j^{\mathrm{WFMC}} = v_j \\ w_{\mathrm{coag}}^{\mathrm{WFMC}} = \dfrac{1}{v_i + v_j}; \quad v_{\mathrm{coag}}^{\mathrm{WFMC}} = v_i + v_j \end{cases} \tag{4-28}$$

$$\begin{cases} P_i^{\mathrm{birth}} = \dfrac{v_j}{v_i + v_j} \\ P_j^{\mathrm{birth}} = \dfrac{v_i}{v_i + v_j} \end{cases} \tag{4-29}$$

where Equations (4-27) to (4-29) from WFMC method follow exactly the coagulation rule with MFA method. Therefore, WFMC method can assimilate to MFA method only if all the above conditions are satisfied. It should be noted that the initial particle weight is not enforced to satisfy the $w(v_i)= 1/v_i$ in the present numerical simulation case. Hence, HFF method used in the present study is a newly proposed scheme when compared with MFA method.

4.3 Results and Discussion

Moments of different orders and particle size distributions are considered as reference for evaluating numerical simulation results. The *k*th-order moment is defined as:

$$M_k = \int_0^{\infty} v^k n(v) dv \tag{4-30}$$

The low-order moments usually have some practical meaning, such as M_0 is the total particle number density and M_1 is the total particle mass/volume faction.

In the present study, the numerical results obtained by using the WFMC method for different fraction functions are represented as the stepwise constant fraction functions, C = 0.5, C = 0.7, C = 0.9 with $P_{\text{critical}} = 2.0$, HFF and EFF, respectively for simplification.

4.3.1 Case 1: Constant coagulation kernel and initial monodispersed population

4.3.1.1 Numerical validation

A case with constant coagulation kernel and initial monodispersed population is considered in which the analytical solution is well known (Friedlander, 2000). Numerical results of the direct simulation Monte Carlo (DSMC) (Gillespie, 1975), MMC (Zhao and Zheng, 2009) and the developed WFMC methods for different fraction functions, α are compared with the analytical solutions, respectively. For the initial conditions of this numerical studied case, the initial particle size distribution is monodispersed as follows:

$$n(u,0) = \begin{cases} 10^6, & \text{if} \quad u = 1 \\ 0, & \text{if} \quad u > 1 \end{cases} \tag{4-31}$$

and the constant coagulation kernel is expressed as:

$$\beta(i,j) = 10^{-5}, \qquad i,j = 1,2,3,..., \tag{4-32}$$

where the exact solutions of PSD and kth moment are available from Friedlander (Friedlander, 2000).

Figure 4.2 shows that results of four orders of moments (i.e., M_0, M_1, M_2, M_3) are obtained by different MC method schemes which are compared to the analytical solutions. In the present study, 2000 numerical particles are used in all the numerical

simulations with 400 repetitions as they have been proved to gain the results with high computational accuracy and reliable variance. Other numerical results are simulated by the developed WFMC method for different fraction functions, α (e.g., stepwise constant fraction functions, C = 0.5, 0.7 and 0.9 with P_{critical}=2.0, HFF and EFF). In the present study, the effects of different conservation schemes are investigated. The label "CN" is used while the conserve number removal scheme is chosen, otherwise the conserve volume removal scheme is chosen.

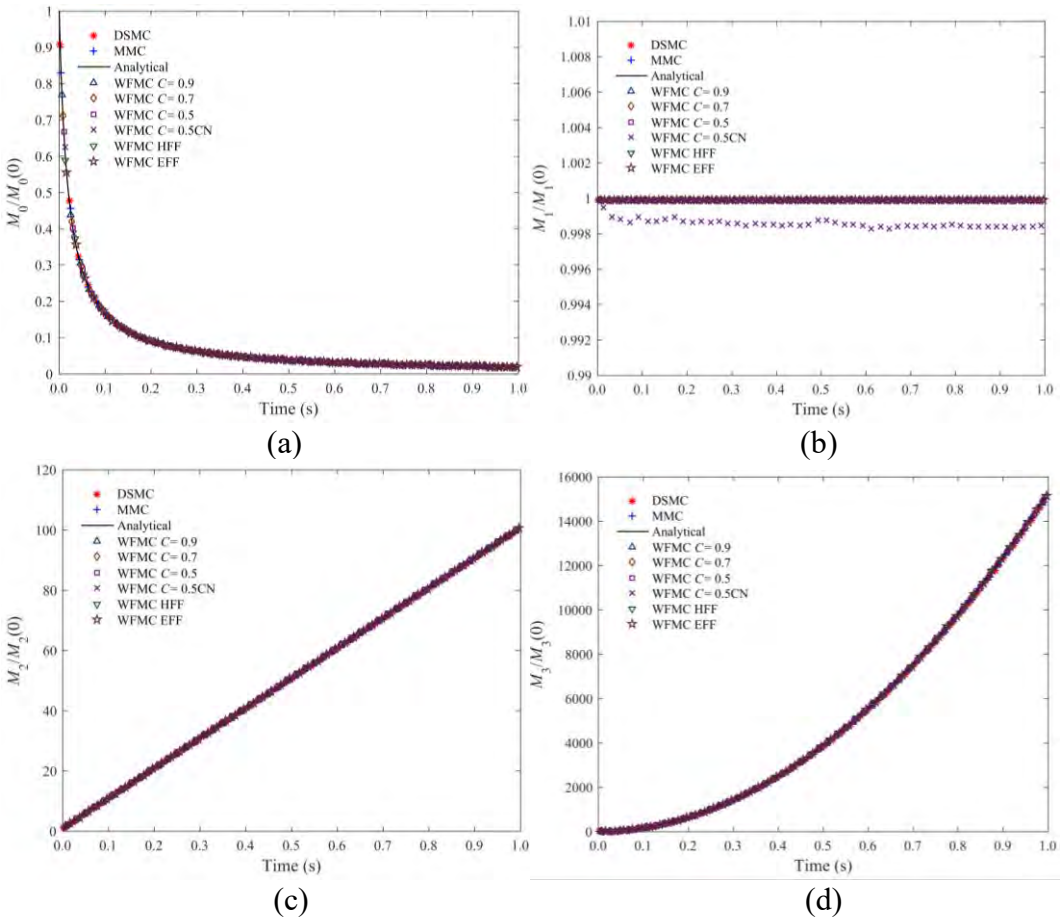

Figure 4.2 Comparison of four orders of moments for different Monte Carlo method schemes (i.e., DSMC, MMC and WFMC) with the analytical solutions (Jiang and Chan, 2021a).

Figure 4.2 shows an excellent agreement between the analytical solutions and numerical results of moments of four orders for different Monte Carlo method

schemes (i.e., DSMC, MMC and WFMC methods) with stepwise constant fraction functions, C, and hyperbolic and exponential fraction functions (HFF and EFF), respectively). However, it should be noted that conserve number removal scheme (i.e., 0.5CN) may result in an extreme small deviation within 0.2% relative error in total particle volume (M_1) as shown in Figure 4.2(b).

4.3.1.2 Stochastic error of the moments

The relative standard deviation (RSD) is used to quantify the stochastic error as follows:

$$\mathrm{RSD} = \frac{\sqrt{\frac{1}{P-1}\sum_{i=1}^{P}(M_{ki} - \bar{M}_k)^2}}{\bar{M}_k} \tag{4-33}$$

In Figure 4.3(a), the relative standard deviations (RSDs) of M_0 in the DSMC, MMC and WFMC methods with stepwise constant fraction functions have the similar trends and lower RSDs when compared with WFMC method with HFF and EFF, respectively. The RSDs of M_1 are kept at zero for all MC method schemes except for WFMC method with conserved number removal scheme (0.5CN) in Figure 4.3(b). Generally speaking, all MC method schemes can keep the perfect mass balance expect for the WFMC method with conserve volume removal scheme.

For RSDs of M_2 and M_3 moments in Figures 4.3(c) and (d), the DSMC method has the highest RSD among other MC method schemes. WFMC method shows great capability in the reduction of stochastic error especially for HFF and EFF, and stepwise constant fraction function with $C = 0.5$. Besides, the lower RSDs on higher order moments (i.e., M_2 and M_3) are observed for the stepwise constant fraction function with decreases in fraction constant, C.

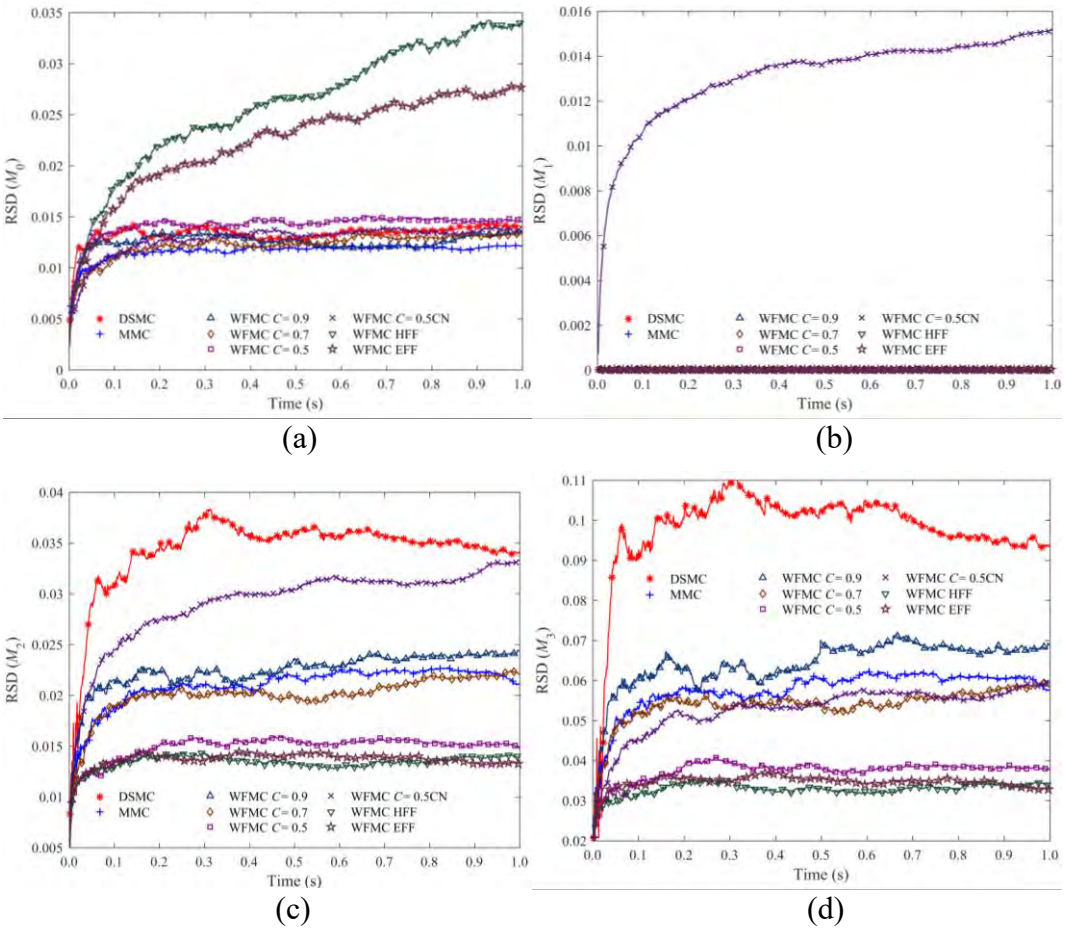

Figure 4.3 Comparison of RSD in four orders of moments for different MC method schemes (Jiang and Chan, 2021a).

Figures 4.4(a) shows the particle size distributions (PSDs) at the end of simulation time, t = 1 s where the PSD is fully developed. An excellent agreement with numerical results and analytical solutions is obtained. The results of different MC method schemes are found to have almost the same trends and values.

Figure 4.4(b) shows the number of numerical particles used in particle size interval for different MC method schemes at t = 1.0 s. Among different MC method schemes, DSMC method shows the narrowest PSD. As a result, only a few numerical particles are used or even no numerical particle is used to represent the real particles in the larger size spectrum which lead to the large fluctuation in higher order

moments (i.e., M_2 and M_3). The numerical PSD of MMC method becomes slightly wider when compared with DSMC method, and more numerical particles are then used to represent the real particles in the larger size spectrum. On the other hand, the fraction functions are introduced to 'twist' the numerical PSD in WFMC method. Although there are less numerical particles to represent the smaller sized real particles, the more numerical particles are found to represent the larger sized real particles. Considering the results of stepwise constant fraction functions, it is clear that there are lower number of numerical particles in smaller size regime while the higher number of numerical particles in larger size regime with decreasing the fraction constant, C from 0.9 to 0.5.

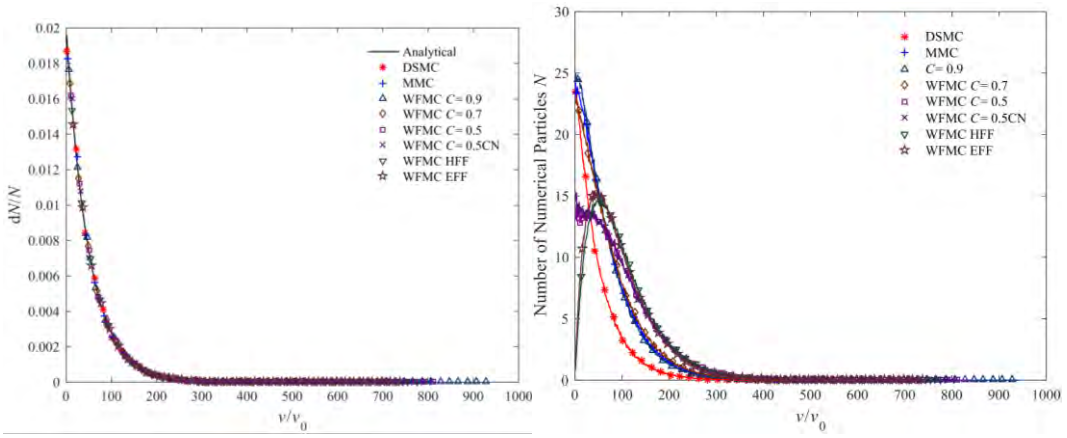

(a) (b)

Figure 4.4 Comparison of the PSDs with analytical solutions and number of numerical particles in each particle size interval for different MC method schemes at t = 1.0 s (Jiang and Chan, 2021a).

Figure 4.5 shows the average particle weight in each size interval, $\overline{w}$, for different MC method schemes at t = 1.0 s. The average particle weight is defined as

$$\overline{w}(v) = \frac{\sum_{i=1}^{N} w(v_i)\delta(v_i, v)}{\sum_{i=1}^{N} \delta(v_i, v)} \tag{4-34}$$

where δ is Dirac delta function. Direct simulation Monte Carlo (DSMC) method has constant average particle weight for different particle sizes as all numerical particles in DSMC method have the equal particle weight. The average particle weight decreases slightly with increasing particle size in MMC method. Different stepwise constant fraction functions of WFMC method can lead to different weight functions which implies that fraction functions are adopted to adjust the weight functions, which is one of the most important characteristics of this new WFMC method. For stepwise constant fraction function of WFMC method, similar trend is found in MMC method while WFMC method has higher weight for small particles and lower weight for large particles. Another interesting finding is that the weight functions of WFMC method with both HFF and EFF are nearly linear in this logarithmic coordinate but with different slopes. This linearity shows that these types of weight functions are power-law weight function which is similar to the weight function in weighted flow algorithm (WFA) (DeVille et al., 2011).

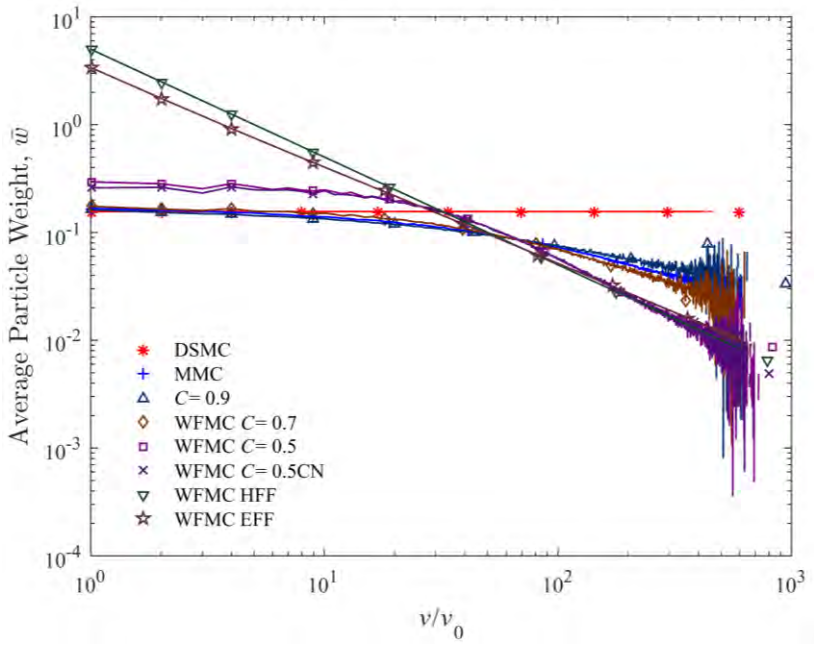

Figure 4.5 Average particle weight distributions for different MC method schemes (Jiang and Chan, 2021a).

4.3.2 Case 2: Free molecular coagulation kernel and initial monodispersed population

Free molecular coagulation kernel has been widely used in aerosol science and technology for particles in free molecular regime. However, there is no analytical solution for this coagulation kernel, therefore the numerical simulation results of sectional method (SM) are used as a reference (Prakash et al., 2003). In the present study, different Monte Carlo method schemes are compared with the sectional method. To simplify, only hyperbolic fraction function (HFF) of WFMC method is used. The initial particle size distribution is monodispersed with the typical initial total number density of 10^{17} #/m^3 and initial particle size of 1.2407 nm, respectively.

The coagulation kernel of particles, *i* and *j*, in free molecular regime is given by Friedlander (2000):

$$\beta_{ij}=(\frac{3}{4\pi})^{\frac{1}{6}}(\frac{6k_bT}{\rho_p})^{\frac{1}{2}}(\frac{1}{v_i}+\frac{1}{v_j})^{\frac{1}{2}}(v_i^{\frac{1}{3}}+v_j^{\frac{1}{3}})^2 \tag{4-35}$$

where T is the local temperature and is set as 300K in the present study, v_i is the volume of ith particle, ρ_p is the particle density and is set as 1800 kg/m^3. In the present study, all the numerical simulations used are 2000 numerical particles and the number of repetition simulation is 400, respectively.

Figure 4.6 shows an excellent agreement of moments of four orders with free molecular coagulation kernel case for different MC method schemes and sectional method, respectively. All these MC method schemes show a perfect mass balance.

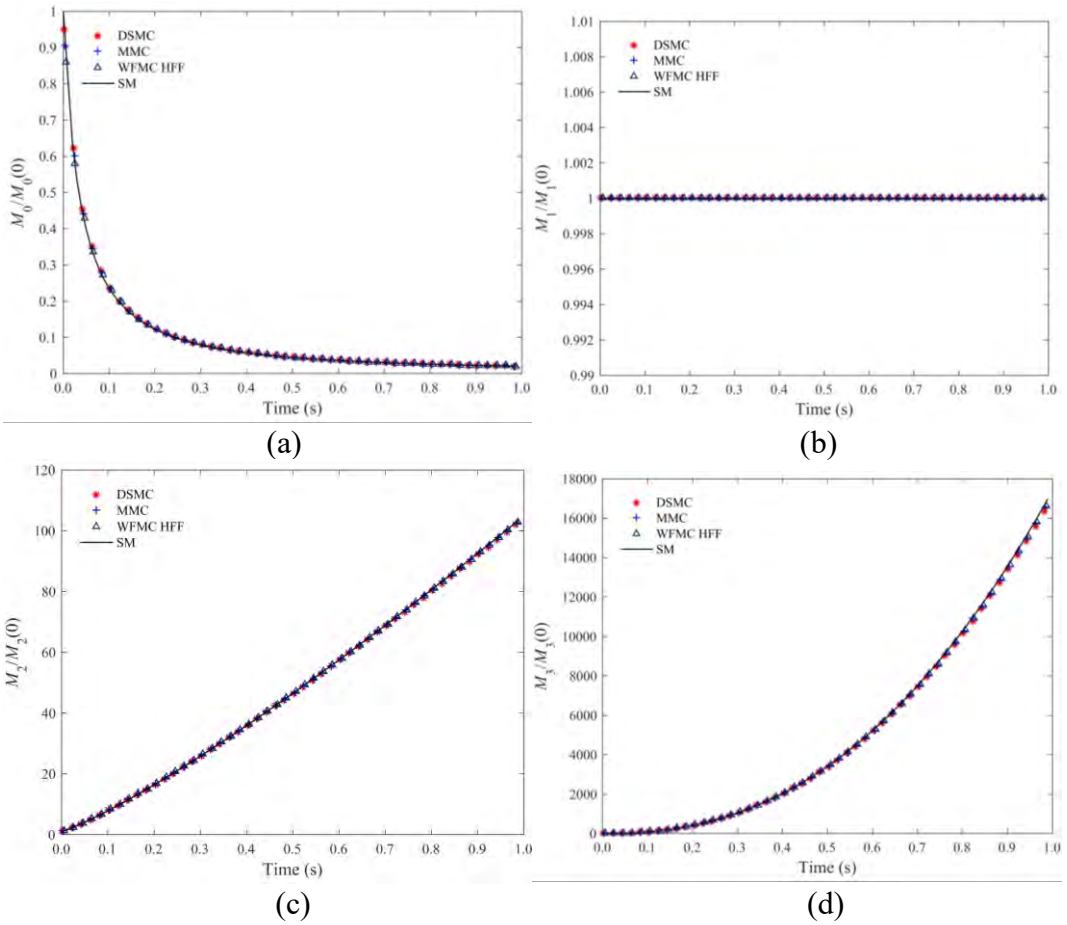

Figure 4.6 Comparison of four orders of moments with free molecular coagulation kernel for different MC method schemes and sectional method (Jiang and Chan, 2021a).

In Figure 4.7, there are similar RSD trends of each moment, M_i with free molecular coagulation kernel for different MC method schemes. Moreover, it is worth to note that the proposed and developed WFMC method with HFF has higher RSD for M_0 but it has lower RSDs in higher moments (i.e., M_2, M_3) when compared with DSMC and MMC methods. This new WFMC method has shown a great reduction of stochastic error on higher order moments.

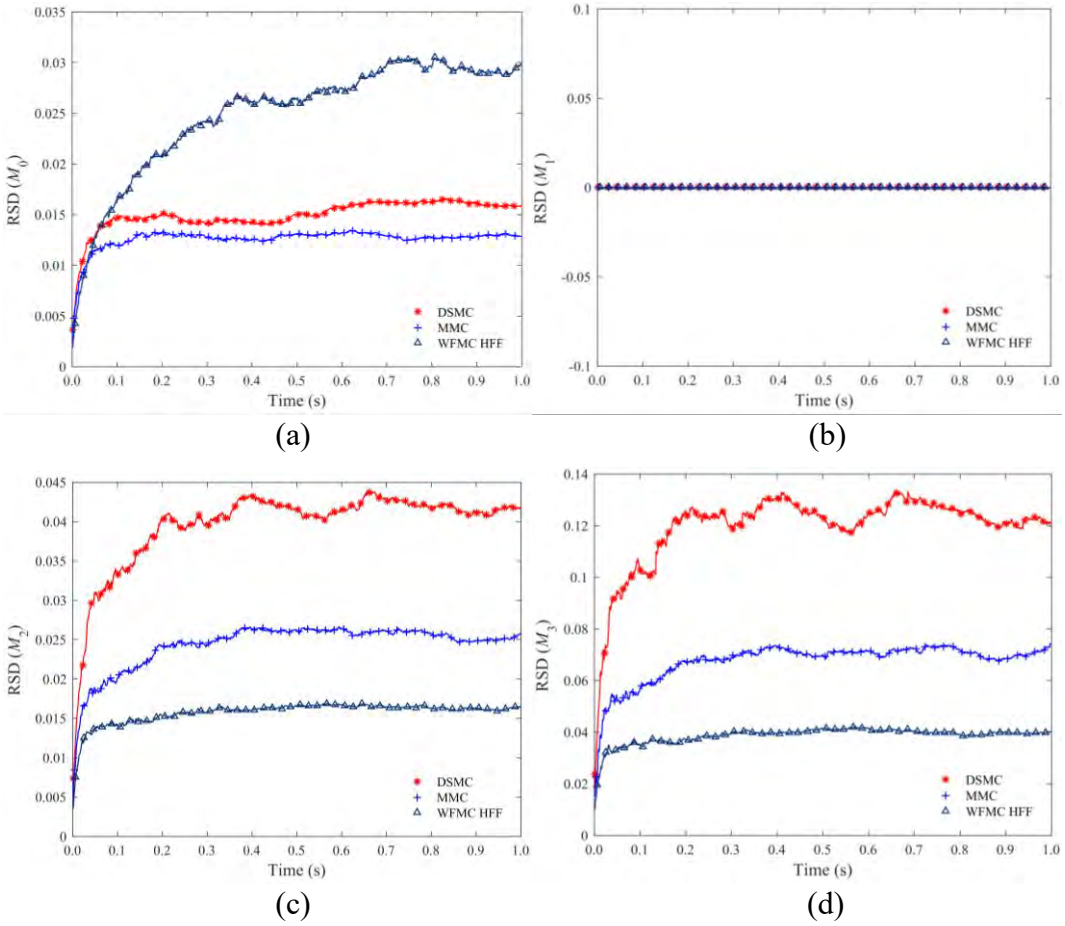

Figure 4.7 Comparison of RSDs in four orders of moments with free molecular coagulation kernel for different MC method schemes (Jiang and Chan, 2021a).

4.3.3 Case 3: Free molecular coagulation kernel and initial exponential distributed particle population

In Case 3, the free molecular coagulation kernel is adopted and the initial size distribution is represented by an exponential function (Zhao and Zheng, 2009) as:

$$n(v,0) = [N_0 \exp(-v / v_{g0})] / v_{g0} \tag{4-36}$$

where v_{g0} is initial mean volume and $v_{g0} = 1\times10^{-22}$ m^3 is used (Liu and Chan, 2018a) in the present study. The numerical results of the DSMC, MMC and WFMC methods are shown in Figure 4.8.

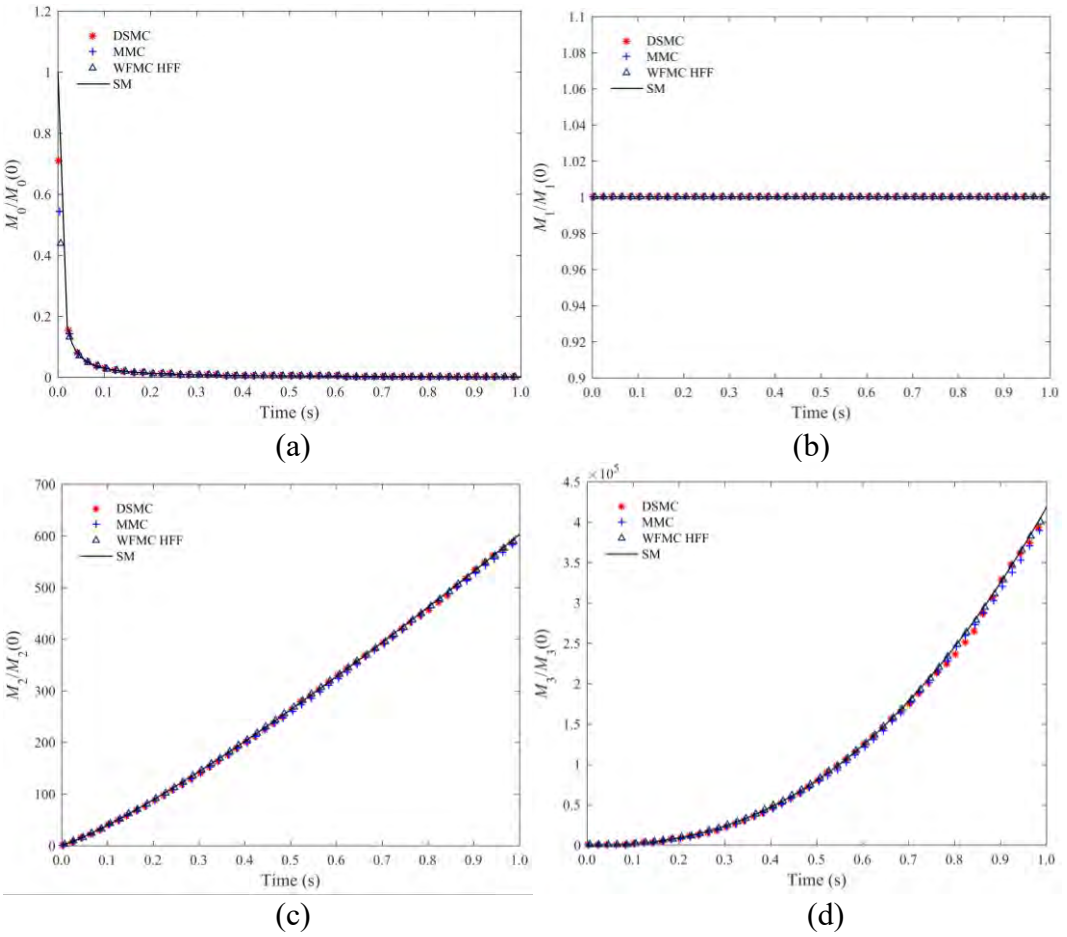

Figure 4.8 Comparison of four orders of moments with free molecular coagulation kernel and initial exponential distribution (Jiang and Chan, 2021a).

Figure 4.8 shows an excellent agreement of four orders of moments with free molecular coagulation kernel and initial exponential distribution for different MC method schemes and sectional method, respectively.

Figure 4.9 shows the PSDs at different simulation times, t = 0.1 s, t = 0.5 s and t = 1.0 s, respectively (t = 0 s is an initial exponential distribution). An excellent agreement with MC and SM is obtained. The results of different MC method schemes are also found to have excellent agreement**.** As simulation time advances, PSDs shift to the larger-size regime due to the coagulation events. Figure 4.9 also shows that the widest PSD can be found in WFMC results when compared with

DSMC and MMC methods, especially in the larger-size regime, which will have higher contribution for higher order moments. Therefore, it is indicated that WFMC method can predict the larger particle size distribution more accurately as well as the higher order moments.

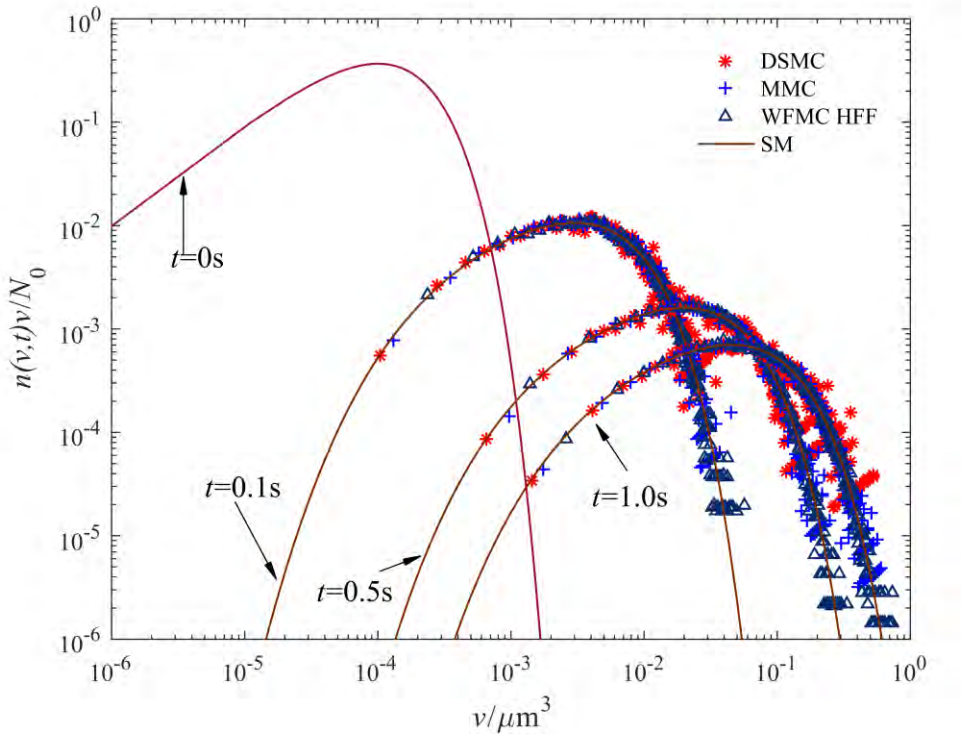

Figure 4.9 Particle size distributions for different MC method schemes and sectional method (Jiang and Chan, 2021a).

4.3.4 Computational efficiency analysis

In order to evaluate the computational efficiency of the WFMC method in the present study, the normalized computational time, τ, is defined as follows:

$$\tau = t / t_{\text{ref}} \tag{4-37}$$

where t_{ref} is the reference time and t is the amount of computational time required for corresponding DSMC, MMC and WFMC methods, respectively. In the present study, the reference value is the computational time of constant coagulation case

(Case 1) obtained from the DSMC method. The normalized computational times, τ for the studied cases are listed in Table 4.1.

Table 4.1 Normalized computational times, τ obtained from different cases using DSMC, MMC and WFMC methods (Jiang and Chan, 2021a).

Parameter	DSMC	MMC	WFMC C= 0.5CN	WFMC C= 0.5	WFMC C= 0.7	WFMC C= 0.9	WFMC EFF	WFMC HFF
Case 1	1.0	1.4	1.5	1.8	1.5	1.5	2.8	1.6
Case 2	4.3	7.4	-	-	-	-	-	8.1
Case 3	4.1	7.8	-	-	-	-	-	8.3

Table 4.1 shows that τ of the DSMC method generates the lowest values than other MC methods. This is because although the same initial number of numerical particles is used for these MC methods, the number of numerical particles is continuously decreased as time evolution due to the coagulation events, which has lower computational cost. However, computational accuracy will also decrease with decreasing number of total numerical particles.

In Table 4.1, the computational cost in WFMC method with HFF is slightly higher than in MMC method, which is attributed to two factors. On the one hand, although both WFMC and MMC methods can keep constant number of numerical particles, WFMC method has to deal with more complex coagulation kernel when compared with MMC method (i.e., the kernel function is $\max(w_i,w_j)\beta_{ij}/\alpha_{ij}$ in WFMC method and $\max(w_i,w_j)\beta_{ij}$ in MMC method). Hence, the larger CPU time is taken for calculating the coagulation kernel in WFMC method. On the other hand, the coagulation kernel function in WFMC method is always larger than in MMC method (for example $\alpha_{ij}\leq 1$). The larger total coagulation rate, C_0 in WFMC

method leads to a shorter coagulation waiting time for event-driven schemes as shown in Equation 4.11 or more coagulation events for time-driven schemes as shown in Equation 4.13 and a higher computational time**.** This can also explain the varying time-consuming for different types of fraction function in WFMC method.

4.5 Summary

A new weighted function Monte Carlo (WFMC) method is well developed and validated in the present study. In WFMC method, a new coagulation rule is derived which allows the changes in mean number of real coagulation events between two numerical particles. Then in order to maintain the constant number of numerical particles, the probabilistic removal scheme is also constructed. This new WFMC method can reduce stochastic error by adjusting the weight function to 'twist' the numerical particle size distribution and change the number of numerical particles that represent the real particle in each size interval. The method for particle coagulation is validated by three classical cases. An excellent agreement between the numerical simulation results of WFMC and analytical solutions/sectional methods is obtained. The WFMC method shows a significant stochastic error reduction in higher-order moments with slightly higher computational cost because there are more numerical particles to represent real physical particles in larger size regime. Besides, the new WFMC method also shows the significant advantage of tracking the PSD over the larger size regime which is traditionally insufficient in classical direct simulation Monte Carlo (DSMC) and multi-Monte Carlo (MMC) methods.

Chapter 5 Modelling of Soot Particle Size Distributions by LPT-WFMC method

5.1 Introduction

In the present study, the newly proposed and developed weighted fraction Monte Carlo method (WFMC) method (Jiang and Chan, 2021a) is further developed and coupled with the Lagrangian particle tracking (LPT) to study the soot formation and evolution in ethylene laminar premixed flames with the detailed soot model (Jiang and Chan, 2021b). Soot aerosol dynamic processes (i.e., nucleation, surface growth, condensation, coagulation, and oxidation) are modelled by the WFMC method while each weighted soot particle is tracked using Lagrangian approach which can provide detailed information of soot particle trajectory and the history of individual soot particles.

Firstly, the newly developed LPT-WFMC method is validated by both the experimental results (Abid et al., 2008) and the numerical results of the direct simulation Monte Carlo (DSMC) (Gillespie, 1975) and multi-Monte Carlo (MMC) (Zhao et al., 2009) methods. The stochastic error and accuracy together with the computational efficiency for predicting soot particle size distribution (PSD) are investigated and compared among different MC methods. The evolution of soot number density, volume fraction and particle size distribution are investigated under different flame conditions. The effects of different parameters of the detailed soot model on the results of soot PSD are also conducted by studying their parametric sensitivity analysis.

5.2 Numerical Methodology

5.2.1 Gas-phase model

The governing equations for gas-phase combustion including the conservation of mass, momentum, energy and mass fractions of gas species are introduced in Section 3.3.2. In the present study, the gas-phase governing equations are solved by the opensource computational fluid dynamics (CFD) library OpenFOAM (Jasak et al., 2007). The governing equations are integrated with the finite volume method (FVM). The discretization schemes for convection and diffusion terms are second-order upwind and central difference, respectively. The pressure-velocity coupling is achieved by the pressure-implicit with splitting of operators (PISO) algorithm (Issa, 1986). The detailed chemical mechanisms of 101 species and 543 reactions with polycyclic aromatic hydrocarbons (PAHs) chemistry up to pyrene (A4) (also known as the ABF mechanism) is developed by Appel et al. (2000) which have been successfully applied in modelling soot formation in the one-dimensional laminar premixed ethylene-air flames (Yapp et al., 2015; Hou et al., 2019; Liu et al., 2021b).

5.2.2 Soot model

In the present study, a soot particle is described as a fractal aggregate as joint surface-volume model (Blanquart and Pitsch, 2009b) which consists of the number of primary particles, n_p with diameter, d_p. The total volume, V and total surface, S of a soot aggregate can be expressed as:

$$V=\frac{\pi}{6}n_p d_p^3 \tag{5-1}$$

and

$$S = \pi n_p d_p^2 \tag{5-2}$$

The gyration diameter, d_g can be expressed to be related to the primary particle diameter as described by Thajudeen et al. (2015) and Sorensen (2011):

$$n_p = k_f \left(\frac{d_g}{d_p}\right)^{D_f} \tag{5-3}$$

where k_f is the pre-fractal factor of 1.0 and D_f is the fractal dimension of the aggregates of 1.8 from Blanquart and Pitsch (2009b). The effects of these parameters on population balance model had been fully investigated by Yu et al (2017). In the present study, it is assumed that the diameters of mobility and collision are equal to each other which have been widely used in the previous modelling studies of laminar sooting flames (Blanquart and Pitsch, 2009b; Mueller et al., 2009; Salenbauch et al., 2015; Yapp et al., 2015; Liu et al., 2019a; Kholghy and Kelesidis, 2021). The collision diameter, d_c of the aggregates is determined from the Equation (5-4) (Yapp et al., 2015) as:

$$d_c = d_p n_p^{1/D_f} \tag{5-4}$$

Soot nucleation (Blanquart and Pitsch, 2009b; Mueller et al., 2009), surface reactions of hydrogen abstraction acetylene addition (HACA) (Frenklach and Wang, 1991), condensation of PAH on soot surface (Blanquart and Pitsch, 2009b), oxidation by hydroxide (OH) and oxygen (O_2) (Kazakov et al., 1995), and the particle coagulation are considered in the present study. However, the soot fragmentation in premixed ethylene flame is not considered in the present study after taking into account the negligible effect of oxidation-induced particle fragmentation

under the present flame conditions as described in Saggese et al. (2015). For gas-phase model, only pyrene consumption is considered when solving gas species equation for soot. The source term of species equation for pyrene is accounted by the consumption of soot nucleation and mass growth from pyrene. The details of these soot aerosol dynamic processes can be referred to Wang (2011).

5.2.2.1 Lagrangian formalism

In the Largrangian particle tracking model, each soot particle is tracked individually (Hirche et al., 2019). The fluid characteristics (e.g., velocity, density, etc.) on the soot particles are applied by linear interpolation on control volume (Jasak et al., 2007)**.** The trajectories of the soot particles are evolved by:

$$\begin{cases} \dfrac{d\vec{x}_p}{dt} = \vec{u}_p \\ \dfrac{d\vec{u}_p}{dt} = f_{\text{drag}} + f_s \end{cases} \tag{5-5}$$

where f_{drag} is the particle velocity changed due to the drag force, and f_s represents the contributions from other forces but thermophoretic force is only considered in the present study. The drag force can be formulated by Fan et al. (1997) as:

$$f_{\text{drag}} = \frac{3}{4}\frac{\rho_f}{\rho_p d_p} C_D(\vec{u}_f - \vec{u}_p)\left|\vec{u}_f - \vec{u}_p\right| \tag{5-6}$$

where ρ_f and $\vec{u}_f$ are the density and velocity of surrounded fluid, respectively. The equation for drag coefficient, C_D (Zhu et al., 2007) is written as:

$$C_D = \begin{cases} 24(1 + 0.15Re_p^{0.687}) / Re_p, & Re_p < 1000 \\ 0.44, & Re_p \geq 1000 \end{cases} \tag{5-7}$$

where Re_p is the relative particle Reynolds number:

$$Re_p = \frac{d_p \left| \vec{u}_f - \vec{u}_p \right|}{v} \tag{5-8}$$

The Stokes number, *St* is applied to characterize the inertia effect of soot particles in flow fields (Rigopoulos, 2010) as:

$$St = \tau_p / \tau_f \tag{5-9}$$

where $\tau_p = \rho_p d_p^2 / (18 \rho_f \nu_f)$ is the particle relaxation time and τ_f is a flow characteristic time. If Stokes number is small relative to unity ($St \ll 1$), the soot particle can be assumed to be the non-inertial particle. Then, the trajectories of soot particles are evolved by Bagheri et al. (2012) as:

$$\frac{dx_{p,i}}{dt} = u_{f,i} + u_{T,i} \tag{5-10}$$

where x_p, u_f and u_T are the position coordinates, the fluid velocity and thermophoretic velocity at the location of numerical particle, *p*, respectively. The thermophoretic velocity can then be expressed as proposed by Waldmann (1961):

$$u_T = -\frac{3\nu}{4(1+\frac{\pi}{8}\alpha_m)} \frac{\nabla T}{T} \tag{5-11}$$

where α_m is the accommodation factor with a value of 0.9 (Allen and Raabe, 1982). The inertia effect of soot particles in flame is numerically discussed in Section 5.3.2.1.

5.2.2.2 Nucleation

Soot nucleation (inception) is still not fully understood due to its complex nature. Many debates on soot nucleation mechanisms and PAH are now considered as most likely soot precursors (Frenklach and Wang, 1994; Wang, 2011; Martin et al., 2022). In the present study, the soot nucleation is assumed as

dimerization of PAH due to collision and sticking of PAH species (Blanquart and Pitsch, 2009b) as:

$$\mathrm{PAH} + \mathrm{PAH} \Rightarrow \mathrm{dimer} \tag{5-12}$$

Pyrene (A4) is usually considered as important species for soot nucleation due to its high concentration in flame and thermodynamic stability (Appel et al., 2000). The experimental study by using mass spectrometry also supports the importance of pyrene and similar-sized PAHs in soot nucleation (Faccinetto et al., 2011). The soot nucleation process in the present study is considered as pyrene dimerization (Frenklach and Wang, 1994) as it has been widely used and validated in many research studies, for example, soot in plug flow reactors (Wen et al., 2005), laminar premixed flames (Yapp et al., 2015), and laminar diffusion flames (Selvaraj et al., 2016; Qiu et al., 2019; Hoerlle et al., 2020). The nucleation rate is then calculated according to kinetic theory as (Frenklach and Wang, 1994) with the self-sticking coefficient of 0.025 as used by Blanquart and Pitsch (2009b) and the nuclei size is assumed to be 0.87 nm which is actually the size of single pyrene molecule (Tang et al., 2017). The numerical weight of any new particle is calculated by the number of new nuclei or assigned numerical weight in order to control the number of numerical particles. Since the pyrene molecule is consumed during nucleation events**,** the pyrene consumption rate in nucleation is accounted as a source term in the species equation.

5.2.2.3 Surface reactions

The surface growth and oxidation through the H-abstraction and acetylene addition (HACA) mechanism were developed by Frenklach and Wang (1994). The descriptions of HACA reactions are given in Section 3.4.2.

The increasing soot mass is dominated by HACA surface reactions (Veshkini and Dworkin, 2017). The reaction rate constants of surface growth and soot oxidation are calculated by the kinetic data in Appel et al. (2000). The fraction of surface activate sites (α) for surface reactions with gas species is also adopted (Appel et al., 2000) as:

$$\alpha = \tanh(a / \log \mu_1 + b) \tag{5-13}$$

where μ_1 is the first size moment of the soot particle distribution, and a and b are fitted parameters with the same values used in Appel et al. (2000). For oxidation by OH, the reaction rate constant is calculated with the reaction probability of 0.13 as used in the model of Neoh et al. (1985).

5.2.2.4 Condensation

The collision of gas-phase PAH species on soot surface results in soot condensation process, the soot mass will increase during condensation. As in the model of Appel et al. (2000), pyrene-soot condensation is included in the present study. The condensation rate depends on the collision frequency which can be calculated by the collision theory between pyrene molecules and soot particles (Kronholm and Howard, 2000; Park et al., 2005). The pyrene-soot surface condensation efficiency is assumed to be 0.5 by Zhang et al. (2009) which describes the probability of sticking in each collision event. The pyrene consumption rate in condensation process is accounted as a source term in the species equation.

5.2.2.5 Coagulation

The coagulation process represents the collision of two soot particles of volumes v and u to form a new particle of volume $v + u$ which can be described by

Smoluchowski equation as introduced in Section 4.2. The collision kernel function depends on the Knudsen number, Kn of the collision pairs. The Kn is described as the ratio of the mean free path to collision diameter. The collision kernel functions for different size regimes (i.e., free molecular regime, continuum regime and intermediate regime) are introduced in Section 3.4.2.

5.2.2.6 Monte Carlo method

The WFMC method for particle coagulation is developed and introduced in Section 4. For solving the soot particle population balance model which involves many different aerosol dynamic processes (i.e., nucleation, surface growth, condensation, coagulation, and oxidation) simultaneously, the operator splitting technique is adopted to deal with their different characteristic times to increase the computational efficiency. The Monte Carlo method is applied for stochastic process (i.e., coagulation process) and the deterministic integration method is applied for deterministic processes (i.e., nucleation, surface growth and condensation) with a second order Strang splitting scheme (Zhou et al., 2014). Thus the smart bookkeeping method (Kruis et al., 2000) can be used to evaluate the matrix of collision kernel to avoid a large time of recalculations, and save the computational resources in Monte Carlo simulation.

For coupling the Largrangian particle tracking with WFMC (LPT-WFMC) method, the particle properties (i.e., weight, size, positions, velocities) are evaluated after coagulation events. For “non-coagulated” particle after a coagulation event, the numerical weight in Equation (4-15) is assigned, and other properties (e.g., position, velocity, size etc.) remain unchanged. For “coagulated particle”, its new properties are given (Jiang and Chan, 2021a) as:

$$\begin{cases} w_{\text{coag}} = \alpha_{ij} \min(w_i, w_j) \\ v_{\text{coag}} = v_i + v_j \\ \vec{x}_{\text{coag}} = \dfrac{v_i}{v_i + v_j}\vec{x}_i + \dfrac{v_j}{v_i + v_j}\vec{x}_j \\ \vec{u}_{\text{coag}} = \dfrac{v_i}{v_i + v_j}\vec{u}_i + \dfrac{v_j}{v_i + v_j}\vec{u}_j \end{cases} \tag{5-14}$$

In the present study, the α_{ij} is always adopted in hyperbolic fraction function (HFF) type (in Equation (4-24)).

A brief outline of the implementation of the LPT-WFMC method is given (Jiang and Chan, 2021b) as follows:

Numerical Algorithm: LPT-WFMC method for the gas and soot phase

Step 1. Initialization. The boundary/initial conditions of both the gas and particle phases are assigned. For the gas phase, the initial thermal and flow fields (e.g., temperature, velocity, species mass fraction, etc.) are characterized. For the particle phase, the soot particle properties (e.g., numerical weight, mass density, etc.) are characterized.

Step 2. Choose a time-step, Δt for the gas-phase flow.

Step 3. Solving the gas flow fields. The governing equations of gas-phase combustion (i.e., conservation of mass, momentum, energy and species) are solved where the flow field properties (i.e., velocity, species molar fraction, temperature, etc.) are obtained.

Step 4. Updating the spatial position and velocity of each particle. The motion of particles is governed by Equations (5-5) and (5-10), and thus the particle field can be solved by the Lagrangian particle tracking (LPT) method.

Step 5. Choose a time-step, δt, for the soot aerosol dynamics.

Step 6. Start M (i.e., $M=\Delta t/\delta t$) Monte Carlo loops.

Step 7. Treatment of particle dynamic processes.

Step 8 The properties (e.g., numerical weight, size distribution, etc.) of simulated particles are updated.

Step 9. If the current MC loop number, R does not reach the predetermined MC loop number, M, then start a new MC loop. Otherwise, if R is equal to M, quit the Monte Carlo loop for calculating the soot aerosol dynamics.

Step 10. Advance time, t by using time step, Δt. If $t > t_{\text{stop}}$, the calculation is terminated, and the output results of particles and gas-phase flow fields, else go to Step 2.

In order to obtain an accurate numerical simulation result with reasonable computational time, the number of numerical particles in each control volume should be within a certain range. Although the developed WFMC method can maintain constant number schemes during coagulation process, nucleation process and particles transportation from neighboring cells can introduce the fluctuation on number of numerical particles in the control volume. In MC simulation, resampling (Smith and Matsoukas, 1998) or resizing (Liffman, 1992) are always applied to maintain constant number of numerical particles. However, it has been proved that these methods will introduce stochastic error in numerical simulation (Zhou et al., 2020). In the present study, the number of weighted numerical particles is controlled by the stochastic merging method in Kotalczyk and Kruis (2017) to reduce such resampling error.

5.2.2.7 Feasibility of the LPT-WFMC method for different hydrocarbon fuels

In the present study, the developed LPT-WFMC method is coupled with detailed soot model to study the soot formation and evolution in ethylene laminar premixed flame (Abid et al., 2008). However, it should be noted that the LPT-WFMC method can also apply to study the soot formation and evolution of different hydrocarbon fuels with the detailed chemical kinetic mechanisms (Bramlette and Depcik, 2020). For different hydrocarbon fuels, the chemical kinetic mechanisms of hydrocarbon fuels should be changed while no other change is required in the detailed soot model. For example, Ong (2018) studied both Doshisha n-heptane (C_7H_{16}) and Sandia n-dodecane ($C_{12}H_{26}$) test cases by using the developed Eulerian-Lagrangian method with different skeletal mechanisms for different hydrocarbon fuels. Pang et al. (2011) studied the Doshisha n-heptane test case with

the skeletal n-heptane model comprising 46 species and 112 reactions that are essential to diesel ignition, combustion and soot precursor formation. In contrast, Luo et al. (2014) used the Sandia n-dodecane ($C_{12}H_{26}$) test case with the skeletal mechanism for n-dodecane model comprising 106 species and 420 reactions.

5.3 Results and Discussion

In order to validate the developed LPT-WFMC method with the detailed soot model, the experimental results of one dimensional premixed ethylene-oxygen-argon flames obtained from Abid et al. (2008) are adopted as the benchmark flame cases. The boundary conditions of the present numerical simulation used are the same as the experimental setup as listed in Table 5.1.

Table 5.1 Test flame conditions (i.e., C_2H_4: 16.3%, O_2: 23.7%, Ar: 60%) (Abid et al., 2008).

Flame cases	Cold gas velocity v_0 (cm/s)	Maximum flame temperature T_f (K)
C1	13	1898 ±50
C2	10	1805 ±50
C3	8	1736 ±50
C4	6.53	1710 ±50
C5	5.5	1660 ±50

The gas temperature and species profiles are studied by both reactingFOAM solver in OpenFOAM and Sandia 1-D PREMIX code (Kee et al., 1986) which the Newton algorithm is used for gas-phase steady-state solutions. OpenFOAM and PREMIX both used the fixed mass-flux fraction for species boundary condition. The time step in OpenFOAM is fixed to 1 μs in order to satisfy the time scale for gas phase and aerosol dynamics. The simulated physical time is chosen long enough

to reach a steady-state solution. The schematic diagram of all boundary conditions and meshes of the present study is shown in Figure 5.1.

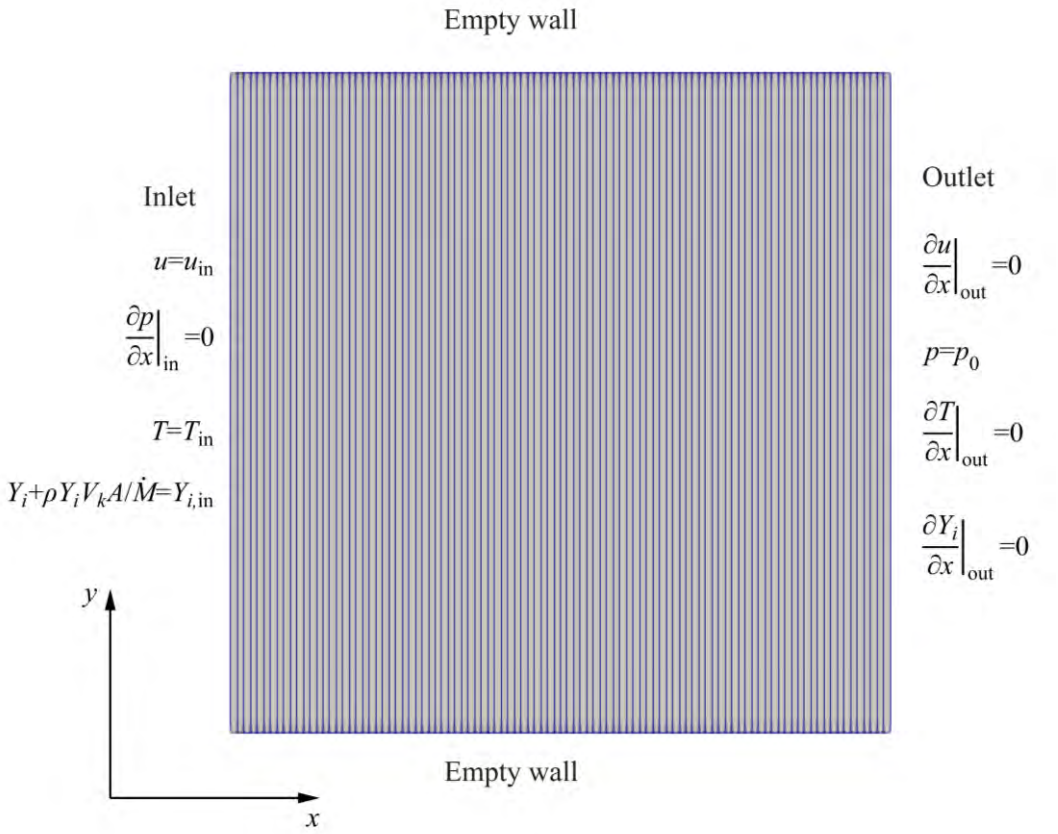

Figure 5.1 A schematic diagram of all boundary conditions and meshes (Jiang and Chan, 2021b).

The mesh grid contains a total of 1000 cells in the x-direction of 2 cm with a single cell in the y-direction because the present study is one-dimensional numerical simulation which is similar to many previous studies (Yapp et al., 2015; Hou et al., 2019; Liu et al., 2019a; Yang and Mueller, 2019; Hou et al., 2020a). The appropriate boundary conditions are deduced from the work of Kee et al. (1986) and Saggese et al. (2016). The Inlet boundary conditions consist of a set of prescribed velocity, burner temperature, mass flow rate of each species and the vanishing gradients for pressure. For the outlet boundary conditions, the pressure

is given as the fixed value with the vanishing gradients for velocity, temperature, and species.

In the present study, one-dimensional flame results from different flame heights above the burner (HAB) along the centerline of burner which is the same as the previous research study from Abid et al. (2008). The advantage of using the absolute HAB is the simple experimental configuration which has been widely used for most of the experimental and numerical studies. However, the disadvantage of using the absolute HAB is the difficulty in comparing the results at different flame conditions. For example, when the two- or three-dimensional flame results from the burners with different sizes are compared, it will be more universal and flexible for making comparison of flame results by using non-dimensional flame height based on its burner geometry (e.g., diameter) such that the effect of burner geometry on the flame results can be minimized.

5.3.1 Flame temperature and gas species concentration profiles

The typical flame temperature and gas species concentration profiles of flame C3 case are selected and presented in Figures 5.2 to 5.4. It is clear that the present numerical simulation results of temperature profiles agree well with both OpenFOAM and PREMIX. However, the numerical results obtained by using the ABF model (Appel et al., 2000) are slightly higher than the experimental results in higher flame height and the discrepancy is especially severe for lower flame height, where the similar trends can also be found in other flame conditions (i.e., flame C1, C2, C4 and C5 cases). Such deviation is attributed to the heat losses of flame to the external environment which is difficult to be modeled (Kee et al., 1986).

Because soot nucleation process is sensitive to flame temperature, it is very common to impose the experimental flame temperature profiles for the numerical simulations (Hou et al., 2019; Yang and Mueller, 2019). In the present study, the numerical simulations are both performed by imposing the experimental flame temperature profile (Abid et al., 2008) and by solving the energy equation (Kee et al., 1986) in order to study the difference between these two approaches.

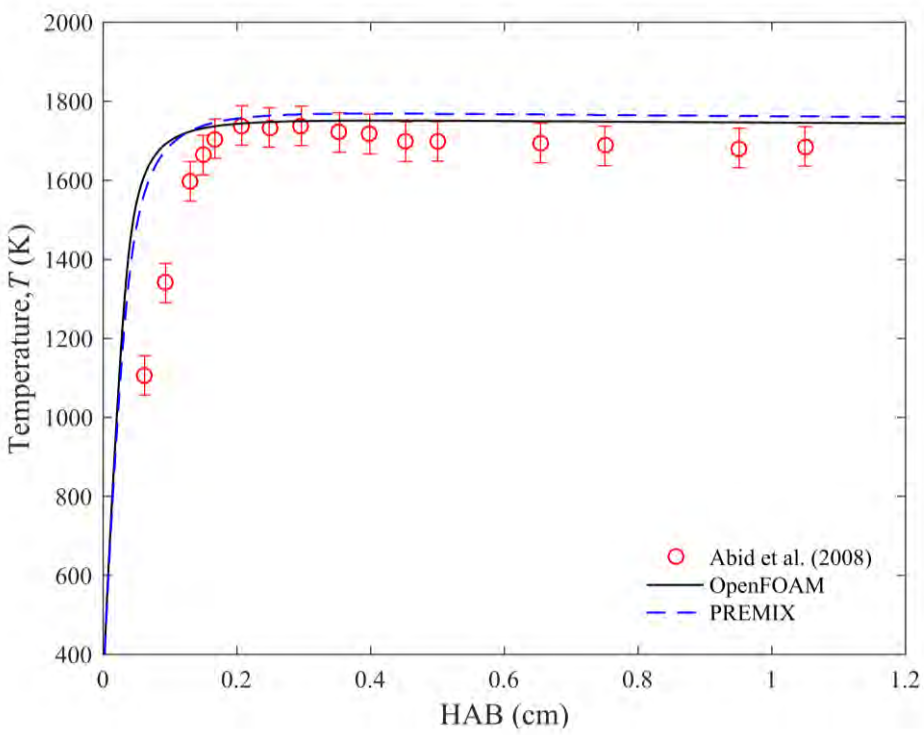

Figure 5.2 Comparison of experimental (Abid et al., 2008) and numerical flame temperature profiles for different HABs at flame C3 case (Jiang and Chan, 2021b).

The gas species concentration profiles of flame C3 case are maintained nearly constant at post-flame region as shown in Figure 5.3. The present numerical simulation results by OpenFOAM (Jasak et al., 2007) agree very well with the PREMIX (Kee et al., 1986) and show accuracy for small molecule species.

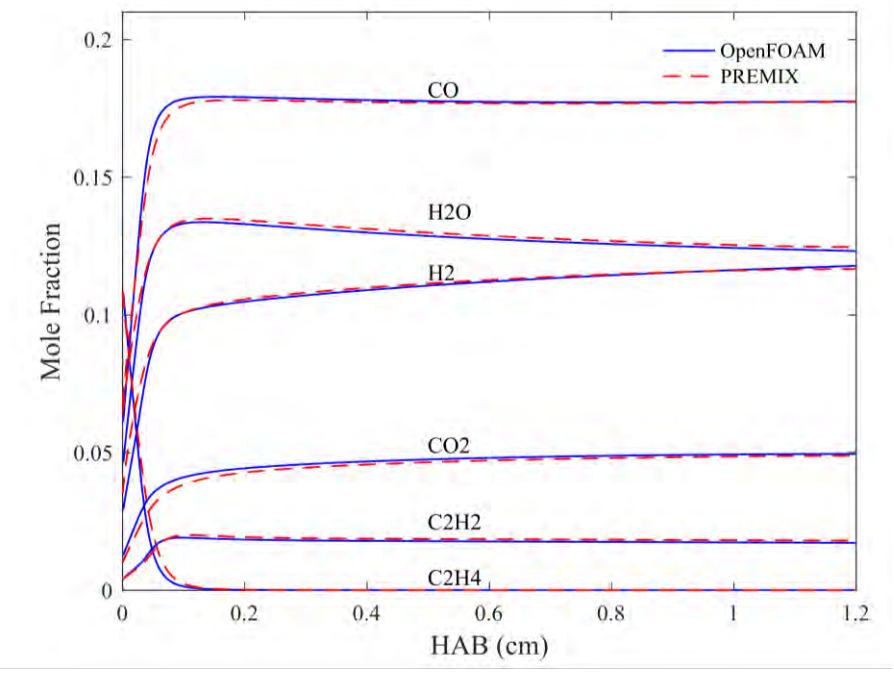

Figure 5.3 Comparison of the main gas species concentration profiles for different HABs by using OpenFOAM and PERMIX codes at flame C3 case (Jiang and Chan, 2021b).

Figure 5.4 shows that the pyrene concentration increases in lower HAB, and then decreases at higher HAB. Such a trend is attributed to the competition between the inception of pyrene by the growth of PAH and the consumption of pyrene by the soot nucleation and condensation processes. In addition, the peak of pyrene mole fraction profiles by imposing the experimental flame temperature profile is lower when compared with that by solving the energy equation. Different flame temperature profiles result in different pyrene mole fraction profiles which show the flame temperature effects on the soot precursors.

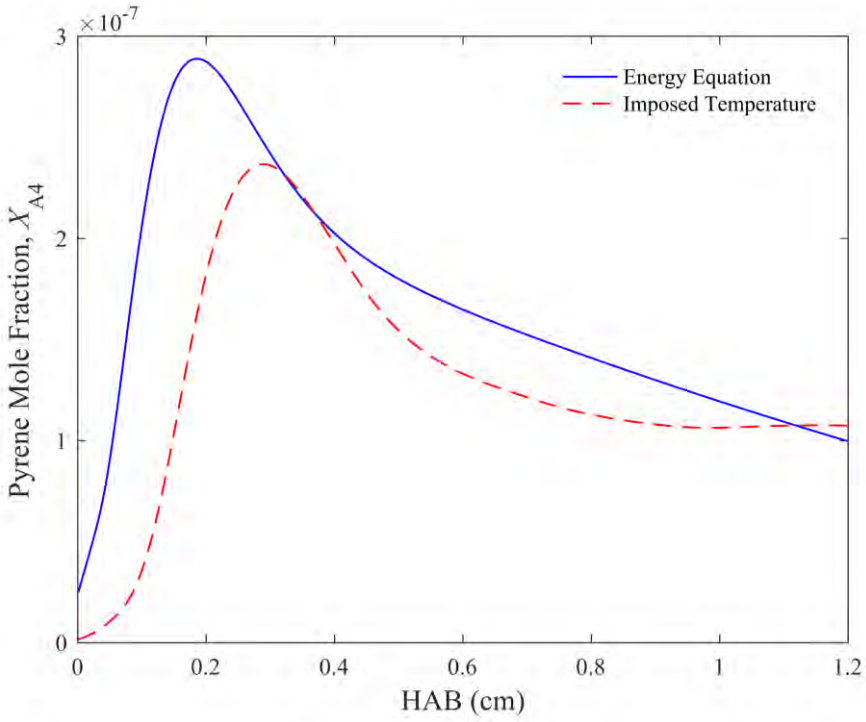

Figure 5.4 Comparison of the pyrene mole fraction profiles for different HABs by solving energy equation and imposing experimental flame temperature profiles at flame C3 case (Jiang and Chan, 2021b).

5.3.2 Evaluation of the numerical algorithm

5.3.2.1 Lagrangian particle tracking

Figure 5.5 shows the average Lagrangian soot particle velocity profiles of flame C3 case for HABs from 0 to 0.12 cm. The average particle velocity in each cell (The mesh grid contains a total of 1000 cells which are enough to resolve the flow fields in the present study) is defined (Jiang and Chan, 2021b) as:

$$\overline{u}_i = \left. \frac{\sum_{j=1}^{N_i} u_{p,j} w_j}{\sum_{j=1}^{N_i} w_j} \right|_{x_{p,j} \in \text{cell } i} \tag{5-15}$$

where $\overline{u}_i$ is the average soot particle velocity in each cell i, $u_{p,j}$ is the velocity of jth particle in each cell i, and w_j is the numerical weight of j particle.

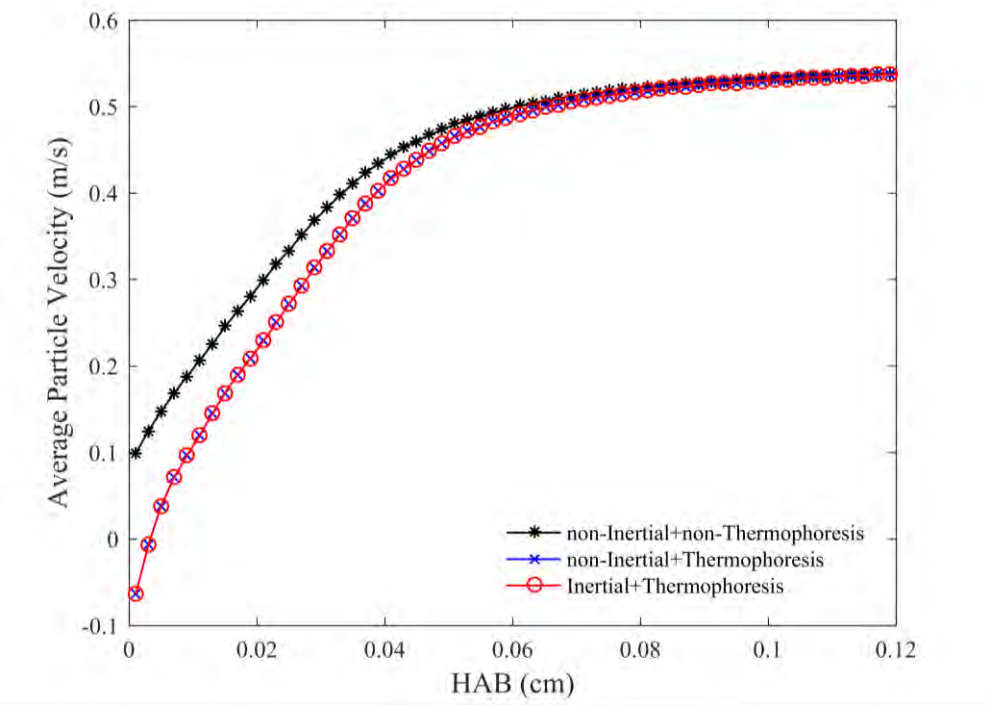

Figure 5.5 Comparison of the average particle velocity profiles with both inertial and thermophoretic effects for different HABs at flame C3 case (Jiang and Chan, 2021b).

It is clear that there is distinctive difference between the average soot particle velocity profiles with or without thermophoretic effect at lower HAB. For higher HAB, such thermophoretic effect is negligible. This can be explained by considering the flame temperature profile in Figure 5.2. For lower HAB, the temperature gradient is large, which leads to a significant thermophoretic effect. For higher HAB, the temperature remains nearly constant, so the thermophoretic effect is minor. Compared with the average particle velocity profiles with or without inertial effect, the results are almost the same. This is attributed to the very low Stokes numbers ($St << 1$) of soot particles at the present flame conditions. It implies that the inertial effect of soot particles is negligible. Therefore, the soot particles are assumed to be the non-inertial particles and the Lagrangian particle trajectories are evolved according to Equation (5-10).

5.3.2.2 Stochastic error analysis of the numerical algorithm

Figure 5.6 shows the comparison of PSDs of flame C3 case by using different Monte Carlo methods (i.e., DSMC, MMC and WFMC methods) at HAB = 0.85 cm. All the numerical simulations used the same number of numerical particles with enough repetitions to obtain the average statistics converge results (i.e., 500 of numerical particles with 200 independent repetitions). The results of normalized number density of soot particles are shown in Figure 5.6, which is given (Jiang and Chan, 2021b) as:

$$n(D_p) = \frac{1}{N}\frac{dN}{d\log D_p} \tag{5-16}$$

where D_p is the particle mobility diameter and N is total soot number density.

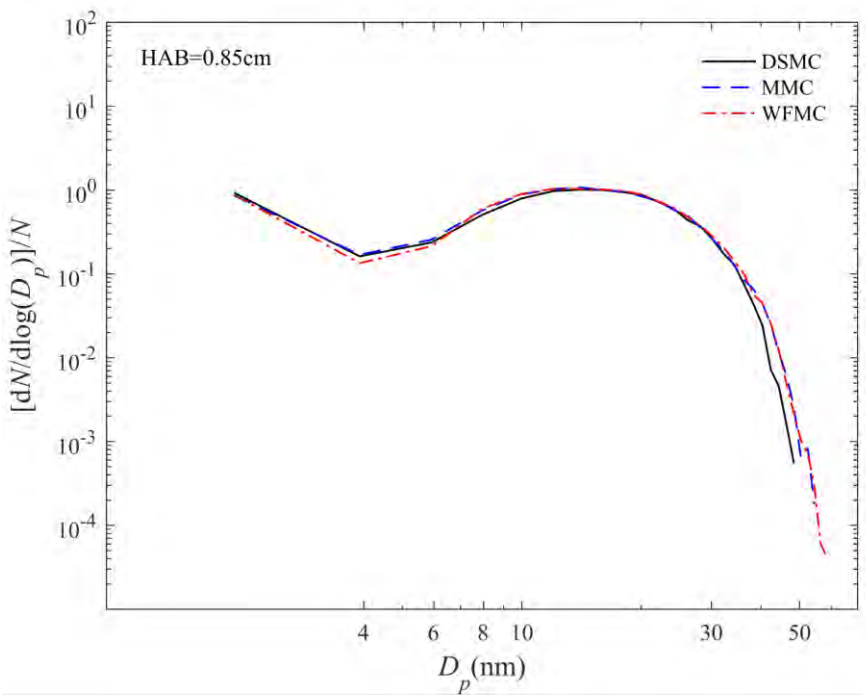

Figure 5.6 Comparison of the average particle size distributions at HAB = 0.85 cm by using DSMC, MMC and WFMC methods for flame C3 case (Jiang and Chan, 2021b).

An excellent agreement is clearly observed among DSMC, MMC and WFMC methods for flame C3 case which is able to validate the presently developed WFMC method as shown in Figure 5.6. Besides, both the WFMC and MMC methods show longer PSDs when compared with DSMC method but the WFMC method shows the longest PSDs among the other two MC methods. It is because WFMC method can change the numerical weight distributions of each particle size. In general, there are always insufficient number of numerical particles to represent larger particles due to their low soot number concentration. In WFMC method, the larger-sized numerical particles are assigned with much smaller numerical weights as shown in Figure 5.7(a). As a result, WFMC method always adopts more numerical particles to represent larger particles (but less to represent smaller particles) as shown in Figure 5.7(b) (where C is the number of numerical particles).

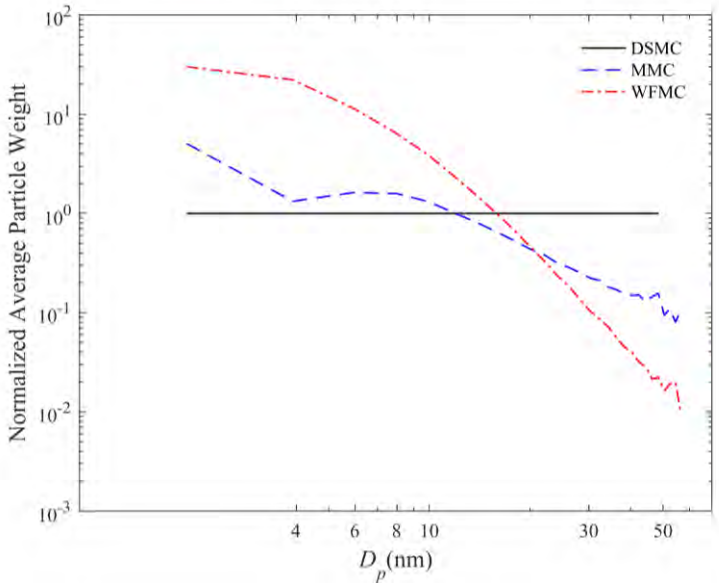

(a)

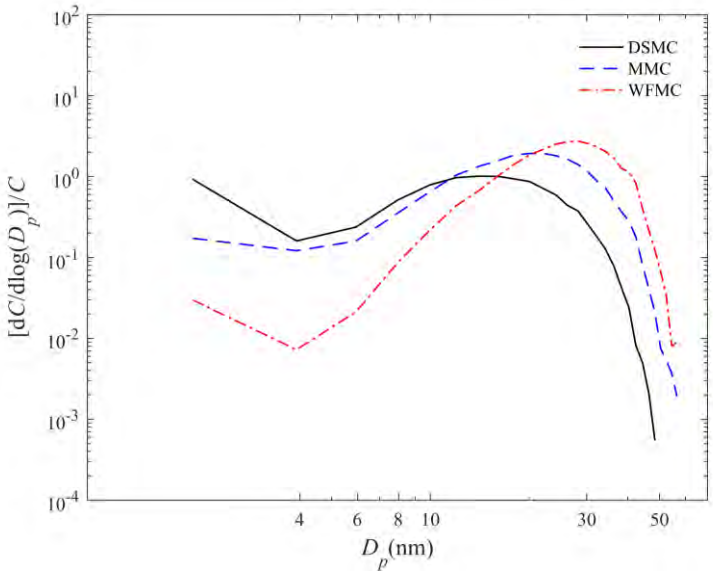

(b)

Figure 5.7 Comparison of (a) normalized average numerical weight distributions and (b) numerical particle size distributions by using DSMC, MMC and WFMC methods for flame C3 case (Jiang and Chan, 2021b).

The variance of PSDs is adopted to quantitatively analyze the statistical uncertainty of different MC methods which is defined (Jiang and Chan, 2021b) as:

$$\sigma^2(D_p) = \frac{1}{N_{\text{rep}} - 1} \sum_{i=1}^{N_{\text{rep}}} (n_i(D_p) - \overline{n(D_p)})^2 \tag{5-17}$$

where $n_i(D_p)$ denotes the *i*th repetition of the normalized soot number density, and $\overline{n(D_p)}$ denotes its sample mean (Jiang and Chan, 2021b) as:

$$\overline{n(D_p)} = \frac{1}{N_{\text{rep}}} \sum_{i=1}^{N_{\text{rep}}} n_i(D_p) \tag{5-18}$$

Figure 5.8 shows the variance ratios of different Monte Carlo methods (i.e., DSMC, MMC and WFMC methods), which are denoted as σ^2_{DSMC}, σ^2_{MMC}, and σ^2_{WFMC}, respectively.

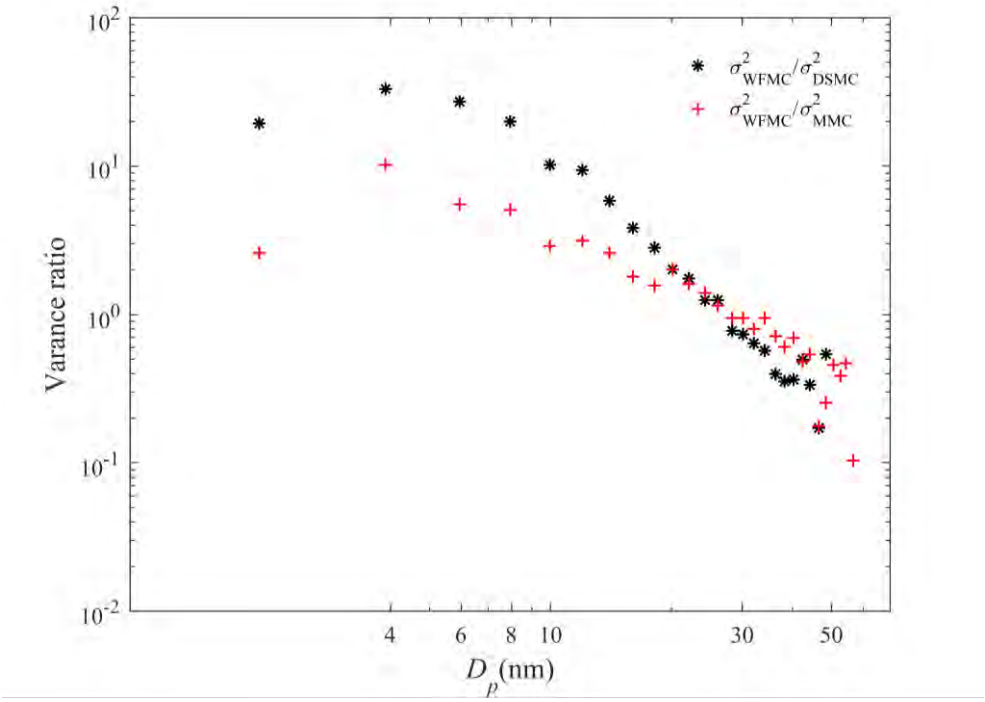

Figure 5.8 Comparison of the variance ratio by using DSMC, MMC and WFMC methods for flame C3 case (Jiang and Chan, 2021b).

With increasing particle size, the variance ratio between WFMC to DSMC, and WFMC to MMC both shows nearly linear trend of decreasing in the logarithm coordinate (except the first point at around 2 nm) as shown in Figure 5.8. It implies that when comparing with DSMC and MMC methods, there are larger variance in WFMC method for smaller particle size regime but smaller variance in larger particle size regime. This analysis supports the capability of WFMC method to improve the accuracy of soot PSDs for larger particle size regime with less accuracy trade-off in smaller particle size regime. Since larger particle size regime has higher contribution for high-order moment but is always poorly represented, it is more important to improve the accuracy of soot PSDs for larger particle size regime. Besides, the reason for the first point not following the linear trend of decreasing is because nucleation is the dominant process at the smallest size regime.

The nucleation is implemented as deterministic integration as described in Section 5.2.2.6, thus different trends on statistical uncertainty are shown. Based on the error analysis, the WFMC method shows great capacity for accurate prediction on the larger particle size, which is also able to further extend the PSDs. Hence, LPT-WFMC method is used for making comparisons with soot experimental measurements in Section 5.3.3.

5.3.2.3 Remarks on the computational cost

As a guideline for comparison to Lagrangian particle tracking with different MC methods, the Lagrangian solver contributes around 41%, 34% and 40% to the total computational time by using DSMC, MMC and WFMC methods, respectively in the present study. The total 60,000 numerical particles are used and 102 transport equations are solved for the gas-phase. The reason for a slightly higher computational time by around 6% for WFMC method than that of MMC method is because of the higher computational cost in coagulation events which can be attributed to two factors. On the one hand, WFMC method must deal with a more complex coagulation kernel when compared with the MMC method (i.e., the kernel function is $\max(w_i,w_j)\beta_{ij}/\alpha_{ij}$ in the WFMC method but is $\max(w_i,w_j)\beta_{ij}$ in the MMC method, as referred to the Equation (4-10)). Hence, a longer computational time is required to calculate the coagulation kernel in the WFMC method. On the other hand, the coagulation kernel function in the WFMC method is always larger than that in the MMC method. The higher total coagulation rate, C_0, leads to more coagulation events in given time interval and higher computational time consumption.

5.3.3 Comparison with soot experimental measurements

5.3.3.1 Soot volume fraction/number density

Figures 5.9 and 5.10 show the total number density and volume fraction of soot particles by the experimental results of flame C1−C5 cases obtained from Abid et al. (2008) and the present numerical simulation results with the developed LPT-WFMC method. As mentioned clearly in Abid et al. (2008), the particle detection limit of their scanning mobility particle sizer (SMPS) was 2.5 nm. Hence, only for particle sizes larger than 2.5 nm were measured in their study. Therefore, for comparison with the present numerical simulation and experimental (Abid et al., 2008) results, particles size smaller than 2.5 nm are also removed from the present numerical simulation results which are handled similar to the previous study of the same premixed flame in Salenbauch et al. (2015).

Figure 5.9 shows similar increasing and decreasing trends in both the numerical simulation and experimental results. The nucleation process dominates at lower HAB and causes a rapid increase in the total soot number density. But for higher HAB, the coagulation process becomes more important. The competition between nucleation and coagulation process causes a decrease in total soot number density at higher HAB. Compared with the results by solving the energy equation, the imposing experimental flame temperature profiles totally shift the results to the right, which show the effects of flame temperature profiles on the total number density profiles of soot particles. Compared with the experimental results, the overestimation of numerical results for total number density of soot particles can be especially observed for lower HAB**.** Similar large overestimation for total number density of soot particles also can be found in previous study of

numerical simulation results (Yang and Mueller, 2019) with both sectional method and method of moments. The overprediction on the total number density of soot particles indicates that the present numerical simulation results of current soot model overpredict the number of smaller particles when compared with the experimental results, which may be attributed to the higher soot nucleation rate used.

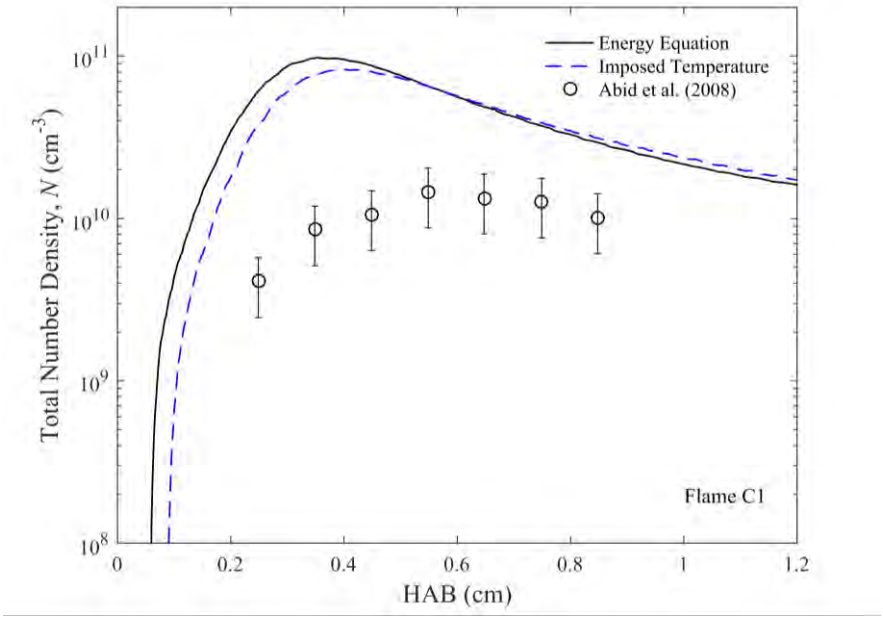

(a) Flame C1

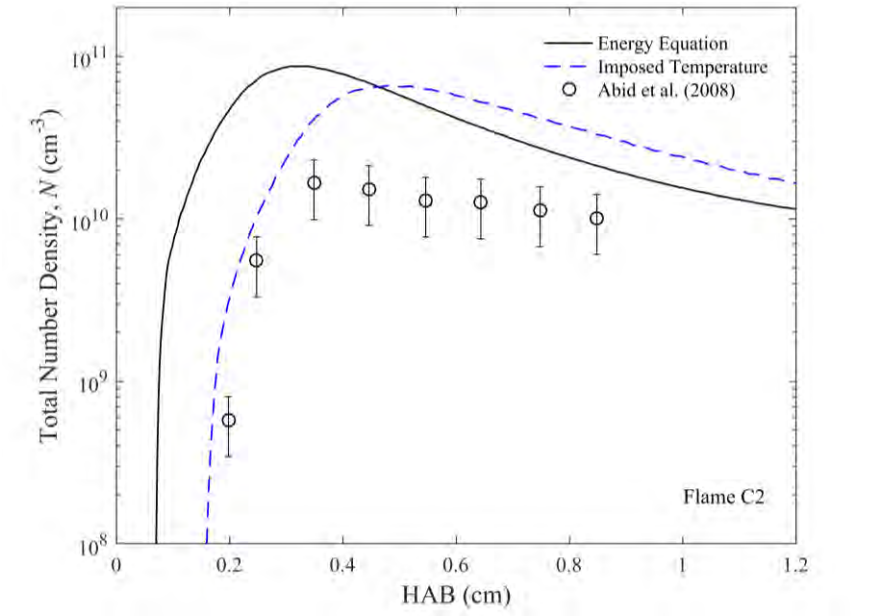

(b) Flame C2

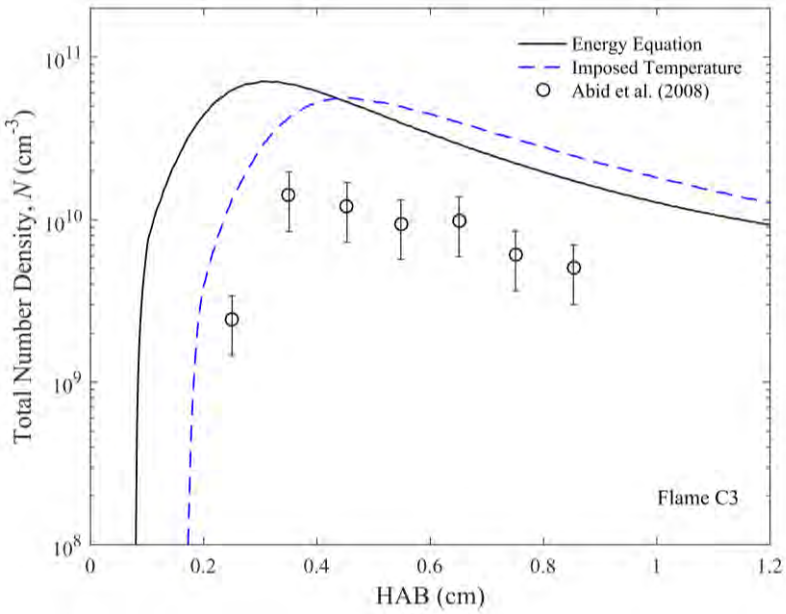

(c) Flame C3

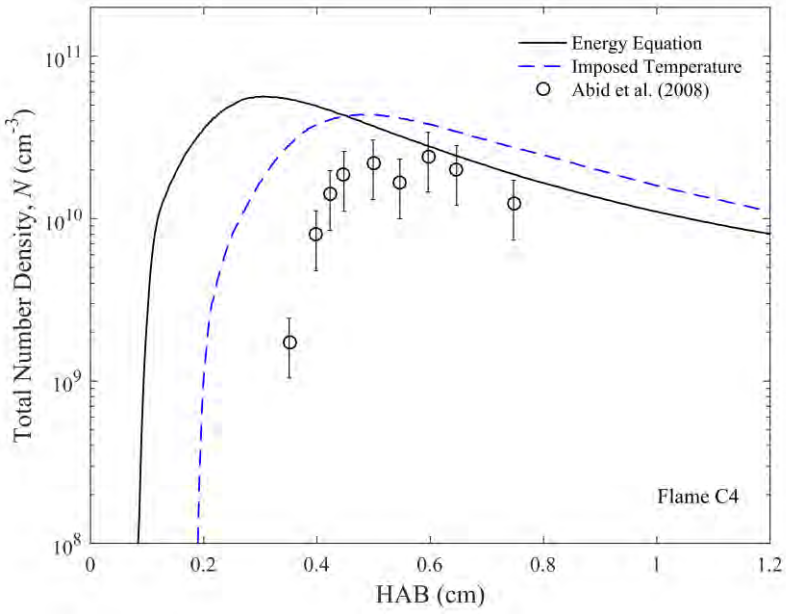

(d) Flame C4

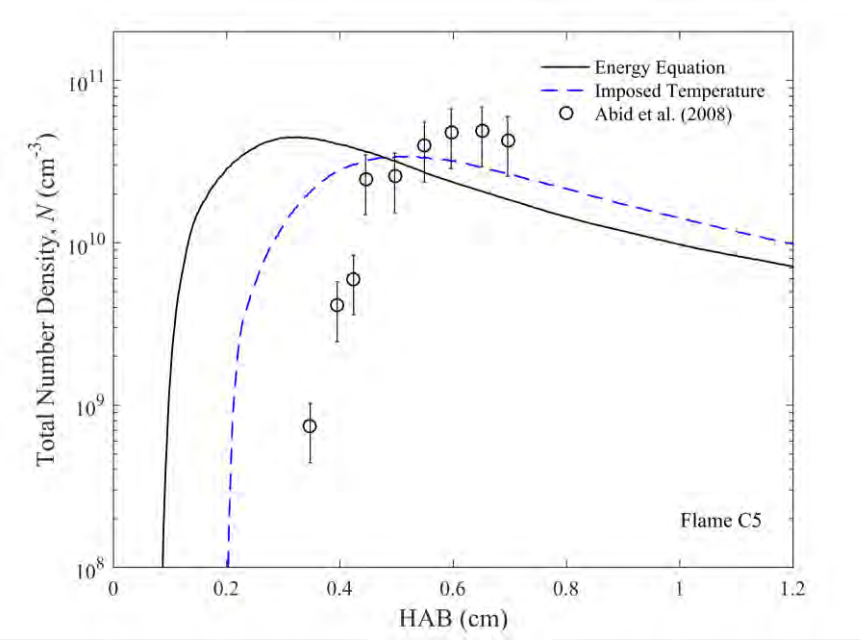

(e) Flame C5

Figure 5.9 Comparison of total number density profiles of soot particles between the present numerical simulation and experimental (Abid et al., 2008) results for different HABs and flame condition cases (Jiang and Chan, 2021b).

In Figure 5.10, the numerical simulation results of soot volume fraction of flame C1 case are close to each other by solving the energy equation and imposing the experimental flame temperature profile. This is because the flame temperature profile in flame C1 case by solving the energy equation is nearly the same as that of the experimental results. For flame C2–C5 cases, the soot volume fractions of the experimental results (Abid et al., 2008) are at the approximate range between the numerical simulation results by solving the energy equation and by imposing the experimental flame temperature profiles. In the present study, the most common soot nucleation model is based on the assumption of soot nucleation as pyrene dimerization. It is generally considered as a mere numerical tool, rather than a realistically physical phenomenon. In addition, the PAH chemistry in ABF mechanism (Appel et al., 2000) is not fully understood. Bakali et al. (2012) reported

that pyrene mole fraction is overestimated in some flame conditions. As a result, the deviations in soot number density and volume fraction can be found.

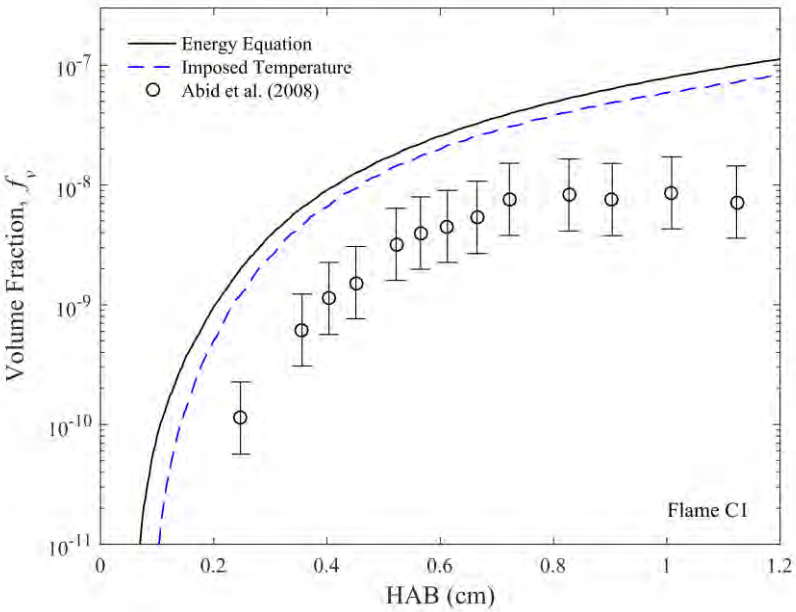

(a) Flame C1

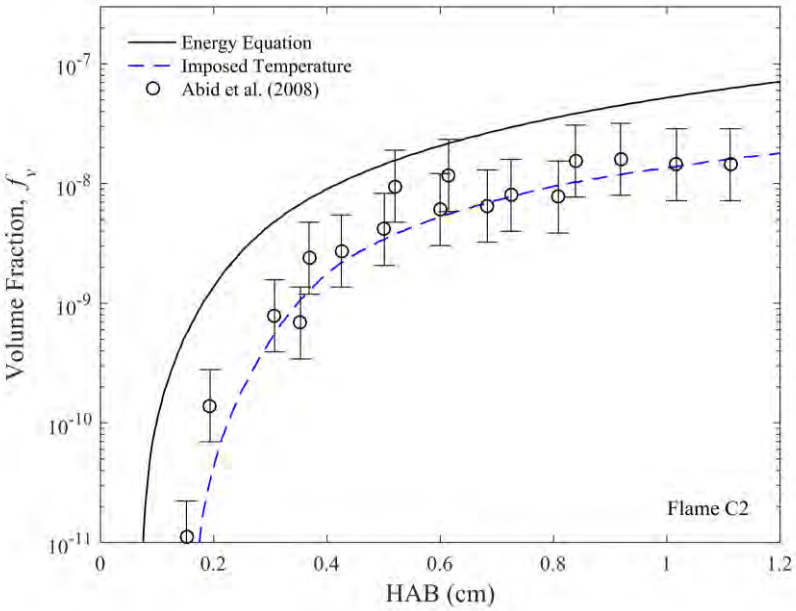

(b) Flame C2

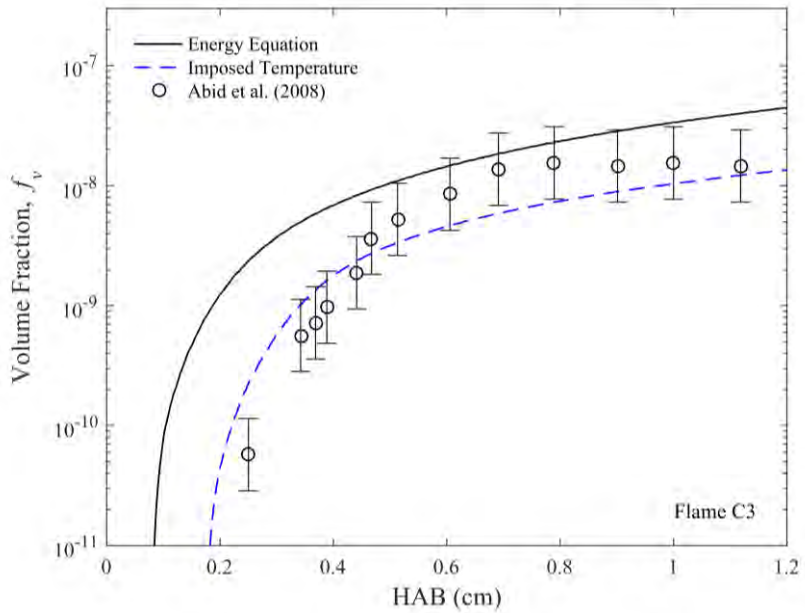

(c) Flame C3

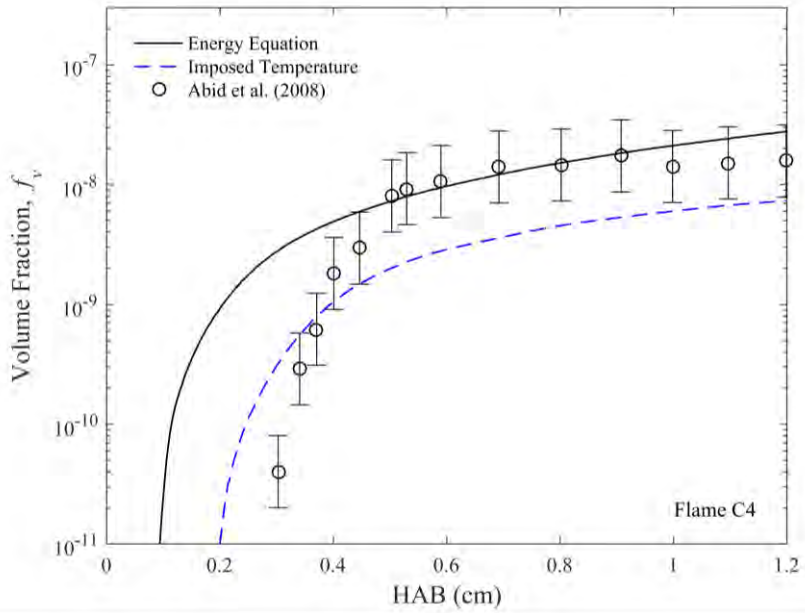

(d) Flame C4

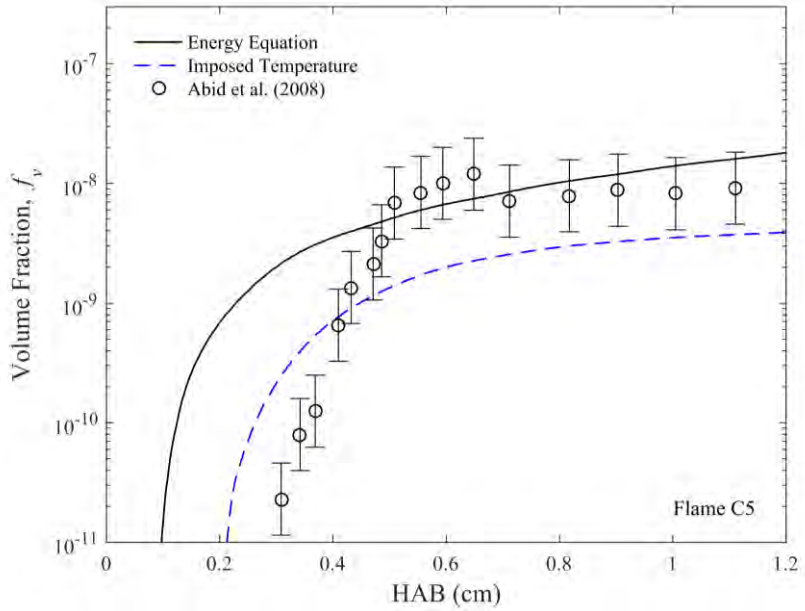

(e) Flame C5

Figure 5.10 Comparison of soot volume fraction profiles between the present numerical simulation and experimental (Abid et al., 2008) results for different HABs and flame condition cases (Jiang and Chan, 2021b).

5.3.3.2 Soot particle size distributions

The results of PSDs for different heights above the burner (HABs) are shown in Figures 5.11 to 5.15. By imposing the experimental flame temperature profiles, the results are totally shifted to the left as compared to the results of solving the energy equation. As shown in Figure 5.4, imposing of the experimental flame temperature profile lowers the peak of pyrene concentration, thus reduces the nucleation rate as well as the condensation rate, and shifts the PSDs to smaller particle size regime.

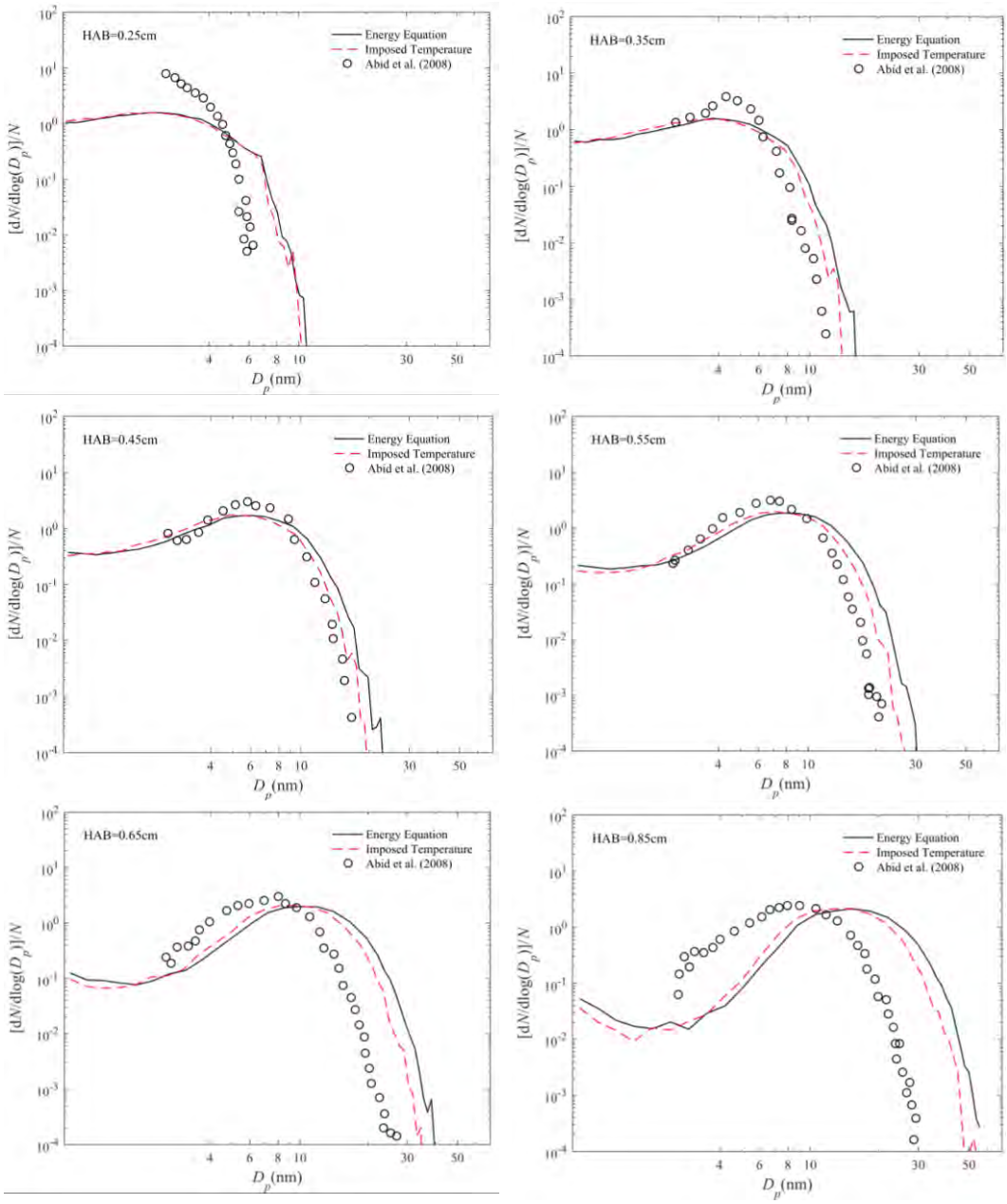

Figure 5.11 Comparison of particle size distributions of flame C1case between the present numerical simulation and experimental (Abid et al., 2008) results for different HABs (Jiang and Chan, 2021b).

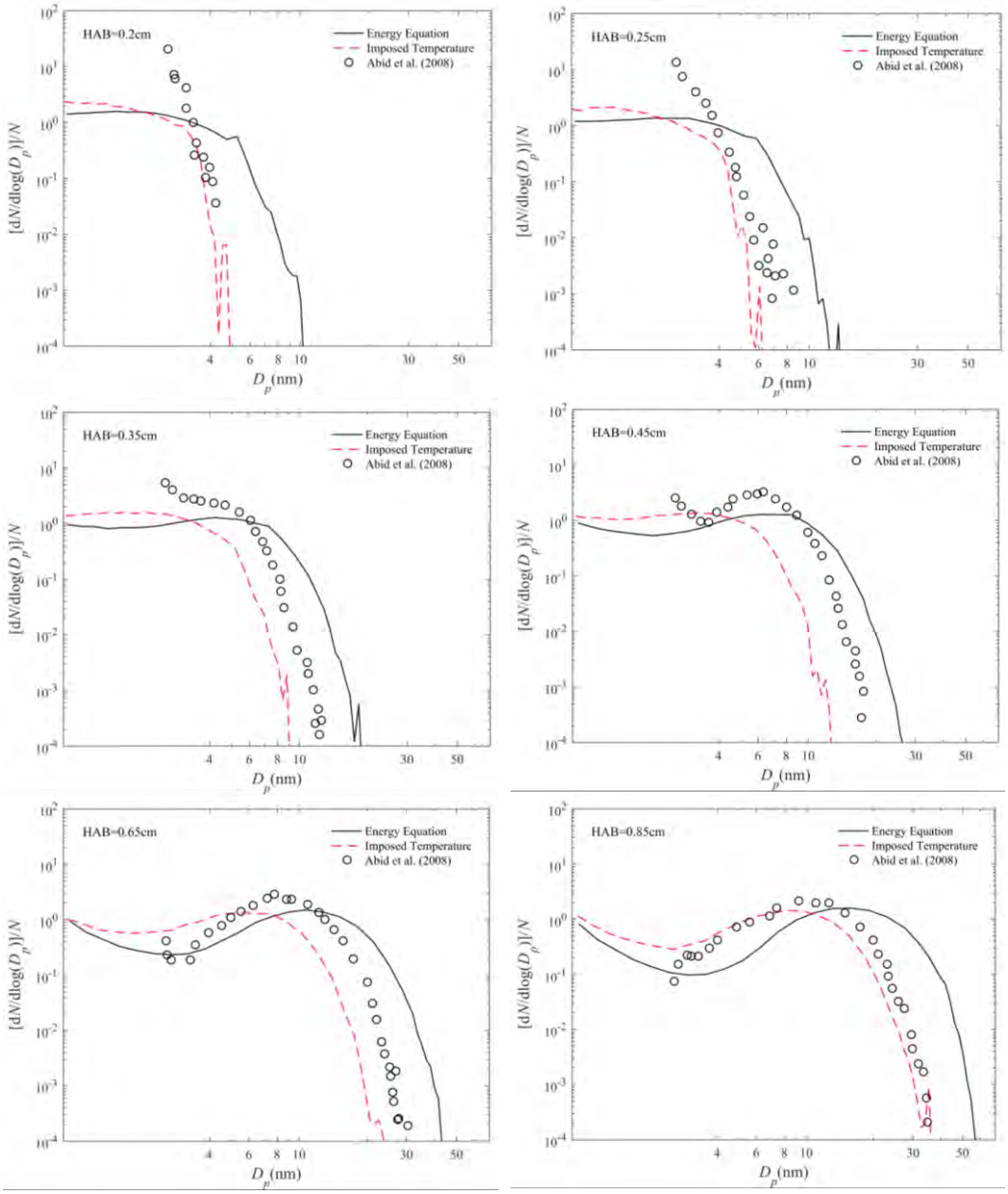

Figure 5.12 Comparison of particle size distributions of flame C2 case between the present numerical simulation and experimental (Abid et al., 2008) results for different HABs (Jiang and Chan, 2021b).

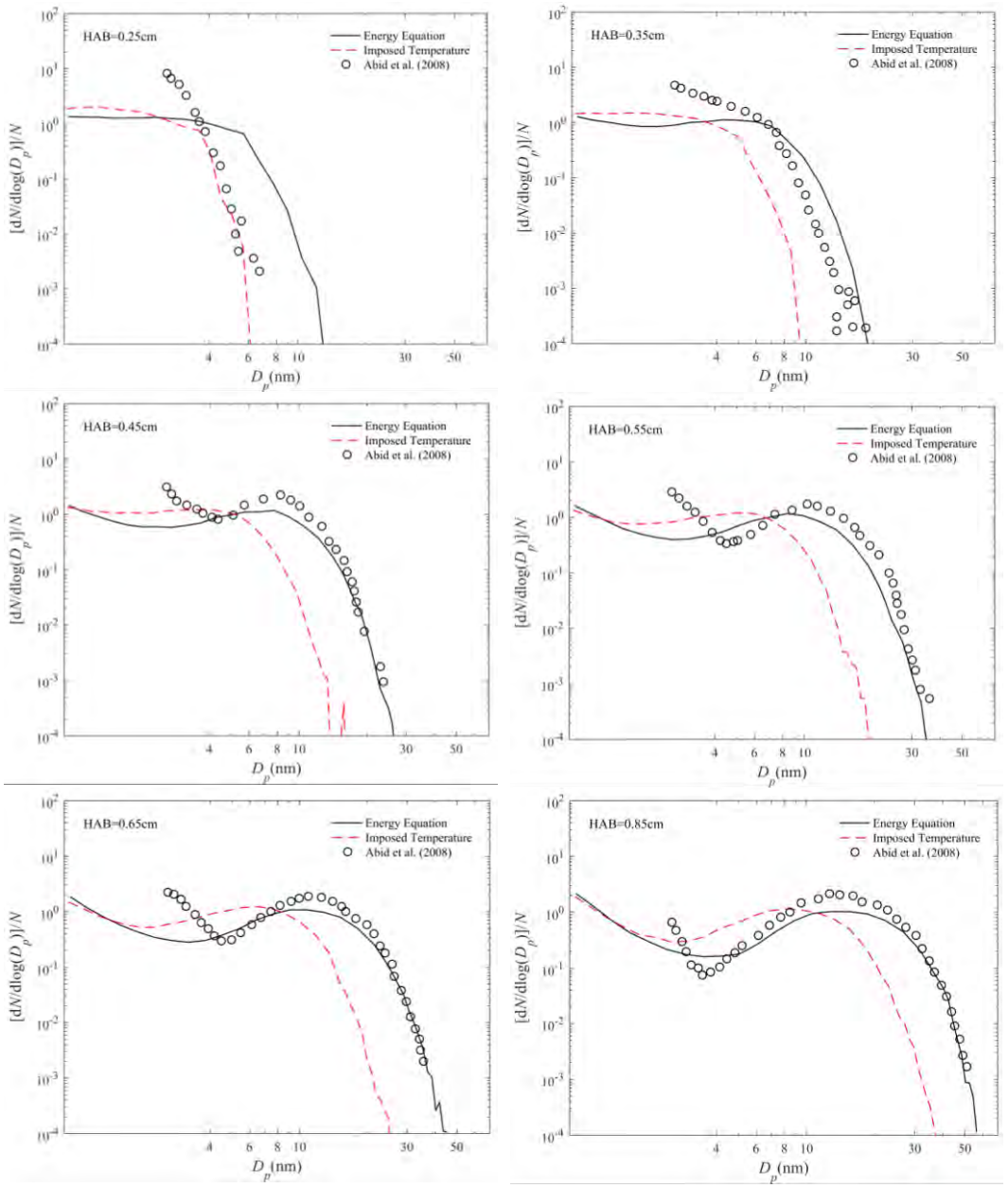

Figure 5.13 Comparison of particle size distributions of flame C3 case between the present numerical simulation and experimental (Abid et al., 2008) results for different HABs (Jiang and Chan, 2021b).

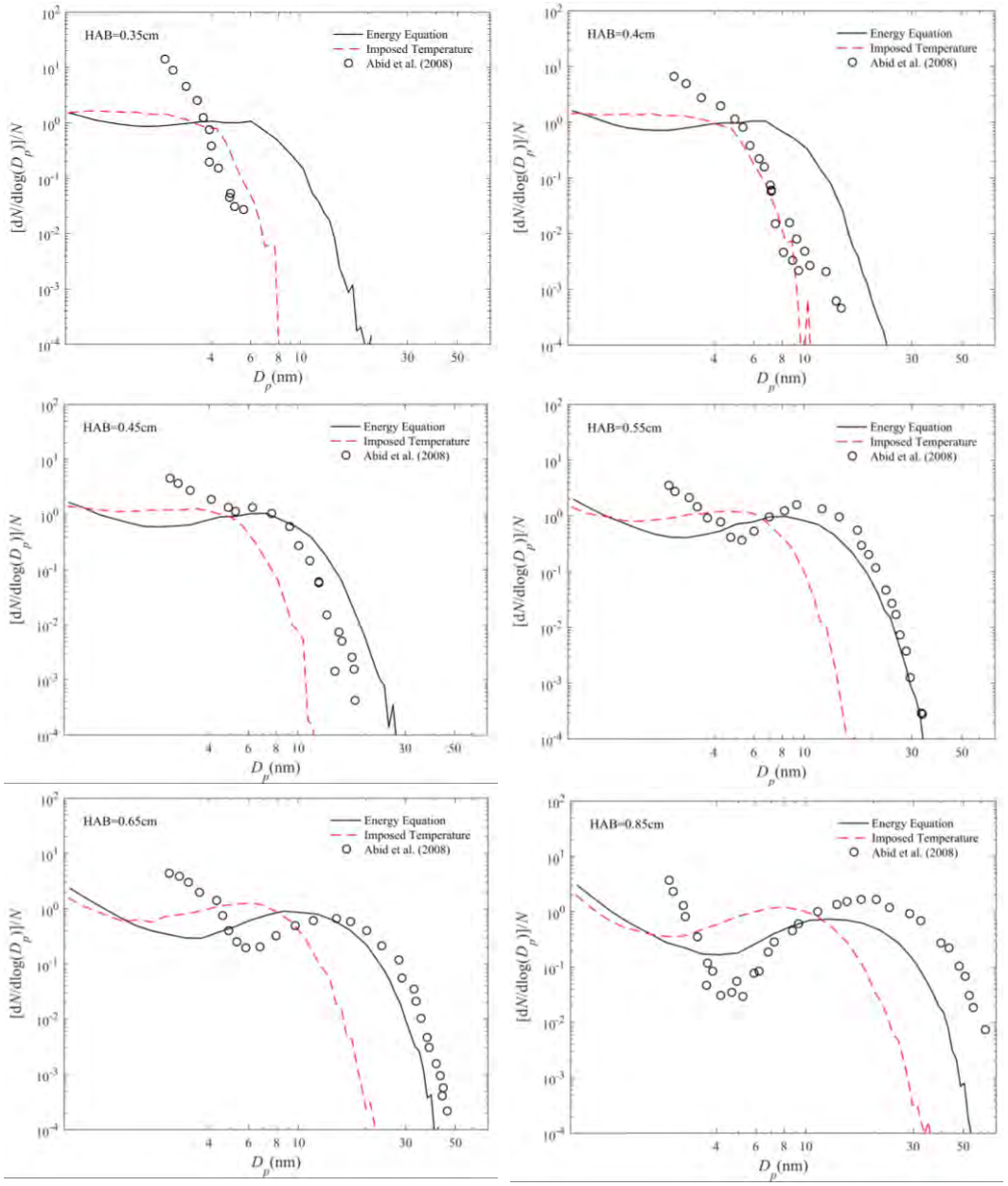

Figure 5.14 Comparison of particle size distributions of flame C4 case between the present numerical simulation and experimental (Abid et al., 2008) results for different HABs (Jiang and Chan, 2021b).

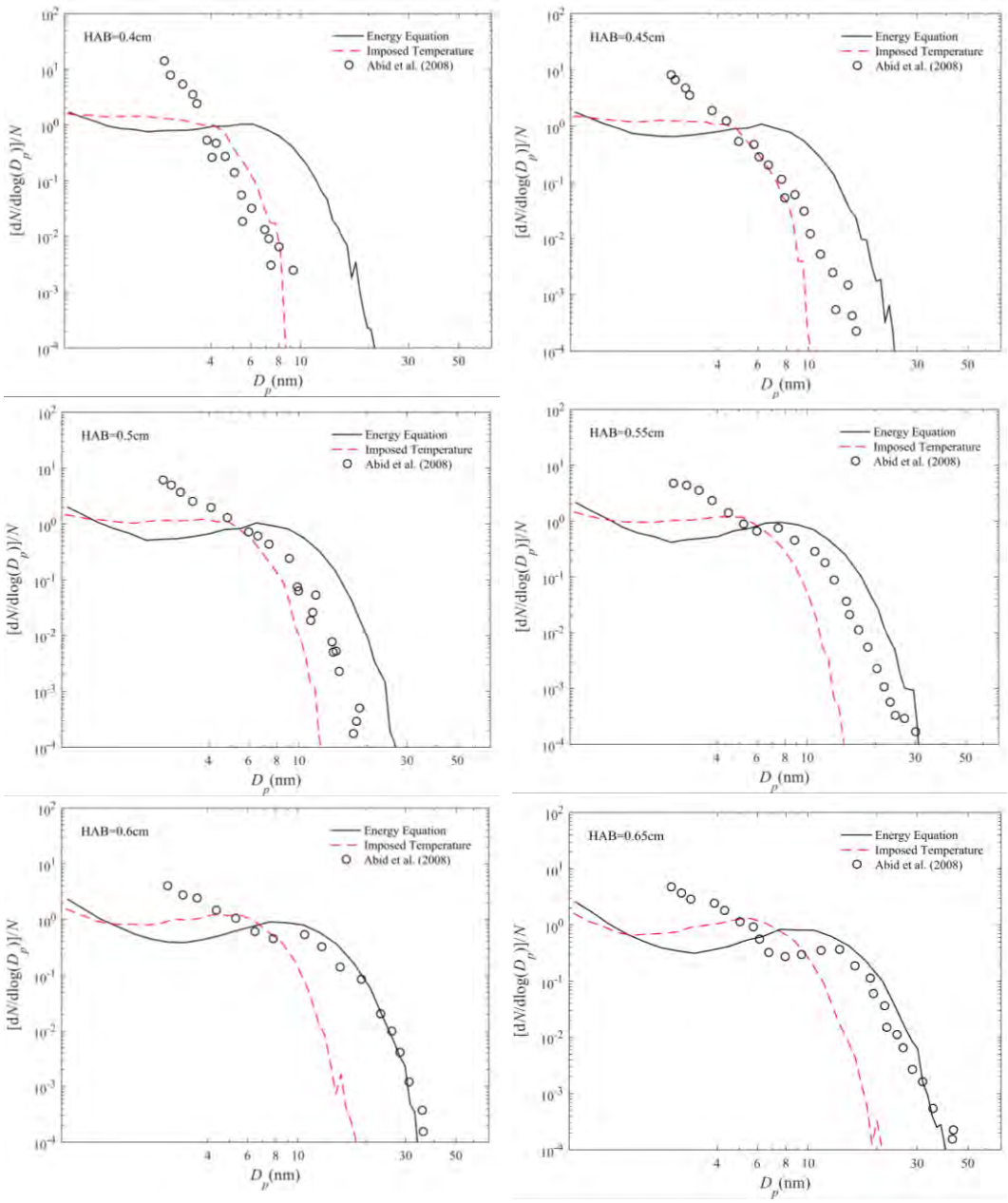

Figure 5.15 Comparison of particle size distributions of flame C5 case between the present numerical simulation and experimental (Abid et al., 2008) results for different HABs (Jiang and Chan, 2021b).

Compared with the PSDs of numerical simulation and experimental results, the qualitative agreement can be found. However, the discrepancies of PSDs at lower HAB (i.e., 0.25 and 0.35 cm) flame region cannot be neglected, especially for the PSDs at smaller size regime (i.e., mobility diameter D_p < 4 nm). Such similar large deviations of PSDs can also be found in the previous studied numerical

simulation results of burner-stabilized stagnation flame (Yapp et al., 2015; Hou et al., 2019). Both Yapp et al. (2015) and Hou et al. (2019) also highlighted that such deviation was mainly attributed to two reasons: First the soot nucleation mechanism was still poorly understood and the current nucleation mechanism was rather an approximation. Second the gas-phase PAH chemistry was still far from reliable. Bakali et al. (2012) reported that ABF mechanism overestimated pyrene mole fraction in the sooting region by a significant factor (more than 10) compared with experiments. However, the nucleation rate is very sensitive to the pyrene concentration. In the present study, the deviation of simulated PSDs at smaller particle size regime indicates that the current adopted soot nucleation mechanism needs further improvement along with more accurate PAH chemistry. As the deviation of PSD is mainly attributed to the overestimation of nucleation rate used in the present study. The improvement of PAH chemistry and soot nucleation mechanisms is thus required. That is also the reason why a better understanding of soot nucleation at atomics level is one of the main objectives of the present study for attempting to fill this knowledge gap. The molecular dynamics simulation is also applied to study some possible nucleation pathways in Chapters 6 and 7. On the other hand, the fairly good agreement between numerical simulation and experimental results in PSDs at higher HAB (i.e., HAB $\geqslant$ 0.45 cm) flame region for larger particle size regime (i.e., mobility diameter $D_p \geqslant 6$ nm) can be found. The PSDs of experimental results are within the range between the PSDs results by imposing the experimental flame temperature profile and solving the energy equation. The relatively good agreement is attributed to the coagulation process which becomes dominant at higher HAB flame region. The study of different soot dynamic process rates supports this argument as shown in Figure 5.16. For higher

HAB (i.e., HAB ⩾ 0.45 mm), the PSDs finally evolve to distinctly bimodal distribution, and this is clearly captured by our developed LPT-WFMC method, which shows the accuracy of prediction for PSDs from Lagrangian point of view. Since the essential information about soot PSDs is critical for soot prediction, the present numerical simulation results of LPT-WFMC method show that detailed information (e.g., coordinates, velocity, diameter) of soot formation and evolution can be obtained by the present Lagrangian particle tracking method.

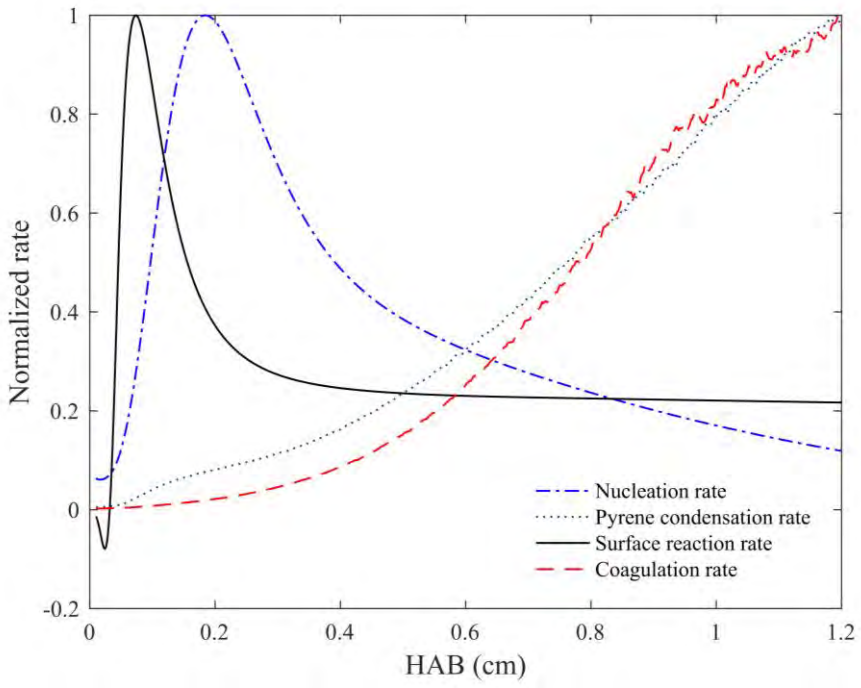

Figure 5.16 Normalized rate profiles of different soot dynamic processes for different HABs (Jiang and Chan, 2021b).

In Lagrangian particle tracking approach, the history of individual soot particle can be tracked. In here, flame C3 case is selected to study the rates of different soot dynamic processes as a typical example. Figure 5.16 shows the rates of nucleation, condensation, surface growth and coagulation for flame C3 case at different HABs. All the rates are normalized by their corresponding maximum

values. At lower HAB flame region, nucleation and surface reaction rates dominate the soot dynamic processes and the PSDs is of unimodal distribution (e.g., PSDs at HAB = 0.25 and 0.35 cm). At higher HAB flame region, the nucleation rate decreases significantly because most of the particles are formed which leads to condensation and consumes more pyrene. Hence, the pyrene concentrations are then decreased as shown in Figure 5.4. The surface reaction rate is also decreased along with the decreasing of H-atom mole fraction since the rate of surface reaction is proportional to H-atom concentration (Wang, 2011). Although the pyrene condensation rate is increased, but the mass addition by pyrene condensation is relatively small when compared with the surface growth (Veshkini and Dworkin, 2017). Thus, the coagulation process finally dominates PSDs and the PSDs gradually evolves to be of bimodal distribution.

5.3.4 Parametric sensitivity analysis

Figure 5.17 schematically shows the typical bimodal PSDs. In order to quantitatively characterize the computed PSDs, four selected characteristic points on a bimodal PSDs are defined as (Singh et al., 2006; Yapp et al., 2015): (a) the inception peak for nucleation process; (b) a trough for bimodal PSDs, (c) the coagulation peak by coagulation and surface growth processes; and (d) the ‘‘largest’’ particle. Here the ‘‘largest’’ particle is defined as the largest diameter with normalized number density of soot particles, $n(D_p) = 10^{-2}$.

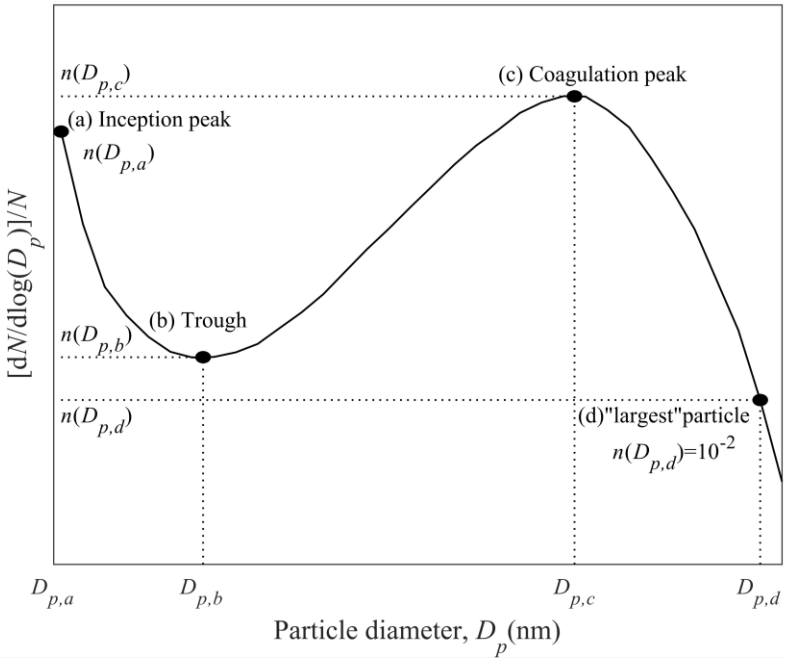

Figure 5.17 Characteristic particle size distribution function (Jiang and Chan, 2021b).

Table 5.2 Model parameters for detailed population balance model (Jiang and Chan, 2021b).

Parameters	Ranges	Value	References
(a) Aggregates morphology	Coalescence to aggregation	VSH model	Blanquart et al. (2009)
(b) Soot density, ρ (g/cm^3)	$0.6 \le \rho \le 2$	1.4	Yapp et al. (2015)
(c) pyrene-pyrene sticking probability, $\gamma_{A4\text{-}A4}$	$0 \le \gamma_{A4\text{-}A4} \le 1$	0.025	Blanquart et al. (2009)
(d) pyrene-particle sticking probability, $\gamma_{A4\text{-}P}$	$0 \le \gamma_{A4\text{-}P} \le 1$	0.5	Zhang et al. (2009)
(e) particle -particle sticking probability, $\gamma_{P\text{-}P}$	$0 \le \gamma_{P\text{-}P} \le 1$	1	Hou et al. (2019)

In order to study the influence of soot model parameters to the bimodal PSDs, some critical parameters have been taken into the consideration of the parametric sensitivity analysis which include (a) morphology of soot aggregates, (b) density of soot aggregates, (c) pyrene-pyrene sticking probability, (d) the pyrene-particle

sticking probability and (e) the particle-particle sticking probability. The parameters ranges and values used for the base cases and references are listed in Table 5.2 (Jiang and Chan, 2021b).

The flame C3 case is selected as a typical example to illustrate the effect of different parameters on the bimodal PSDs. The numerical simulation is carried out at HAB = 0.85 cm where the PSDs are fully evolved to the bimodal distribution. By varying the studied parameters in Table 5.2, parametric sensitivity analysis is applied for the bimodal PSDs. Although many previous sensitivity studies for soot PSDs were conducted (Singh, 2006; Yapp et al., 2015; Hou et al., 2019; Hou et al., 2020a), the effect of parameters was only qualitatively analyzed. In the present study, the parametric sensitivity of PSDs is quantitatively studied for determining the relative changes in position for some critical points. To quantitatively characterize the parametric sensitivity to the bimodal PSDs, the position changes of characteristic points are defined (Jiang and Chan, 2021b) as:

$$S_n = \frac{\log[n(D_p)|_{\text{upper}}] - \log[n(D_p)|_{\text{lower}}]}{\log[n(D_{p,a})|_{\text{base}}] - \log[n(D_{p,d})|_{\text{base}}]} \tag{5-19}$$

$$S_D = \frac{\log[D_p|_{\text{upper}}] - \log[D_p|_{\text{lower}}]}{\log[D_{p,d}|_{\text{base}}] - \log[D_{p,a}|_{\text{base}}]} \tag{5-20}$$

Equations (5-19) and (5-20) describe the relative changes in positions of $n(D_p)$ and D_p for the characteristic points. The subscripts of upper and lower mean the values at upper and lower bounds of studied parameters, respectively. The logarithmic value is used here since the PSDs are always studied at logarithm coordinates. If $|S|< 0.1$, the parameter is assumed not sensitive to the position of characteristic point on bimodal PSDs, for $0.1 \leqslant |S| < 0.2$ where the parameter is

sensitive, and the symbol, $\rightarrow$ is used to denote their change tendency. For $0.2 \leqslant |S|$, the parameter is very sensitive, and the symbol, $\Longrightarrow$ is used to denote their significant change tendency.

For coalescence model, all soot particles are assumed to be spheres, particle will fully coalescence after coagulation events. However, each primary particle in soot aggregates is connected only through a point in the aggregation model. In the present base case, the joint volume-surface multi-variate (VSH) model is used between these two limit models. Detailed information about this model can be referred to Blanquart and Pitsch (2009b).

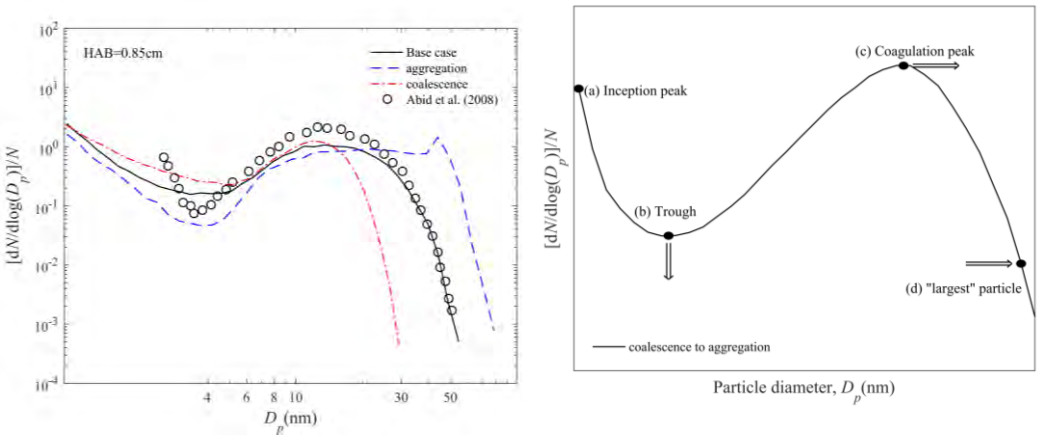

Figure 5.18 Parametric sensitivity analysis of PSDs for different coagulation models (Jiang and Chan, 2021b).

Figure 5.18 shows the effects of soot particle coagulation model on bimodal PSDs. The results show the position of trough, coagulation peak and "largest" particles are very sensitive to coagulation model. As coagulation model is adopted from coalescence to aggregation, the trough will drop down, and both coagulation peak and "largest" particles will shift to the larger particle size regime. Since all soot particles are assumed to be spherical particles in

coalescence model, but the aggregates are assumed to be a point connected by the primary particle in aggregation model, thus larger mobility diameters are found in aggregation model.

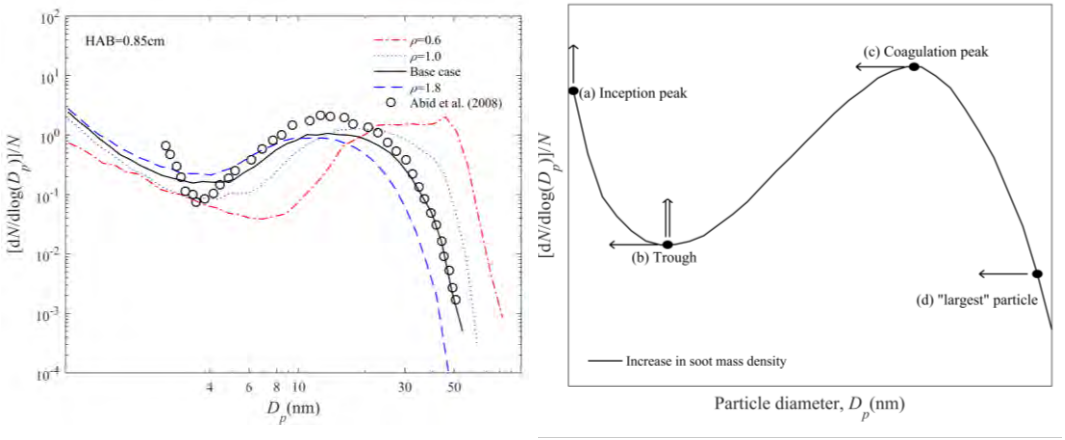

Figure 5.19 Parametric sensitivity analysis of PSDs for different soot densities (Jiang and Chan, 2021b).

Figure 5.19 shows the parametric sensitivity analysis of soot mass density on bimodal PSDs. The results show that only the position of trough is very sensitive to the soot density. As soot mass density increases, higher inception peak and trough can be found. Meanwhile, trough, coagulation peak and “largest” particles will shift to the smaller particle size regime. For lower soot mass density, the growth of soot particle sizes is more rapid for given mass growth rate. On the other hand, the coagulation kernel is also the function of particle mass density in free molecular regime. Hence, the smaller soot mass density results in larger coagulation kernel, while the coagulation events occur more frequently which results in more soot particles in larger particle size regime.

Figures 5.20 to 5.22 show the effects of $\gamma_{A4\text{-}A4}$, $\gamma_{A4\text{-}P}$, and $\gamma_{P\text{-}P}$ on bimodal PSDs, respectively. Increasing $\gamma_{A4\text{-}A4}$ will directly increase the nucleation rate, and results in rising inception peak while decreasing both the trough and coagulation peaks. Besides, the positions of trough, coagulation peak and "largest particle" are systematically shifted to the larger particle size regime. With the increase of $\gamma_{A4\text{-}P}$, the position of "largest particle" nearly maintains unchanged, while the peak positions of coagulation and inception are changed significantly with only a minor shift on the trough. With the decrease of $\gamma_{P\text{-}P}$, it is clearly shown that the trough is vanished at relatively low $\gamma_{P\text{-}P}$ (i.e., $\gamma_{P\text{-}P}$= 0.1 for the present numerical study). As a result, the bimodal PSDs is then evolved to the unimodal PSDs. The inception peak is also decreased dramatically, together with a slightly higher coagulation peak. Both the positions of coagulation peak and "largest particle" will also be shifted to the smaller particle size regime. For the lower of $\gamma_{P\text{-}P}$, the coagulation effect is minor, thus the size of largest particles due to the coagulation events becomes smaller. The PSDs are then mainly dominated by nucleation and surface growth processes, and lead to the unimodal PSDs. Overall, the $\gamma_{A4\text{-}A4}$ is shown as the most sensitive parameter on bimodal PSDs because these four selected characteristic points are all very sensitive to $\gamma_{A4\text{-}A4}$.

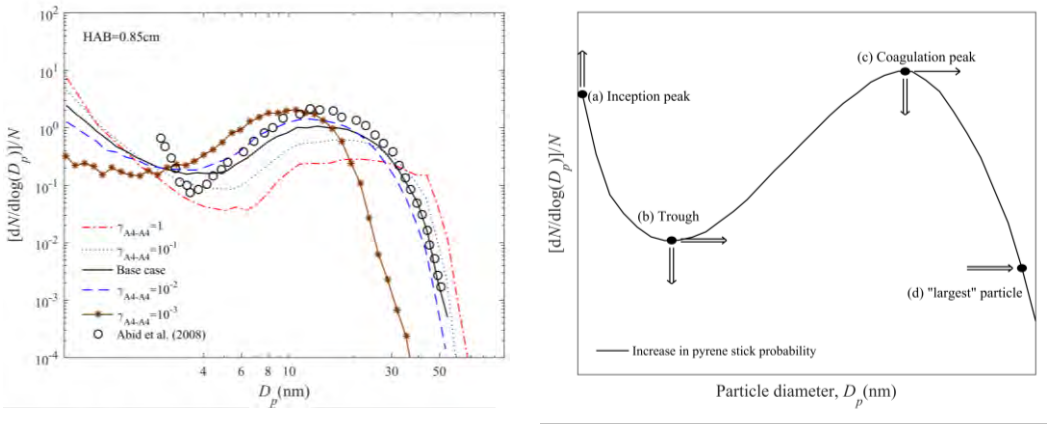

Figure 5.20 Parametric sensitivity analysis of PSDs for different pyrene-pyrene sticking probabilities (Jiang and Chan, 2021b).

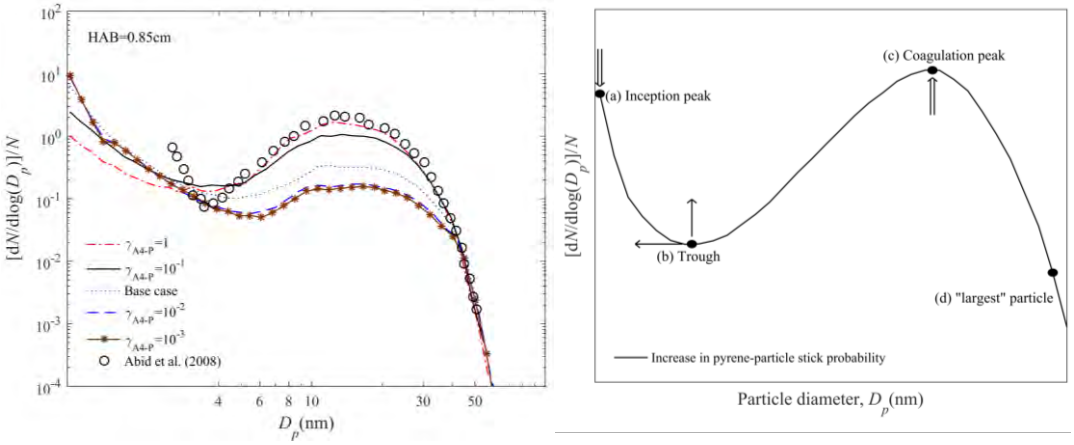

Figure 5.21 Parametric sensitivity analysis of PSDs for different pyrene-particle sticking probabilities (Jiang and Chan, 2021b)

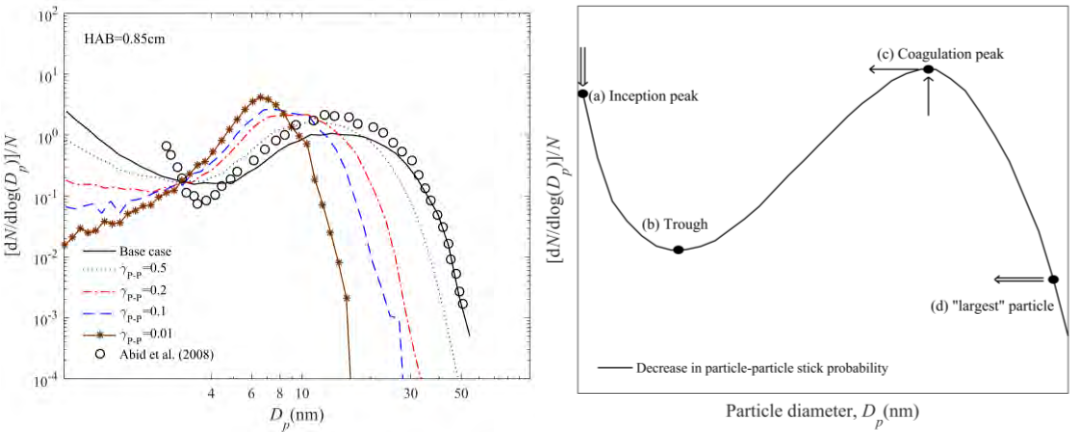

Figure 5.22 Parametric sensitivity analysis of PSDs for different particle-particle sticking probabilities (Jiang and Chan, 2021b).

5.4 Summary

Lagrangian particle tracking with a weighted fraction Monte Carlo (LPT-WFMC) method is developed and coupled with a detailed soot model to study the soot formation and evolution (Jiang and Chan, 2021b). The weighted soot particle is used in the MC framework and is tracked using Lagrangian approach. The WFMC method is derived based on the MMC method (with adjustable weight distribution by introducing the fraction function α) (Jiang and Chan, 2021a). The LPT-WFMC method is validated for soot prediction in the one-dimensional laminar premixed ethylene flame by comparison with the results of DSMC, MMC and the experiments. In the present study, stochastic error analysis has proved that the LPT-WFMC method can extend the soot PSDs and reduce the statistical error for larger particle size regime. It is because LPT-WFMC method can change the numerical weight distribution to assign more numerical particles to larger particle size regime, while there are always insufficient number of numerical particles and poor representation in the larger particle size regime.

The numerical simulation results for soot number density and volume fraction show similar trends with experimental results (Abid et al., 2008), but still with some overprediction for soot number density as similar to some previous studies (Yang and Mueller, 2019). The numerical simulation results of soot PSDs show a fairly good agreement with experimental results at higher HAB of flame region with larger particle size regime (i.e., HAB $\geqslant$ 0.45cm and $D_p > 6$ nm) while the coagulation and surface growth processes are well captured. However, for lower HAB flame region and smaller particle size regime (i.e., $D_p < 4$ nm HAB $\leqslant$ 0.35 cm), the large deviations from simulated PSDs and experimental results are not

negligible. Such discrepancies for total number density and PSDs at lower HAB flame region and smaller particle size regime indicate that a better understanding and modelling of the soot nucleation and the chemistry of PAHs is still one of the most challenging problems in the research field. The soot PSDs is finally evolved to bimodal distribution which can be explained by studying the rate of soot dynamic process. Parametric sensitivity analysis is also performed to provide a better understanding and gain insight of the effects of those critical parameters on simulated PSDs.

Chapter 6 Molecular Dynamics Simulation of PAH Dimerization

6.1 Introduction

Soot nucleation mechanism still remains one of the least understood areas due to its complex nature, though the physical dimerization of pyrene has been widely used and applied in the numerical modelling for studying the soot formation and evolution (Wen et al., 2005; Yapp et al., 2015; Selvaraj et al., 2016; Qiu et al., 2019; Hoerlle et al., 2020; Martin et al., 2022). Theoretical and experimental results suggest that small to medium sized polycyclic aromatic hydrocarbons (PAH) dimers are thermodynamically unstable under flame temperature (Wang, 2011; Elvati and Violi, 2013; Zhang et al., 2019; Liu et al., 2021c). In addition, experimental evidence shows that the presence of rim-based pentagonal rings during the soot formation process by using high resolution atomic force microscopy (HR-AFM) indicates the importance of these pentagon-containing species in soot formation. Many different possible nucleation mechanisms involved these pentagon-containing species have been proposed including the radical chain propagation mechanism which involves pentagon-containing resonantly stabilized radicals (RSRs) (Johansson et al., 2018) and the mechanisms with the combination of π-stacking and covalent bonding nucleation for rim-based pentagonal rings species (Martin et al., 2019). Recently, Pascazio et al. (2020) have proposed a crosslinking reaction mechanism between two peripheral penta-rings to form aromatic penta-linked hydrocarbon (APLH) species by using hybrid density functional theory, while the dynamics process of the dimerization of these species is yet to be elucidated. In the present study, the dimerization processes of different crosslinked polycyclic

aromatic hydrocarbon (PAH) structures (i.e., aromatic penta-linked hydrocarbon (APLH), pericondensed polyaromatic hydrocarbon (PCAH) and aromatic aryl-linked hydrocarbon (AALH) are firstly investigated to obtain atomistic insights for the dynamics and kinetics of the dimerization by using the molecular dynamics (MD) simulation with the reactive force field (ReaxFF).

The collisional association and dissociation processes of each PAH species are investigated under different temperatures, impact parameters and orientations. The lifetime of PAH dimers is quantified to investigate their thermostability. The dissociation of the PAH dimers is also statistically analyzed by the Rice-Ramsperger-Kassel (RRK) theory of unimolecular dissociation to gain a deeper insight of the energy transformation, and the contributions of intermolecular and intramolecular degrees of freedom.

6.2 Numerical Methodology

In the present study, three typical PAH species (i.e., APLH, PCAH and AALH) with similar size but different crosslinked structures are selected for studying their dynamics and kinetics of dimerization process. The structures of these PAH species are shown in Figure 6.1 which are the same PAH structures as those studied by Pascazio et al. (2020).

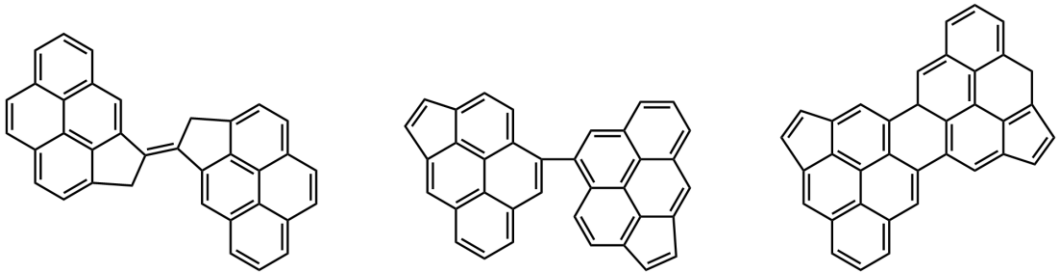

2a 2b 2c

Figure 6.1 Structures of some PAHs considered in the present study: an APLH (2a), an AALH (2b) and a PCAH (2c) (Pascazio et al., 2020).

The interaction energies for these three PAH dimers calculated by the ReaxFF are compared with those calculated by the semi-empirical quantum force of PM3 (Stewart, 1989) and dispersion corrected density function theory (DFT-D3) (Grimme et al., 2010; Grimme et al., 2011) at the B3LYP/def2-TZVP level of theory (Beck, 1993; Weigend et al., 1998; Weigend and Ahlrichs, 2005; Weigend, 2006) which was also used to investigate the $\pi-\pi$ interaction of PAH dimers and the results were found to be close to the benchmark CCSD(T) results in the previous studies of Silva et al. (2016). The intermolecular potential energy versus PAH−PAH center-of-mass (C.O.M.) separation of molecules 2a, ab and 2c are presented in Figures 6.2(a), (b) and (c), respectively. The results show that the ReaxFF provides similar trends and has better accuracy than the PM3 method in comparison with the results of B3LYP-D3/def2-TZVP. Although the binding energy calculated by the ReaxFF has some deviations from the high accuracy DFT method (B3LYP-D3/def2-TZVP), it has been widely accepted and utilized to predict the thermodynamics of PAHs and simulate the association and dissociation of precondensed PAHs (Mao et al., 2017a; Mao et al., 2017b; Keller et al., 2019; Yuan et al., 2019). In addition, ReaxFF has higher computational efficiency than PM3 and B3LYP-D3/def2-TZVP. Therefore, ReaxFF is adequate to investigate the interaction between PAH molecules in

the present study. The binding energy obtain by ReaxFF for 2a, 2b and 2c dimers are –37.98, –32.55 and –39.10 kcal/mol, respectively. In the present study, the DFT calculations are carried out using ORCA package (Neese, 2012) and the MD calculations are performed using the Large-scale Atomic/Molecular Massively Parallel Simulator (LAMMPS) package (Plimpton, 1995). The parameter sets for ReaxFF used in the present study can be found in Appendix**.**

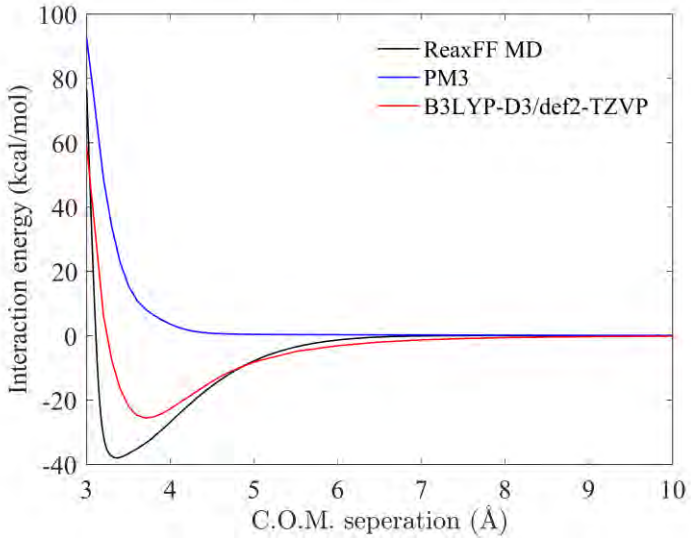

(a) Molecule 2a

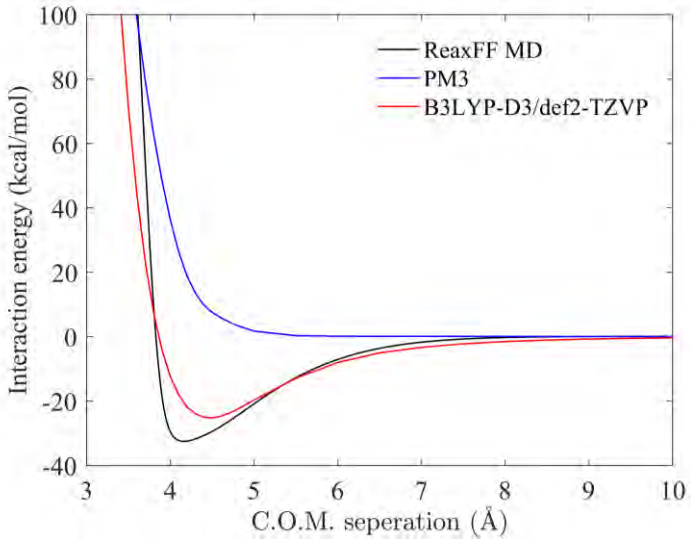

(b) Molecule 2b

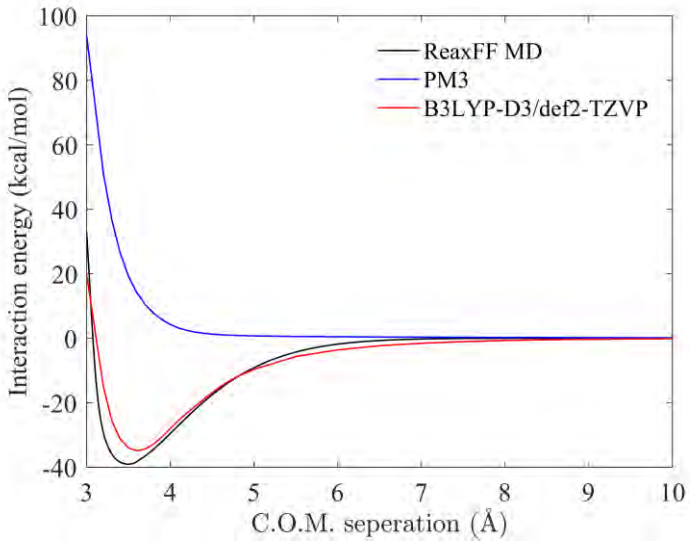

(c) Molecule 2c

Figure 6.2 Comparison of the computed potential energy curves of molecules 2a, 2b and 2c from the ReaxFF MD (van Duin et al., 2001), PM3 (Stewart, 1989) and DFT (B3LYP-D3/def2-TZVP) levels of theory (Weigend and Ahlrichs, 2005; Weigend, 2006).

The initial configurations for the present study are shown in Figure 6.3. Before studying the bimolecular collision of PAHs, two PAH monomers are held with the fixed PAH−PAH C.O.M. separation (L_d) of 30 Å to ensure no interaction between the two molecules. The orientation of the starting molecules is randomly sampled in three axes (Bowal, 2020). Conjugate gradient method is firstly used under the ReaxFF for energy minimization. Then the vibrational equilibrium of each monomer is conducted at the target equilibrium temperature with a MD time step of 0.25 fs by using the Nosé-Hoover thermostat (Evans and Holian, 1985) with a damping factor of 100 time steps. Binary collisions between PAH monomer are then performed in the microcanonical ensemble (NVE) with a MD timestep of 0.25 fs which allows collisions to occur smoothly as used in the previous studies of Mao et al. (2017a) and Mao et al. (2018) The conservation of total energy for all trajectories is always less than 1%. The time evolution of total energy for

a representative trajectory is presented in Figure A1.1 of Appendix. A relative collision energy of 3RT/2 kcal/mol is added to the PAH1 molecule while the rotational velocities are sampled from Maxwellian distributions (Chakraborty et al., 2020). In Figure 6.3, the initial translational and rotational velocities are represented by the black straight and curve arrows, respectively. The different impact parameters (i.e., offset distances of the two PAHs) of the colliding molecules are investigated, ranging from 0 to $4r_g$ where r_g is the radius of gyration of PAH molecule which are equal to 4.86, 4.51 and 4.41 Å of molecules 2a, 2b and 2c, respectively. The initial temperature (T) is typically sampled ranging from 500K to 2000K (Mao et al., 2017a; Chakraborty et al., 2020; Pascazio et al., 2020). A total of 115,500 binary collisions are also performed in the present study in order to reach statistical significance. The trajectories of binary collision is recorded within the total simulation time of 110 ps or is halted when the C.O.M. separation between dissociating PAH molecules exceeds 23 Å (Chakraborty et al., 2020). In the present study, the snapshots of MD results are prepared by visual molecular dynamics (VMD) (Humphrey et al., 1996).

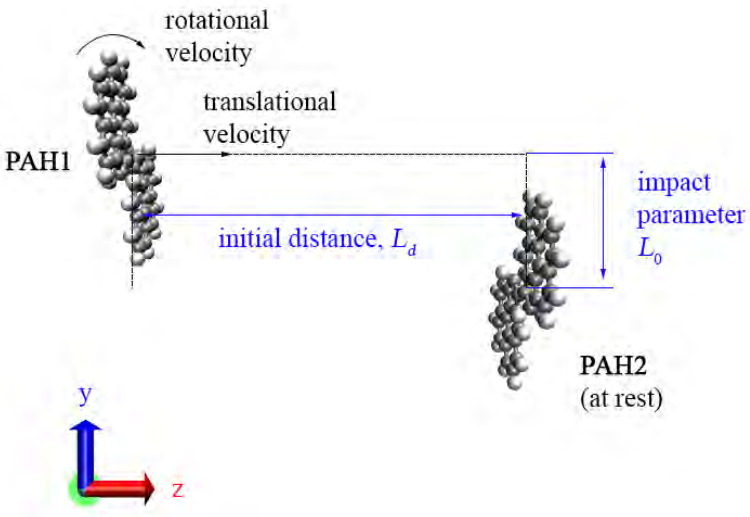

Figure 6.3 The initial configurations of the binary collision events.

6.3 Results and Discussion

6.3.1 PAH + PAH association

The trajectories of binary collisions can be obtained by considering time evolution of the C.O.M. separation between the colliding PAH monomers. These trajectories could be classified into two categories: reactive and nonreactive trajectories as described in Chakraborty et al. (2020). The reactive trajectories resulted in forming PAH dimers while no dimerization behavior is found in nonreactive trajectories. The typical nonreactive and reactive trajectories are shown in Figure 6.4(a) and (b), respectively.

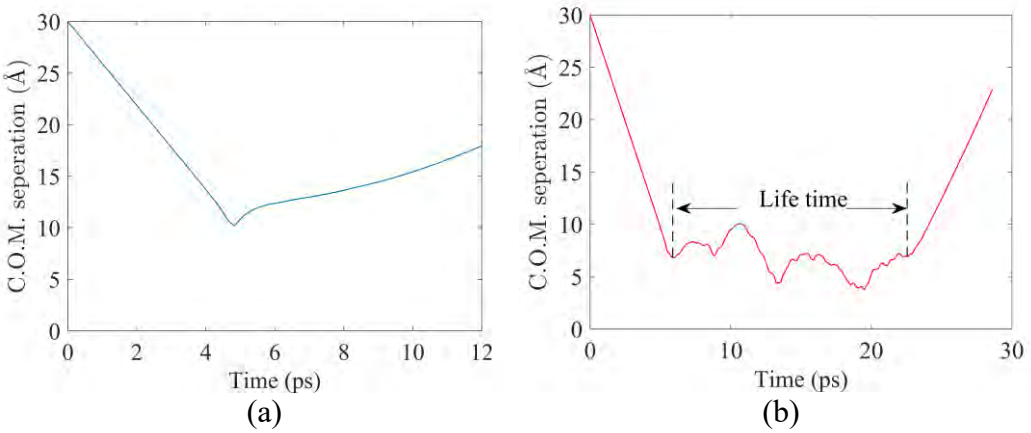

Figure 6.4 Representative (a) nonreactive trajectorie s and (b) reactive trajectories.

In Figure 6.4(a), the colliding PAH monomer (PAH1) comes close to its counterpart (PAH2) for nonreactive trajectory and is then directly scattered off without vibrating with the other PAH molecules. In Figure 6.4(b), the colliding PAH molecule comes close to its counterpart for reactive trajectories, the vibrationally/rotationally excited PAH2* dimer is formed by PAH + PAH association. The interaction between each PAH molecule results in oscillation in C.O.M. separation between the two PAH monomers within a certain lifetime range.

In the present study, the lifetime of dimers is defined as the difference in time between the final and initial turning points in reactive trajectories as shown in Figure 6.4(b). Trajectories having lifetime longer than 1.2 ps were defined as the reactive ones by Chakraborty et al. (2020). The dynamics and kinetics of PAH association and dimers dissociation are investigated and the dynamics and kinetics of 2a molecules association and 2a dimer dissociation are shown in Figure 6.5 as an example.

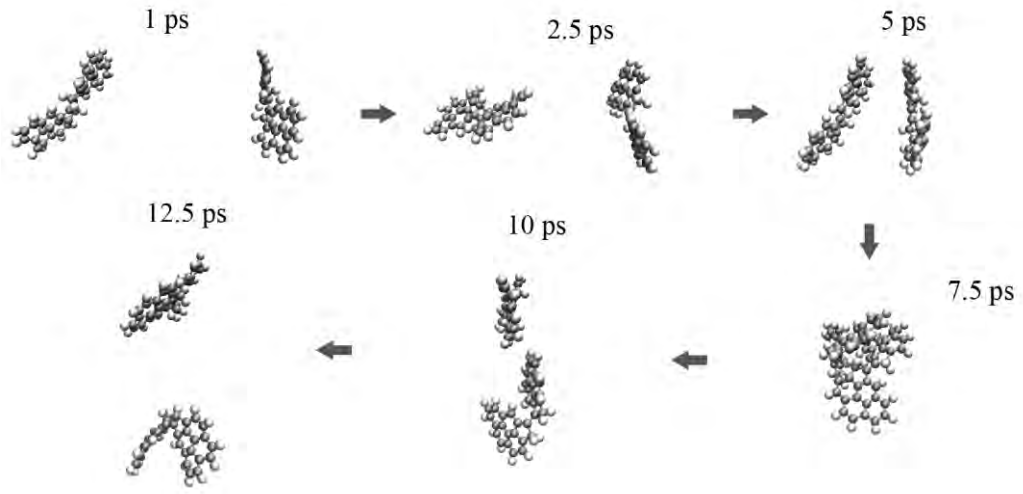

Figure 6.5 The binary collision dynamics of 2a molecules.

The lifetime of each PAH dimer is recorded for the range of temperature and impact parameters. For simplification, only the lifetime distributions of 2a dimers at different temperatures and center-to-center collisions are shown in Figure 6.6 as an example. The lifetime distributions of 2b and 2c dimers from center-to-center collisions can be found in Figures A1.2 and A1.3 of Appendix, respectively. It is clear that most of the binary collisions of 2a molecule result in forming longer life 2a dimers (i.e., the lifetime exceeds 80 ps) at lower temperature (especially at 500 to 1000K). With the increase of the temperature, the overall lifetime of the 2a dimers decreases. At higher temperature (i.e., 1750K and 2000K), almost

none of the dimers can survive over 40 ps. Similar trends can be found for 2b and 2c dimers in Figures A1.2 and A1.3 of Appendix**,** respectively. In addition, the results show that 2c dimers have a longer lifetime when compared with 2a and 2b dimers. The overall results show a negative correlation between the temperature and the lifetime of these PAH dimers.

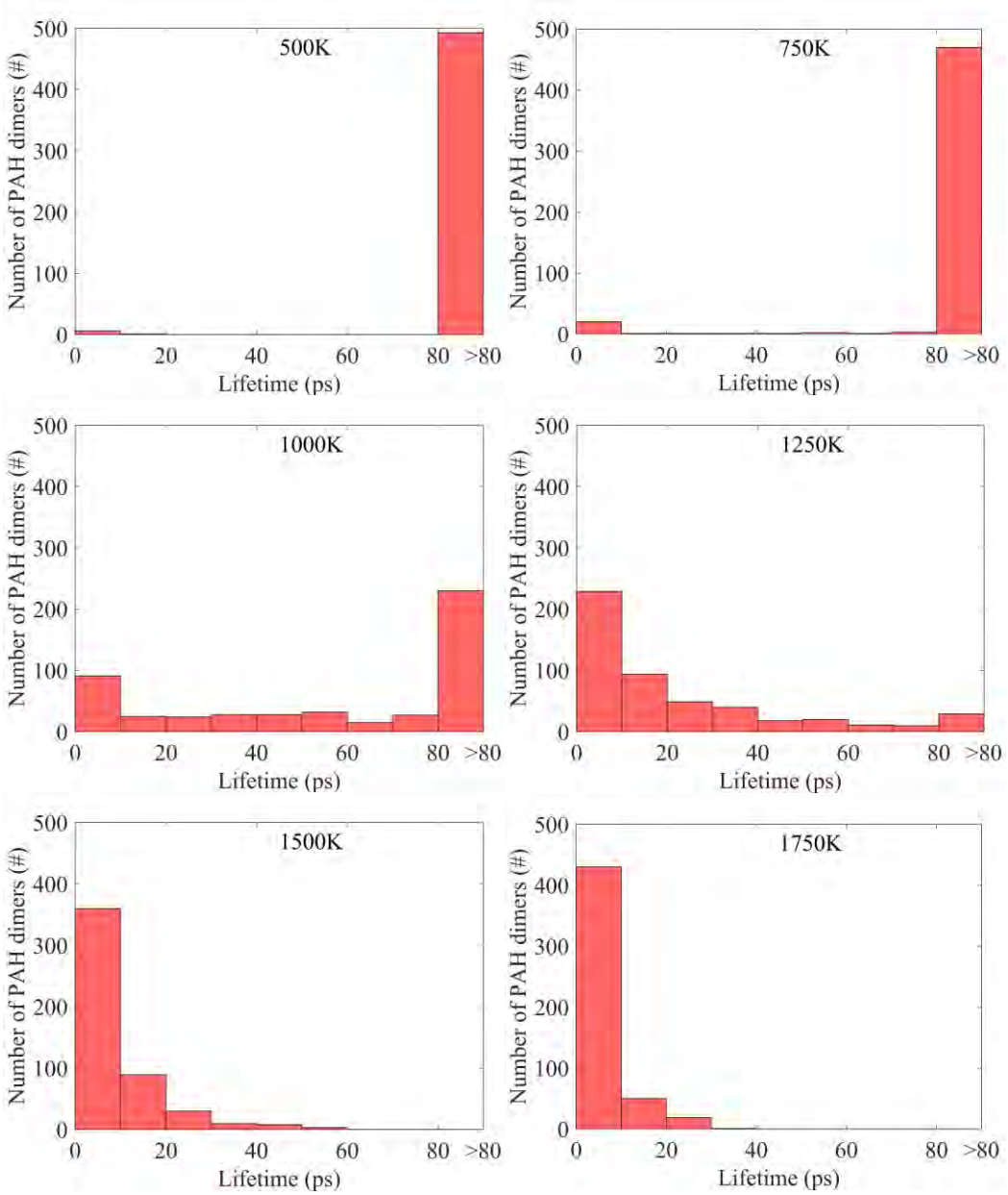

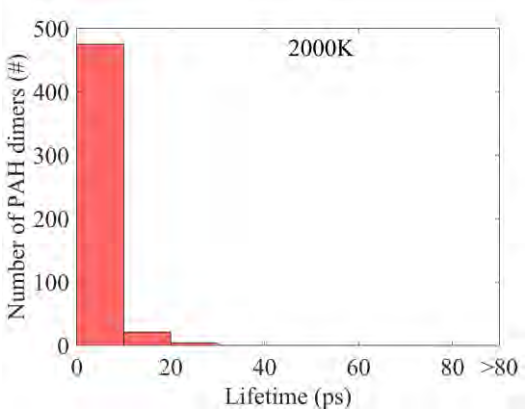

Figure 6.6 Lifetime distributions of the 2a dimers at different temperatures.

In order to study the effects of impact parameters on the lifetime distributions, Figure 6.7 shows the lifetime distributions of 2a dimers formed by collisions at different impact parameters at 1500K as an example. The results clearly show that the lifetime of PAH dimers decreases with increasing impact parameters.

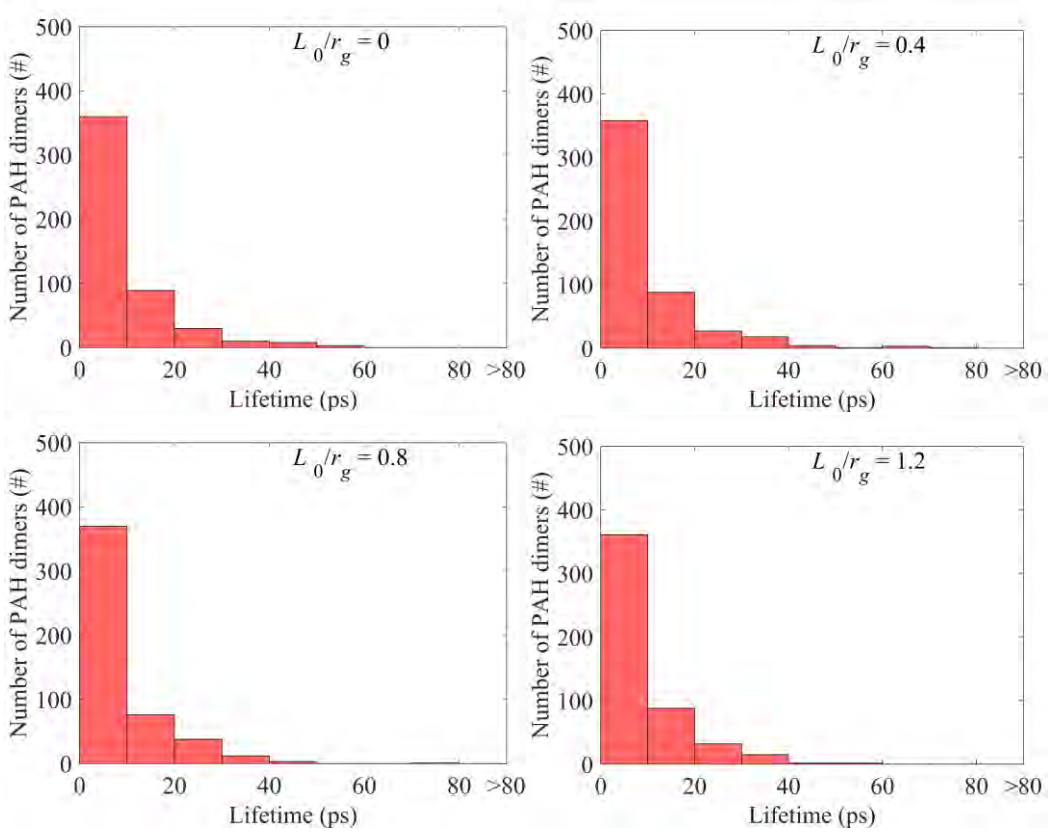

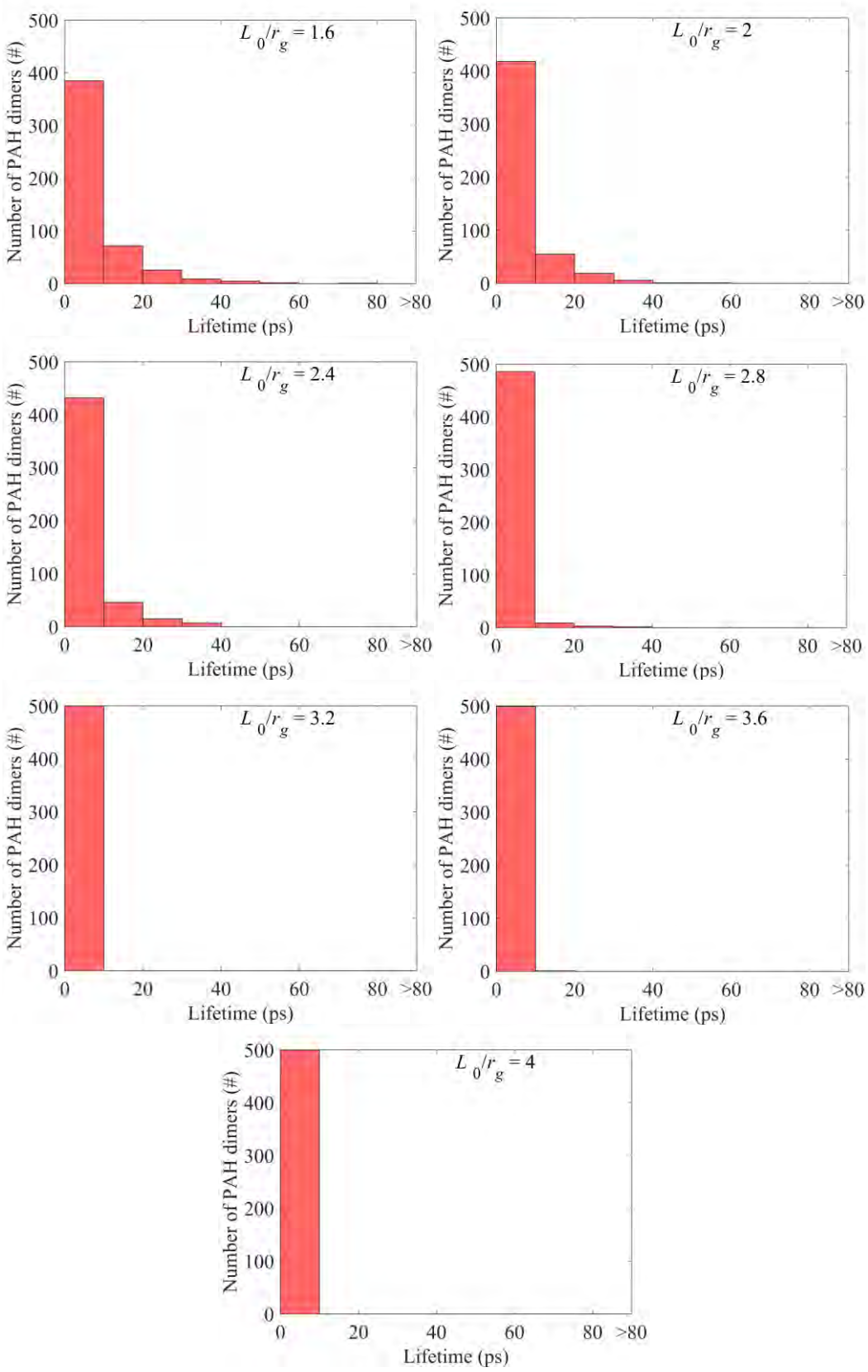

Figure 6.7 Distributions of the number of surviving 2a dimers formed at 1500K at different nondimensional impact parameters (L_0/r_g).

Since not all collisions can successfully form PAH dimers, the association probability ($P(L_0)$) of the dimerization process for PAHs is thus defined as the ratio of the total number of reactive trajectories and total number of trajectories considered (Chakraborty et al., 2020). The association probabilities at different impact parameters and temperatures are shown in Figure 6.8, the mentioned error bars are standard deviations. It is noteworthy that association probability is non-uniform in the ranges of the studied impact parameters. For each temperature, the association probability decreases at the larger impact parameter, and when the nondimensional impact parameter (L_0/r_g) reaches 4.0, the association probability decreases to zero. Furthermore, it also shows that the higher temperature results in lower association probability. This trend is the same as the previous study of PAH clustering behavior (Totton et al., 2012).

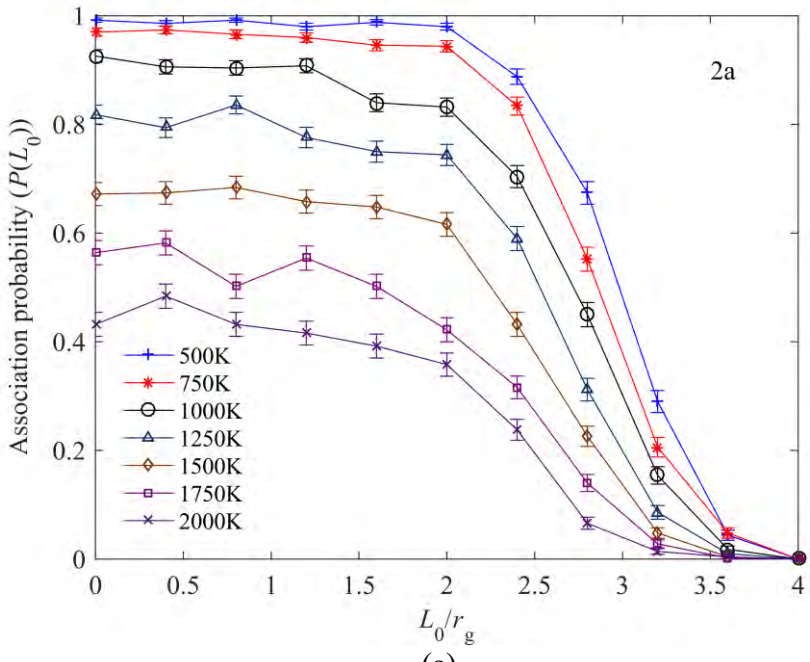

(a)

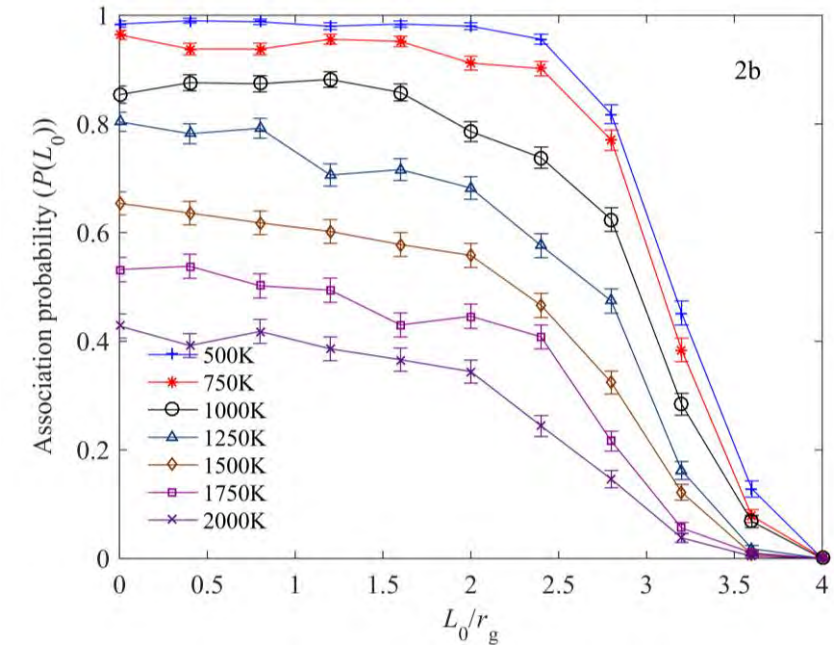

(b)

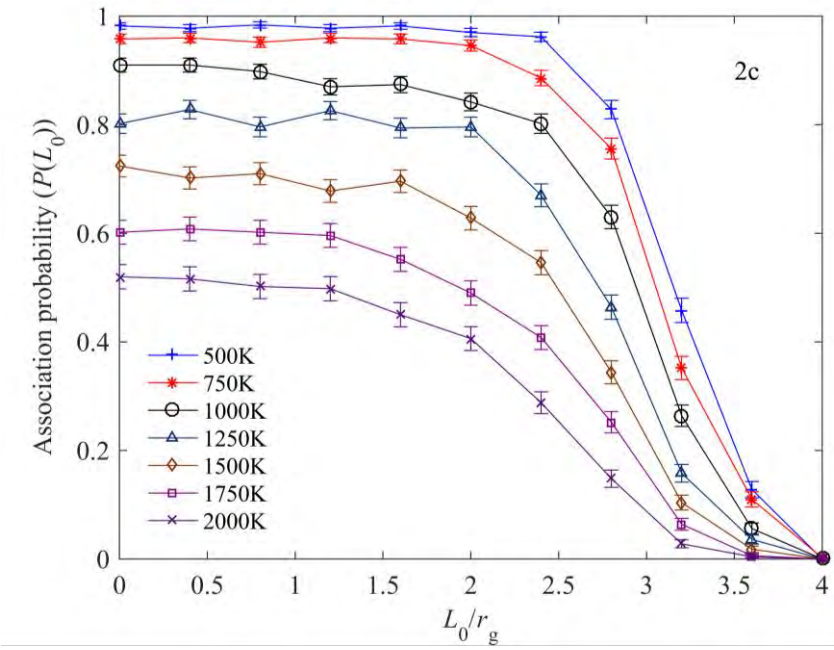

(c)

Figure 6.8 Association probability (P(L_0)) of forming 2a, 2b and 2c dimers at different impact parameters and temperatures.

Following previous chemical dynamics studies (Paul et al., 2015), the association rate constant $k(T)$ with satisfactory precision can be expressed (Chakraborty et al., 2020) as:

$$k(T) \cong \sigma(\bar{E}_{rel})v(\bar{E}_{rel}) \tag{6-1}$$

where σ is the reaction cross section and v is the average relative velocity (Chakraborty et al., 2020). The $v(\bar{E}_{rel})$ can be determined from relative translational energy, 3RT/2 for temperature T (Chakraborty et al., 2020) as:

$$\bar{E}_{rel} = \frac{1}{2}\mu v(\bar{E}_{rel})^2 \tag{6-2}$$

where μ is the reduced mass (Paul et al., 2015). The reaction cross section is obtained by integrating the association probability ($P(L_0)$) over the collision area, $2\pi L_0$ for each impact parameter (Chakraborty et al., 2020) as:

$$\sigma = \int_0^{L_0\,max} [P(L_0)2\pi L_0]dL_0 \tag{6-3}$$

The logarithm of reaction cross sections is computed according to Equation (6-3) are shown in Figure 6.9 where the ln σ is plotted versus temperatures.

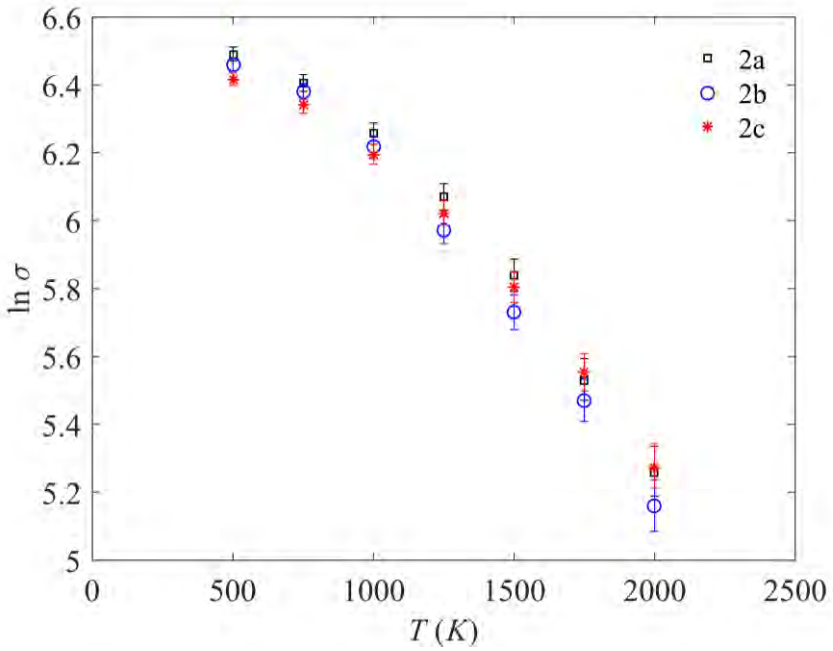

Figure 6.9 Logarithm of reaction cross sections at different temperatures for 2a, 2b and 2c dimerization.

The values of these reaction cross section are listed in Table 6.1, the mentioned error bars are standard deviations. The results show that the logarithm reaction cross section decreases linearly with the increase of the temperature. Such linearity of the reaction cross section can be also found in the previous work of molecule association (Swamy and Hase, 1984). Therefore, the reaction cross section is expressed (Chambers and Thompson, 1995) as:

$$\sigma = a\exp(-bT) \tag{6-4}$$

Table 6.1 Reaction cross section ($Å^2$) for 2a, 2b and 2c at different temperatures

	Temperature						
Species	500 K	750 K	1000 K	1250 K	1500 K	1750 K	2000 K
2a	659.45 ±13.30	605.03 ±14.95	521.38 ±16.41	432.65 ±16.71	343.12 ±16.42	252.29 ±15.42	192.33 ±14.06
2b	638.35 ±11.79	590.47 ±13.63	501.50 ±15.91	392.42 ±15.94	307.30 ±15.72	237.30 ±14.77	173.87 ±13.27
2c	611.71 ±13.40	566.38 ±13.08	490.49 ±14.42	412.74 ±14.83	331.18 ±14.94	257.81 ±14.16	195.47 ±12.82

Then the $k(T)$ is computed according to Equation (6-1). Figure 6.10 shows the results of ln $k(T)$ at different temperatures where the values of $k(T)$ are listed in Table 6.2. It should be pointed out that $k(T)$ represents the microcanonical association rate constant. The results show that apart from the result of 500 K, the association rate constant decreases with increasing temperature, which is due to the competition between decreases of the reaction cross section and the increases of the average relative velocity. Such decreasing trend also can be found in the previous study of pyrene-pyrene dimerization process (Chakraborty et al., 2020). In addition, similar values of association rate constant can be found in 2a, 2b and 2c dimerization

which indicate that there is no significant difference in association between different crosslink structures.

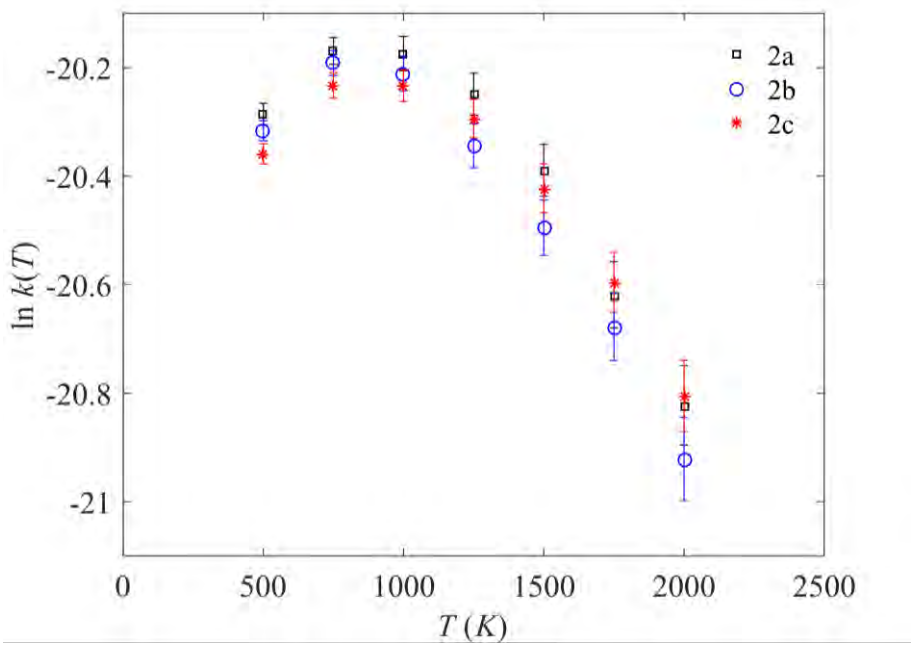

Figure 6.10 Logarithm of k (T) at different temperatures.

Table 6.2 Association rate constants ($\times 10^{-9}$ cm^3/(molecule·sec)) for 2a, 2b and 2c dimerization.

Species	Temperature						
	500 K	750 K	1000 K	1250 K	1500 K	1750 K	2000 K
2a	1.55 ±0.03	1.74 ±0.04	1.73 ±0.05	1.61 ±0.06	1.40 ±0.07	1.11 ±0.07	0.90 ±0.07
2b	1.50 ±0.03	1.70 ±0.04	1.67 ±0.05	1.46 ±0.06	1.26 ±0.06	1.05 ±0.07	0.82 ±0.06
2c	1.44 ±0.03	1.63 ±0.04	1.63 ±0.05	1.54 ±0.06	1.35 ±0.06	1.14 ±0.06	0.92 ±0.06

6.3.2 PAH2* → 2 PAH dissociation

The highly vibrationally/rotationally excited PAH2* dimers are formed due to the binary collisions of two PAH molecules. The total classical energy of

an excited PAH dimer is a sum of the rotational and vibrational components of PAH monomers which are assigned from Maxwellian distributions. The translational energy is the value of 3RT/2 kcal/mol and the association energy is –37.98 kcal/mol for 2a, –32.55 kcal/mol for 2b and –39.10 kcal/mol for 2c, respectively. All of these excited PAH dimers can dissociate because the available energy is greater than the dissociation energy of the dimers. The lifetime of an excited PAH dimer is recorded to start with the dimer formation and end with dimer dissociation. The dissociation probability is thus defined as $N(t)/N(0)$ at different impact parameters and temperatures, where $N(t)$ is the number of surviving PAH dimers at time t and $N(0)$ is the total number of dimers formed. It is worth noting that the $N(t)/N(0)$ can be excellently fitted by a mono-exponential distribution from the previous study of pyrene dimer dissociation in Chakraborty et al. (2020) as:

$$\frac{N(t)}{N(0)} = \exp(-kT) \tag{6-5}$$

Typical $N(t)/N(0)$ of center-to-center collisions ($L_0 = 0$) of 2a molecules from 500 to 2000 K with the exponential fits as shown in Figure 6.11 is taken as an example.

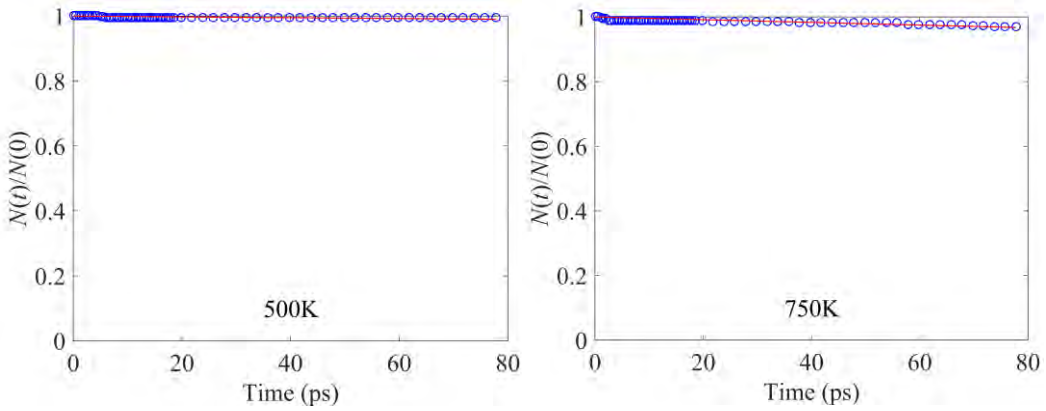

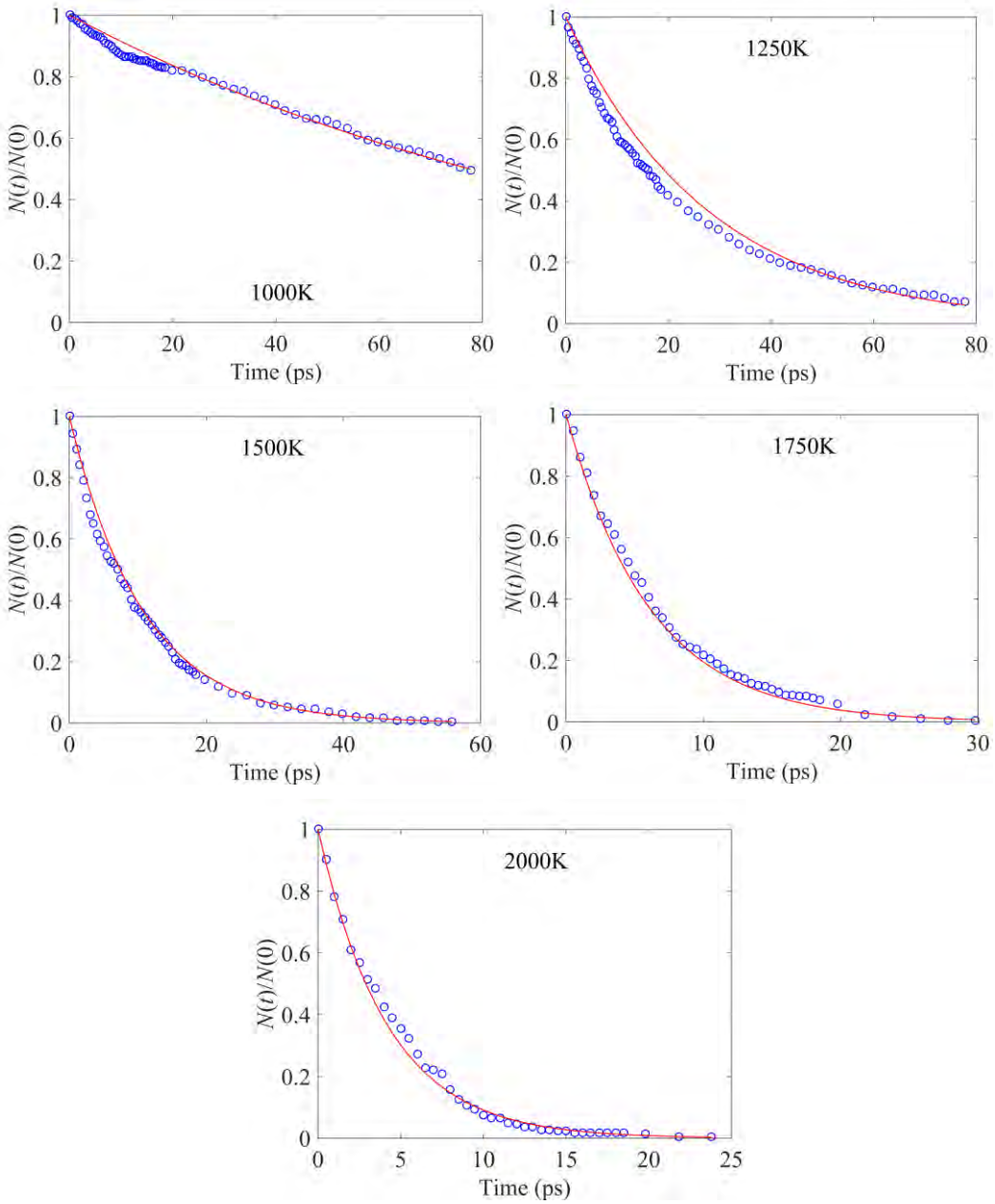

Figure 6.11 Typical $N(t)/N(0)$ and exponential fits for an excited PAH dimer dissociation where the hollow symbols and curves represent the simulation results and the exponential fits (in Equation 6-5), respectively.

The results in Figure 6.11 show that $N(t)$ decays exponentially which is in accordance with the RRKM theory of unimolecular kinetics (Bunker and Hase, 1973), indicating that the relaxation time of intramolecular vibrational energy redistribution (IVR) is shorter when compared to the time scale of dimerization

(Hase, 1986). However, the abovementioned study only shows the temperature on the dissociation probability. For accounting the effects of impact parameter, the mean number of PAH dimers, $\bar{n}_{\text{dimer}}(T, t)$ at each temperature and lifetime is defined (Mao et al., 2017a) as:

$$\bar{n}_{\text{dimer}}(T,t)=\frac{\int_0^{L_{0\max}}[n_{\text{dimer}}(T,t,L_0)\times 2\pi L_0]dL_0}{\pi L_{0\max}^2} \tag{6-6}$$

where $n_{\text{dimer}}(T, t, L_0)$ is the number of surviving PAH dimers at temperature T, impact parameter L_0, and lifetime t. The mean percentage of dimerization (i.e., $n_{\text{dimer}}(T, t)/\ \bar{n}_{\text{dimer}}(T,0)$) of different survival lifetime are shown in Figure. 6.12. The dissociation rate constants in Equation (6-5) are also listed in Table 6.3.

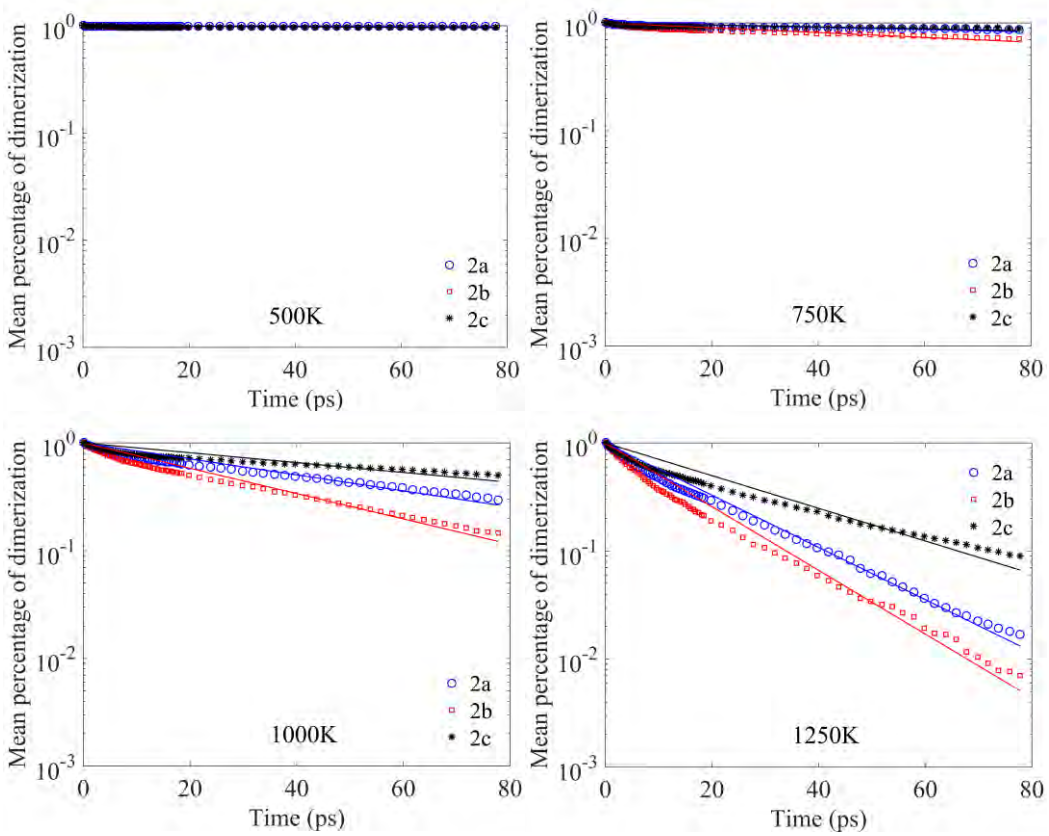

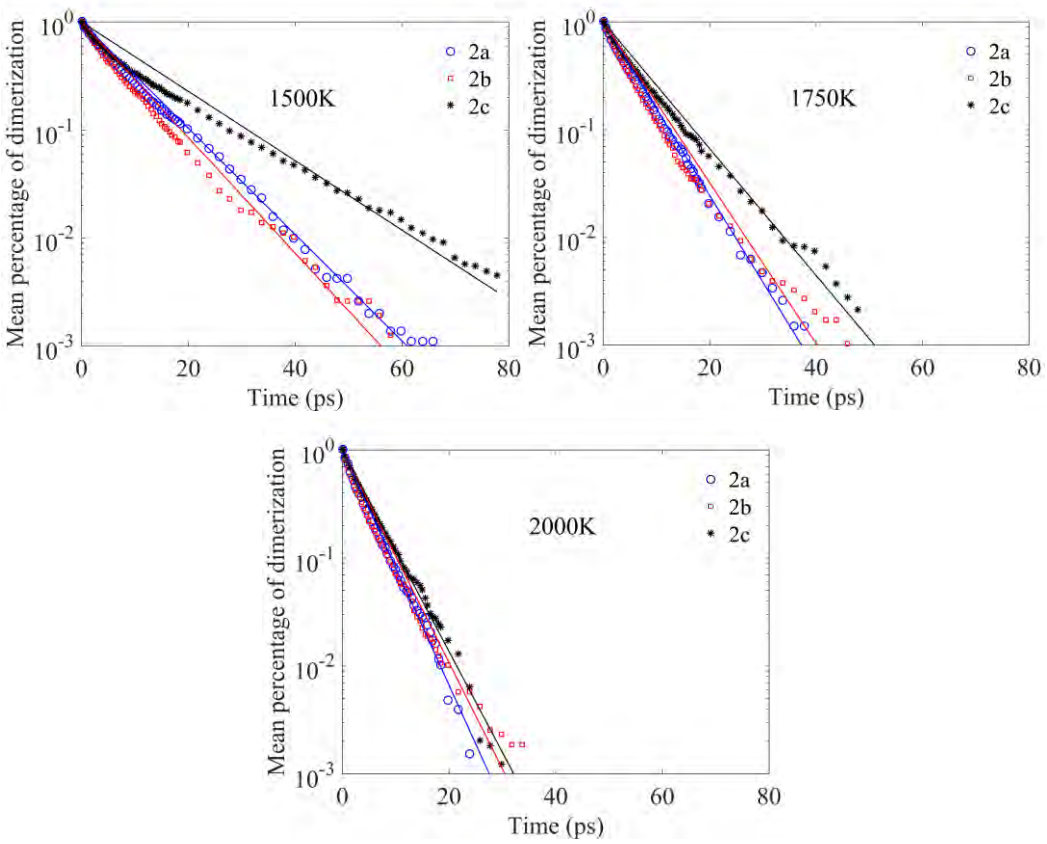

Figure 6.12 Mean percentage of dimerization and exponential fits for an excited PAH dimer dissociation where the hollow and solid symbols, and line represent the simulation results and the exponential fits (in Equation 6-5), respectively.

Table 6.3 Rate constants (ps^{-1}) for PAH2* → 2 PAH dissociation for the exponential fits to $\bar{n}_{dimer}(T, t)/\ \bar{n}_{dimer}(T,0)$.

Species	Temperature						
	500 K	750 K	1000 K	1250 K	1500 K	1750 K	2000 K
2a	3.71×10^{-4}	2.40×10^{-3}	1.71×10^{-2}	5.57×10^{-2}	1.13×10^{-1}	1.85×10^{-1}	2.51×10^{-1}
2b	5.70×10^{-4}	5.16×10^{-3}	2.71×10^{-2}	6.79×10^{-2}	1.23×10^{-1}	1.72×10^{-1}	2.27×10^{-1}
2c	5.30×10^{-4}	2.10×10^{-3}	1.05×10^{-2}	3.48×10^{-2}	7.40×10^{-2}	1.36×10^{-1}	2.15×10^{-1}

Figure 6.12 shows that dissociation rate constants increase when increasing the temperature because the higher initial vibrational and rotational energies are available for PAH2* at higher temperature, which makes PAH2* more prone to

dissociate. In the lower temperature range (i.e., 500K−1250K), 2c dimers show the lowest dissociation rate constant as they have the highest association energy (−39.10 kcal/mol) while 2b dimers show the lowest dissociation rate constant as they have the lowest association energy (−32.55 kcal/mol). These findings are in accordance with the results of previous free energy profile where 2a and 2c dimers bind more strongly than 2b dimers despite the all three being of similar sizes in the temperature range of 500K–1000K in the metadynamic study of Pascazio et al. (2020). However, the discrepancy of dissociation rate constants between different PAH structures is minor in the higher temperature range (i.e., 1750K to 2000K). This can be explained that the rotational and translational energy (3/2RT + 3/2RT) of PAHs are relatively low when compared with their binding energy at the lower temperature. Hence, the dissociation rate constant is mainly affected by the binding energy. The rotational and translational energy of PAHs are higher than the binding energy when the temperature is increased, thus the contribution of binding energy in dissociation rate constant is negligible. These findings support that PCAH dimers have higher thermodynamic stability when compared with APLH and AALH dimers. The previous study of Elvati et al. (2019) showed that only the PAH with size larger than circumcoronene can form sufficient long lifetime dimers under flame condition. However, the concentration of large PAHs is too low to account for the observed soot particles (Wang, 2011). Thus, the physical dimerization of these crosslinked structures is unlikely to play a major role, suggesting that other pathways are needed.

In order to obtain the contribution from different degrees of freedom in this unimolecular dissociation reaction, a statistical analysis based on RRK theory is

performed (Chakraborty et al., 2020). The expression describing the rate constant for a unimolecular reaction by RRK theory (Baer et al., 1996) is:

$$k(E) = v(\frac{E(T) - E_0}{E(T)})^{s-1} \tag{6-7}$$

where v, E_0 and s are the frequency factor, unimolecular threshold energy, and number of degrees of freedom, respectively (Chakraborty et al., 2020). The Equation (6-7) is found from the classical harmonic limit of RRKM theory (Baer et al., 1996). The microcanonical rate constant is calculated as a function of energy because simulation of dimerization is performed in the NVE with fixed total energy. It can be found in the snapshot that extensive intermolecular rotational and translational motions take place in the excited PAH dimer. To quantify the contribution of rotational and translational degrees of freedom in this dissociation reaction, only three rotational and three translational intermolecular degrees of freedom take part in the dissociation of dimers at the first stage (Chakraborty et al., 2020). For fitting the computed dissociation rate constant with the Equation (6-7), the total energy E (Chakraborty et al., 2020) is then given as:

$$E(T) = \frac{3}{2}RT + \frac{3}{2}RT + E_0 \tag{6-8}$$

where the term 3/2RT represents the contribution from the average translational and rotational energy terms. The E_0 is the unimolecular threshold with the value of binding energy used from the present study. Table 6.4 and Figure 6.13 show the results of fitting to Equation (6-7).

Table 6.4 RRK Parameters v (ps^{-1}) and s with least-squares regression coefficient r for RRK fits to $k(E)$ with the Equation (6-7) with the contributions from translational and rotational degrees of freedom.

	Fitting Parameters		
Species	v	s	r
2a	1290	6.73	0.994
2b	331	6.24	0.991
2c	463	6.25	0.997

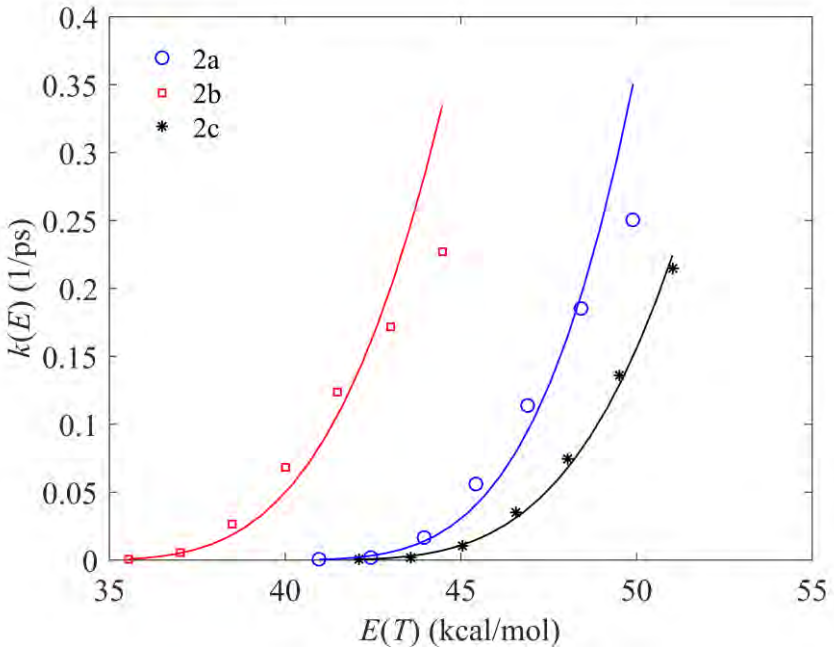

Figure 6.13 Microcanonical rate constants ($k(E)$) and the curve fittings to RRK in Equation (6-7).

It is clear that the microcanonical rate constants can be well represented by the RRK equation as shown in Figure 6.13. In the present study, the value of s for PAH dissociation is considered to be six which includes three rotational and three translational degrees of freedom. From Table 6.4, the results are close to the number degrees of freedom which indicate that translation and rotation modes are closely coupled to the reaction coordinate and readily exchange energy with it (Schranz et al., 1991). Thus, translation and rotation modes play a major role in

dimer dissociation process. However, the molecular dynamics study of collisional association and dissociation of pyrene dimers from Schuetz and Frenklach (2002) suggested that some amount of energy from the intermolecular modes can be absorbed and trapped during the process of pyrene dimer formation, and then transferred into the rotational and vibrational modes of the molecules. Similar conclusion has also recently been confirmed by the statistical analysis by Chakraborty et al. (2020). Following their studies, it is assumed that the intramolecular vibrational modes also participate in the dissociation of PAH2* dimers in the present study (Chakraborty et al., 2020). To evaluate the contributions from the intermolecular and intramolecular vibrational modes, the total energy E is further expressed as (Chakraborty et al., 2020)

$$E(T) = sRT + E_0 \tag{6-9}$$

Similar RRK fit is then performed, with the s of $3N - 6$ where N is the number of atoms (including $3N - 12$ intramolecular vibrational modes and 6 intermolecular vibrational modes). In the present study, the s values for 2a, 2b and 2c dimers are 330, 318 and 318, respectively. Table 6.5 and Figure 6.14 show the results of fitting parameters in Equation (6-7).

Table 6.5 RRK Parameters v (1/ps) and s with least-squares regression coefficient r for RRK fits to $k(E)$ in Equation (6-7) with the contributions from translational, rotational and vibrational degrees of freedom.

	Fitting Parameters		
Species	v	s	r
2a	2.40	84.93	0.990
2b	1.95	85.65	0.998
2c	1.25	72.50	0.977

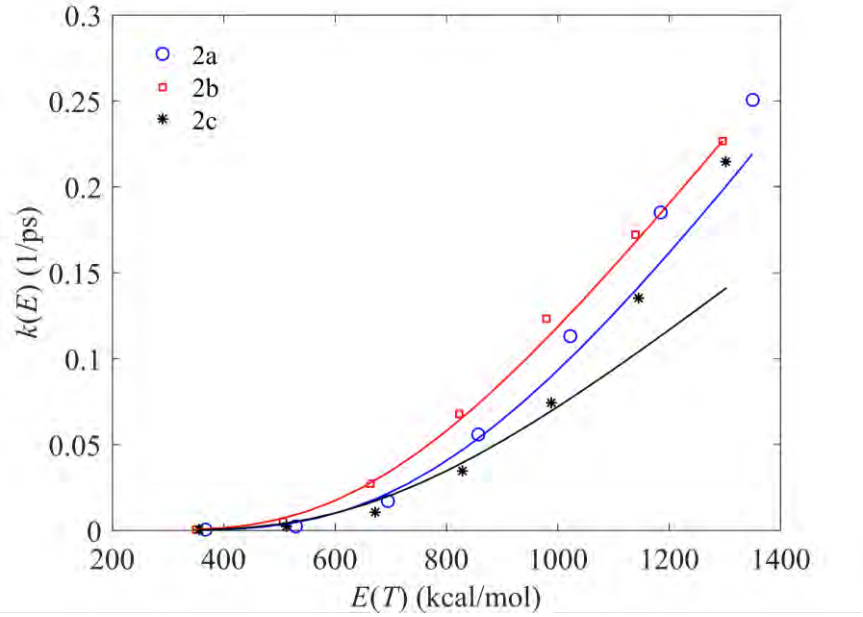

Figure 6.14 Microcanonical rate constants ($k(E)$) and the curve fittings to RRK in Equation (6-7).

A well-fitted microcanonical rate constant by Equation (6-7) can be observed in Figure 6.14, which confirms that the PAH2* dimer dissociation can be well described by the RRK theory (Chakraborty et al., 2020). However, the fitting with RRK harmonic unimolecular rate constant equation shows smaller values for s than the reactant's number of vibrational degrees of freedom, that is, $3N$–6. Such underestimation also can be found in the previous unimolecular dissociation studies by RRK theory (Schranz et al., 1991; Chambers and Thompson, 1995) which suggests that many of the vibrational modes are not strongly coupled to the reaction coordinates (Schranz et al., 1991). In the present numerical simulation, energy transfer between intramolecular and intermolecular degrees of freedom would be expected to be more restricted while the intramolecular vibrational modes only partially participate in the rapid intramolecular vibrational energy redistribution (IVR) process.

6.4 Summary

In the present study, the association and dissociation kinetics of crosslinked polycyclic aromatic hydrocarbon (PAH) dimerization by molecular dynamics simulation with ReaxFF are investigated. The ReaxFF shows that the PAH−PAH interaction can be well described by comparing with B3LYP-D3/def2-TZVP levels of theory. The binary collision of PAH monomers is then performed in microcanonical ensembles at different initial temperatures and impact parameters. In PAH association process, the association probability, reaction cross section and association rate constant are well quantified. The microcanonical association rate constant is found to decrease with increasing temperature in the higher temperature range (i.e., 1750 to 2000K). Among all the species in collisional association processes, no significant differences are found. It reveals that there is no significant difference in association process for different crosslink structures with similar size. Considering the PAH dimers dissociation, the higher dissociation rate constant is obtained for PAH dimers with lower binding energy in the lower temperature range (i.e., 500K to 1250K). However, minor discrepancy of dissociation rate constants between different PAH structures is found due to the negligible contribution from the binding energy in the higher temperature range (i.e., 1750K to 2000K). In addition, the results of PAH association and dissociation processes, and the short lifetime (almost none of dimers can survive over 40 ps at 1750K to 2000K) support that physical dimerization of PAHs is unlikely to play a major role in soot formation under typical combustion conditions.

The dissociation of highly excited PAH dimers is further studied. The excited PAH dimers are formed due to the binary collision of PAH monomers, then

the energy transfer also occurs between the intermolecular and intramolecular vibrational modes. The exponential decay of PAH dimers in accordance with Rice–Ramsperger–Kassel–Marcus (RRKM) theory of unimolecular dissociation suggests that the rapid intramolecular vibrational energy redistribution (IVR) takes place. In addition, the contributions of dimer dissociation from different degrees of freedom are obtained by the RRK unimolecular reaction theory. The intermolecular rotational and translational models are closely coupled to the reaction coordinates and play an important role in the PAH dimer dissociation process while intramolecular vibrational modes only partially participate in the rapid IVR process.

Chapter 7 Soot Formation and Evolution by ReaxFF MD Simulations

7.1 Introduction

The physical dimerization of crosslinked polycyclic aromatic hydrocarbons (PAHs) is investigated in detail by using the reactive force field (ReaxFF) molecular dynamics (MD) simulations in Chapter 6. However, soot formation and evolution involve complex physical and chemical processes. The theoretical and experimental results show that the formation of soot particles is unlikely to occur only through the physical pathways (Elvati and Violi, 2013; Martin et al., 2022). In the present study, the formation and evolution of soot particles are investigated by using ReaxFF MD simulations. Both physical and chemical processes in the transformation from PAHs to the soot nanoparticles are revealed in the ethylene flames. In addition to considering the importance of carbon dioxide addition in the advanced combustion technology (i.e., exhaust gas recirculation (EGR) in engines, flue gas recirculation (FGR) in furnaces/boilers) and oxy-fuel combustion (Qureshi et al., 2021; Serrano et al., 2021), the effects of carbon dioxide addition on the soot formation and evolution have received much research attention (Tang et al., 2016; Wu et al., 2019; Wang et al., 2021b). The chemical effects of the carbon dioxide addition on the soot formation and evolution pathways needs to be further investigated.

Several important PAH species are extracted from the ethylene flames. The transformation starting from the PAH and small-molecule species to the final soot nanoparticle is studied for different high temperatures and carbon dioxide additions. Three stages of soot formation and evolution processes including nucleation, surface growth and coagulation, and graphitization are investigated.

The chemical effects of the carbon dioxide addition on the soot properties and reaction pathways are also analyzed.

7.2 Numerical Methodology

7.2.1 PAH precursor selection

The previous mass-resolved studies demonstrated the importance of pyrene and similar-sized PAHs as the soot precursors because the mass range 200–400 u always showed high intensity normally by aerosol mass spectrometer (Dobbins et al., 1998; Faccinetto et al., 2011; Maricq, 2011; Shariatmadar et al., 2022). Most of the previous ReaxFF MD studies of soot formation often consider several widely recognized single components (Mao et al., 2017b; Shabnam et al., 2019). In order to provide a closer soot precursor composition pool as the real flame conditions, the composition of soot precursors is extracted from the chemical kinetic simulation of premixed ethylene–oxygen–argon flames from Abid et al. (2008). The boundary conditions of the numerical simulation used are the same as their experimental setup (C_2H_4: 16.3%, O_2: 23.7%, Ar: 60%) (Jiang and Chan, 2021b). As the soot nucleation is a dominant process at lower height above burner (HAB) (Hou et al., 2019; Liu et al., 2019a), the species composition of flame no. C3 with the inlet boundary condition of velocity of 8.0 cm/s at HAB= 0.25 cm is extracted to investigate soot formation process in the present study. The species profiles are obtained by Sandia 1-D PREMIX code (Kee et al., 1986) calculation. The detailed chemical kinetic mechanism of KAUST Mech 2 (KM2) is also used as it focuses on C1–C4 hydrocarbon fuels and describes in a detailed way the PAH chemistry up to coronene (Wang et al., 2013; Wang et al., 2015; Valencia et al., 2021). The proposed

KM2 mechanism (Wang et al., 2013; Wang et al., 2015) has already been validated in the premixed flames (Wang et al., 2013; Dasappa and Camacho, 2021) and counterflow flames (Wang et al., 2015; Kalbhor and van Oijen, 2020). The results show that the PAH concentration profiles can be well predicted in the detailed chemical kinetic mechanism. There are several newly developed mechanisms based on KM2 mechanism to predict the formation of PAH precursor and have also been fully validated in the experimental studies (Park et al., 2015; Selvaraj et al., 2016; Dasappa and Camacho, 2021).

In the present study, only the aromatic compounds with four or more rings are extracted from the chemical kinetic calculation as the soot precursor composition pool of ReaxFF MD simulation to ensure the presence of pyrene and similar-sized PAHs, of which their important role in soot inception experiments have been suggested (Schuetz and Frenklach, 2002; Zhao et al., 2005a; Mouton et al., 2015; Do et al., 2021). The KM2 mechanism is used in the chemical kinetic calculations because it can provide accurate results of large PAHs concentration. All the considered PAH molecules are listed in Figure 7.1. These PAHs show some structures (i.e., aliphatic side chains, five membered rings, and radicals) which may contribute to the PAHs interaction and bond formation (Norinaga et al., 2009; Bagley and Wornat, 2011; Ono et al., 2015; Shi et al., 2021).

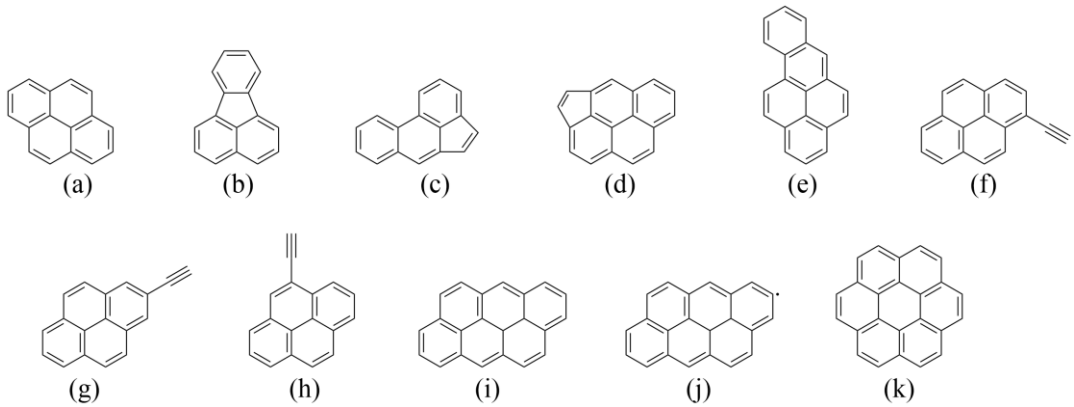

Figure 7.1 Consideration of PAH molecules for the ReaxFF MD simulations: (a) pyrene, (b) fluoranthene, (c) ace-phenanthrene, (d) cyclopenta[cd]pyrene, (e) benzo[a]pyrene, (f) 1-ethynyl pyrene, (g) 2-ethynyl pyrene, (h) 4-ethynyl pyrene, (i) anthanthrene, (j) 2-anthanthrenyl radical and (k) coronene.

The present ReaxFF MD simulation box contains a total of 50 numbers of PAH molecules as it is suitable for rapid MD simulation for the present simulated system. The number of PAH molecules of each species can be obtained by the results of chemical kinetic calculation of each PAH species distribution. In addition, the soot formation and evolution processes are complex which are also affected by the small molecule species (Yuan et al., 2019), In the present study, the small-molecule species of acetylene, H and OH radicals are also selected to include in the MD simulation box by considering their important contribution to the soot formation and oxidation, which is similar to the previous study (Yuan et al., 2019; Zhao et al., 2020). Different numbers of CO_2 molecules are added to the reactive system to investigate the effects of CO_2 on the formation and evolution of incipient soot nanoparticles. The simulation conditions of simulated system are listed in Table 7.1.

Table 7.1 The initial conditions of the present MD simulations.

PAH molecule species	Small molecule species	Additive (# CO_2)	Temperature (K)	Initial density (g/cm^3)
1# pyrene,	30# C_2H_2,	0 *	3000	0.2
1# fluoranthene,	20# OH,	30 *		
6# ace-phenanthrene,	20# H	45 *		
16# cyclopenta[cd]pyrene,		60 *		
1# benzo[a]pyrene,		90 *		
1# 1-ethynyl pyrene,		180 *		
1# 2-ethynyl pyrene,		210		
1# 4-ethynyl pyrene,		270 *		
15# anthanthrene,		300		
1# 2-anthanthrenyl,		360		
6# coronene		540		

*: number of additive molecules referred from (Zhao et al., 2020).

7.2.2 Simulation setup

The present ReaxFF MD simulation is conducted under the canonical ensemble (i.e., the NVT ensemble) (Allen and Tildesley, 2017). The energy minimization and equilibration of the simulated system are firstly conducted at 5 K. After the equilibration, the ReaxFF MD simulations are performed for 1 ns (i.e., 1000 ps) at 3000 K. The time step of 0.1 fs is applied to the equilibrium process and NVT MD simulations which allows molecular collisions to occur smoothly as used in the previous studies of Yuan et al. (2019). The temperature of simulated system is controlled using a Nose-Hoover thermostat algorithm (Evans and Holian, 1985) with a damping constant of 10 fs. The present ReaxFF simulations are also conducted at higher density (i.e., 0.2 g/cm^3) and temperature (i.e., 3000K) which is a common strategy (Chenoweth et al., 2008; Castro-Marcano et al., 2012; Wang et al., 2021a) in the accelerated ReaxFF-MD simulations because the time scales of MD simulations (~nanoseconds) are orders of magnitude lower than the time scale of soot formation (~milliseconds) obtained from the experimental

results (Shabnam et al., 2019). In addition, each simulated case is performed with three repetitions and the MD simulation results are obtained from the average values of all three repetitions to reduce the statistical noise. The ReaxFF MD simulation is performed by the commonly large-scale atom/molecule parallel simulator (LAMMPS) package (Plimpton, 1995). The chemical reaction pathways are analyzed by the Chemical Trajectory Analyzer (ChemTraYzer) scripts (Döntgen et al., 2015). The visualization of simulation results is carried out using Visual Molecular Dynamics (VMD) software (Humphrey et al., 1996).

7.3 Results and Discussion

7.3.1 Incipient soot formation

The initial conditions for different CO_2 additions at 3000K are listed in Table 7.1. The time evolutions of the simulated system for zero CO_2 case are shown in Figures 7.2(a) to (i).

In Figure 7.2(i) at 1000 ps, these four clusters actually represent a whole cluster which is the same as a large cluster in the MD box center because the MD simulations are performed with the periodic boundary conditions. In Figure 7.2(a), the system starts with several PAH molecules and some small molecule species. Followed by a series of chemical reactions between these PAHs and small hydrocarbon (HC) species, the PAH clusters with cross-linked structure are formed as shown in Figures 7.2(b) and (c). Further chemical reactions with the coagulation and graphitization are taken place. The soot nanoparticle is finally formed and then the soot structure is transformed to fullerene-like (in Figure 7.2 (i)). The results show

the overall evolution of gas-phase molecules to a nascent soot nanoparticle at 3000 K in 1 ns.

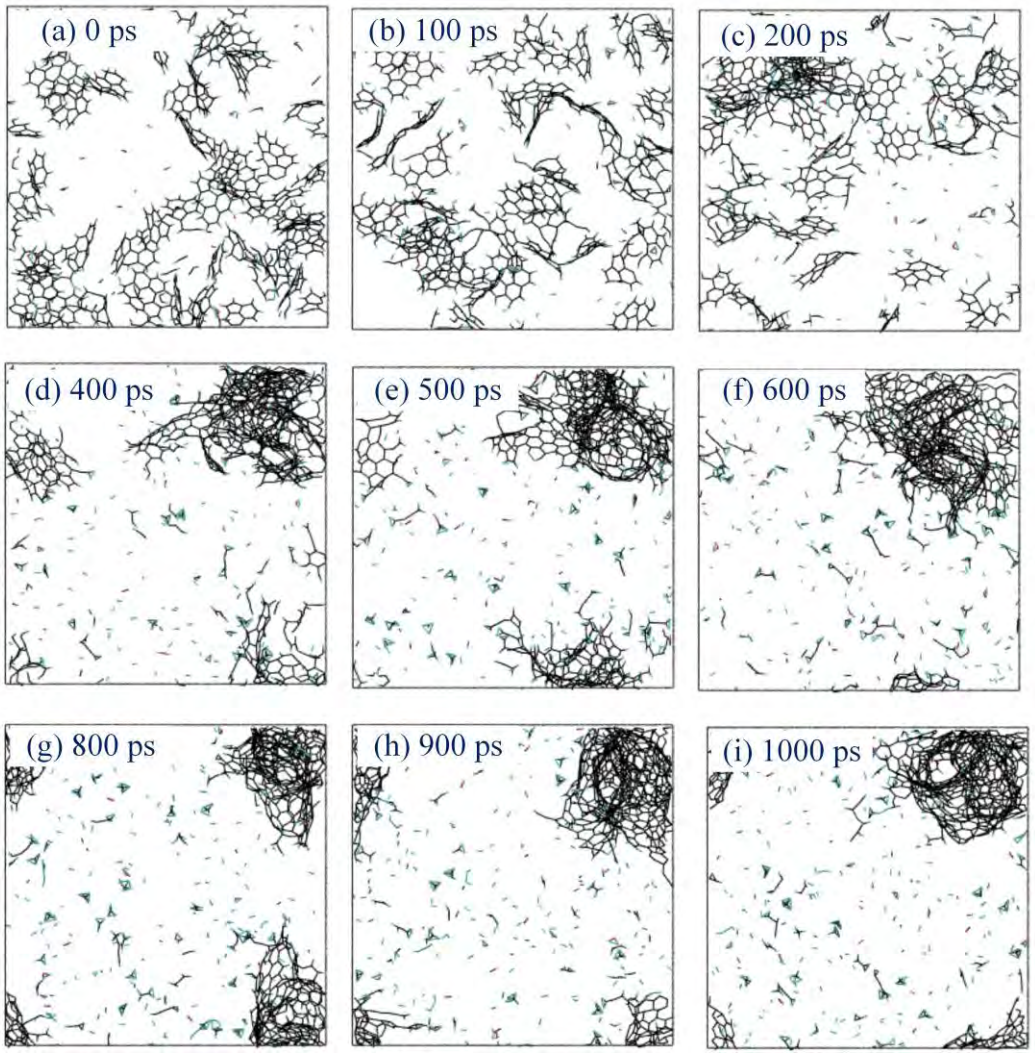

Figure 7.2 The evolution of PAHs and soot particles in the reactive system for zero carbon dioxide case at 3000 K.

To further investigate the formation and evolution processes of soot nanoparticle, it is assumed that the molecule with the maximal carbon atoms is the largest soot nanoparticle in the simulated system for statistical convenience (Zhao et al., 2020). Figure 7.3 shows the time evolution of number of carbon atoms and H/C ratio of the largest soot particle in the simulated system. The results show that the C atom number increases rapidly until it reaches the peak at around 400 ps

and then it remains in a stable condition. On the other hand, a rapid decrease of H/C ratio can be found until it gradually drops to 0.1.

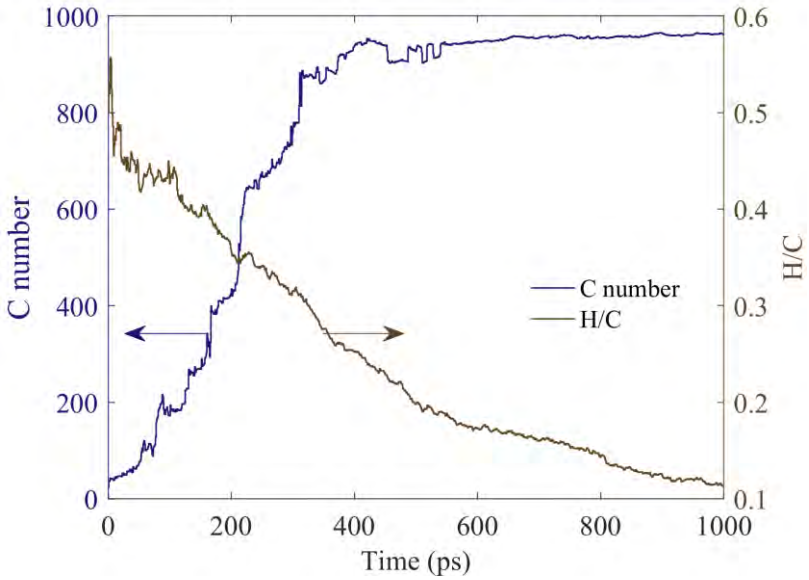

Figure 7.3 The evolution of C atom number and the H/C ratio for the largest soot nanoparticle at 3000 K.

To study the time evolution of the number density and mass fraction of soot nanoparticles, the incipient soot nanoparticles are regarded as the molecules with the number of carbon atoms exceeds 32. It is because the number of carbon atoms of smallest PAH (pyrene) in the simulated system is 16 and the dimerization of pyrene leads to the inception of soot nanoparticles. The assumptions and statistical method are similar to the previous study in (Zhao et al., 2020) of which the reasonable results of number density and mass fraction of initial soot nanoparticles are obtained. Then, the mass fraction is defined as the ratio of the mass of soot nanoparticles which are regarded as the molecules with the number of carbon atoms exceeds 32 to the total mass of molecules in the simulated systems, and the number density of soot nanoparticles is calculated based on the ratio of the number of soot nanoparticles to the soot volume of the MD simulation box

(Zhao et al., 2020). The results of number density and mass fraction of soot nanoparticles are shown in Figure 7.4. The soot number density in the simulated system rapidly increases to the peak at around 150 ps, then rapidly decreases to 0.01 #/nm^3 (i.e., the system only contains one soot nanoparticle) at around 400 ps and remains in a stable condition. The mass fraction of soot nanoparticles increases rapidly until it reaches the peak and remains in a stable condition.

From Figures 7.3 and 7.4 of the time evolution of soot nanoparticle properties, the formation and evolution processes of soot nanoparticle can be approximately divided into three stages. In the first stage (i.e., 0 to 150 ps), both the number density and mass fraction of soot nanoparticles increase rapidly due to the dimerization and mass growth of PAHs (Zhao et al., 2020). In the second stage (i.e., 150 to 400 ps), the mass fraction of soot nanoparticles continuously increases to the peak while the number density of soot nanoparticles decreases because of the coagulation and surface reaction of soot nanoparticles are taken place. In the third stage (i.e., 400 to 1000 ps), the number density of soot nanoparticles decreases to 0.01 #/nm^3 because there is only a single soot nanoparticle in the simulated system due to the nanoparticle coagulation. While the H/C ratio continuously decreases due to graphitization to form the fullerene-like structure as shown in Figures 7.2(d) to (i).

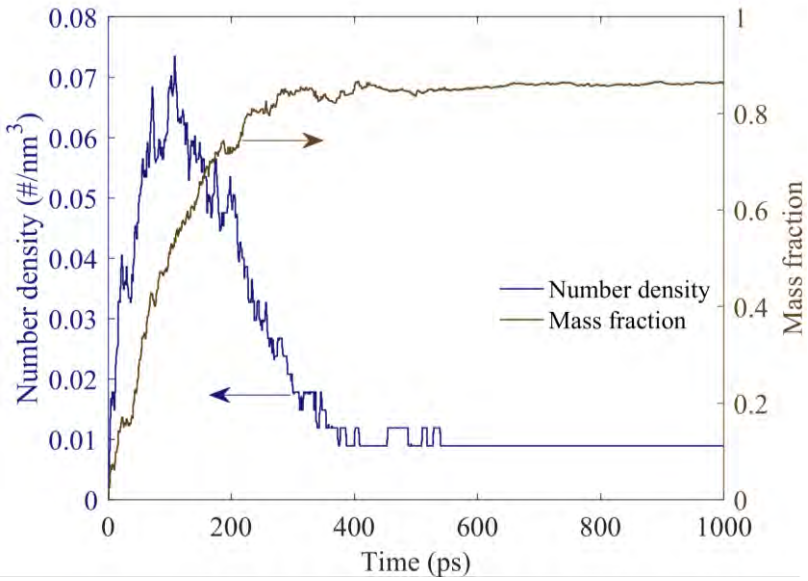

Figure 7.4 The number density and mass fraction of soot nanoparticles at 3000 K.

Figure 7.5 shows the time evolutions of small molecule intermediates (e.g., H, OH, H_2, CO, CO_2 and H_2O) during the soot formation process. The initial H and OH radicals are rapidly consumed and then fluctuated at around 0 because of their high reactivities. The rapid increase of H_2O molecules is found due to the chemical reaction between H and OH radicals at early stage. However, the amount of H_2O continuously decreases after 50 ps because the chemical reaction between H_2O and C radicals consumes H_2O and produces CO and H_2 during the MD simulation**.** The number of CO_2 is nearly zero which indicates that there is almost no CO_2 involved in the chemical reaction under the present MD simulation condition.

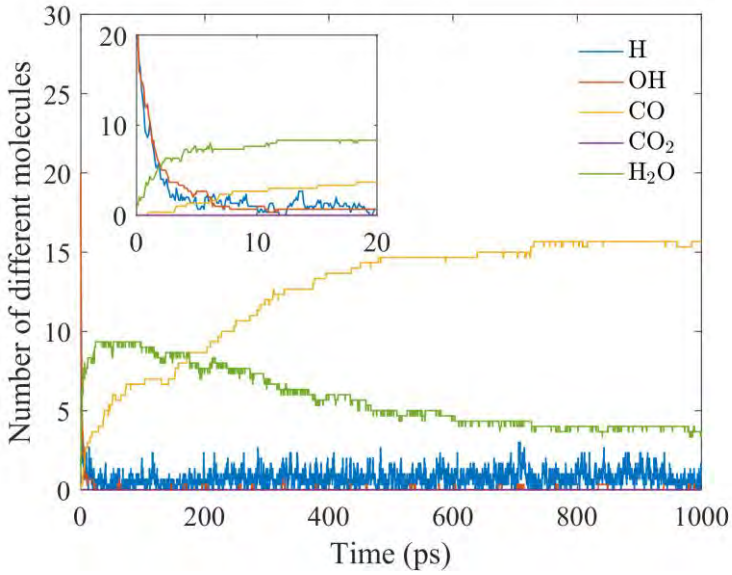

Figure 7.5 Time evolutions of major intermediates during the soot formation process.

7.3.2 Effects of carbon dioxide addition

7.3.2.1 Overall effects of carbon dioxide addition

Figure. 7.6 shows the MD simulation results of the mass percentage of the final soot nanoparticles (i.e., at 1 ns) where the mass of additional CO_2 molecules is not accounted into the total mass to avoid the effect of CO_2 dilution. The results show the nearly linear correlation between the final soot mass percentage and the initial amount of CO_2 molecules. The lower final soot mass percentage implies that the increasing number of CO_2 molecules can suppress the mass growth of soot nanoparticles. In addition, the collision of PAHs is delayed with the increasing number of CO_2 molecules, the number of soot nanoparticles reaches the peak at 100.3, 103.0, 157.9, 117.5, 124.4, 143.0, 123.5, 146.1, 166.4, 172.6 and 171.2 ps with the increasing number of 0, 30, 45, 60, 90, 180, 210, 270, 300, 360 and 540 CO_2 molecules, respectively. It is because that the addition of CO_2 molecules can suppress the coagulation process of PAHs.

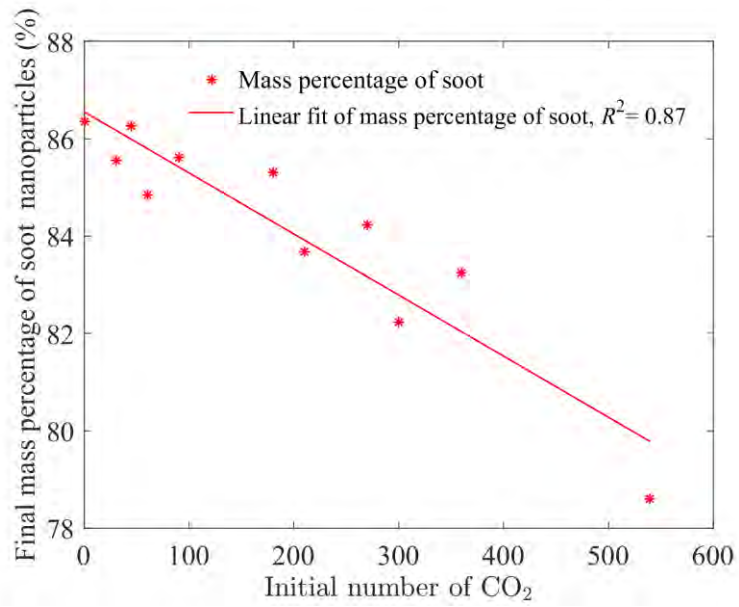

Figure 7.6 Final mass percentage of soot nanoparticles for different CO_2 additions.

Figure 7.7 shows the results of the number of CO_2 consumption for different CO_2 additions. The linear growth of the number of CO_2 consumption can be found with the increasing number of CO_2 addition. The results indicate that CO_2 addition can lead to more CO_2 molecules involved in the chemical reaction of soot formation and evolution processes.

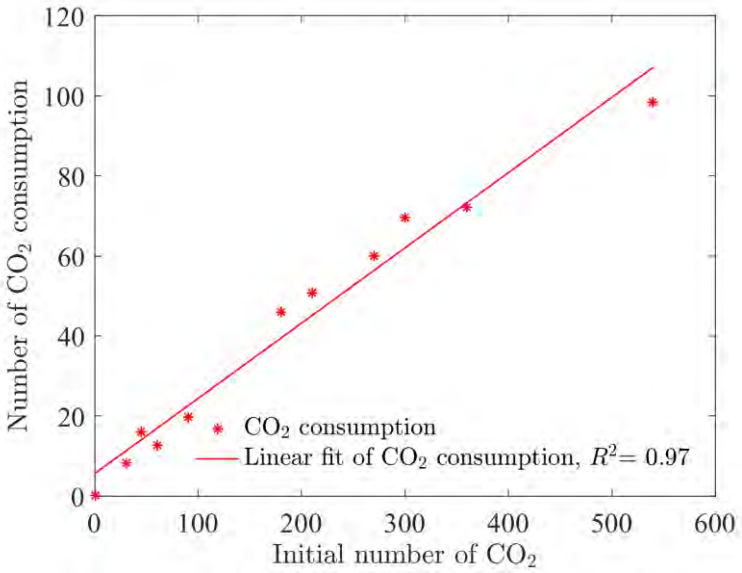

Figure 7.7 The number of CO_2 consumption for different CO_2 additions.

The final production of important radicals (i.e., H and OH) and the time evolution of important molecule species (i.e., H_2O and CO) for different CO_2 additions are shown in Figures 7.8 and 7.9, respectively. In Figure 7.8, the number of H radical production decreases with the addition of CO_2, while the number of OH radical production increases with the addition of CO_2. It may be attributed to the increases of the reaction probability between CO_2 molecules and H radicals with addition of more CO_2 molecules as shown in Equation (7-1), which leads to producing more OH radicals and CO molecules. As a result, the soot oxidation by OH radicals is enhanced. In addition, the less amount of H radical production may lead to the reduction of the PAHs activity to inhibit the mass growth of soot nanoparticles as well as delay the soot nucleation through the collision of aryl radical during the first stage as the H radicals are important intermediate species in H-abstraction-C_2H_2-addition (HACA) mechanism for PAH dehydrogenates.

$$CO_2 + H \leftrightarrow CO + OH \tag{7-1}$$

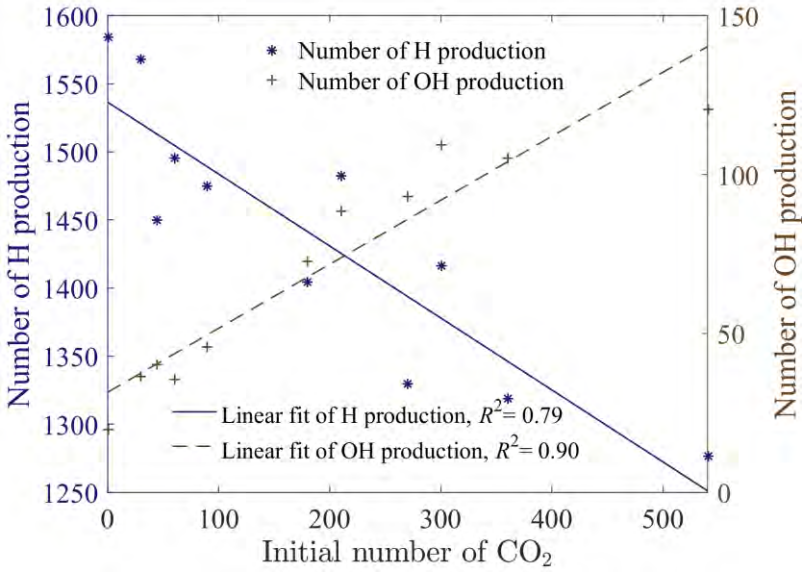

Figure 7.8 Evolution of the final production of H and OH radicals for different CO_2 additions.

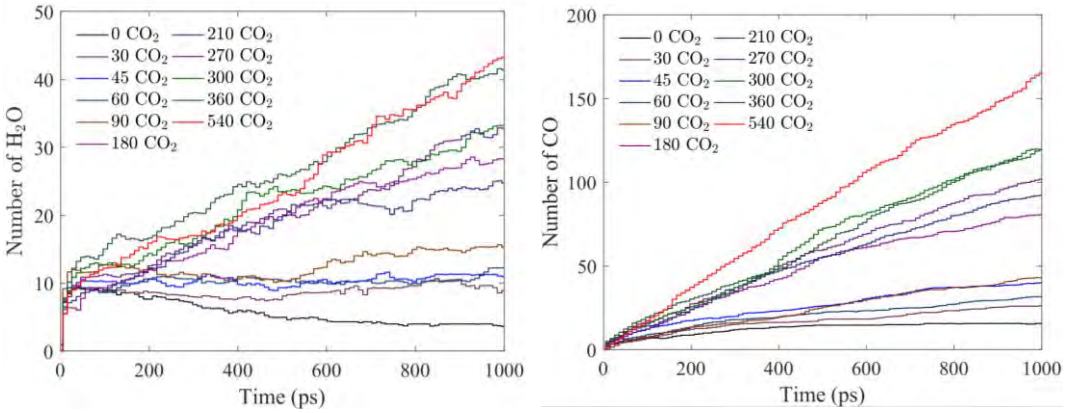

Figure 7.9 Evolution of the number of H_2O and CO molecules for different CO_2 additions.

Figure 7.9 shows the evolution of the number of H_2O and CO molecules for different CO_2 additions. It is clearly that the number of H_2O and CO molecules increases with more CO_2 molecules added, which can be explained as follows: with the increasing number of CO_2 addition, more OH radicals and CO molecules are produced by Equation (7-1). In addition, the newly formed OH radicals are highly reactive, some of them involve the reaction with H atoms to form H_2O while the others are reacted with the PAHs and C1–C4 hydrocarbon species. Hence, they involve the dehydrogenation reaction to form H_2O and the decarbonization reaction to form CO, respectively. As a result, more production of H_2O and CO can be found with the CO_2 addition.

7.3.2.2 Effects on the largest soot particle

Figure 7.10 shows the evolution of the number of C atoms for the largest soot nanoparticle under different CO_2 additions at 3000 K. The number of C atoms in the largest soot nanoparticle reaches the peak at around 400 ps. In addition, with more CO_2 added, it will lower the number of C atoms for the largest soot nanoparticle. In Figure 7.11, the number of C atoms for the largest soot nanoparticle

decreases with increasing the addition of CO_2 molecules. For example, it reduces to near 86 carbon atoms with the addition of 540 CO_2 molecules at 1 ns.

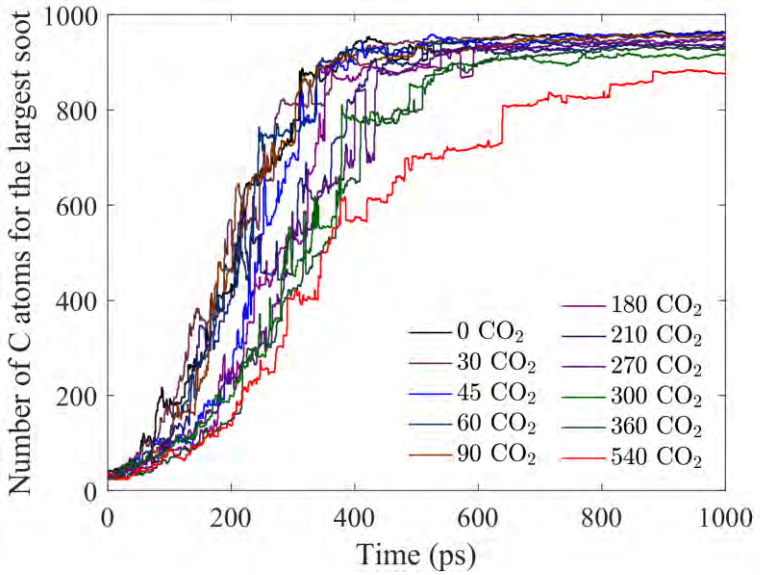

Figure 7.10 The evolution of the number of C atoms for the largest soot nanoparticle under different CO_2 additions at 3000 K.

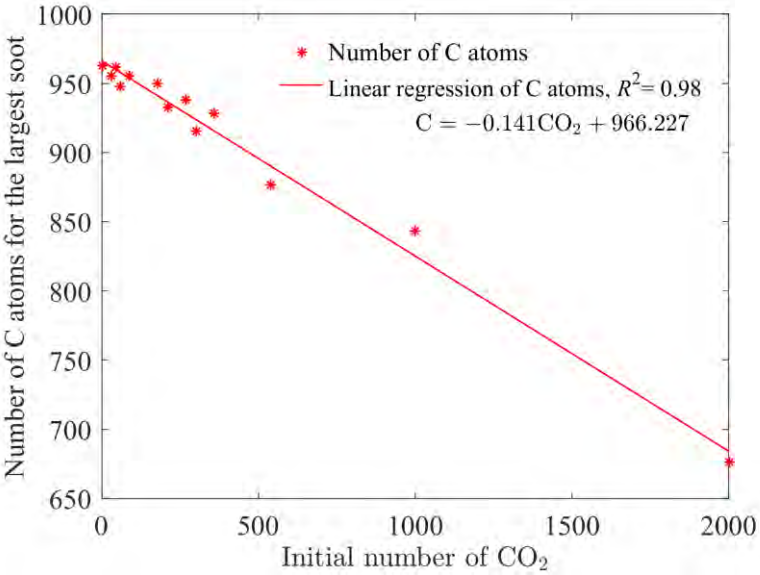

Figure 7.11 The number of C atoms for the largest soot nanoparticle under different CO_2 additions at 3000 K in 1ns.

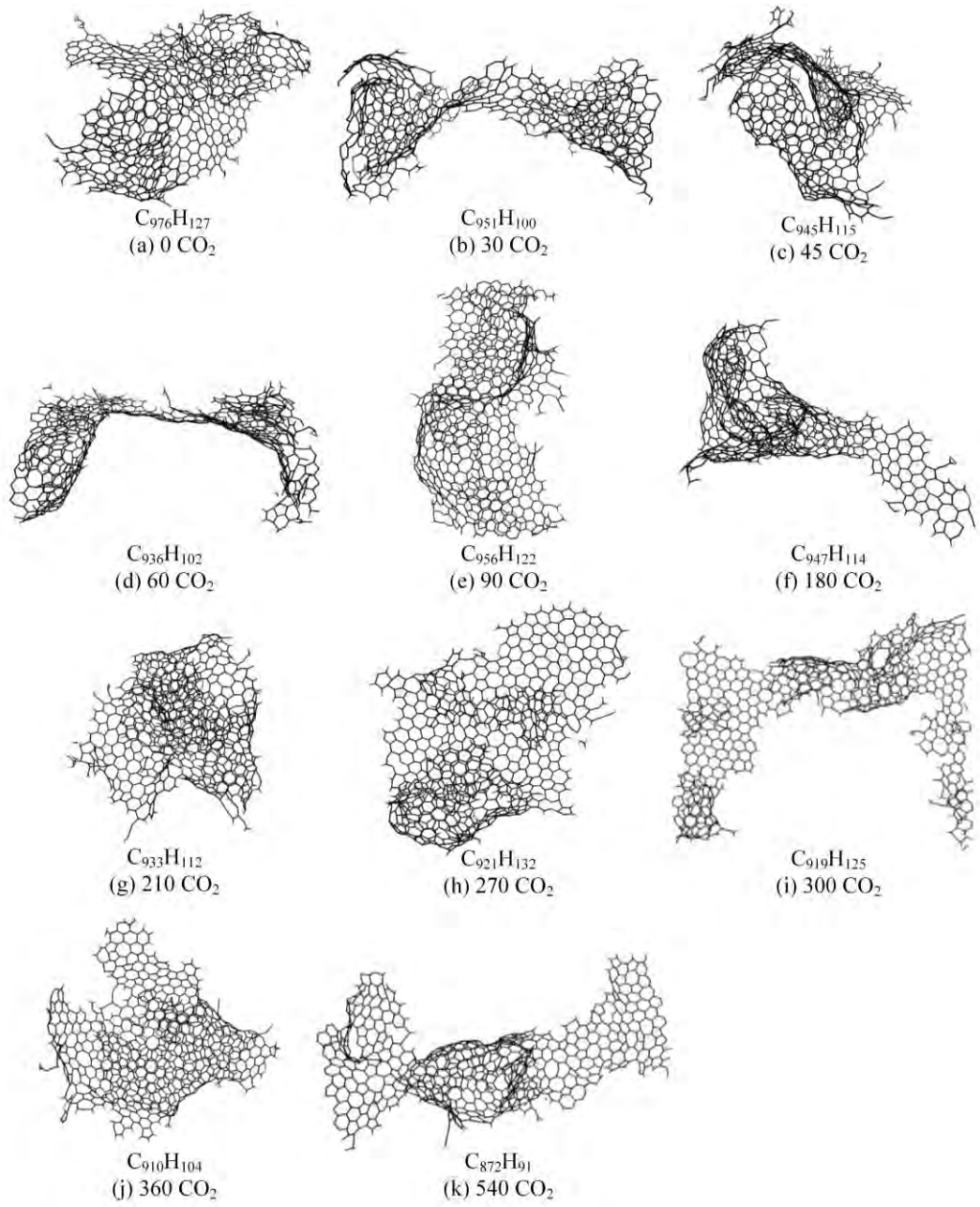

Figure 7.12 The final morphology of the largest soot nanoparticle for different CO_2 additions at 1000 ps.

Figure 7.12 shows the final morphology of the largest soot nanoparticle for different CO_2 additions at 1000 ps (i.e., 1 ns). In Figure 7.12(a), the largest soot nanoparticle is formed without CO_2 addition which shows a curved surface with some near spherical structure, which is relatively smooth. With increasing number of initial CO_2 molecules, the number of carbon atoms decreases and the final soot

morphology tends to show a two-dimensional plane structure. In addition, the structure of soot nanoparticle shows more aliphatic chains on the soot particle surface with more CO_2 added. In Figure 7.12(g), the structure of the largest soot nanoparticle shows a large area of with flat mesh surface with the addition of 540 CO_2 molecules. The results of the final morphology of the largest soot nanoparticle shows that CO_2 addition can suppress the transformation process of the soot nanoparticle structure from the planar network to the curved, fullerene-like structure.

7.3.2.3 Chemical effects of carbon dioxide addition

The evolution of reactive system is fully calculated and analyzed during 0 to 1000 ps, which contains the full details of the three stages of soot formation and evolution processes. It is observed that the formation of incipient soot nanoparticles occurs through the dimerization of PAH precursors. The mass growth of PAHs and soot nanoparticles is achieved by adding some HC species on the active sites of PAHs, which is mainly produced by the dehydrogenation reaction via H radicals. An increase in the number of CO_2 addition can decrease the production of H radicals thus lower dehydrogenation reaction, and also decrease the PAHs activities. In addition, CO_2 can also directly attack the aromatic and aliphatic sites of PAHs as shown in Figures 7.13 and 7.14, respectively. The H, C and O atoms are marked in white, gray and blue, respectively in order to distinguish different species in the chemical reaction. It is observed that a CO_2 molecule is directly added on one aromatic site of six-carbon ring in PAH (in Figure 7.13 (b)). After 0.4 ps, the C–O bond is broken (in Figure 7.13(d)) with the formation of a CO molecule and aryloxy radical.

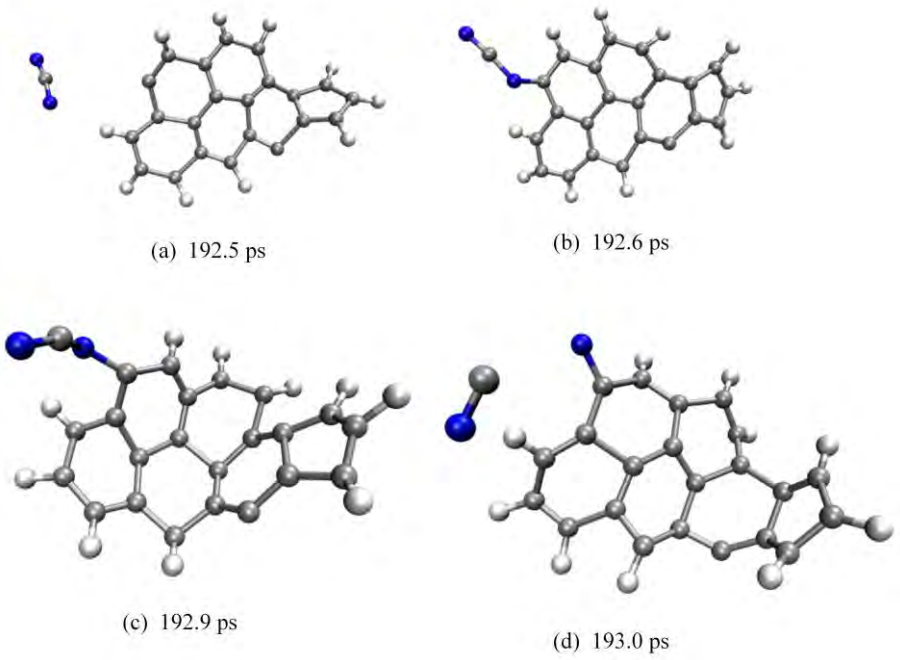

Figure 7.13 Reaction pathway of an aromatic site of PAHs attacked by the addition of 270 CO_2 at 3000 K.

In Figure 7.14, the C–O bond is firstly formed between the O atom in CO_2 and one aliphatic site of PAH (in Figure 7.14(b)), and is then followed by the destruction of C–O bond (in Figure 7.14(c)). After 5.2 ps, the C–C bond on the aliphatic chain is broken to form a CO molecule, and a C atom is removed from the PAH molecule (in Figure 7.14(e)). The surrounding CO_2 reacts continuously with the active site to cause the removal of C atoms to form CO molecule and lead to the mass loss of PAHs.

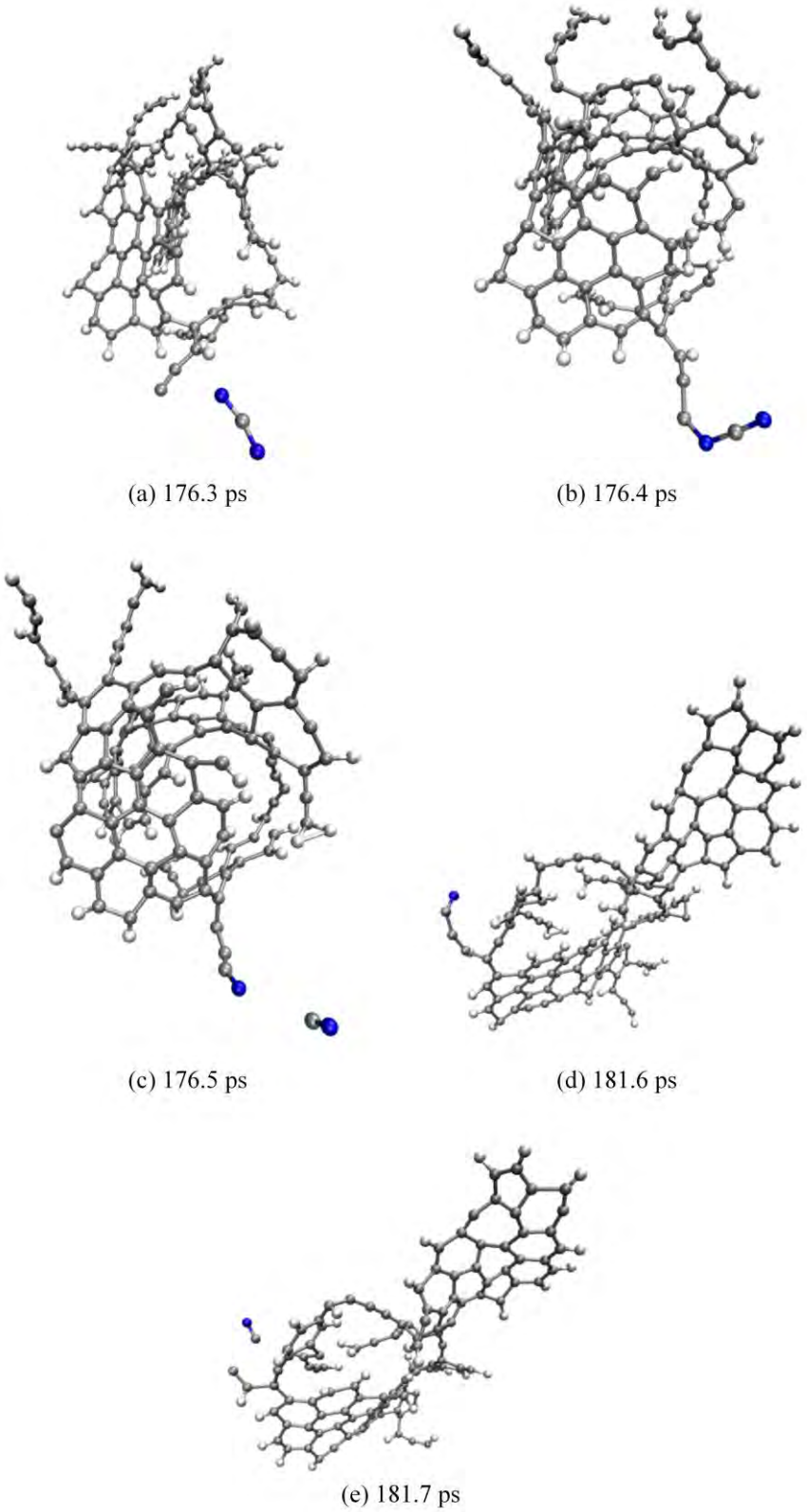

Figure 7.14 Reaction pathway of the aliphatic site of PAHs attacked by the addition of 270 CO_2 at 3000 K.

The mass growth of PAHs and soot nanoparticles is mainly followed by the hydrogen-abstraction-carbon-addition (HACA) and carbon-addition-hydrogen-migration (CAHM) (Dong et al., 2020). In the HACA, the active sites of PAHs are formed by dehydrogenation reactions through H radicals at high temperature, and then the small HC molecules react with the active sites to result in mass growth of soot nanoparticle. Similar growth mode can be observed in the ReaxFF MD simulation as shown in Figure 7.15. The C atom in acetylene is bonded on the activated site of six-carbon ring with PAH (in Figure 7.15(b)), and subsequently the migration of H atom (in Figure 7.15(d)) to result in the mass growth of PAHs.

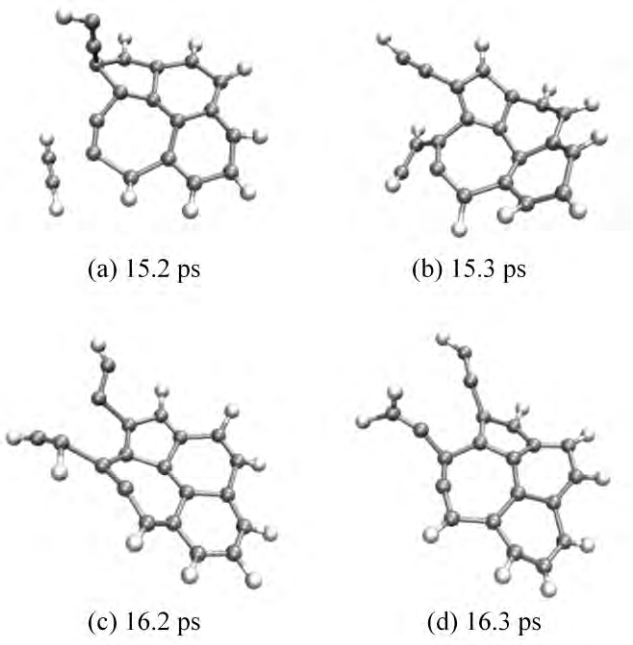

Figure 7.15 Reaction pathway of the acetylene addition on PAHs with the addition of 270 CO_2 at 3000 K.

In addition, there are other growth modes observed in the ReaxFF MD simulation as shown in Figure 7.16. In Figure 7.16(b), the C atom on the acetylene is firstly added on the PAH, without having undergone the dehydrogenation reaction though H radicals, which is similar to the carbon-addition-hydrogen-migration

(CAHM). After 2.6 ps (i.e, the reaction pathways from Figures 7.16(b) to 7.16(d)), the six-carbon ring is broken (in Figure 7.16(d)) and is then connected with the aliphatic chain to form a macrocyclic structure (an eight-carbon ring) as shown in Figure 7.16(e). The formation of such large ring structures can also be found in the previous ReaxFF MD simulations (Han et al., 2017; Zhao et al., 2020).

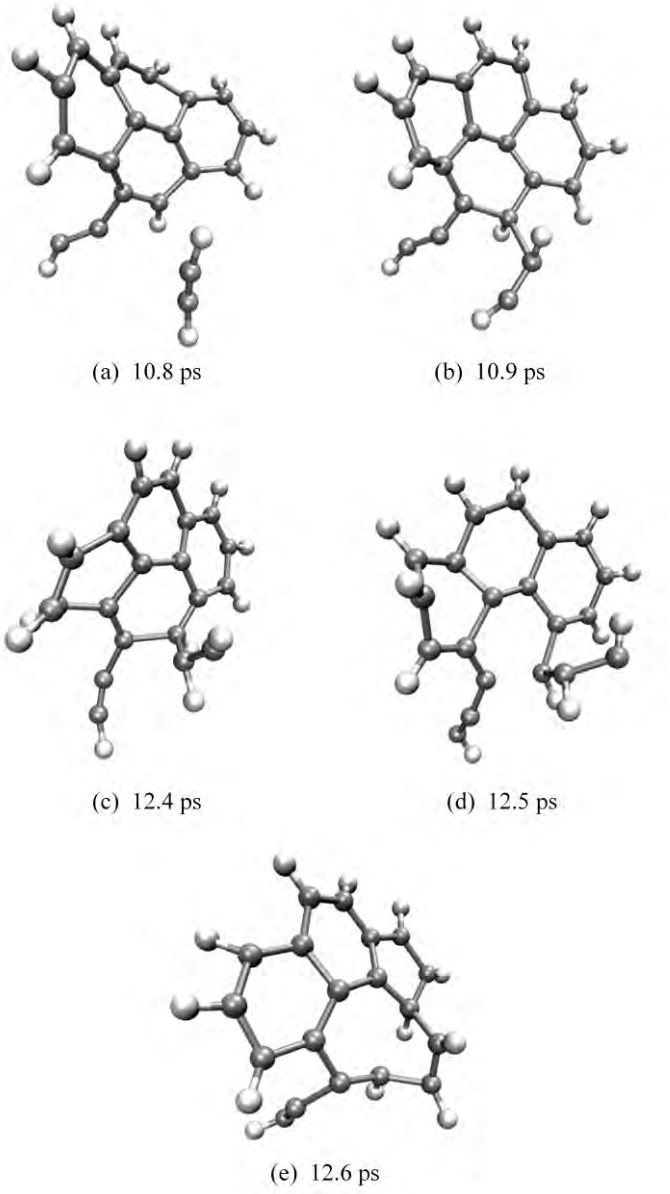

Figure 7.16 Other reaction pathways of acetylene addition on PAHs with the formation of C8 ring under the addition of 270 CO_2 at 3000 K.

The chemical effect of CO_2 on the soot formation and evolution is investigated. In Table 7.2, all the reaction pathways are observed in which CO_2 are involved for the addition of 270 CO_2 molecules. The most observed reaction related to CO_2 is $CO_2+H\leftrightarrow CO+OH$, which is consistent with the result analysis of small species. The reaction continuously consumes the H radical and produces CO and OH radicals. In addition, CO_2 can also directly react with PAHs/soot nanoparticles and remove C atoms from the aliphatic chain on PAHs/soot nanoparticles. Only a few reactions with small HC species (C1-C4) occur, which is because of the low concentrations of small HC species when compared with the dominant species of PAHs in the present reactive system. The low concentrations of small HC species result in low collision probability between CO_2 and small HC molecules. These observed reactions show that CO_2 addition can mainly suppress the nucleation and mass growth processes of soot nanoparticles through the consumption of H radicals.

Table 7.2 The reaction pathways for the addition of 270 CO_2 molecules during 1000 ps at 3000 K.

Reaction types	Examples	Number of observations
CO2 with PAHs/soot nanoparticles	$PAH+CO_2\rightarrow PAH+2CO$	26
CO_2 with small hydrocarbon species (C1-C4)	$CO_2+C_2H_3\rightarrow C_2H_2+CO+OH$	10
CO_2 with H radicals	$CO_2+H\leftrightarrow CO+OH$	37

7.4 Summary

In the present study, the formation and evolution of soot nanoparticles from polycyclic aromatic hydrocarbons (PAHs) and some aliphatic hydrocarbons in the ethylene flames are investigated by using the reactive force field (ReaxFF) molecular dynamics (MD) simulations for different carbon dioxide (CO_2) additions at high temperature. The transition from PAHs to the final soot nanoparticles reveals the potential mechanism of soot formation and evolution processes which can be divided into three stages. The first stage is the soot nucleation through the dimerization of activated PAH molecules, which results in an increase of soot number density. The second stage is related to the soot surface growth and coagulation including the addition of small HC molecules to the active sites of polycyclic aromatic hydrocarbons (PAHs), oxidation reaction through reacting with CO_2 molecules and OH radicals, and coagulation of PAHs to form the largest soot nanoparticles. The continuous growth in soot mass while decrease in soot number density can be found in this stage. The third stage is mainly the graphitization process to finally form a curved fullerene-like structure.

The effects of CO_2 addition on the reaction pathways of soot formation and evolution are investigated. On the one hand, CO_2 continuously consumes the H radicals through the reaction: $CO_2+H \leftrightarrow CO+OH$, thus reduces the activity of PAH precursors. As a result, the nucleation and surface growth of soot nanoparticles are suppressed. On the other hand, CO_2 molecule and OH radical can also directly attack the PAHs/soot nanoparticles and continuously remove C atoms. Therefore, the oxidation process is thus enhanced by the addition of CO_2.

Chapter 8 Conclusions and Recommendations for Future Work

8.1 Review of the Present Research Study

The present study mainly focused on the numerical simulation of aerosol dynamics as well as the interaction between particles and turbulent flows with the newly proposed and developed computational fluid dynamics (CFD) based Monte Carlo method. The research work in this thesis can be divided into four major parts.

In the first part of the present research, a weighted operator fraction Monte Carlo (WFMC) method is newly proposed and developed for studying the particle coagulation in Chapter 4. The fraction function with the probabilistic removal is introduced for adjusting weight function and maintaining the number of numerical particles. This newly developed WFMC method is fully validated by both analytical solutions and sectional method for comparing their numerical simulation results for different classical cases (i.e., constant kernel, free-molecular coagulation kernel and different initial size distributions cases). The results obtained from WFMC method show excellent agreement with both analytical solutions and sectional method. The lower stochastic error can be found in WFMC method when compared with different Monte Carlo (MC) schemes.

The second part of the present research is the further development of Lagrangian particle tracking with weighted fraction Monte Carlo (LPT-WFMC) method to study the soot formation and evolution in Chapter 5. The fully verified WFMC method is further coupled with Lagrangian particle tracking method based on the detailed soot model for studying the soot formation and evolution in ethylene

laminar premixed flames. Soot number density, volume fraction and particle size distribution are obtained. This new LPT-WFMC method can be further extended to the particle size distributions (PSDs), which can improve the accuracy for predicting soot PSDs at larger particle size regime. The effects of different parameters (i.e., coagulation models, soot densities and sticking probabilities) in the present detailed soot model used are also fully studied by the parametric sensitivity analysis.

The third part of the present research is to investigate the dimerization processes of different crosslinked polycyclic aromatic hydrocarbons (PAHs) by the molecular dynamics (MD) simulation as the PAHs dimerization is always regarded as an important process in the soot nucleation in many detailed soot models. The collisional association and dissociation processes of each PAH species are investigated under different temperatures, impact parameters and orientations. The results of lifetime of the PAH dimers and the rate constants for the association and dissociation are obtained. The dissociation rate constant of PAH dimers is fully analyzed by the Rice-Ramsperger-Kassel-Marcus (RRKM) theory of unimolecular dissociation.

The fourth part of the present research is to study the formation and evolution of soot nanoparticles by using reactive force field (ReaxFF) and the molecular dynamics (MD) with different carbon dioxide additions. Three stages of the formation and evolution of soot nanoparticles including soot nucleation, surface growth and coagulation and graphitization from polycyclic aromatic hydrocarbons (PAHs) to a curved fullerene-like soot particle are revealed. The chemical effects of different carbon dioxide additions on the soot formation and evolution pathways are studied by using ReaxFF MD simulation.

8.2 Main Conclusions of the Thesis

8.2.1 Conclusions of the development of weighted fraction Monte Carlo method

The newly developed and proposed weighted fraction Monte Carlo (WFMC) method is fully validated with corresponding analytical solutions, sectional method and different MC schemes for different classical cases (i.e., constant kernel, free-molecular coagulation kernel and different initial size distributions cases). The results of moments of different orders and particle size distributions (PSDs) are obtained which show excellent agreements between the numerical simulation results of the WFMC method and analytical solutions/SM results.

The stochastic error of different MC methods is analyzed. The WFMC method shows a significant reduction in stochastic error for higher-order moments with a slightly higher computational cost when compared with different MC methods. The WFMC method is proved able to adjust the weight function to "twist" the numerical PSD and change the number of numerical particles that represents real particles in each size interval. The lower stochastic error is obtained for higher-order moments in WFMC method since more numerical particles are used to represent real physical particles in larger size regime. In addition, the developed WFMC method also shows the significant advantage of tracking the PSD over the larger size regime, which is traditionally insufficient in the classical DSMC and MMC methods.

8.2.2 Conclusions of modelling the soot particle size distributions by LPT-WFMC method

The newly developed weighted fraction Monte Carlo (WFMC) method is further coupled with the Lagrangian particle tracking (LPT) method with the detailed soot model to study the soot formation and evolution in ethylene premixed flames.

The LPT-WFMC method is firstly validated for soot prediction in one-dimensional laminar premixed ethylene flame by comparison with the results of DSMC, MMC and the experiments. The results of number density, volume fraction and particle size distribution of soot particles are obtained, which show good agreement with the results of DSMC, MMC and the experiments. In addition, stochastic error analysis has proved that the LPT-WFMC method can be further extended to the soot PSDs and can reduce the statistical error for larger particle size regime. There are always insufficient number of numerical particles and poor representation in traditional MC methods. This newly developed LPT-WFMC method can adjust the numerical weight distribution to assign more numerical particles to larger particle size regime for the stochastic error reduction.

Similar trends as experimental results can be found in the numerical simulation results for soot number density and volume fraction, while the overprediction for soot number density is also obtained which is similar to some previous research studies. Besides, the numerical simulation results of soot PSDs show that a fairly good agreement with experimental results at higher HAB of flame region with larger particle size regime (i.e., HAB $\geq$ 0.45 cm and D_p> 6 nm) while coagulation and surface growth processes are well captured. However, the large deviations from simulated PSDs and experimental results are not negligible for

lower HAB flame region and smaller particle size regime (i.e., D_p < 4 nm and HAB ≤ 0.35 cm). Such discrepancies for total number density and PSDs at lower HAB flame region and smaller particle size regime indicate that a better understanding and modelling of the soot nucleation and the chemistry of PAHs is still one of the most challenging problems in the research field. The soot PSDs is finally evolved to bimodal distribution which can be explained by studying the rate of soot dynamic process. Parametric sensitivity analysis is also performed to provide a better understanding and gain insight of the effect of those critical parameters on simulated PSDs.

8.2.3 Conclusions of molecular dynamics simulations of PAH dimerization

The association and dissociation kinetics of crosslinked PAH dimerization are studied by using ReaxFF molecular dynamics (MD) simulation to investigate the role of crosslinked PAH dimerization in the soot nucleation. The ReaxFF is firstly proved able to well describe the PAH−PAH interaction by comparing with the results of B3LYP-D3/def2-TZVP levels of theory. The binary collision of PAH monomers is then performed in microcanonical ensembles at different initial temperatures and impact parameters. The results of the dynamic behaviors during the PAH dimerization are obtained.

In PAH association process, the association probability, reaction cross section and association rate constant are well quantified. The microcanonical association rate constant is found to decrease with increasing temperature in the higher temperature range (i.e., 1750 to 2000 K). The results of association rate constant reveal that there is no significant difference in association process for different crosslink structures with the similar size. Considering the PAH dimers

dissociation, higher dissociation rate constant is obtained for PAH dimers with lower binding energy in the lower temperature range (i.e., 500 to 1250 K). It is because the rotational and translational energy (3/2RT + 3/2RT) of PAHs are relatively low when compared with their binding energy at the lower temperature range. Hence, the dissociation rate constant is mainly affected by the binding energy. However, minor discrepancy of dissociation rate constants between different PAH structures is found due to the negligible contribution from the binding energy in the higher temperature range (i.e., 1750 to 2000 K). In addition, the results of PAH association and dissociation processes, and the short lifetime (almost none of dimers can survive over 40 ps from 1750 to 2000 K) support that physical dimerization of PAHs is unlikely to play a major role in soot formation under typical combustion conditions.

The dissociation of highly excited PAH dimers is further studied. The excited PAH dimers are formed due to the binary collision of PAH monomers, then the energy transfer also occurs between the intermolecular and intramolecular vibrational modes. The exponential decay of PAH dimers in accordance with RRKM theory of unimolecular dissociation suggests that rapid intramolecular vibrational energy redistribution (IVR) takes place. In addition, the contributions of PAH dimer dissociation from different degrees of freedom are obtained by using the RRK unimolecular reaction theory. The intermolecular rotational and translational models are closely coupled to the reaction coordinates and play an important role in the PAH dimer dissociation process while intramolecular vibrational modes only partially participate in the rapid IVR process.

8.2.4 Conclusions of soot formation and evolution by ReaxFF MD simulations

Soot formation and evolution processes are further investigated by considering the transition from polycyclic aromatic hydrocarbons (PAHs) and some aliphatic hydrocarbons in the ethylene flames to the soot nanoparticles through ReaxFF molecular dynamics (MD) simulations at high temperature. The effects of carbon dioxide (CO_2) additions on the soot formation are also studied in order to gain the insight of CO_2 involved chemistry on soot formation pathways.

The transition from PAHs to the final soot nanoparticles reveals the potential mechanism of soot formation and evolution processes which can be divided into three stages. The first stage is the soot nucleation through the dimerization of activated PAH molecules, which results in an increase of soot number density. The second stage is related to the soot surface growth and coagulation including the addition of small HC molecules to the active sites of PAHs, oxidation reaction through reacting with CO_2 molecules and OH radicals, and coagulation of PAHs to form the largest soot nanoparticles. The continuous growth in soot mass while the decrease in soot number density can be found in this stage. The third stage is mainly the graphitization process to finally form a curved fullerene-like structure.

The effects of CO_2 addition on the reaction pathways of soot formation and evolution are investigated. On the one hand, CO_2 continuously consumes the H radicals through the reaction: $CO_2+H \leftrightarrow CO+OH$, thus reduces the activity of PAH precursors. As a result, the nucleation and surface growth of soot nanoparticles are suppressed. On the other hand, CO_2 molecule and OH radical can also directly attack the PAHs/soot nanoparticles and can continuously remove C atoms. Therefore, the oxidation process is thus enhanced by the addition of CO_2.

8.3 Recommendations for Future Work

This thesis presents the numerical simulations for understanding the soot formation and evolution in combustion processes. The soot formation and evolution with their aerosol dynamics processes in the combustion flames are studied by Lagrangian particle tracking with weighted fraction Monte Carlo (LPT-WFMC) method, while the soot formation and the transformation from PAHs to the soot nanoparticles are investigated by the reactive force field molecular dynamics (ReaxFF MD) simulations. The aim of this thesis is achieved by developing a stochastic error reduction Monte Carlo method for solving soot formation and evolution with complex simultaneous aerosol dynamics in combustion flames. Polycyclic aromatic hydrocarbon (PAH) dimerization and soot formation are studied by using ReaxFF MD simulations. However, further research work is still recommended to overcome the limitations of the present developed numerical methods.

8.3.1 Limitations of the present research study

The limitations of this newly proposed and developed Lagrangian particle tracking with weighted fraction Monte Carlo (LPT-WFMC) method and the ReaxFF molecular dynamics (MD) simulations are as follows:

1. In the present study, the morphology of fractal-like soot particles is described by the surface-volume model. However, the properties of individual primary particles cannot be obtained. In addition, the assumption about the fractal dimension of the soot aggregates is required to made for deriving their simulated mobility diameters. Therefore, a detailed soot model with full

description of each primary particle is required to simulate soot morphology and their formation and evolution.

2. In the present study, the developed LPT-WFMC method is used to investigate soot formation and evolution in one-dimensional burner stabilized ethylene laminar premixed flames for the numerical validation purpose. However, the burner-stabilized stagnation (BSS) flame technique is always applied to avoid the probe perturbation in soot sampling. Therefore, the application of the developed LPT-MC method can be extended to simulate the soot formation and evolution in two/three-dimensional burner-stabilized stagnation flame with the comparison of more reliable experimental dataset available in literature.

3. In the present study, dynamic association and dissociation of aromatic crosslinked hydrocarbons is studied by ReaxFF MD simulations to investigate the role of PAH dimerization in soot nucleation process. However, the previous research studies have already pointed out that physical dimerization of medium-sized PAH molecules is unlikely to occur at flame conditions through studying the thermodynamic properties (i.e., free energy) of PAH dimers. In addition, the chemical dimerization of aryl radicals with the covalent bond formation is also regarded as an important nucleation pathway. Therefore, the dynamics of such chemical dimerization with the covalent bond formation/breakage can be further studied by ReaxFF MD simulations.

8.3.2 Recommendations for future work

Considering the above-mentioned limitations on the present study, recommendations for future research are made as follows:

1. Detailed description of soot morphology. The newly developed LPT-MC method can be further developed and coupled with the detailed soot model with the description of primary particles. A soot aggregate consists of primary particles and the relative position of these primary particles can be tracked in the detailed soot model. The detailed information of soot morphology can then be directly obtained.

2. Numerical simulation of the burner-stabilized stagnation (BSS) flames. The developed LPT-WFMC method can be further extended to simulate and validate the experimental/numerical data of two/three-dimensional burner-stabilized stagnation flames if more reliable experimental dataset available in literature. More detailed information about the soot formation and evolution processes (i.e., the trajectory of each soot particle and the spatial distribution of soot particles) can be obtained and the full potential of this developed LPT-WFMC method can be achieved using numerical simulation of two/three-dimensional BSS flames.

3. Numerical simulation of chemical dimerization. The study of PAH collision can be further extended to study the dynamic of the collision between aryl radicals to obtain the details of the chemical dimerization by ReaxFF MD simulations. The details of reactive association and dissociation, and the thermostability of the reactive dimers during the chemical dimerization can provide insight of soot nucleation via chemical nucleation pathways.

Appendix

A1 Additional Supplementary Figures

The conservation of total energy for representative trajectories is shown during the PAH collisions.

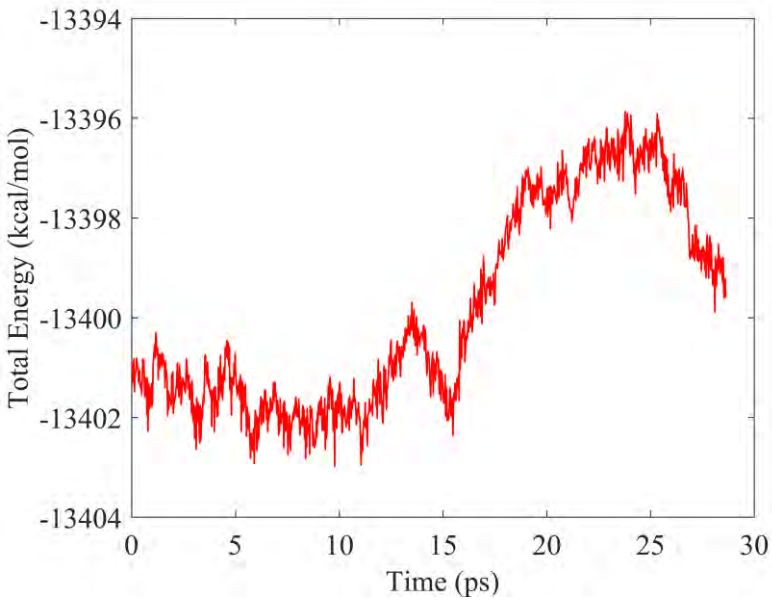

Figure A1.1 The historical representative trajectories of total energy.

The lifetimes of each PAH dimer are recorded from different temperatures and impact parameters. The trends in the lifetime distribution observed for different PAH species lead to similar conclusions, the difference being the overall lifetime of dimers. Some additional Figures A2 and A3 are included here for further clarification.

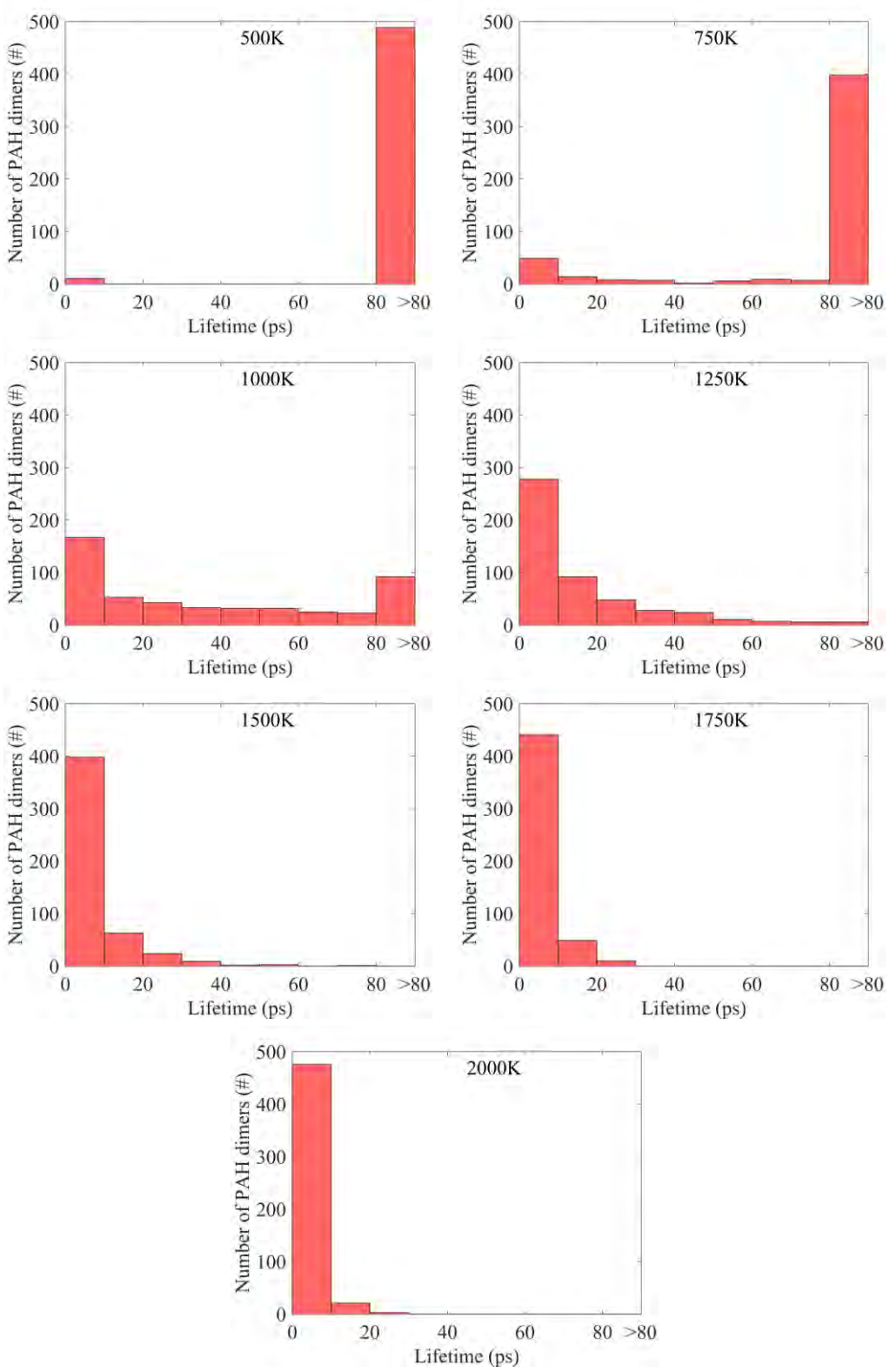

Figure A1.2 Lifetime distributions of the 2b dimers for different temperatures.

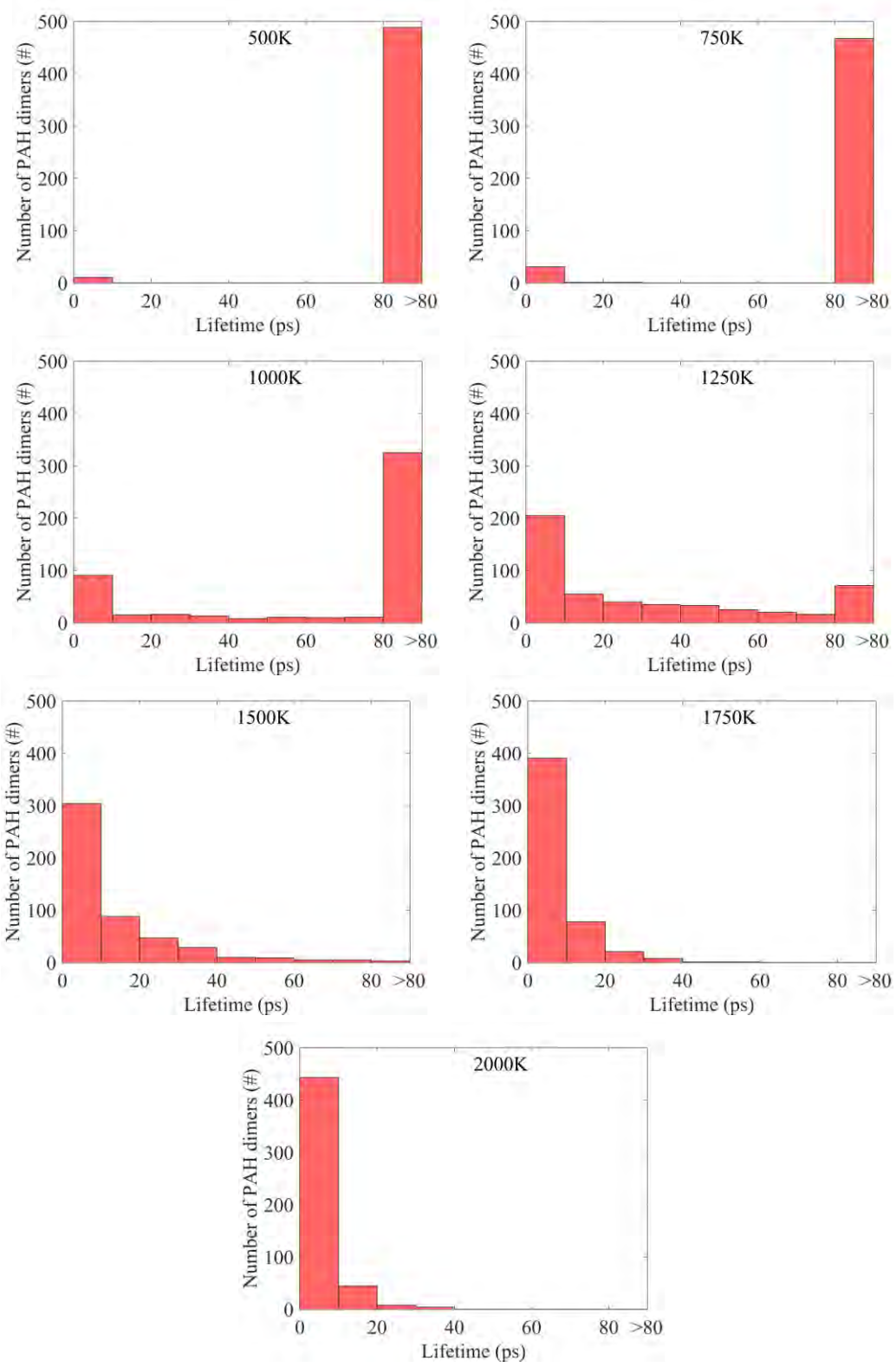

Figure A1.3 Lifetime distributions of the 2c dimers for different temperatures

A2 **Reactive MD-force Field: C/H** (Mao et al., 2017b)

```
Reactive MD-force field: C/H
     39.0000 ! Number of general parameters
     50.0000 !Overcoordination parameter
      9.5469 !Overcoordination parameter
     26.5405 !Valency angle conjugation parameter
      1.7224 !Triple bond stabilisation parameter
      6.8702 !Triple bond stabilisation parameter
     70.0000 !C2-correction
      1.0588 !Undercoordination parameter
      4.6000 !Triple bond stabilisation parameter
     12.1176 !Undercoordination parameter
     13.3056 !Undercoordination parameter
    -70.5044 !Triple bond stabilization energy
      0.0000 !Lower Taper-radius
     10.0000 !Upper Taper-radius
      2.8793 !Not used
     33.8667 !Valency undercoordination
      6.0891 !Valency angle/lone pair parameter
      1.0563 !Valency angle
      2.0384 !Valency angle parameter
      6.1431 !Not used
      6.9290 !Double bond/angle parameter
      0.3989 !Double bond/angle parameter: overcoord
      3.9954 !Double bond/angle parameter: overcoord
     -2.4837 !Not used
      5.7796 !Torsion/BO parameter
     10.0000 !Torsion overcoordination
      1.9487 !Torsion overcoordination
     -1.2327 !Conjugation 0 (not used)
      2.1645 !Conjugation
      1.5591 !vdWaals shielding
      0.1000 !Cutoff for bond order (*100)
      2.1365 !Valency angle conjugation parameter
      0.6991 !Overcoordination parameter
     50.0000 !Overcoordination parameter
      1.8512 !Valency/lone pair parameter
      0.5000 !Not used
     20.0000 !Not used
      5.0000 !Molecular energy (not used)
      0.0000 !Molecular energy (not used)
      2.6962 !Valency angle conjugation parameter

  2      ! Nr of atoms; cov.r; valency;a.m;Rvdw;Evdw;gammaEEM;cov.r2;#
         alfa;gammavdW;valency;Eunder;Eover;chiEEM;etaEEM;n.u.
         cov r3;Elp;Heat inc.;n.u.;n.u.;n.u.;n.u.
         ov/un;val1;n.u.;val3,vval4
```

```
C  1.3674    4.0000   12.0000    2.0453    0.1444    0.8485    1.1706    4.0000
   9.0000    1.5000    4.0000   30.0000   79.5548    4.8446    7.0000    0.0000
   1.1168    0.0000  181.0000   14.2732   24.4406    6.7313    0.8563    0.0000
  -4.1021    5.0000    1.0564    4.0000    2.9663    0.0000    0.0000    0.0000

H  0.8930    1.0000    1.0080    1.3550    0.0930    0.8203   -0.1000    1.0000
   8.2230   33.2894    1.0000    0.0000  121.1250    3.7248    9.6093    1.0000
  -0.1000    0.0000   61.6606    3.0408    2.4197    0.0003    1.0698    0.0000
 -19.4571    4.2733    1.0338    1.0000    2.8793    0.0000    0.0000    0.0000

   3          ! Nr of bonds; Edis1;LPpen;n.u.;pbe1;pbo5;13corr;pbo6
              pbe2;pbo3;pbo4;n.u.;pbo1;pbo2;ovcorr
1  1   80.8865  107.9944   52.0636    0.5218   -0.3636    1.0000   34.9876    0.7769
         6.1244   -0.1693    8.0804    1.0000   -0.0586    8.1850    1.0000    0.0000
1  2  180.6309    0.0000    0.0000   -0.4794    0.0000    1.0000    6.0000    0.6281
        12.2202    1.0000    0.0000    1.0000   -0.0670    6.8158    0.0000    0.0000
2  2  153.3934    0.0000    0.0000   -0.4600    0.0000    1.0000    6.0000    0.7300
         6.2500    1.0000    0.0000    1.0000   -0.0790    6.0552    0.0000    0.0000

   1        ! Nr of off-diagonal terms; Ediss;Ro;gamma;rsigma;rpi;rpi2
   1  2     0.1200    1.3861    9.8561    1.1254   -1.0000   -1.0000

   6     ! Nr of angles;at1;at2;at3;Thetao,o;ka;kb;pv1;pv2
   1  1  1   74.9085   44.7514    0.9144    0.0000    0.0050    0.3556    2.5715
   1  1  2   68.0294   13.4722    5.5819    0.0000    0.6849    0.0000    1.0031
   2  1  2   68.4575   22.1235    1.2937    0.0000    3.0000    0.0000    1.5009
   1  2  2    0.0000    0.0000    6.0000    0.0000    0.0000    0.0000    1.0400
   1  2  1    0.0000    7.5000    5.0000    0.0000    0.0000    0.0000    1.0400
   2  2  2    0.0000   27.9213    5.8635    0.0000    0.0000    0.0000    1.0400

   3     ! Nr of torsions;at1;at2;at3;at4;V1;V2;V3;V2(BO);vconj;n.u;n
1  1  1  1    2.1207   26.8713    0.5160   -9.0000   -2.8394    0.0000    0.0000
1  1  1  2    1.4658   44.1251    0.4411   -5.3120   -2.1894    0.0000    0.0000
2  1  1  2    1.4787   40.5128    0.4396   -5.2756   -3.0000    0.0000    0.0000
```

References

Aamir, E. 2010, Population balance model-based optimal control of batch crystallisation processes for systematic crystal size distribution design, Loughborough University.

Abid, A. D., Heinz, N., Tolmachoff, E. D., Phares, D. J., Campbell, C. S. and Wang, H. 2008, On evolution of particle size distribution functions of incipient soot in premixed ethylene–oxygen–argon flames, *Combustion and Flame,* Vol. 154, pp. 775-788.

Agarwal, A. K., Dhar, A., Sharma, N. and Shukla, P. C. 2019, Engine exhaust particulates*,* Springer.

Alakoskela, J.-M. I. and Kinnunen, P. K. 2001, Probing phospholipid main phase transition by fluorescence spectroscopy and a surface redox reaction, *The Journal of Physical Chemistry B,* Vol. 105, pp. 11294-11301.

Alder, B. J. and Wainwright, T. E. 1959, Studies in molecular dynamics. I. General method, *The Journal of Chemical Physics,* Vol. 31, pp. 459-466.

Aldous, D. J. 1999, Deterministic and stochastic models for coalescence (aggregation and coagulation): a review of the mean-field theory for probabilists, *Bernoulli,* Vol. 5, pp. 3-48.

Alfè, M., Apicella, B., Barbella, R., Rouzaud, J.-N., Tregrossi, A. and Ciajolo, A. 2009, Structure–property relationship in nanostructures of young and mature soot in premixed flames, *Proceedings of the Combustion Institute,* Vol. 32, pp. 697-704.

Ali, S. 2014, Direct Quadrature Conditional Moment Closure for Turbulent Non-Premixed Combustion, Queen Mary University of London.

Allen, M. and Raabe, O. 1982, Re-evaluation of Millikan's oil drop data for the motion of small particles in air, *Journal of Aerosol Science,* Vol. 13, pp. 537-547.

Allen, M. P. and Tildesley, D. J. 2017, Computer simulation of liquids*,* Oxford University Press.

Alopaeus, V., Laakkonen, M. and Aittamaa, J. 2006, Solution of population balances with breakage and agglomeration by high-order moment-conserving method of classes, *Chemical Engineering Science,* Vol. 61, pp. 6732-6752.

Amin, H. M. and Roberts, W. L. 2021, Investigating soot parameters in an ethane/air counterflow diffusion flame at elevated pressures, *Combustion Science and Technology,* Vol. 193, pp. 1827-1842.

Apicella, B., Russo, C., Carpentieri, A., Tregrossi, A. and Ciajolo, A. 2022, PAHs and fullerenes as structural and compositional motifs tracing and distinguishing organic carbon from soot, *Fuel,* Vol. 309, Article ID: 122356.

Appel, J., Bockhorn, H. and Frenklach, M. 2000, Kinetic modeling of soot formation with detailed chemistry and physics: laminar premixed flames of C2 hydrocarbons, *Combustion and Flame,* Vol. 121, pp. 122-136.

Babovsky, H. 1999, On a Monte Carlo scheme for Smoluchowski's coagulation equation, *Monte Carlo Methods and Applications,* Vol. 5, pp. 1-18.

Baer, T., Hase, W. L. and William, L. 1996, Unimolecular reaction dynamics: theory and experiments*,* Oxford University Press on Demand.

Bagheri, G., Salmanzadeh, M., Golkarfard, V. and Ahmadi, G. 2012, Simulation of solid particles behavior in a heated cavity at high Rayleigh numbers, *Aerosol Science and Technology,* Vol. 46, pp. 1382-1391.

Bagley, S. P. and Wornat, M. J. 2011, Identification of five-to seven-ring polycyclic aromatic hydrocarbons from the supercritical pyrolysis of n-decane, *Energy & Fuels,* Vol. 25, pp. 4517-4527.

Bakali, A., Mercier, X., Wartel, M., Acevedo, F., Burns, I., Gasnot, L., Pauwels, J.-F. and Desgroux, P. 2012, Modeling of PAHs in low pressure sooting premixed methane flame, *Energy,* Vol. 43, pp. 73-84.

Balthasar, M. and Kraft, M. 2003, A stochastic approach to calculate the particle size distribution function of soot particles in laminar premixed flames, *Combustion and Flame,* Vol. 133, pp. 289-298.

Barrett, J. and Webb, N. 1998, A comparison of some approximate methods for solving the aerosol general dynamic equation, *Journal of Aerosol Science,* Vol. 29, pp. 31-39.

Batterham, R., Hall, J. and Barton, G. 1981, Pelletizing kinetics and simulation of full scale balling circuits, *3rd International Symposium on Agglomeration*, pp. 136-150.

Battin-Leclerc, F., Simmie, J. M. and Blurock, E. 2013, Cleaner combustion, Developing Detailed Chemical Kinetic Models. Series: Green Energy and Technology. Cham: , Springer International Publishing AG.

Beck, A. D. 1993, Density-functional thermochemistry. III. The role of exact exchange, *J. Chem. Phys,* Vol. 98, pp. 5648-5652.

Blanquart, G. and Pitsch, H. 2009a, Analyzing the effects of temperature on soot formation with a joint volume-surface-hydrogen model, *Combustion and Flame,* Vol. 156, pp. 1614-1626.

Blanquart, G. and Pitsch, H. 2009b, A joint volume-surface-hydrogen multi-variate model for soot formation, Combustion Generated Fine Carbonaceous Particles, KIT Scientific Publishing, pp. 437-463.

Blevins, L. G., Fletcher, R. A., Benner Jr, B. A., Steel, E. B. and Mulholland, G. W. 2002, The existence of young soot in the exhaust of inverse diffusion flames, *Proceedings of the Combustion Institute,* Vol. 29, pp. 2325-2333.

Bockhorn, H. 2013, Soot formation in combustion: mechanisms and models, Springer Science & Business Media.

Boje, A. and Kraft, M. 2022, Stochastic population balance methods for detailed modelling of flame-made aerosol particles, *Journal of Aerosol Science,* Vol. 159, Article ID: 105895.

Bond, T. C., Doherty, S. J., Fahey, D. W., Forster, P. M., Berntsen, T., DeAngelo, B. J., Flanner, M. G., Ghan, S., Kärcher, B. and Koch, D. 2013, Bounding the role of black carbon in the climate system: A scientific assessment, *Journal of Geophysical Research: Atmospheres,* Vol. 118, pp. 5380-5552.

Bové, H., Bongaerts, E., Slenders, E., Bijnens, E. M., Saenen, N. D., Gyselaers, W., Van Eyken, P., Plusquin, M., Roeffaers, M. B. and Ameloot, M. 2019, Ambient black carbon particles reach the fetal side of human placenta, *Nature Communications,* Vol. 10, pp. 1-7.

Bowal, K. 2021. Modelling the Self-Assembly and Structure of Carbonaceous Nanoparticles. PhD Thesis, University of Cambridge, UK.

Bramlette, R. B. and Depcik, C. D. 2020, Review of propane-air chemical kinetic mechanisms for a unique jet propulsion application, *Journal of the Energy Institute,* Vol. 93, pp. 857-877.

Brown, L. M., Collings, N., Harrison, R. M., Maynard, R. L. and Maynard, A. D. 2003, Ultrafine particles in the atmosphere, World Scientific.

Bunker, D. L. and Hase, W.-L. 1973, On non‐RRKM unimolecular kinetics: Molecules in general, and CH3NC in particular, *The Journal of Chemical Physics,* Vol. 59, pp. 4621-4632.

Burcat, A. 1984, Thermochemical data for combustion calculations, Combustion Chemistry, Springer, pp. 455-473.

Cai, Y., Zhang, Z. and Zhou, L. 2022, Experimental study on correlation between PAHs and soot in laminar co-flow diffusion flames of n-heptane at elevated pressure, *Fuel,* Vol. 309, Article ID: 122107.

Carey, V. 2002, Molecular dynamics simulations and liquid-vapor phase-change phenomena, *Microscale Thermophysical Engineering,* Vol. 6, pp. 1-2.

Castro-Marcano, F., Kamat, A. M., Russo Jr, M. F., van Duin, A. C. and Mathews, J. P. 2012, Combustion of an Illinois No. 6 coal char simulated using an atomistic char representation and the ReaxFF reactive force field, *Combustion and Flame,* Vol. 159, pp. 1272-1285.

Cenker, E. 2014, Imaging measurements of soot particle size and soot volume fraction with laser-induced incandescence at Diesel engine conditions, Ecole Centrale Paris.

Chakraborty, D., Lischka, H. and Hase, W. L. 2020, Dynamics of pyrene-dimer association and ensuing pyrene-dimer dissociation, *The Journal of Physical Chemistry A,* Vol. 124, pp. 8907-8917.

Chambers, C. C. and Thompson, D. L. 1995, Further studies of the classical dynamics of the unimolecular dissociation of RDX, *The Journal of Physical Chemistry,* Vol. 99, pp. 15881-15889.

Chan, T. L., Liu, S. and Yue, Y. 2018, Nanoparticle formation and growth in turbulent flows using the bimodal TEMOM, *Powder Technology,* Vol. 323, pp. 507-517.

Chenoweth, K., Van Duin, A. C. and Goddard, W. A. 2008, ReaxFF reactive force field for molecular dynamics simulations of hydrocarbon oxidation, *The Journal of Physical Chemistry A,* Vol. 112, pp. 1040-1053.

Cheung, S. C., Yeoh, G. H. and Tu, J. 2009, A review of population balance modelling for isothermal bubbly flows, *The Journal of Computational Multiphase Flows,* Vol. 1, pp. 161-199.

Chong, S. T. 2018, Modeling of Turbulent Sooting Flames, The University of Michigan.

Chung, S.-H. and Violi, A. 2011, Peri-condensed aromatics with aliphatic chains as key intermediates for the nucleation of aromatic hydrocarbons, *Proceedings of the Combustion Institute,* Vol. 33, pp. 693-700.

Coelho, P. and Carvalho, M. 1995, Modeling of soot formation and oxidation in turbulent diffusion flames, *Journal of Thermophysics and Heat Transfer,* Vol. 9, pp. 644-652.

Cygan, R. T. and Kubicki, J. D. 2018, Molecular modeling theory: Applications in the geosciences*,* Walter de Gruyter.

D'Alessio, A., Barone, A., Cau, R., D'Anna, A. and Minutolo, P. 2005, Surface deposition and coagulation efficiency of combustion generated nanoparticles in the size range from 1 to 10 nm, *Proceedings of the Combustion Institute,* Vol. 30, pp. 2595-2603.

D'Anna, A. 2009, Combustion-formed nanoparticles, *Proceedings of the Combustion Institute,* Vol. 32, pp. 593-613.

Dale, S. 2021, BP statistical review of world energy, *British Petroleum Company*.

Dasappa, S. and Camacho, J. 2021, Evolution in size and structural order for incipient soot formed at flame temperatures greater than 2100 K, *Fuel,* Vol. 291, Article ID: 120196.

Debry, E., Sportisse, B. and Jourdain, B. 2003, A stochastic approach for the numerical simulation of the general dynamics equation for aerosols, *Journal of Computational Physics,* Vol. 184, pp. 649-669.

Dederichs, A. S. 2004, Flamelet Modelling of Soot Formation in Diffusion Flames. PhD Thesis, Lund University.

DeVille, L., Riemer, N. and West, M. 2019, Convergence of a generalized weighted flow algorithm for stochastic particle coagulation, *Journal of Computational Dynamics,* Vol. 6, Article ID: 69.

DeVille, R. L., Riemer, N. and West, M. 2011, Weighted Flow Algorithms (WFA) for stochastic particle coagulation, *Journal of Computational Physics,* Vol. 230, pp. 8427-8451.

di Veroli, G. and Rigopoulos, S. 2010, Modeling of turbulent precipitation: A transported population balance - PDF method, *AIChE Journal,* Vol. 56, pp. 878-892.

Do, H.-Q., Tran, L.-S., Gasnot, L., Mercier, X. and El Bakali, A. 2021, Experimental study of the influence of hydrogen as a fuel additive on the formation of soot precursors and particles in atmospheric laminar premixed flames of methane, *Fuel,* Vol. 287, Article ID: 119517.

Dobbins, R., Fletcher, R. and Lu, W. 1995, Laser microprobe analysis of soot precursor particles and carbonaceous soot, *Combustion and Flame,* Vol. 100, pp. 301-309.

Dobbins, R., Fletcher, R. A. and Chang, H.-C. 1998, The evolution of soot precursor particles in a diffusion flame, *Combustion and Flame,* Vol. 115, pp. 285-298.

Dobbins, R. A. and Subramaniasivam, H. 1994, Soot precursor particles in flames, Soot Formation in Combustion, Springer, pp. 290-301.

Dong, X., Jia, M., Chang, Y., Wang, P. and Niu, B. 2020, Kinetic modeling study of polycyclic aromatic hydrocarbon formation and oxidation for oxygenated fuels including methanol, n-Butanol, methyl butanoate, and dimethyl ether, *Energy & Fuels,* Vol. 34, pp. 4882-4898.

Donnet, J.-B. 1994, Fifty years of research and progress on carbon black, *Carbon,* Vol. 32, pp. 1305-1310.

Döntgen, M., Przybylski-Freund, M.-D., Kröger, L. C., Kopp, W. A., Ismail, A. E. and Leonhard, K. 2015, Automated discovery of reaction pathways, rate constants, and transition states using reactive molecular dynamics simulations, *Journal of Chemical Theory and Computation,* Vol. 11, pp. 2517-2524.

Du, J., Strenzke, G., Bück, A. and Tsotsas, E. 2022, Monte Carlo modeling of spray agglomeration in a cylindrical fluidized bed: From batch-wise to continuous processes, *Powder Technology,* Vol. 396, pp. 113-126.

Efendiev, Y. 2004, Modeling and simulation of multi-component aerosol dynamics, *Computational & Applied Mathematics,* Vol. 23, pp. 401-423.

Efendiev, Y. and Zachariah, M. 2002, Hybrid Monte Carlo method for simulation of two-component aerosol coagulation and phase segregation, *Journal of Colloid and Interface Science,* Vol. 249, pp. 30-43.

Eibeck, A. and Wagner, W. 2000, An efficient stochastic algorithm for studying coagulation dynamics and gelation phenomena, *SIAM Journal on Scientific Computing,* Vol. 22, pp. 802-821.

Eibeck, A. and Wagner, W. 2001a, Stochastic algorithms for studying coagulation dynamics and gelation phenomena, *Monte Carlo Methods and Applications,* Vol. 7, pp. 157-166.

Eibeck, A. and Wagner, W. 2001b, Stochastic particle approximations for Smoluchoski's coagulation equation, *Annals of Applied Probability*, pp. 1137-1165.

Elvati, P., Turrentine, K. and Violi, A. 2019, The role of molecular properties on the dimerization of aromatic compounds, *Proceedings of the Combustion Institute,* Vol. 37, pp. 1099-1105.

Elvati, P. and Violi, A. 2013, Thermodynamics of poly-aromatic hydrocarbon clustering and the effects of substituted aliphatic chains, *Proceedings of the Combustion Institute,* Vol. 34, pp. 1837-1843.

Evans, D. J. and Holian, B. L. 1985, The nose–hoover thermostat, *The Journal of Chemical Physics,* Vol. 83, pp. 4069-4074.

Faccinetto, A., Desgroux, P., Ziskind, M., Therssen, E. and Focsa, C. 2011, High-sensitivity detection of polycyclic aromatic hydrocarbons adsorbed onto soot particles using laser desorption/laser ionization/time-of-flight mass spectrometry: An approach to studying the soot inception process in low-pressure flames, *Combustion and Flame,* Vol. 158, pp. 227-239.

Fairweather, M., Jones, W. and Lindstedt, R. 1992, Predictions of radiative transfer from a turbulent reacting jet in a cross-wind, *Combustion and Flame,* Vol. 89, pp. 45-63.

Fan, C., Guan, Z., Wei, J., Pan, M., Huang, H. and Wei, M. 2022, An assessment of soot chemical property from a modern diesel engine fueled with dimethyl carbonate-diesel blends, *Fuel,* Vol. 309, Article ID: 122220.

Fan, J., Zhang, X., Chen, L. and Cen, K. 1997, New stochastic particle dispersion modeling of a turbulent particle-laden round jet, *Chemical Engineering Journal,* Vol. 66, pp. 207-215.

Feitelberg, A., Longwell, J. and Sarofim, A. 1993, Metal enhanced soot and PAH formation, *Combustion and Flame,* Vol. 92, pp. 241-253.

Findik, F., Yilmaz, R. and Köksal, T. 2004, Investigation of mechanical and physical properties of several industrial rubbers, *Materials & design,* Vol. 25, pp. 269-276.

Frenkel, D. and Smit, B. 2001, Understanding molecular simulation: from Algorithms to Applications*,* Elsevier.

Frenklach, M. and Wang, H. 1991, Detailed modeling of soot particle nucleation and growth, in Symposium (International) on Combustion, Vol. 23, pp. 1559-1566.

Frenklach, M. and Wang, H. 1994, Detailed mechanism and modeling of soot particle formation, Soot Formation in Combustion, Springer, pp. 165-192.

Frenklach, M. 2002a, Method of moments with interpolative closure, *Chemical Engineering Science,* Vol. 57, pp. 2229-2239.

Frenklach, M. 2002b, Reaction mechanism of soot formation in flames, *Physical Chemistry Chemical Physics,* Vol. 4, pp. 2028-2037.

Frenklach, M. and Mebel, A. M. 2020, On the mechanism of soot nucleation, *Physical Chemistry Chemical Physics,* Vol. 22, pp. 5314-5331.

Friedlander, S. K. 2000, Smoke, dust, and haze*,* Oxford University Press.

Garcia, A. L., Van Den Broeck, C., Aertsens, M. and Serneels, R. 1987, A Monte Carlo simulation of coagulation, *Physica A: Statistical Mechanics and its Applications,* Vol. 143, pp. 535-546.

Gelbard, F., Tambour, Y. and Seinfeld, J. H. 1980, Sectional representations for simulating aerosol dynamics, *Journal of Colloid and Interface Science,* Vol. 76, pp. 541-556.

Gillespie, D. T. 1975, An exact method for numerically simulating the stochastic coalescence process in a cloud, *Journal of Atmospheric Sciences,* Vol. 32, pp. 1977-1989.

Glassman, I. 1989, Soot formation in combustion processes, in Symposium (international) on Combustion, Vol. 22, pp. 295-311.

Gleason, K., Carbone, F. and Gomez, A. 2021, PAHs controlling soot nucleation in 0.101—0.811 MPa ethylene counterflow diffusion flames, *Combustion and Flame,* Vol. 227, pp. 384-395.

Golovitchev, V. I., Tao, F. and Chomiak, J. 1999, Numerical evaluation of soot formation control at diesel-like conditions by reducing fuel injection timing, *SAE Transactions*, pp. 1705-1719.

Goodson, M. and Kraft, M. 2002, An efficient stochastic algorithm for simulating nano-particle dynamics, *Journal of Computational Physics,* Vol. 183, pp. 210-232.

Gordon, R. G. 1968, Error bounds in equilibrium statistical mechanics, *Journal of Mathematical Physics,* Vol. 9, pp. 655-663.

Grimme, S., Antony, J., Ehrlich, S. and Krieg, H. 2010, A consistent and accurate ab initio parametrization of density functional dispersion correction (DFT-D) for the 94 elements H-Pu, *The Journal of Chemical Physics,* Vol. 132, Article ID: 154104.

Grimme, S., Ehrlich, S. and Goerigk, L. 2011, Effect of the damping function in dispersion corrected density functional theory, *Journal of Computational Chemistry,* Vol. 32, pp. 1456-1465.

Gu, M., Liu, F., Consalvi, J.-L. and Gülder, Ö. L. 2021, Effects of pressure on soot formation in laminar coflow methane/air diffusion flames doped with n-heptane and toluene between 2 and 8 atm, *Proceedings of the Combustion Institute,* Vol. 38, pp. 1403-1412.

Guo, J., Tang, Y., Raman, V. and Im, H. G. 2021, Numerical investigation of pressure effects on soot formation in laminar coflow ethylene/air diffusion flames, *Fuel,* Vol. 292, Article ID: 120176.

Hagen, F., Hardock, F., Koch, S., Sebbar, N., Bockhorn, H., Loukou, A., Kubach, H., Suntz, R., Trimis, D. and Koch, T. 2021, Why Soot is not Alike Soot: A Molecular/Nanostructural Approach to Low Temperature Soot Oxidation, *Flow, Turbulence and Combustion,* Vol. 106, pp. 295-329.

Haibo, Z., Chuguang, Z. and Minghou, X. 2005, Multi-Monte Carlo approach for general dynamic equation considering simultaneous particle coagulation and breakage, *Powder Technology,* Vol. 154, pp. 164-178.

Hairuddin, A. A. 2014, Implementation of conditional moment closure in a zero-dimensional model for HCCI engines and comparison with experiment, University of Southern Queensland.

Han, S., Li, X., Nie, F., Zheng, M., Liu, X. and Guo, L. 2017, Revealing the initial chemistry of soot nanoparticle formation by ReaxFF molecular dynamics simulations, *Energy & Fuels,* Vol. 31, pp. 8434-8444.

Hansen, N., Cool, T. A., Westmoreland, P. R. and Kohse-Höinghaus, K. 2009, Recent contributions of flame-sampling molecular-beam mass spectrometry to a fundamental understanding of combustion chemistry, *Progress in Energy and Combustion Science,* Vol. 35, pp. 168-191.

Harris, S. J. and Weiner, A. M. 1983, Surface growth of soot particles in premixed ethylene/air flames, *Combustion Science and Technology,* Vol. 31, pp. 155-167.

Harris, S. J. and Weiner, A. M. 1985, Chemical kinetics of soot particle growth, *Annual Review of Physical Chemistry,* Vol. 36, pp. 31-52.

Hase, W. L. 1986, Unimolecular and intramolecular dynamics. Relationship to potential energy surface properties, *The Journal of Physical Chemistry,* Vol. 90, pp. 365-374.

Haynes, B. S. and Wagner, H. G. 1981, Soot formation, *Progress in Energy and Combustion Science,* Vol. 7, pp. 229-273.

He, Y. and Zhao, H. 2016, Conservative particle weighting scheme for particle collision in gas-solid flows, *International Journal of Multiphase Flow,* Vol. 83, pp. 12-26.

Herdman, J. D. and Miller, J. H. 2008, Intermolecular potential calculations for polynuclear aromatic hydrocarbon clusters, *The Journal of Physical Chemistry A,* Vol. 112, pp. 6249-6256.

Hirche, D., Birkholz, F. and Hinrichsen, O. 2019, A hybrid Eulerian-Eulerian-Lagrangian model for gas-solid simulations, *Chemical Engineering Journal,* Vol. 377, Article ID: 119743.

Hiroyasu, H., Kadota, T. and Arai, M. 1983, Development and use of a spray combustion modeling to predict diesel engine efficiency and pollutant emissions: Part 1 combustion modeling, *Bulletin of JSME,* Vol. 26, pp. 569-575.

Hoerlle, C. A., França, F. H. R., Pagot, P. R. and Pereira, F. M. 2020, Effects of radiation modeling on non-premixed sooting flames simulations under oxyfuel conditions, *Combustion and Flame,* Vol. 217, pp. 294-305.

Holder, B., Aplin, J. D., Gomez-Lopez, N., Heazell, A. E., James, J. L., Jones, C. J., Jones, H., Lewis, R. M., Mor, G. and Roberts, C. T. 2021, 'Fetal side'of the placenta: anatomical mis-annotation of carbon particle 'transfer'across the human placenta, *Nature Communications,* Vol. 12, pp. 1-5.

Homann, K. H. 1998, Fullerenes and soot formation—new pathways to large particles in flames, *Angewandte Chemie International Edition,* Vol. 37, pp. 2434-2451.

Hou, D., Lindberg, C. S., Manuputty, M. Y., You, X. and Kraft, M. 2019, Modelling soot formation in a benchmark ethylene stagnation flame with a new detailed population balance model, *Combustion and Flame,* Vol. 203, pp. 56-71.

Hou, D., Lindberg, C. S., Wang, M., Manuputty, M. Y., You, X. and Kraft, M. 2020a, Simulation of primary particle size distributions in a premixed ethylene stagnation flame, *Combustion and Flame,* Vol. 216, pp. 126-135.

Hou, D., Zong, D., Lindberg, C. S., Kraft, M. and You, X. 2020b, On the coagulation efficiency of carbonaceous nanoparticles, *Journal of Aerosol Science,* Vol. 140, Article ID: 105478.

Hou, D., Pascazio, L., Martin, J., Zhou, Y., Kraft, M. and You, X. 2022, On the reactive coagulation of incipient soot nanoparticles, *Journal of Aerosol Science,* Vol. 159, Article ID: 105866.

Hounslow, M., Ryall, R. and Marshall, V. 1988, A discretized population balance for nucleation, growth, and aggregation, *AIChE journal,* Vol. 34, pp. 1821-1832.

Hsu, T.-J. and Mou, C.-Y. 1992, Molecular dynamics study of liquid-solid transition of dense Lennard-Jones liquid, *Molecular Physics,* Vol. 75, pp. 1329-1344.

Hu, H. H., Patankar, N. A. and Zhu, M. 2001, Direct numerical simulations of fluid–solid systems using the arbitrary Lagrangian–Eulerian technique, *Journal of Computational Physics,* Vol. 169, pp. 427-462.

Hu, X., Yu, Z., Chen, L., Huang, Y., Zhang, C., Salehi, F., Chen, R., Harrison, R. M. and Xu, J. 2022, Morphological and nanostructure characteristics of soot particles emitted from a jet-stirred reactor burning aviation fuel, *Combustion and Flame,* Vol. 236, Article ID: 111760.

Hulburt, H. M. and Katz, S. 1964, Some problems in particle technology: A statistical mechanical formulation, *Chemical Engineering Science,* Vol. 19, pp. 555-574.

Humphrey, W., Dalke, A. and Schulten, K. 1996, VMD: visual molecular dynamics, *Journal of Molecular Graphics,* Vol. 14, pp. 33-38.

Huo, Z., Cleary, M. J., Sirignano, M. and Masri, A. R. 2021, A sectional soot formation kinetics scheme with a new model for coagulation efficiency, *Combustion and Flame,* Vol. 230, Article ID: 111444.

Issa, R. I. 1986, Solution of the implicitly discretised fluid flow equations by operator-splitting, *Journal of Computational Physics,* Vol. 62, pp. 40-65.

Jacobson, M. Z. 2001, Strong radiative heating due to the mixing state of black carbon in atmospheric aerosols, *Nature,* Vol. 409, pp. 695-697.

Jacobson, M. Z. 2010, Short-term effects of controlling fossil-fuel soot, biofuel soot and gases, and methane on climate, Arctic ice, and air pollution health, *Journal of Geophysical Research: Atmospheres,* Vol. 115, Article ID: 14209.

Jander, H. and Wagner, H. G. 1990, Soot formation in combustion*,* An International Round Table Discussion.

Jasak, H., Jemcov, A. and Tukovic, Z. 2007, OpenFOAM: A C++ library for complex physics simulations, 20 pp, in International Workshop on Coupled Methods in Numerical Dynamics, IUC, Dubrovnik, Croatia, September 19-21 2007.

Jeong, J. I. and Choi, M. 2001, A sectional method for the analysis of growth of polydisperse non-spherical particles undergoing coagulation and coalescence, *Journal of Aerosol Science,* Vol. 32, pp. 565-582.

Jiang, H., Yu, M., Shen, J. and Xie, M. 2021, Inverse Gaussian distributed method of moments for agglomerate coagulation due to Brownian motion in the entire size regime, *International Journal of Heat and Mass Transfer,* Vol. 173, Article ID: 121229.

Jiang, X. and Chan, T. L. 2021a, A new weighted fraction Monte Carlo method for particle coagulation, *International Journal of Numerical Methods for Heat & Fluid Flow,* Vol. 31, pp. 3009-3029.

Jiang, X. and Chan, T. L. 2021b, Lagrangian particle tracking with new weighted fraction Monte Carlo method for studying the soot particle size distributions in premixed flames, *International Journal of Numerical Methods for Heat & Fluid Flow.* Early access on September 2, 2021.

Johansson, K., Head-Gordon, M., Schrader, P., Wilson, K. and Michelsen, H. 2018, Resonance-stabilized hydrocarbon-radical chain reactions may explain soot inception and growth, *Science,* Vol. 361, pp. 997-1000.

Kalbhor, A. and van Oijen, J. 2020, Effects of hydrogen enrichment and water vapour dilution on soot formation in laminar ethylene counterflow flames, *International Journal of Hydrogen Energy,* Vol. 45, pp. 23653-23673.

Kanda, H., Hiramatsu, T. and Goto, M. 2021, Molecular dynamics simulation and thermodynamic model of triple point of Lennard-Jones fluid in cylindrical nanopores, *Chemical Engineering Science,* Vol. 244, Article ID: 116829.

Karlsson, A., Török, S., Roth, A. and Bengtsson, P.-E. 2022, Numerical scattering simulations for estimating soot aggregate morphology from nephelometer scattering measurements, *Journal of Aerosol Science,* Vol. 159, Article ID: 105828.

Kazakov, A. and Foster, D. E. 1998, Modeling of soot formation during DI diesel combustion using a multi-step phenomenological model, *SAE Transactions*, pp. 1016-1028.

Kazakov, A. and Frenklach, M. 1998, Dynamic modeling of soot particle coagulation and aggregation: Implementation with the method of moments and application to high-pressure laminar premixed flames, *Combustion and Flame,* Vol. 114, pp. 484-501.

Kazakov, A., Wang, H. and Frenklach, M. 1995, Detailed modeling of soot formation in laminar premixed ethylene flames at a pressure of 10 bar, *Combustion and Flame,* Vol. 100, pp. 111-120.

Kee, R. J., Dixon-Lewis, G., Warnatz, J., Coltrin, M. E. and Miller, J. A. 1986, A Fortran computer code package for the evaluation of gas-phase multicomponent transport properties, *Sandia National Laboratories Report SAND86-8246,* Vol. 13, pp. 80401-1887.

Kelesidis, G. A. and Pratsinis, S. E. 2021, Determination of the volume fraction of soot accounting for its composition and morphology, *Proceedings of the Combustion Institute,* Vol. 38, pp. 1189-1196.

Keller, M. 2019, Development of a multi-scale approach using chemical kinetics and reactive force field molecular dynamics to model soot formation and oxidation, Institut polytechnique de Paris.

Keller, M., de Bruin, T., Matrat, M. l., Nicolle, A. and Catoire, L. 2019, A theoretical multiscale approach to study the initial steps involved in the chemical reactivity of soot precursors, *Energy & Fuels,* Vol. 33, pp. 10255-10266.

Kennedy, I. M. 1997, Models of soot formation and oxidation, *Progress in Energy and Combustion Science,* Vol. 23, pp. 95-132.

Khan, I.M. and Greeves, G. 1974, A method for calculating the formation and combustion of soot in diesel engines, *Heat Transfer in Flames,* Chapter 25, Scripta, Washington DC, USA.

Kholghy, M. R. and Kelesidis, G. A. 2021, Surface growth, coagulation and oxidation of soot by a monodisperse population balance model, *Combustion and Flame,* Vol. 227, pp. 456-463.

Khosousi, A. and Dworkin, S. B. 2015, Soot surface reactivity during surface growth and oxidation in laminar diffusion flames, *Combustion and Flame,* Vol. 162, pp. 4523-4532.

Kim, C., Xu, F., Sunderland, P., El-Leathy, A. and Faeth, G. 2006, Soot formation and oxidation in laminar flames, AIAA 2006-1508, 17 pp in 44th AIAA Aerospace Sciences Meeting and Exhibit, January 9-12, 2006, Reno, Nevada, USA.

Kim, D., Zhang, Y. and Kook, S. 2021, Influence of wall-wetting conditions on in-flame and exhaust soot structures in a spark ignition direct injection petrol engine, *International Journal of Engine Research,* Vol. 22, pp. 1958-1973.

Komninos, N. and Rakopoulos, C. 2012, Modeling HCCI combustion of biofuels: A review, *Renewable and Sustainable Energy Reviews,* Vol. 16, pp. 1588-1610.

Kong, D., Zhou, M., Wang, S., Luo, K., Li, D. and Fan, J. 2021, Eulerian-Lagrangian Simulation of Chemical Looping Combustion with Wide Particle Size Distributions, *Chemical Engineering Science*, Vol. 245, Article ID: 116849.

Kotalczyk, G. and Kruis, F. E. 2017, A Monte Carlo method for the simulation of coagulation and nucleation based on weighted particles and the concepts of stochastic resolution and merging, *Journal of Computational Physics,* Vol. 340, pp. 276-296.

Köylü, Ü. Ö., Faeth, G. M., Farias, T. L. and Carvalho, M. d. G. 1995, Fractal and projected structure properties of soot aggregates, *Combustion and Flame,* Vol. 100, pp. 621-633.

Kraft, M. 2005, Modelling of particulate processes, *KONA Powder and Particle Journal,* Vol. 23, pp. 18-35.

Krishna, S., Sreedhar, I. and Patel, C. M. 2021, Molecular dynamics simulation of polyamide-based materials–A review, *Computational Materials Science,* Vol. 200, Article ID: 110853.

Kronholm, D. F. and Howard, J. B. 2000, Analysis of soot surface growth pathways using published plug-flow reactor data with new particle size distribution measurements and published premixed flame data, *Proceedings of the Combustion Institute,* Vol. 28, pp. 2555-2561.

Krossing, I. and Slattery, J. M. 2006, Semi-empirical methods to predict the physical properties of ionic liquids: An overview of recent developments, *Zeitschrift für Physikalische Chemie,* Vol. 220, pp. 1343-1359.

Kruis, F. E., Maisels, A. and Fissan, H. 2000, Direct simulation Monte Carlo method for particle coagulation and aggregation, *AIChE Journal,* Vol. 46, pp. 1735-1742.

Kruis, F. E., Wei, J., van der Zwaag, T. and Haep, S. 2012, Computational fluid dynamics based stochastic aerosol modeling: combination of a cell-based weighted random walk method and a constant-number Monte-Carlo method for aerosol dynamics, *Chemical Engineering Science,* Vol. 70, pp. 109-120.

Kumar, S. and Ramkrishna, D. 1996a, On the solution of population balance equations by discretization—I. A fixed pivot technique, *Chemical Engineering Science,* Vol. 51, pp. 1311-1332.

Kumar, S. and Ramkrishna, D. 1996b, On the solution of population balance equations by discretization—II. A moving pivot technique, *Chemical Engineering Science,* Vol. 51, pp. 1333-1342.

Kuo, K. K. 1986, Principles of combustion*,* Wiley-Interscience.

Kwon, H. and Xuan, Y. 2021, Pyrolysis of bio-derived dioxolane fuels: A ReaxFF molecular dynamics study, *Fuel,* Vol. 306, Article ID: 121616.

Lahaye, J. 2013, Soot in Combustion Systems and Its Toxic Properties*,* Springer Science & Business Media.

Lee, K., Thring, M. and Beer, J. 1962, On the rate of combustion of soot in a laminar soot flame, *Combustion and Flame,* Vol. 6, pp. 137-145.

Lee, K. and Matsoukas, T. 2000, Simultaneous coagulation and break-up using constant-N Monte Carlo, *Powder Technology,* Vol. 110, pp. 82-89.

Lennard-Jones, J. E. 1931, Cohesion, *Proceedings of the Physical Society,* Vol. 43, pp. 461-482**.**

Leverant, C. J., Harvey, J. A., Alam, T. M. and Greathouse, J. A. 2021, Machine Learning Self-Diffusion Prediction for Lennard-Jones Fluids in Pores, *The Journal of Physical Chemistry C,* Vol. 125, pp. 25898-25906.

Li, M., Wu, H., Liu, X., Wei, Z., Tian, H., Zhang, Q. and Li, Z. 2021a, Numerical investigations on pilot ignited high pressure direct injection natural gas engines: A review, *Renewable and Sustainable Energy Reviews,* Vol. 150, Article ID: 111390.

Li, X., Zheng, M., Ren, C. and Guo, L. 2021b, ReaxFF molecular dynamics simulations of thermal reactivity of various fuels in pyrolysis and combustion, *Energy & Fuels,* Vol. 35, pp. 11707-11739.

Liffman, K. 1992, A direct simulation Monte-Carlo method for cluster coagulation, *Journal of Computational Physics,* Vol. 100, pp. 116-127.

Liguori, N., Croce, R., Marrink, S. J. and Thallmair, S. 2020, Molecular dynamics simulations in photosynthesis, *Photosynthesis Research,* Vol. 144, pp. 273-295.

Lin, J. and Chen, Z. 2013, A modified TEMOM model for Brownian coagulation of nanoparticles based on the asymptotic solution of the sectional method, *Science China Technological Sciences,* Vol. 56, pp. 3081-3092.

Lin, Y., Lee, K. and Matsoukas, T. 2002, Solution of the population balance equation using constant-number Monte Carlo, *Chemical Engineering Science,* Vol. 57, pp. 2241-2252.

Lindstedt, P. R. 1994, Simplified soot nucleation and surface growth steps for non-premixed flames, Soot Formation in Combustion, Springer, pp. 417-441.

Liu, A., Gao, Z., Rigopoulos, S., Luo, K. H. and Zhu, L. 2022, Modelling of laminar diffusion flames with biodiesel blends and soot formation, *Fuel,* Vol. 317, Article ID: 122897.

Liu, F., Guo, H., Smallwood, G. J. and Gülder, Ö. L. 2003, Numerical modelling of soot formation and oxidation in laminar coflow non-smoking and smoking ethylene diffusion flames, *Combustion Theory and Modelling,* Vol. 7, Article ID: 301.

Liu, H. and Chan, T. 2018a, Two-component aerosol dynamic simulation using differentially weighted operator splitting Monte Carlo method, *Applied Mathematical Modelling,* Vol. 62, pp. 237-253.

Liu, H. and Chan, T. L. 2018b, Differentially weighted operator splitting Monte Carlo method for simulating complex aerosol dynamic processes, *Particuology,* Vol. 36, pp. 114-126.

Liu, H., Yu, Y., Wang, C., Xu, H. and Ma, X. 2021a, Brownian coagulation of particles in the gasoline engine exhaust system: Experimental measurement and Monte Carlo simulation, *Fuel,* Vol. 303, Article ID: 121340.

Liu, P., Guo, J., Quadarella, E., Bennett, A., Gubba, S. R., Saxena, S., Chatakonda, O., Kloosterman, J. W., He, X. and Im, H. G. 2021b, The effect of preheating temperature on PAH/soot formation in methane/air co-flow flames at elevated pressure, *Fuel*, Vol. 313, Article ID: 122656.

Liu, P., Jin, H., Chen, B., Yang, J., Li, Z., Bennett, A., Farooq, A., Sarathy, S. M. and Roberts, W. L. 2021c, Rapid soot inception via α-alkynyl substitution of polycyclic aromatic hydrocarbons, *Fuel,* Vol. 295, Article ID: 120580.

Liu, S. and Chan, T. L. 2017a, A coupled CFD-Monte Carlo method for simulating complex aerosol dynamics in turbulent flows, *Aerosol Science and Technology,* Vol. 51, pp. 269-281.

Liu, S. and Chan, T. L. 2017b, A stochastically weighted operator splitting Monte Carlo (SWOSMC) method for the numerical simulation of complex aerosol dynamic processes, *International Journal of Numerical Methods for Heat & Fluid Flow,* Vol. 27, pp. 263-278.

Liu, S., Chan, T. L., He, Z., Lu, Y., Jiang, X. and Wei, F. 2019a, Soot formation and evolution characteristics in premixed methane/ethylene-oxygen-argon burner-stabilized stagnation flames, *Fuel,* Vol. 242, pp. 871-882.

Liu, S., Chan, T. L., Lin, J. and Yu, M. 2019b, Numerical study on fractal-like soot aggregate dynamics of turbulent ethylene-oxygen flame, *Fuel,* Vol. 256, Article ID: 115857.

Liu, Y., Song, C., Lv, G., Zhang, W. and Chen, H. 2021d, Evaluation of the oxidative reactivity and electrical properties of soot particles, *Carbon,* Vol. 178, pp. 37-47.

Luo, Z., Som, S., Sarathy, S. M., Plomer, M., Pitz, W. J., Longman, D. E. and Lu, T. 2014, Development and validation of an n-dodecane skeletal mechanism for spray combustion applications, *Combustion Theory and Modelling,* Vol. 18, pp. 187-203.

Macadam, S., Beér, J. M., Safofim, A. F. and Hoffmann, A. B. 1996, Soot surface growth by polycyclic aromatic hydrocarbon and acetylene addition, in Symposium (International) on Combustion, Vol. 26, pp. 2295-2302.

Maisels, A., Kruis, F. E. and Fissan, H. 2004, Direct simulation Monte Carlo for simultaneous nucleation, coagulation, and surface growth in dispersed systems, *Chemical Engineering Science,* Vol. 59, pp. 2231-2239.

Mann, D. J., Halls, M. D. and Hase, W. L. 2002, Direct dynamics studies of CO-assisted carbon nanotube growth, *The Journal of Physical Chemistry B,* Vol. 106, pp. 12418-12425.

Mao, Q., Ren, Y., Luo, K. and Van Duin, A. C. 2017a, Dynamics and kinetics of reversible homo-molecular dimerization of polycyclic aromatic hydrocarbons, *The Journal of Chemical Physics,* Vol. 147, Article ID: 244305.

Mao, Q., Van Duin, A. C. and Luo, K. 2017b, Formation of incipient soot particles from polycyclic aromatic hydrocarbons: a ReaxFF molecular dynamics study, *Carbon,* Vol. 121, pp. 380-388.

Mao, Q., Hou, D., Luo, K. H. and You, X. 2018, Dimerization of polycyclic aromatic hydrocarbon molecules and radicals under flame conditions, *The Journal of Physical Chemistry A,* Vol. 122, pp. 8701-8708.

Mao, Q. and Luo, K. H. 2019, Trace metal assisted polycyclic aromatic hydrocarbons fragmentation, growth and soot nucleation, *Proceedings of the Combustion Institute,* Vol. 37, pp. 1023-1030.

Marchisio, D. L., Pikturna, J. T., Fox, R. O., Vigil, R. D. and Barresi, A. A. 2003a, Quadrature method of moments for population-balance equations, *AIChE Journal,* Vol. 49, pp. 1266-1276.

Marchisio, D. L., Vigil, R. D. and Fox, R. O. 2003b, Quadrature method of moments for aggregation–breakage processes, *Journal of Colloid and Interface Science,* Vol. 258, pp. 322-334.

Marchisio, D. L. and Fox, R. O. 2005, Solution of population balance equations using the direct quadrature method of moments, *Journal of Aerosol Science,* Vol. 36, pp. 43-73.

Marchisio, D. L. and Fox, R. O. 2013, Computational Models for Polydisperse Particulate and Multiphase Systems*,* Cambridge University Press.

Maricq, M. M. 2011, Physical and chemical comparison of soot in hydrocarbon and biodiesel fuel diffusion flames: A study of model and commercial fuels, *Combustion and Flame,* Vol. 158, pp. 105-116.

Martin, J. W., Hou, D., Menon, A., Pascazio, L., Akroyd, J., You, X. and Kraft, M. 2019, Reactivity of polycyclic aromatic hydrocarbon soot precursors: implications of localized π-radicals on rim-based pentagonal rings, *The Journal of Physical Chemistry C,* Vol. 123, pp. 26673-26682.

Martin, J. 2020, Investigating the Role of Curvature on the Formation and Thermal Transformations of Soot, PhD Thesis, University of Cambridge, UK.

Martin, J. W., Slavchov, R. I., Yapp, E. K., Akroyd, J., Mosbach, S. and Kraft, M. 2017, The polarization of polycyclic aromatic hydrocarbons curved by pentagon incorporation: the role of the flexoelectric dipole, *The Journal of Physical Chemistry C,* Vol. 121, pp. 27154-27163.

Martin, J. W., Salamanca, M. and Kraft, M. 2022, Soot inception: Carbonaceous nanoparticle formation in flames, *Progress in Energy and Combustion Science,* Vol. 88, Article ID: 100956.

Massot, M., Laurent, F., Kah, D. and De Chaisemartin, S. 2010, A robust moment method for evaluation of the disappearance rate of evaporating sprays, *SIAM Journal on Applied Mathematics,* Vol. 70, pp. 3203-3234.

McGraw, R. 1997, Description of aerosol dynamics by the quadrature method of moments, *Aerosol Science and Technology,* Vol. 27, pp. 255-265.

Megaridis, C. and Dobbins, R. 1989, Soot aerosol dynamics in a laminar ethylene diffusion flame, in Symposium (International) on Combustion, Vol. 22, pp. 353-362.

Meimaroglou, D. and Kiparissides, C. 2014, Review of Monte Carlo methods for the prediction of distributed molecular and morphological polymer properties, *Industrial & Engineering Chemistry Research,* Vol. 53, pp. 8963-8979.

Menz, W. J. and Kraft, M. 2013, A new model for silicon nanoparticle synthesis, *Combustion and Flame,* Vol. 160, pp. 947-958.

Menz, W. J., Patterson, R. I., Wagner, W. and Kraft, M. 2013, Application of stochastic weighted algorithms to a multidimensional silica particle model, *Journal of Computational Physics,* Vol. 248, pp. 221-234.

Meyer, C. and Deglon, D. 2011, Particle collision modeling–a review, *Minerals Engineering,* Vol. 24, pp. 719-730.

Micklow, G. and Gong, W. 2002, A multistage combustion model and soot formation model for direct-injection diesel engines, *Proceedings of the Institution of Mechanical Engineers, Part D: Journal of Automobile Engineering,* Vol. 216, pp. 495-504.

Mitrakos, D., Hinis, E. and Housiadas, C. 2007, Sectional modeling of aerosol dynamics in multi-dimensional flows, *Aerosol science and technology,* Vol. 41, pp. 1076-1088.

Morán, J., Poux, A. and Yon, J. 2021, Impact of the competition between aggregation and surface growth on the morphology of soot particles formed in an ethylene laminar premixed flame, *Journal of Aerosol Science,* Vol. 152, Article ID: 105690.

Morawietz, T. and Artrith, N. 2021, Machine learning-accelerated quantum mechanics-based atomistic simulations for industrial applications, *Journal of Computer-Aided Molecular Design,* Vol. 35, pp. 557-586.

Mortier, W. J., Ghosh, S. K. and Shankar, S. 1986, Electronegativity-equalization method for the calculation of atomic charges in molecules, *Journal of the American Chemical Society,* Vol. 108, pp. 4315-4320.

Mosbach, S., Celnik, M. S., Raj, A., Kraft, M., Zhang, H. R., Kubo, S. and Kim, K.-O. 2009, Towards a detailed soot model for internal combustion engines, *Combustion and Flame,* Vol. 156, pp. 1156-1165.

Moss, J., Stewart, C. and Young, K. 1995, Modeling soot formation and burnout in a high temperature laminar diffusion flame burning under oxygen-enriched conditions, *Combustion and Flame,* Vol. 101, pp. 491-500.

Mouton, T., Mercier, X. and Desgroux, P. 2015, Evidence of nucleation flames: A valuable tool for the study of soot particles inception, in Proceedings of 7th European Combustion Meeting, Budapest, Hungary, March 30 to April 2, 2015.

Mueller, M. E., Blanquart, G. and Pitsch, H. 2009, A joint volume-surface model of soot aggregation with the method of moments, *Proceedings of the Combustion Institute,* Vol. 32, pp. 785-792.

Mueller, M., Blanquart, G. and Pitsch, H. 2011, Modeling the oxidation-induced fragmentation of soot aggregates in laminar flames, *Proceedings of the Combustion Institute,* Vol. 33, pp. 667-674.

Murer, M., Furlan, V., Formica, G., Morganti, S., Previtali, B. and Auricchio, F. 2021, Numerical simulation of particles flow in Laser Metal Deposition technology comparing Eulerian-Eulerian and Lagrangian-Eulerian approaches, *Journal of Manufacturing Processes,* Vol. 68, pp. 186-197.

Nagle, J. and Strickland-Constable R .F. 1962, Oxidation of carbon between 1000-2000°C, pp. 154-164, in Proceedings of Fifth Conference on Carbon, London, England, UK.

Neese, F. 2012, The ORCA program system, *Wiley Interdisciplinary Reviews: Computational Molecular Science,* Vol. 2, pp. 73-78.

Neoh, K., Howard, J. and Sarofim, A. 1985, Effect of oxidation on the physical structure of soot, in Symposium (International) on Combustion, Vol. 20, pp. 951-957.

Nishida, K. and Hiroyasu, H. 1989, Simplified three-dimensional modeling of mixture formation and combustion in a DI diesel engine, *SAE Transactions*, pp. 276-293.

Nobili, A., Cuoci, A., Pejpichestakul, W., Pelucchi, M., Cavallotti, C. and Faravelli, T. 2022, Modeling soot particles as stable radicals: a chemical kinetic study on formation and oxidation. Part I. Soot formation in ethylene laminar premixed and counterflow diffusion flames, *Combustion and Flame*, Available online on March 5, 2022, Article ID: 112073.

Norinaga, K., Deutschmann, O., Saegusa, N. and Hayashi, J.-i. 2009, Analysis of pyrolysis products from light hydrocarbons and kinetic modeling for growth of polycyclic aromatic hydrocarbons with detailed chemistry, *Journal of Analytical and Applied Pyrolysis,* Vol. 86, pp. 148-160.

Noroozi, J. and Smith, W. R. 2021, Force-Field-Based Computational Study of the Thermodynamics of a Large Set of Aqueous Alkanolamine Solvents for Post-Combustion CO2 Capture, *Journal of Chemical Information and Modeling,* Vol. 61, pp. 4497-4513.

Olin, M., Rönkkö, T. and Dal Maso, M. 2015, CFD modeling of a vehicle exhaust laboratory sampling system: sulfur-driven nucleation and growth in diluting diesel exhaust, *Atmospheric Chemistry and Physics,* Vol. 15, pp. 5305-5323.

Omar, H. M. and Rohani, S. 2017, Crystal population balance formulation and solution methods: a review, *Crystal Growth & Design,* Vol. 17, pp. 4028-4041.

Omidvarborna, H., Kumar, A. and Kim, D.-S. 2015, Recent studies on soot modeling for diesel combustion, *Renewable and Sustainable Energy Reviews,* Vol. 48, pp. 635-647.

Ong, J. C. 2017, Development of Lagrangian Soot Tracking Method for the Study of Soot Morphology in Diesel Spray Combustion, PhD Thesis, University of Nottingham, UK.

Ono, K., Matsukawa, Y., Dewa, K., Watanabe, A., Takahashi, K., Saito, Y., Matsushita, Y., Aoki, H., Era, K. and Aoki, T. 2015, Formation mechanisms of soot from high-molecular-weight polycyclic aromatic hydrocarbons, *Combustion and Flame,* Vol. 162, pp. 2670-2678.

Orhan, K., Mayerle, R. and Pandoe, W. W. 2015, Assesment of energy production potential from tidal stream currents in Indonesia, *Energy Procedia,* Vol. 76, pp. 7-16.

Ouyang, H., Gopalakrishnan, R. and Hogan Jr, C. J. 2012, Nanoparticle collisions in the gas phase in the presence of singular contact potentials, *The Journal of Chemical Physics,* Vol. 137, Article ID: 064316.

Pachano, L., Xu, C., García-Oliver, J. M., Pastor, J. M., Novella, R. and Kundu, P. 2021, A two-equation soot-in-flamelet modeling approach applied under Spray A conditions, *Combustion and Flame,* Vol. 231, Article ID: 111488.

Panchal, A. and Menon, S. 2021, A hybrid Eulerian-Eulerian/Eulerian-Lagrangian method for dense-to-dilute dispersed phase flows, *Journal of Computational Physics,* Vol. 439, Article ID: 110339.

Pang, K. M., Ng, H. K. and Gan, S. 2011, Development of an integrated reduced fuel oxidation and soot precursor formation mechanism for CFD simulations of diesel combustion, *Fuel,* Vol. 90, pp. 2902-2914.

Park, S., Rogak, S., Bushe, W., Wen, J. and Thomson, M. 2005, An aerosol model to predict size and structure of soot particles, *Combustion Theory and Modelling,* Vol. 9, pp. 499-513.

Park, S., Wang, Y., Chung, S. H. and Sarathy, S. M. 2015, A PAH growth mechanism and effect of alcohol addition on PAH formation in counterflow ethylene diffusion flames, 5 pp, in Proceedings of 7th European Combustion Meeting. Budapest, Hungary, March 30 to April 2, 2015.

Pascazio, L., Martin, J. W., Menon, A., Hou, D., You, X. and Kraft, M. 2020, Aromatic penta-linked hydrocarbons in soot nanoparticle formation, *Proceedings of the Combustion Institute,* Vol. 38, pp. 1523-1532.

Pascazio, L., Martin, J. W., Botero, M. L., Sirignano, M., D'Anna, A. and Kraft, M. 2021, Mechanical properties of soot particles: the impact of crosslinked polycyclic aromatic hydrocarbons, *Combustion Science and Technology,* Vol. 193, pp. 643-663.

Patankar, N. and Joseph, D. 2001, Modeling and numerical simulation of particulate flows by the Eulerian–Lagrangian approach, *International Journal of Multiphase Flow,* Vol. 27, pp. 1659-1684.

Patel, R. G., Desjardins, O., Kong, B., Capecelatro, J. and Fox, R. O. 2017, Verification of Eulerian–Eulerian and Eulerian–Lagrangian simulations for turbulent fluid–particle flows, *AIChE Journal,* Vol. 63, pp. 5396-5412.

Patterson, M., Kong, S.-C., Hampson, G. and Reitz, R. D. 1994, Modeling the effects of fuel injection characteristics on diesel engine soot and NOx emissions, *SAE Transactions*, pp. 836-852.

Patterson, R. I., Wagner, W. and Kraft, M. 2011, Stochastic weighted particle methods for population balance equations, *Journal of Computational Physics,* Vol. 230, pp. 7456-7472.

Patterson, R. I. and Wagner, W. 2012, A Stochastic Weighted Particle Method for Coagulation--Advection Problems, *SIAM Journal on Scientific Computing,* Vol. 34, pp. B290-B311.

Paul, A. K., Kolakkandy, S. and Hase, W. L. 2015, Dynamics of Na+ (Benzene)+ Benzene Association and Ensuing Na+ (Benzene) 2* Dissociation, *The Journal of Physical Chemistry A,* Vol. 119, pp. 7894-7904.

Pejpichestakul, W. 2019, Chemical and physical pathways of PAH and soot formation in laminar flames, Université libre de Bruxelles.

Peter Atkins, P. and De Paula, J. 2014, Atkins' Physical Chemistry, OUP Oxford.

Plimpton, S. 1995, Fast parallel algorithms for short-range molecular dynamics, *Journal of Computational Physics,* Vol. 117, pp. 1-19.

Prakash, A., Bapat, A. and Zachariah, M. 2003, A simple numerical algorithm and software for solution of nucleation, surface growth, and coagulation problems, *Aerosol Science & Technology,* Vol. 37, pp. 892-898.

Pueschel, R., Boering, K., Verma, S., Howard, S., Ferry, G., Goodman, J., Allen, D. and Hamill, P. 1997, Soot aerosol in the lower stratosphere: Pole-to-pole variability and contributions by aircraft, *Journal of Geophysical Research: Atmospheres,* Vol. 102, pp. 13113-13118.

Qian, H.-J., van Duin, A. C., Morokuma, K. and Irle, S. 2011, Reactive molecular dynamics simulation of fullerene combustion synthesis: ReaxFF vs DFTB potentials, *Journal of Chemical Theory and Computation,* Vol. 7, pp. 2040-2048.

Qiu, L., Hua, Y., Cheng, X., Zhuang, Y. and Qian, Y. 2019, Numerical investigation of soot formation in a methane diffusion flame doped with n-heptane at elevated pressure, *Energy & Fuels,* Vol. 33, pp. 11941-11947.

Qureshi, Y., Ali, U. and Sher, F. 2021, Part load operation of natural gas fired power plant with CO2 capture system for selective exhaust gas recirculation, *Applied Thermal Engineering,* Vol. 190, Article ID: 116808.

Rakopoulos, C., Rakopoulos, D., Giakoumis, E. and Kyritsis, D. 2004, Validation and sensitivity analysis of a two zone Diesel engine model for combustion and emissions prediction, *Energy Conversion and Management,* Vol. 45, pp. 1471-1495.

Raman, V. and Fox, R. O. 2016, Modeling of fine-particle formation in turbulent flames, *Annual Review of Fluid Mechanics,* Vol. 48, pp. 159-190.

Ramkrishna, D. 2000, Population Balances: Theory and Applications to Particulate Systems in Engineering, Elsevier.

Ranzi, E., Frassoldati, A., Grana, R., Cuoci, A., Faravelli, T., Kelley, A. and Law, C. K. 2012, Hierarchical and comparative kinetic modeling of laminar flame speeds of hydrocarbon and oxygenated fuels, *Progress in Energy and Combustion Science,* Vol. 38, pp. 468-501.

Rappe, A. K. and Goddard III, W. A. 1991, Charge equilibration for molecular dynamics simulations, *The Journal of Physical Chemistry,* Vol. 95, pp. 3358-3363.

Razavi, S., Koplik, J. and Kretzschmar, I. 2014, Molecular dynamics simulations: insight into molecular phenomena at interfaces, *Langmuir,* Vol. 30, pp. 11272-11283.

Reizer, E., Viskolcz, B. and Fiser, B. 2021, Formation and growth mechanisms of polycyclic aromatic hydrocarbons: A mini-review, *Chemosphere*, Article ID: 132793.

Richter, H., Benish, T. G., Mazyar, O. A., Green, W. H. and Howard, J. B. 2000, Formation of polycyclic aromatic hydrocarbons and their radicals in a nearly sooting premixed benzene flame, *Proceedings of the Combustion Institute,* Vol. 28, pp. 2609-2618.

Rigopoulos, S. and Jones, A. G. 2003, Finite-element scheme for solution of the dynamic population balance equation, *AIChE Journal,* Vol. 49, pp. 1127-1139.

Rigopoulos, S. 2010, Population balance modelling of polydispersed particles in reactive flows, *Progress in Energy and Combustion Science,* Vol. 36, pp. 412-443.

Rodrigues, P., Franzelli, B., Vicquelin, R., Gicquel, O. and Darabiha, N. 2018, Coupling an LES approach and a soot sectional model for the study of sooting turbulent non-premixed flames, *Combustion and Flame,* Vol. 190, pp. 477-499.

Russo Jr, M. F. and van Duin, A. C. 2011, Atomistic-scale simulations of chemical reactions: Bridging from quantum chemistry to engineering, *Nuclear Instruments and Methods in Physics Research Section B: Beam Interactions with Materials and Atoms,* Vol. 269, pp. 1549-1554.

Sabbah, H., Biennier, L., Klippenstein, S. J., Sims, I. R. and Rowe, B. R. 2010, Exploring the role of PAHs in the formation of soot: Pyrene dimerization, *The Journal of Physical Chemistry Letters,* Vol. 1, pp. 2962-2967.

Saggese, C. 2015, Detailed Kinetic Modeling of Soot Formation in Combustion Processes, PhD Thesis, Politecnico di Milano, Italy.

Saggese, C., Ferrario, S., Camacho, J., Cuoci, A., Frassoldati, A., Ranzi, E., Wang, H. and Faravelli, T. 2015, Kinetic modeling of particle size distribution of soot in a premixed burner-stabilized stagnation ethylene flame, *Combustion and Flame,* Vol. 162, pp. 3356-3369.

Saggese, C., Cuoci, A., Frassoldati, A., Ferrario, S., Camacho, J., Wang, H. and Faravelli, T. 2016, Probe effects in soot sampling from a burner-stabilized stagnation flame, *Combustion and Flame,* Vol. 167, pp. 184-197.

Saini, D., Gunture, Kaushik, J., Aggarwal, R., Tripathi, K. M. and Sonkar, S. K. 2021, Carbon Nanomaterials Derived from Black Carbon Soot: A Review of Materials and Applications, *ACS Applied Nano Materials,* Vol. 4, pp. 12825–12844.

Salenbauch, S., Cuoci, A., Frassoldati, A., Saggese, C., Faravelli, T. and Hasse, C. 2015, Modeling soot formation in premixed flames using an extended conditional quadrature method of moments, *Combustion and Flame,* Vol. 162, pp. 2529-2543.

Salmaso, V. and Moro, S. 2018, Bridging molecular docking to molecular dynamics in exploring ligand-protein recognition process: an overview, *Frontiers in Pharmacology,* Vol. 9, Article ID: 923.

Schranz, H. W., Raff, L. M. and Thompson, D. L. 1991, Statistical and nonstatistical effects in bond fission reactions of SiH2 and Si2H6, *The Journal of Chemical Physics,* Vol. 94, pp. 4219-4229.

Schuetz, C. A. and Frenklach, M. 2002, Nucleation of soot: Molecular dynamics simulations of pyrene dimerization, *Proceedings of the Combustion Institute,* Vol. 29, pp. 2307-2314.

Seinfeld, J. H. and Pandis, S. N. 2016, Atmospheric chemistry and physics: from air pollution to climate change*,* John Wiley & Sons.

Selvaraj, P., Arias, P. G., Lee, B. J., Im, H. G., Wang, Y., Gao, Y., Park, S., Sarathy, S. M., Lu, T. and Chung, S. H. 2016, A computational study of ethylene–air sooting flames: Effects of large polycyclic aromatic hydrocarbons, *Combustion and Flame,* Vol. 163, pp. 427-436.

Senftle, T. P., Hong, S., Islam, M. M., Kylasa, S. B., Zheng, Y., Shin, Y. K., Junkermeier, C., Engel-Herbert, R., Janik, M. J. and Aktulga, H. M. 2016, The ReaxFF reactive force-field: development, applications and future directions, *npj Computational Materials,* Vol. 2, pp. 1-14.

Serrano, J., Martín, J., Gomez-Soriano, J. and Raggi, R. 2021, Theoretical and experimental evaluation of the spark-ignition premixed oxy-fuel combustion concept for future CO2 captive powerplants, *Energy Conversion and Management,* Vol. 244, Article ID: 114498.

Shabnam, S., Mao, Q., Van Duin, A. C. and Luo, K. 2019, Evaluation of the effect of nickel clusters on the formation of incipient soot particles from polycyclic aromatic hydrocarbons via ReaxFF molecular dynamics simulations, *Physical Chemistry Chemical Physics,* Vol. 21, pp. 9865-9875.

Shah, B., Ramkrishna, D. and Borwanker, J. 1977, Simulation of particulate systems using the concept of the interval of quiescence, *AIChE Journal,* Vol. 23, pp. 897-904.

Shao, C., Campuzano, F., Zhai, Y., Wang, H., Zhang, W. and Sarathy, S. M. 2022, Effects of ammonia addition on soot formation in ethylene laminar premixed flames, *Combustion and Flame,* Vol. 235, Article ID: 111698.

Shaohua, W. 2018, Numerical Study of Soot Formation and Oxidation Processes, PhD Thesis, National University of Singapore, Singapore.

Shariatmadar, H., Hampp, F. and Lindstedt, R. 2022, The evolution of species concentrations in turbulent premixed flames crossing the soot inception limit, *Combustion and Flame,* Vol. 235, Article ID: 111726.

Shen, H., Luo, Z., Xiong, R., Liu, X., Zhang, L., Li, Y., Du, W., Chen, Y., Cheng, H. and Shen, G. 2021, A critical review of pollutant emission factors from fuel combustion in home stoves, *Environment International,* Vol. 157, Article ID: 106841.

Shi, X., Wang, Q. and Violi, A. 2021, Reaction pathways for the formation of five-membered rings onto polyaromatic hydrocarbon framework, *Fuel,* Vol. 283, Article ID: 119023.

Shiea, M., Buffo, A., Vanni, M. and Marchisio, D. 2020, Numerical methods for the solution of population balance equations coupled with computational fluid dynamics, *Annual Review of Chemical and Biomolecular Engineering,* Vol. 11, pp. 339-366.

Siegla, D. 2013, Particulate Carbon: Formation during Combustion, Springer Science & Business Media.

Silva, N. J., Machado, F. B., Lischka, H. and Aquino, A. J. 2016, π–π stacking between polyaromatic hydrocarbon sheets beyond dispersion interactions, *Physical Chemistry Chemical Physics,* Vol. 18, pp. 22300-22310.

Singh, J. 2006, Detailed soot modelling in laminar premixed flames, PhD Thesis, University of Cambridge, UK.

Singh, J., Balthasar, M., Kraft, M. and Wagner, W. 2005, Stochastic modeling of soot particle size and age distributions in laminar premixed flames, *Proceedings of the Combustion Institute,* Vol. 30, pp. 1457-1465.

Singh, J., Patterson, R. I., Kraft, M. and Wang, H. 2006, Numerical simulation and sensitivity analysis of detailed soot particle size distribution in laminar premixed ethylene flames, *Combustion and Flame,* Vol. 145, pp. 117-127.

Singh, R. K. and Agarwal, A. K. 2022, Chapter 7- Soot and NOx Modelling for Diesel Engines, In Engine Modeling and Simulation, Springer, pp. 195-217.

Sirignano, M., Collina, A., Commodo, M., Minutolo, P. and D'Anna, A. 2012, Detection of aromatic hydrocarbons and incipient particles in an opposed-flow flame of ethylene by spectral and time-resolved laser induced emission spectroscopy, *Combustion and Flame,* Vol. 159, pp. 1663-1669.

Sirignano, M. and Russo, C. 2021, Pyrene dimerization in controlled temperature environment: An experimental study, *Proceedings of the Combustion Institute,* Vol. 38, pp. 1173-1180.

Slavinskaya, N. A., Riedel, U., Dworkin, S. B. and Thomson, M. J. 2012, Detailed numerical modeling of PAH formation and growth in non-premixed ethylene and ethane flames, *Combustion and Flame,* Vol. 159, pp. 979-995.

Smith, M. and Matsoukas, T. 1998, Constant-number Monte Carlo simulation of population balances, *Chemical Engineering Science,* Vol. 53, pp. 1777-1786.

Smoluchowski, M. v. 1916, Drei vortrage uber diffusion, brownsche bewegung und koagulation von kolloidteilchen, *Zeitschrift fur Physik,* Vol. 17, pp. 557-585.

Sorensen, C. 2011, The mobility of fractal aggregates: a review, *Aerosol Science and Technology,* Vol. 45, pp. 765-779.

Sorensen, C. and Feke, G. 1996, The morphology of macroscopic soot, *Aerosol Science and Technology,* Vol. 25, pp. 328-337.

Stanmore, B. R., Brilhac, J.-F. and Gilot, P. 2001, The oxidation of soot: a review of experiments, mechanisms and models, *Carbon,* Vol. 39, pp. 2247-2268.

Stein, S. E. and Fahr, A. 1985, High-temperature stabilities of hydrocarbons, *The Journal of Physical Chemistry,* Vol. 89, pp. 3714-3725.

Steinfeld, J. I., Francisco, J. S. and Hase, W. L. 1999, Chemical Kinetics and Dynamics*,* Prentice Hall Upper Saddle River, NJ.

Stephan, S., Schaefer, D., Langenbach, K. and Hasse, H. 2021, Mass transfer through vapour–liquid interfaces: a molecular dynamics simulation study, *Molecular Physics,* Vol. 119, Article ID: e1810798.

Stewart, J. J. 1989, Optimization of parameters for semiempirical methods II. Applications, *Journal of Computational Chemistry,* Vol. 10, pp. 221-264.

Stillinger, F. H. and Weber, T. A. 1985, Computer simulation of local order in condensed phases of silicon, *Physical Review B,* Vol. 31, Article ID: 5262.

Strickland-Constable, R. 1944, The interaction of oxygen and carbon filaments at high temperatures, *Transactions of the Faraday Society,* Vol. 40, pp. 333-343.

Stull, D. R. 1965, JANAF Thermochemical Tables*,* Clearinghouse.

Sun, L., Zhou, Y.-X., Wang, X.-D., Chen, Y.-H., Deringer, V. L., Mazzarello, R. and Zhang, W. 2021, Ab initio molecular dynamics and materials design for embedded phase-change memory, *npj Computational Materials,* Vol. 7, pp. 1-8.

Swamy, K. N. and Hase, W. L. 1984, Dynamics of ion-molecule recombination. III. Trends in the recombination efficiency, *Journal of the American Chemical Society,* Vol. 106, pp. 4071-4077.

Sweet, J., Richter, D. H. and Thain, D. 2018, GPU acceleration of Eulerian–Lagrangian particle-laden turbulent flow simulations, *International Journal of Multiphase Flow,* Vol. 99, pp. 437-445.

Tang, Q., Cai, R., You, X. and Jiang, J. 2017, Nascent soot particle size distributions down to 1 nm from a laminar premixed burner-stabilized stagnation ethylene flame, *Proceedings of the Combustion Institute,* Vol. 36, pp. 993-1000.

Tang, Q., Mei, J. and You, X. 2016, Effects of CO2 addition on the evolution of particle size distribution functions in premixed ethylene flame, *Combustion and Flame,* Vol. 165, pp. 424-432.

Tao, F., Srinivas, S., Reitz, R. D. and Foster, D. E. 2005, Comparison of three soot models applied to multi-dimensional diesel combustion simulations, *JSME International Journal Series B Fluids and Thermal Engineering,* Vol. 48, pp. 671-678.

Tesner, P., Smegiriova, T. and Knorre, V. 1971, Kinetics of dispersed carbon formation, *Combustion and Flame,* Vol. 17, pp. 253-260.

Thajudeen, T., Jeon, S. and Hogan Jr, C. J. 2015, The mobilities of flame synthesized aggregates/agglomerates in the transition regime, *Journal of Aerosol Science,* Vol. 80, pp. 45-57.

Totton, T. S., Misquitta, A. J. and Kraft, M. 2012, A quantitative study of the clustering of polycyclic aromatic hydrocarbons at high temperatures, *Physical Chemistry Chemical Physics,* Vol. 14, pp. 4081-4094.

Tsantilis, S., Kammler, H. and Pratsinis, S. 2002, Population balance modeling of flame synthesis of titania nanoparticles, *Chemical Engineering Science,* Vol. 57, pp. 2139-2156.

Turns, S. R. 1996, Introduction to combustion*,* McGraw-Hill Companies New York, NY, USA.

Valencia, S., Ruiz, S., Manrique, J., Celis, C. and da Silva, L. F. F. 2021, Soot modeling in turbulent diffusion flames: review and prospects, *Journal of the Brazilian Society of Mechanical Sciences and Engineering,* Vol. 43, pp. 1-24.

van Duin, A. C., Dasgupta, S., Lorant, F. and Goddard, W. A. 2001, ReaxFF: a reactive force field for hydrocarbons, *The Journal of Physical Chemistry A,* Vol. 105, pp. 9396-9409.

Vander Wal, R. L. and Tomasek, A. J. 2003, Soot oxidation: dependence upon initial nanostructure, *Combustion and Flame,* Vol. 134, pp. 1-9.

Vashisth, A., Ashraf, C., Zhang, W., Bakis, C. E. and Van Duin, A. C. 2018, Accelerated ReaxFF simulations for describing the reactive cross-linking of polymers, *The Journal of Physical Chemistry A,* Vol. 122, pp. 6633-6642.

Veshkini, A., Dworkin, S. B. and Thomson, M. J. 2014, A soot particle surface reactivity model applied to a wide range of laminar ethylene/air flames, *Combustion and Flame,* Vol. 161, pp. 3191-3200.

Veshkini, A. and Dworkin, S. B. 2017, A computational study of soot formation and flame structure of coflow laminar methane/air diffusion flames under microgravity and normal gravity, *Combustion Theory and Modelling,* Vol. 21, pp. 864-878.

Violi, A. 2004, Modeling of soot particle inception in aromatic and aliphatic premixed flames, *Combustion and Flame,* Vol. 139, pp. 279-287.

Violi, A., Kubota, A., Truong, T., Pitz, W., Westbrook, C. and Sarofim, A. 2002, A fully integrated kinetic monte carlo/molecular dynamics approach for the simulation of soot precursor growth, *Proceedings of the Combustion Institute,* Vol. 29, pp. 2343-2349.

Vishwanathan, G. and Reitz, R. D. 2010, Development of a practical soot modeling approach and its application to low-temperature diesel combustion, *Combustion Science and Technology,* Vol. 182, pp. 1050-1082.

Waldheim, B. 2014, Modelling of Soot Formation and Aromatic Growth in Laminar Flames and Reactor Systems, PhD Thesis Imperial College London, UK.

Waldmann, L. 1961, On the motion of spherical pariticles in nonhomogeneous gases, pp. 323-344, In Rarefied Gas Dynamics, Academic Press, New York.

Wang, B., Mosbach, S., Schmutzhard, S., Shuai, S., Huang, Y. and Kraft, M. 2016, Modelling soot formation from wall films in a gasoline direct injection engine using a detailed population balance model, *Applied Energy,* Vol. 163, pp. 154-166.

Wang, H. 2011, Formation of nascent soot and other condensed-phase materials in flames, *Proceedings of the Combustion Institute,* Vol. 33, pp. 41-67.

Wang, Y., Raj, A. and Chung, S. H. 2013, A PAH growth mechanism and synergistic effect on PAH formation in counterflow diffusion flames, *Combustion and Flame,* Vol. 160, pp. 1667-1676.

Wang, Y., Raj, A. and Chung, S. H. 2015, Soot modeling of counterflow diffusion flames of ethylene-based binary mixture fuels, *Combustion and Flame,* Vol. 162, pp. 586-596.

Wang, Y., Liu, X., Gu, M. and An, X. 2018, Numerical simulation of the effects of hydrogen addition to fuel on the structure and soot formation of a laminar axisymmetric coflow C2H4/(O2-CO2) diffusion flame, *Combustion Science and Technology,* Vol. 191, pp. 1743-1768.

Wang, Y. and Chung, S. H. 2019, Soot formation in laminar counterflow flames, *Progress in Energy and Combustion Science,* Vol. 74, pp. 152-238.

Wang, Y., Gu, M., Zhu, Y., Cao, L., Wu, J., Lin, Y. and Huang, X. 2021a, Analysis of soot formation of CH4 and C2H4 with H2 addition via ReaxFF molecular dynamics and pyrolysis–gas chromatography/mass spectrometry, *Journal of the Energy Institute,* Vol. 100, pp. 177-188.

Wang, Y., Gu, M., Zhu, Y., Cao, L., Zhu, B., Wu, J., Lin, Y. and Huang, X. 2021b, A review of the effects of hydrogen, carbon dioxide, and water vapor addition on soot formation in hydrocarbon flames, *International Journal of Hydrogen Energy,* Vol. 46, pp. 31400-31427.

Wang, Y., Pan, M., Huang, H., Zhou, X., Wei, J. and Chen, H. 2021c, Physicochemical properties of exhaust soot from lower and higher alcohols: Characterizations and impact on soot oxidation behavior, *Fuel,* Vol. 311, Article ID: 122524.

Warnatz, J., Maas, U. and Dibble, R. W. 1990, Physical and chemical fundamentals, modeling and simulation, experiments, pollutant formation, Springer.

Wei, J. and Kruis, F. E. 2013, A GPU-based parallelized Monte-Carlo method for particle coagulation using an acceptance–rejection strategy, *Chemical Engineering Science,* Vol. 104, pp. 451-459.

Weigend, F., Häser, M., Patzelt, H. and Ahlrichs, R. 1998, RI-MP2: optimized auxiliary basis sets and demonstration of efficiency, *Chemical Physics Letters,* Vol. 294, pp. 143-152.

Weigend, F. and Ahlrichs, R. 2005, Balanced basis sets of split valence, triple zeta valence and quadruple zeta valence quality for H to Rn: Design and assessment of accuracy, *Physical Chemistry Chemical Physics,* Vol. 7, pp. 3297-3305.

Weigend, F. 2006, Accurate Coulomb-fitting basis sets for H to Rn, *Physical Chemistry Chemical Physics,* Vol. 8, pp. 1057-1065.

Wen, J. Z., Thomson, M., Park, S., Rogak, S. and Lightstone, M. 2005, Study of soot growth in a plug flow reactor using a moving sectional model, *Proceedings of the Combustion Institute,* Vol. 30, pp. 1477-1484.

Wentzel, M., Gorzawski, H., Naumann, K.-H., Saathoff, H. and Weinbruch, S. 2003, Transmission electron microscopical and aerosol dynamical characterization of soot aerosols, *Journal of Aerosol Science,* Vol. 34, pp. 1347-1370.

Woo, M., Nishida, R. T., Schriefl, M. A., Stettler, M. E. and Boies, A. M. 2021, Open-source modelling of aerosol dynamics and computational fluid dynamics: Nodal method for nucleation, coagulation, and surface growth, *Computer Physics Communications,* Vol. 261, Article ID: 107765.

Woods, I. and Haynes, B. 1991, Soot surface growth at active sites, *Combustion and Flame,* Vol. 85, pp. 523-525.

Woolley, R. M. and Fairweather, M. 2009, Conditional moment closure modelling of soot formation in turbulent, non-premixed methane and propane flames, *Fuel,* Vol. 88, pp. 393-407.

Wu, J., Chen, L., Bengtsson, P.-E., Zhou, J., Zhang, J., Wu, X. and Cen, K. 2019, Effects of carbon dioxide addition to fuel on soot evolution in ethylene and propane diffusion flames, *Combustion and Flame,* Vol. 199, pp. 85-95.

Xi, J. and Zhong, B. J. 2006, Soot in diesel combustion systems, *Chemical Engineering & Technology: Industrial Chemistry - Plant Equipment - Process Engineering-Biotechnology,* Vol. 29, pp. 665-673.

Xie, X., Zheng, S., Sui, R., Luo, Z., Liu, S. and Consalvi, J.-L. 2021, Effects of Acetylene Addition to the Fuel Stream on Soot Formation and Flame Properties in an Axisymmetric Laminar Coflow Ethylene/Air Diffusion Flame, *ACS Omega,* Vol. 6, pp. 10371-10382.

Xiong, G., Zeng, D., Panda, P. P. and Wang, Y. 2021, Laser induced incandescence measurement of soot in ethylene buoyant turbulent diffusion flames under normal and reduced oxygen concentrations, *Combustion and Flame,* Vol. 230, Article ID: 111456.

Xu, F., Lin, K.-C. and Faeth, G. 1998, Soot formation in laminar premixed methane/oxygen flames at atmospheric pressure, *Combustion and Flame,* Vol. 115, pp. 195-209.

Xu, F., El-Leathy, A., Kim, C. and Faeth, G. 2003, Soot surface oxidation in hydrocarbon/air diffusion flames at atmospheric pressure, *Combustion and Flame,* Vol. 132, pp. 43-57.

Xu, Z., Zhao, H. and Zheng, C. 2015, Accelerating population balance-Monte Carlo simulation for coagulation dynamics from the Markov jump model, stochastic algorithm and GPU parallel computing, *Journal of Computational Physics,* Vol. 281, pp. 844-863.

Xue, X., Meng, L., Ma, Y. and Zhang, C. 2017, Molecular reactive force-field simulations on the carbon nanocavities from methane pyrolysis, *The Journal of Physical Chemistry C,* Vol. 121, pp. 7502-7513.

Yan, Z., Gainey, B. and Lawler, B. 2022, A parametric modeling study of thermal barrier coatings in low-temperature combustion engines, *Applied Thermal Engineering,* Vol. 200, Article ID: 117687.

Yang, S. and Mueller, M. E. 2019, A multi-moment sectional method (MMSM) for tracking the soot number density function, *Proceedings of the Combustion Institute,* Vol. 37, pp. 1041-1048.

Yapp, E. K., Chen, D., Akroyd, J., Mosbach, S., Kraft, M., Camacho, J. and Wang, H. 2015, Numerical simulation and parametric sensitivity study of particle size distributions in a burner-stabilised stagnation flame, *Combustion and Flame,* Vol. 162, pp. 2569-2581.

Yapp, E. K., Patterson, R. I., Akroyd, J., Mosbach, S., Adkins, E. M., Miller, J. H. and Kraft, M. 2016, Numerical simulation and parametric sensitivity study of optical band gap in a laminar co-flow ethylene diffusion flame, *Combustion and Flame,* Vol. 167, pp. 320-334.

Yazicioglu, A. G., Megaridis, C. M., Campbell, A., Lee, K.-O. and Choi, M. Y. 2001, Measurement of fractal properties of soot agglomerates in laminar coflow diffusion flames using thermophoretic sampling in conjunction with transmission electron microscopy and image processing, *Combustion Science and Technology,* Vol. 171, pp. 71-87.

Yu, M., Lin, J. and Chan, T. 2008, A new moment method for solving the coagulation equation for particles in Brownian motion, *Aerosol Science and Technology,* Vol. 42, pp. 705-713.

Yu, M. and Chan, T. L. 2015, A bimodal moment method model for submicron fractal-like agglomerates undergoing Brownian coagulation, *Journal of Aerosol Science,* Vol. 88, pp. 19-34.

Yu, M., Lin, J., Seipenbusch, M. and Cao, J. 2017, Verification of size-resolved population balance modeling for engineered nanoparticles under high concentration, *Chemical Engineering Journal,* Vol. 323, pp. 592-604.

Yuan, H., Kong, W., Liu, F. and Chen, D. 2019, Study on soot nucleation and growth from PAHs and some reactive species at flame temperatures by ReaxFF molecular dynamics, *Chemical Engineering Science,* Vol. 195, pp. 748-757.

Yuan, H., Kong, W. and Xia, J. 2021, Steered molecular dynamics and stability analysis on PAH dimerisation and condensation on fullerene and soot surfaces, *Physical Chemistry Chemical Physics,* Vol. 23, pp. 19590-19601.

Zhang, C., Chen, L., Ding, S., Xu, H., Li, G., Consalvi, J. L., and Liu, F. 2019, Effects of soot inception and condensation PAH species and fuel preheating on soot formation modeling in laminar coflow CH4/air diffusion flames doped with n-heptane/toluene mixtures, *Fuel*, Vol. 253, pp. 1371-1377.

Zhang, Q. 2009, Detailed Modeling of Soot Formation/Oxidation in Laminar Coflow Diffusion Flames*,* PhD Thesis, University of Toronto, Canada.

Zhao, B., Yang, Z., Johnston, M. V., Wang, H., Wexler, A. S., Balthasar, M. and Kraft, M. 2003, Measurement and numerical simulation of soot particle size distribution functions in a laminar premixed ethylene-oxygen-argon flame, *Combustion and Flame,* Vol. 133, pp. 173-188.

Zhao, B., Yang, Z., Li, Z., Johnston, M. V. and Wang, H. 2005a, Particle size distribution function of incipient soot in laminar premixed ethylene flames: effect of flame temperature, *Proceedings of the Combustion Institute,* Vol. 30, pp. 1441-1448.

Zhao, B., Uchikawa, K. and Wang, H. 2007, A comparative study of nanoparticles in premixed flames by scanning mobility particle sizer, small angle neutron scattering, and transmission electron microscopy, *Proceedings of the Combustion Institute,* Vol. 31, pp. 851-860.

Zhao, H., Kruis, F. E. and Zheng, C. 2009, Reducing statistical noise and extending the size spectrum by applying weighted simulation particles in Monte Carlo simulation of coagulation, *Aerosol Science and Technology,* Vol. 43, pp. 781-793.

Zhao, H., Zheng, C. and Xu, M. 2005b, Multi-Monte Carlo method for particle coagulation: description and validation, *Applied Mathematics and Computation,* Vol. 167, pp. 1383-1399.

Zhao, H. and Zheng, C. 2009, Correcting the multi-Monte Carlo method for particle coagulation, *Powder Technology,* Vol. 193, pp. 120-123.

Zhao, H. and Zheng, C. 2011, Two-component Brownian coagulation: Monte Carlo simulation and process characterization, *Particuology,* Vol. 9, pp. 414-423.

Zhao, H., Kruis, F. E. and Zheng, C. 2011, Monte Carlo simulation for aggregative mixing of nanoparticles in two-component systems, *Industrial & Engineering Chemistry Research,* Vol. 50, pp. 10652-10664.

Zhao, J., Lin, Y., Huang, K., Gu, M., Lu, K., Chen, P., Wang, Y. and Zhu, B. 2020, Study on soot evolution under different hydrogen addition conditions at high temperature by ReaxFF molecular dynamics, *Fuel,* Vol. 262, Article ID: 116677.

Zhou, K. and He, Z. 2014, Monte Carlo simulation of aerosol evolution in a planar mixing layer, *International Journal of Numerical Methods for Heat & Fluid Flow,* Vol. 24, pp. 1769-1781.

Zhou, K., He, Z., Xiao, M. and Zhang, Z. 2014, Parallel Monte Carlo simulation of aerosol dynamics, *Advances in Mechanical Engineering,* Vol. 6, Article ID: 435936.

Zhou, K. and Chan, T. L. 2016, Operator splitting Monte Carlo method for aerosol dynamics, Aerosols-Science and Case Studies, IntechOpen.

Zhou, K., Jiang, X. and Chan, T. L. 2020, Error analysis in stochastic solutions of population balance equations, *Applied Mathematical Modelling,* Vol. 80, pp. 531-552.

Zhou, Q., Wang, Y., Wang, X. and Bai, Y. 2022, Experimental investigation into the oxidation reactivity, morphology and graphitization of soot particles from diesel/ n-octanol mixtures, *Journal of Environmental Sciences,* Vol. 112, pp. 218-230.

Zhu, H., Zhou, Z., Yang, R. and Yu, A. 2007, Discrete particle simulation of particulate systems: theoretical developments, *Chemical Engineering Science,* Vol. 62, pp. 3378-3396.